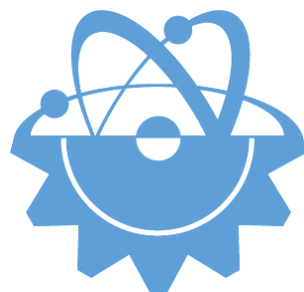


ISSN-Printed: 2536-5010
ISSN-Online: 2536-5134

Volume 14, No 2, 2024

EJT

EUROPEAN JOURNAL OF TECHNIC



Email (for orders and customer services enquiries): info@ineseg.org, ejt@ineseg.org

Visit our home page on www.ineseg.org

All Rights Reserved. No part of this publication may be reproduced, stored in a retrieval system or transmitted in any form or by any means, electronic, mechanical, photocopying, recording, scanning or otherwise, except under the terms of the Copyright, under the terms of a license issued by the Copyright International Engineering, Science & Education Group (INESEG), without the permission in writing of the Publisher. Requests to the Publisher should be addressed to the Permissions Department, International Engineering, Science & Education Group (INESEG), or emailed to info@ineseg.org

Designations used by companies to distinguish their products are often claimed as trademarks. All brand names and product names used in this journal are trade names, service marks, trademarks or registered trademarks of their respective owners. The Publisher is not associated with any product or vendor mentioned in this journal.

This publication is designed to provide accurate and authoritative information in regard to the subject matter covered. It is sold on the understanding that the Publisher is not engaged in rendering professional services. If professional advice or other expert assistance is required, the services of a competent professional should be sought.



EUROPEAN JOURNAL OF TECHNIQUE (EJT)

ISSN-Printed: 2536-5010

ISSN-Online: 2536-5134

Scope: European Journal of Technique (EJT) established in 2010. It is a peer –reviewed international journal to be of interest and use to all those concerned with research in various fields of, or closely related to, Engineering disciplines. European Journal of Technique (EJT) aims to provide a highly readable and valuable addition to the literature which will serve as an indispensable reference tool for years to come. The coverage of the journal includes all new theoretical and experimental findings in the fields of Engineering or any closely related fields. The journal also encourages the submission of critical review articles covering advances in recent research of such fields as well as technical notes.

The scopes include:

- Mechanical Engineering
- Textile Engineering
- Electrical-Electronics Engineering
- Computer and Informatics Engineering
- Civil and Architecture Engineering
- Mining Engineering
- Chemical Engineering
- Metallurgical and Materials Engineering
- Environmental Engineering
- Food Engineering
- Geological Engineering
- Industrial Engineering
- Renewable Energy

EDITORIAL BOARD MEMBERS

Editor-in-Chief

- Musa YILMAZ

Publisher Of Journal

- Heybet KILIÇ

ETHICS and POLICIES

European Journal of Technique (EJT) is committed to following the Code of Conduct and Best Practice Guidelines of COPE (Committee on Publication Ethics). It is a duty of our editors to follow Cope Guidance for Editors and our peer-reviewers must follow COPE Ethical Guidelines for Peer Reviewers. We expect all prospective authors to read and understand our Ethics Policy before submitting any manuscripts to our journals.

Please note that submitted manuscripts may be subject to checks using the iThenticate service, in conjunction with CrossCheck, in order to detect instances of overlapping and similar text.

The [iThenticate](#) software checks submissions against millions of published research papers, documents on the web, and other relevant sources. If plagiarism or misconduct is found, consequences are detailed in the policy.

The chief goal of our policy is threefold: to provide advice for our authors, to maintain the scholarly integrity of our journals and their content, and to detail the ethical responsibilities of EJT, our editors and authors.

We expect all authors to read and understand our ethics policy before submitting to any of our journals. This is in accordance with our commitment to the prevention of ethical misconduct, which we recognise to be a growing problem in academic and professional publications. It is important to note that most incidents of plagiarism, redundant publication, copyright infringement or similar occur because of a lack of understanding, and not through fraudulent intent. Our policy is one of prevention and not persecution.

If you have any questions, please contact the relevant editorial office, or European Journal of Technique (EJT)' ethics representative: ejtineseg@gmail.com

Download a PDF version of the Ethics and Policies [PDF,392KB].

Authors' Responsibilities

Authors should:

- Ensure that all researched work submitted is original, fully referenced and that all authors are represented accurately. The submission must be exclusive and not under consideration elsewhere.
- Provide accurate contact details for a designated corresponding author, who shall be deemed by the publisher and editor as fully responsible for the authorship of the paper and all communications concerning the ethical status and originality of the paper. This includes any queries or investigations that may arise, pre- or post publication.
- Openly disclose the source of all data and third party material, including previously unpublished work by the authors themselves. Anything that could compromise the originality of the submission should be expressly avoided and/or discussed with the editorial office in the first instance.
- Identify any third party material that they intend to include in their article, and obtain written permission for re-use in each instance from the relevant copyright holders. Such permissions should be submitted once the manuscript is accepted, or requires small changes to be accepted. For further guidance on seeking permission to use 3rd party material please see the Rights and Permissions section.
- Openly disclose any conflict of interest - for example, if publication were to benefit a company or services in which the author(s) has a vested interest.

- Expect to formally agree publication terms which defines the author and the publishers rights for the work. Visit our website for further information.
- Expect the editor to scan submissions using plagiarism detection software at [iThenticate](#) to check a paper's originality before sending out for review.
- Fully correspond and comply with the editor and publisher in any requests for source data, proof of authorship or originality in a timely manner, providing reasonable explanation for discrepancies or failures to disclose vital information.
- Fully co-operate with any consequent investigations if the editor and/or publisher are dissatisfied with the evidence available or the explanations provided.
- Expect transparency, efficiency and respect from the publisher and the editor during the submissions process.
- Remain in good communication with both the publisher and the editor.
- When necessary, submit corrigenda in a timely and responsible fashion.
- Co-operate fully with the publication of errata and with the retraction of articles found to be unethical, misleading or damaging.
- Remain in good communication with the editor(s), the publisher and any co-authors.

Editors' Responsibilities

Editors should:

- Read and understand [COPE](#) guidelines as well as EJT's ethics policy, and follow them during all editorial processes.
- Protect the reputation of their journal(s) and published work by only publishing content of the highest quality and relevance in a timely and responsible manner.
- Carry out thorough, objective and confidential peer review for original article submissions that pass the initial quality check and editorial assessment, in adherence with [COPE](#) guidelines and EJT's ethics policy.
- Detail and justify any article types which will not be peer reviewed (e.g. editorials, opinion pieces etc.).
- Provide a transparent review and publication process as far as is possible, with full respect and care paid to the author(s).
- Provide advice and give reasonable explanation and updates to authors during the submissions process and once a decision has been made.
- Allow authors the right to appeal any editorial decision.
- Only accept papers based on the original merit, quality and relevance of their content.
- Support authors in queries concerning the originality of their submissions and request the support of EJT if necessary.
- Advise the publisher of any third party material which has been included for which they do not believe sufficient permission has been cleared.

- Be ready and prepared to publish corrections, corrigenda, errata when necessary, as well as retract articles that (the editor and EJT) deem unethical, misleading or damaging.
- Remain in good communication with both the publisher and the author(s).

Reviewers' Responsibilities

Reviewers should:

- Adhere to EJT's policy of confidential peer review of their journals. This includes, but is not restricted to, keeping their identity hidden from authors and not externally distributing any work that is passed to them for their eyes only.
- Only accept invitations to review work that is relevant to their own expertise and speciality.
- Review submitted work in a responsible, impartial and timely manner.
- Report any suspected ethical misconduct as part of a thorough and honest review of the work.
- Avoid the use of unnecessarily inflammatory or offensive language in their appraisal of the work.
- Accept the commitment to review future versions of the work and provide 'follow up' advice to the editor(s), if requested.
- Seek advice from the editor if anything is unclear at the time of invitation.
- Remain in good communication with both the publisher and the editor.

EJT's Responsibilities

EJT will:

- Protect the reputation of our journals and published work by only publishing content of the highest quality and relevance in a timely and responsible manner.
- Provide detailed information concerning both our understanding of publication ethics and our implementation of the same. Emphasise a desire for prevention, not eventual detection, of ethical misconduct.
- Uphold our COPE membership (or of such similar organisations) and keep our editorial offices, publishing staff and society partners up-to-date with their guidelines and policies, adapting our own where appropriate (and publicising any update).
- When necessary, request proof of originality/accuracy from the corresponding author of any work submitted to any of our journals.
- Use plagiarism detection software when necessary for any submission to any journal at any stage of the submissions and publication process.
- Provide a transparent submissions and publication process, with full respect and care paid to the author. This includes detailed and dedicated instructions to authors for each journal, outlining referencing style, accepted article types and submission processes.
- Investigate thoroughly any suggestion of ethical misconduct detected during any stage of the submissions process. This can include, but is not restricted to, the following: plagiarism, redundant publication, fabrication or misuse of data and authorial disputes.

- When necessary, retract articles that we deem to be unethical, misleading or damaging.
- When necessary, publish errata, corrigenda and retractions in a timely and responsible fashion, detailing the decision online in an open access format and publishing in print as soon as possible.
- Remain in good communication with editors, authors, reviewers and society partners (where applicable).

Further reading

- Authorship of the paper: Authorship should be limited to those who have made a significant contribution to the conception, design, execution, or interpretation of the reported study.
- Originality and plagiarism: The authors should ensure that they have written entirely original works, and if the authors have used the work and/or words of others that this has been appropriately cited or quoted.
- Data access and retention: Authors may be asked to provide the raw data in connection with a paper for editorial review, and should be prepared to provide public access to such data.
- Multiple, redundant or concurrent publication: An author should not in general publish manuscripts describing essentially the same research in more than one journal or primary publication. EJT do not view the following uses of a work as prior publication: publication in the form of an abstract; publication as an academic thesis; publication as an electronic preprint. Information on prior publication is included within each EJT and its journal Guideline for Authors.
- Acknowledgement of sources: Proper acknowledgment.
- Disclosure and conflicts of interest: All submissions must include disclosure of all relationships that could be viewed as presenting a potential conflict of interest.
- Fundamental errors in published works: When an author discovers a significant error or inaccuracy in his/her own published work, it is the author's obligation to promptly notify the journal editor or publisher and cooperate with the editor to retract or correct the paper.
- Reporting standards: Authors of reports of original research should present an accurate account of the work performed as well as an objective discussion of its significance.
- Hazards and human or animal subjects: Statements of compliance are required if the work involves chemicals, procedures or equipment that have any unusual hazards inherent in their use, or if it involves the use of animal or human subjects.
- Use of patient images or case details: Studies on patients or volunteers require ethics committee approval and informed consent, which should be documented in the paper.

EJT has also accessed and learned from the existing policies of other publishers and leading experts as well as open access articles that detail and define ethical misconduct.

- 'Plagiarism and the law', Joss Saunders, Learned Publishing, 23:279-202: <http://www.ingentaconnect.com/content/alpsp/lp/2010/00000023/00000004/art00002>
- iThenticate Plagiarism Resources: <http://www.ithenticate.com/resources/6-consequences-of-plagiarism>

EDITORIAL BOARD MEMBERS

Editor-in-Chief : Musa Yilmaz

International Editorial Board

Aayush Shrivastava University of Petroleum and Energy Studies, Dehradun, India
Abdulkarim Oztekin Batman University, Batman, Turkey
Adelino Pereira Engineering Institute of Coimbra, Portugal
Ahmad Fakharian Islamic Azad University, Qazvin, Iran
Ahmed Saber Cairo University, Egypt
Arvind Kumar Jain Rustam Ji Institute of Technology, India
Aydogan Ozdemir Istanbul Technical University, Turkey
Baseem Khan Hawassa University, Hawassa, Ethiopia
Behnam Khakhi University of California Los Angeles, US
Behnam Mohammadi-ivatloo University of Tabriz, Tabriz, Iran
Bharti Dwivedi Institute of Engineering & Technology, Lucknow, UP, India
Carlos A. Castro University of Campinas – UNICAMP, Brasil
Cafer Budak Dicle University, Turkey
Deepak Kumar University of Petroleum & Energy Studies (UPES), India
Ernesto Vazquez Univerity of Nuevo Leon, Mexico
Faisal Khan COMSATS Institute of Information Technology, Pakistan
Farhad Shahnia Murdoch University, Perth, Australia
Farrokh Aminifar University of Tehran, Iran
Fatih Kocyigit Dicle University, Turkey
Fiaz Ahmad National University of Computer and Emerging Sciences, Pakistan
Gouthamkumar Nadakuditi V R Siddhartha Engineering College, India
Hafiz Ahmed School of Mechanical, Coventry University, UK
Hamed Pourgharibshahi Lamar University, US
Hassan Bevrani University of Kurdistan, Iran
Hayri Yildirim Dicle University, Turkey
Hemant Kumar Gianey Thapar University, Patiala, Punjab, India
Hessam Golmohamadi Semnan University, Semnan, Iran
Heybet Kilic Dicle University, Turkey
Hilmy Awad Helwan University, Cairo, Egypt
Hüseyin Acar Dicle University, Turkey
Idris Candan Kocaeli University, Turkey
Jamshed Ahmed Ansari Sukkur IBA University, Pakistan
José A. Domínguez-Navarro University of Zaragoza, Spain
Kalpana Chauhan Galgotias College of Engineering and Technology, India
Khaled Ellithy Qatar University, Doha, Qatar
Kim-Doang Nguyen South Dakota State University, US
Kundan Kumar KIIT University, India
Lalit Kumar GBPIET Pauri, India
Leila Mokhnache University of Batna 2, Algeria
Linqun Bai ABB Inc., US
Mehmet Emin Asker Dicle University, Turkey
Md Shafiullah King Fahd University of Petroleum & Minerals, Saudi Arabia
Mohamed Shaaban Universiti Malaysia Sarawak, Malaysia
Mohammed Albadi Sultan Qaboos University, Oman
Mohd Tariq Aligarh Muslim University, India
Mousa Marzband Northumbria University, Newcastle upon Tyne, United Kingdom
Necmettin Sezgin Batman University, Batman, Turkey
Neeraj Kanwar Manipal University Jaipur, India
Nishant Kumar Indian Institute of Technology Delhi, India
Nitin Kumar Saxena Wolaita Sodo University, Ethiopia
Nouar Tabet University of Sharjah, UAE
Omar Hafez Umm Al-Qura University, Makkah, Saudi Arabia
Omveer Singh Gautam Buddha University, India
Payam Teimourzadeh Baboli University of Mazandaran (UMZ), Iran
Payman Dehghanian George Washington University, US
Ragab A. El Sehiemy Faculty of Engineering, Kafrelsheikh Univrsity, Egypt
Rajeev Kumar Chauhan Galgotias College of Engineering and Technology, India
Rajiv Singh G.B. Pant University of Agriculture & Technology, India
Reza Sharifi Amir Kabir university Tehran, Iran
Rudranarayan Senapati Kalinga Institute of Industrial Technology, India
Saleh Y. Abujarad Universiti Teknologi Malaysia, Malaysia
Sanjay Dambhare College of Engineering, Pune, India
Saptarshi Roy NIT Warangal, India
Shailendra Kumar Indian Institute of Technology Delhi, India
Shariq Riaz The University of Sydney, Australia
Shengen Chen University of Maine, US
Syafaruddin Universitas Hasanuddin, Indonesia
T. Sudhakar Babu VIT University, Vellore, India
Thamer Alquthami King Abdulaziz University, Saudi Arabia
Theofilos Papadopoulos Democritus University of Thrace, Greece
Uday P. Mhaskar CSA Group, US
Vedat Veli Cay Dicle University, Turkey
Yogesh Rohilla K Lakshmipat University, Jaipur, India
Yunfeng Wen School of Electrical Engineering, Chongqing University, China
Zbigniew M. Leonowicz Wroclaw University of Science and Technology, Poland

Publisher of Journal

Heybey Kilic Dicle University, Turkey / TU Delft, Netherland



CONTENTS

Greenhouse Gas Emission Estimation by Artificial Intelligence	103 - 114
Microstructure and Mechanical Properties of Cold Metal Transfer Welded AA6013/SiC Metal Matrix Composites	115 - 121
Analysis of Emotional Authenticity Displayed by Film Actors Using Image Processing Techniques	122 - 127
The Impact of Locally Available Materials on Architectural Heritage: Preliminary Findings from the Güzelşeyh Pavilion, Türkiye	128 - 135
Agricultural Waste-Based Composite Materials: Recycling Processes, Technical Properties, and Industrial Applications	136 - 145
Speed Control of a Single-Phase Induction Motor Using a Fuzzy Logic Based Hysteresis Band PWM	146 - 153
Effect of Cutting Parameters in Turning of AISI 1015 Steel: Comparison of Dry and MQL Conditions	154 - 159
The Effect Of Thin Film CrC Coating On Microstructure And Microhardness Properties Of Manganese Steel Surface	160 - 163
Automated Fault Classification in Solar Panels Using Transfer Learning with EfficientNet and ResNet Models	164 - 173
Comparison of Graphene Oxide-Titanium Oxide (GO-TiO ₂) Composite Film Coating Methods on Glass Substrates and Surface Characterization Study	174 - 181
Evaluating and Mitigating Cybersecurity Threats from System Update Vulnerabilities through the CrowdStrike Case	182 - 188
Evaluation of the Quality of Ready-Mixed Concrete Used in Building Controlled Structures after Electronic Concrete Monitoring System	189 - 194

Greenhouse Gas Emission Estimation by Artificial Intelligence

Serkan Ertugrul^{1*} and Prof. Dr. Necmettin Sezgin²

¹Batman University, Electrical and Electronics Engineering Department, Batman, Turkey. (e-mail: serkanertugrul@gmail.com).

²Batman University, Electrical and Electronics Engineering Department, Batman, Turkey. (e-mail: necmettin.sezgin@batman.edu.tr).

ARTICLE INFO

Received: Jul., 44. 2023

Revised: Sep., 21. 2023

Accepted: Aug. 28. 2024

Keywords:

Deep Learning

Climate Change

Global Warming

Greenhouse Gas

Artificial Neural Networks

Corresponding author: *Serkan Ertuğrul*

ISSN: 2536-5010 / e-ISSN: 2536-5134

DOI: <https://doi.org/10.36222/ejt.1327275>

ABSTRACT

Human activities, particularly the burning of fossil fuels for energy production, industrial processes, and transportation, release significant amounts of greenhouse gases into the atmosphere. Global agreements such as the Paris Agreement have started expressing the goal of reducing human activities and achieving net zero emissions. It is expected that all countries will set targets and work towards reducing greenhouse gas emissions by implementing sustainable and realistic programs. By utilizing data such as financial indicators, population, afforestation, Human Development Index (HDI), and energy consumption, machine learning methods were employed to calculate future greenhouse gas emission levels in some countries. For this purpose, a comparison was made by using deep learning methods, such as Long Short-Term Memory (LSTM) and a hybrid CNN-RNN model, separately with the help of the MATLAB program. Additionally, future greenhouse gas emission predictions were made by comparing the results of the study using LSTM modeling with the predictions obtained through NARX modeling for time-series data. The aim was to emphasize the need for countries to develop sustainable programs by considering various data in order to achieve their greenhouse gas emission reduction targets.

1. INTRODUCTION

This study aims to calculate future greenhouse gas emission levels in Turkey and the United States using financial, economic, and human development indicators, population data, afforestation rates, and energy consumption data. Through a comprehensive analysis of countries' activities contributing to global warming and by bringing together different data sources and utilizing machine learning methods, the study seeks to determine the potential greenhouse gas emissions of countries and provide possible forecasts for actions to prevent these emissions. Turkey and the United States, with their diverse geographical, economic, and social characteristics, provide an important comparison for the development of strategies to combat climate change. Similarly, by selecting examples from different locations, both developed and developing countries can serve as references for designing and implementing effective policies to reduce greenhouse gas emissions. The study aims to contribute to establishing a sound methodology for planning and implementing measures in industries, agriculture, energy, and other facilities without hindering countries' sustainable development, in order to make the most appropriate plans.

It also conducts comparisons using deep learning methods such as Long Short-Term Memory (LSTM) and hybrid CNN-RNN

models to achieve emission reduction goals. Additionally, future greenhouse gas emission predictions are made by comparing LSTM modeling results with those obtained through NARX modeling for time-series data. This study, by emphasizing the importance of data-driven strategies in combating greenhouse gas emissions, has the potential to contribute to the development of sustainable programs that help countries reach their emission reduction targets.

The increasing population, industrialization, and urbanization have greatly polluted the environment, and the continued use of fossil fuels has resulted in increasing environmental damage [1].

The Keeling Curve is a curve used to describe the increase in carbon dioxide levels in the atmosphere [2]. It was established by Charles David Keeling, who collected samples from the Mauna Loa Observatory (MLO) located 3 km above sea level. The measurements taken between 1958 and 2005 demonstrated a rising curve (the Keeling Curve), providing the first evidence of the warming occurring in the atmosphere [3]. The Record of Atmospheric CO₂ Concentration Measured at the Mauna Loa Observatory from 1958 to 2022 can be seen in Figure 1.

In Article 4 of the Paris Agreement, it is stipulated that greenhouse gas emissions in the atmosphere should reach their peak as soon as possible and then be reduced, with the aim of

achieving a balance between emissions and sinks by 2050. The IPCC (The Intergovernmental Panel on Climate Change)'s Special Report on 1.5 Degrees has highlighted the importance of limiting global temperature rise to 1.5 degrees by 2030 and striving to achieve zero degrees by 2050 for the continuity of natural life. The "Glasgow Climate Pact," previously agreed upon at the 26th Conference of the Parties (COP 26) of the United Nations Framework Convention on Climate Change (UNFCCC), was reiterated as a target during the conference [4].

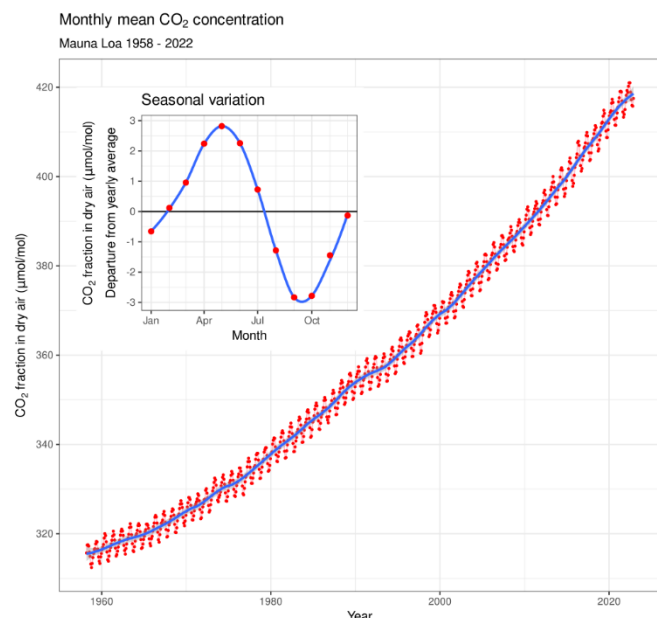


Figure 1. Atmospheric CO₂ concentration measured at the Mauna Loa Observatory (1958-2022) [5]

The increasing population and advancing technology, along with anthropogenic influences, are causing changes in the global climate, which in turn have negative impacts on biodiversity and biological life on Earth [6].

According to the information available on the website of the Ministry of Environment, Urbanization, and Climate Change (2022), the Paris Agreement, which was achieved during COP 21 in 2015, aimed to come into effect after countries responsible for 55% of greenhouse gas emissions committed to fulfilling the conditions outlined in the agreement. This target was achieved on November 4, 2016. The agreement also includes provisions for developed countries to plan the flow of finances in order to ensure low greenhouse gas emissions without compromising food production. Countries that are party to the agreement are required to submit their "National Determined Contributions" that include activities carried out every five years.

According to information published on the United Nations official website in 2022, the Sustainable Development Goals (SDGs) aim to tackle climate change by considering education, health, social protection, and employment opportunities, along with an economic growth strategy. The SDGs emphasize the need to integrate these aspects in the fight against climate change [7].

2. RELATED WORKS

Machine learning methods, specifically "Decision Tree Modeling", "Artificial Neural Networks" and "Support Vector Machines" were employed to predict the trends in carbon dioxide (CO₂) emissions resulting from human activities for

European Union countries and Turkey. The results indicated a decreasing trend in CO₂ emissions in advanced European countries while an increasing trend was observed in Turkey [8].

The Grey Wolf Optimization (GWO) method was applied using data related to Gross Domestic Product (GDP), energy consumption, renewable energy production, population, and urbanization rates. Among various artificial neural network models, the GWO optimization method outperformed others, including Backpropagation Algorithm, Artificial Bee Colony (ABC), and Teaching-Learning Based Optimization (TLBO). The study projected that there would be a reduction in greenhouse gas emissions in Turkey until 2030 [9].

Another study used an artificial neural network model to investigate the intensity of greenhouse gas emissions in Australia, Brazil, China, India, and the United States. The model considered nine different parameters, including economic growth, energy consumption, financial development, research and development (R&D), foreign direct investment, trade openness, industrialization, and urbanization. Different models were applied to various countries using quarterly data from 1980 to the end of 2015. The Backpropagation Algorithm with a Multi-Layer Perceptron achieved nearly zero error in prediction [10].

To model CO₂ emissions using energy consumption data for various energy sources and Gross National Product (GNP) between 2000 and 2009, the Group Method of Data Handling (GMDH) among artificial neural network models was employed. The study observed that the model, despite providing R² (R-squared) values close to zero for training, testing, and overall data, achieved successful predictions with values close to zero for the Absolute Average Relative Deviation (AARD) [11].

In a study encompassing countries in Southeast Asia, such as Malaysia, Indonesia, Singapore, and Vietnam, the modeling of carbon dioxide (CO₂) emissions resulting from various energy sources was conducted. Given the significance of energy consumption in the economy, Gross Domestic Product (GDP) data, an economic indicator, was considered. Two artificial neural network (ANN) models with normalized radial basis and tansig transfer functions were employed for modeling CO₂ emissions successfully [12].

In this study, particular emphasis is placed on the utilization of a broader range of data, including economic indicators, population, and afforestation rates, alongside energy-related information. Additionally, the study highlights the wider time span covered in the dataset compared to previous studies.

3. MATERIAL and METHODOLOGY

3.1. Data Collection

Since 1990, many countries have initiated efforts to combat greenhouse gas emissions by establishing greenhouse gas inventories through the Vienna Convention. However, with the Paris Agreement in 2015, countries started to place more importance on greenhouse gas inventories and improve their record-keeping based on their commitments. In this study, monthly data was obtained, but if such data was unavailable, annual data was used instead. The annual data was then converted into monthly distributions by considering the "Keeling Curve," which predicts monthly variations in a sinusoidal pattern that increases each year.

For each country, the data used in this study was obtained within specific time intervals. The study begins with data from January 1970 and ends with data from December 2022.

Between these dates, any missing data is generally filled using the earliest recorded data from January 1970 up to the first available data point. If the last recorded data is from a date prior to December 2022, it is used to fill in the missing data until December 2022. If sufficient data is not available, it means that particular data is not used for that country. In the context of this study, the Table 1 indicates which dataset was used for the United States and Turkey, denoted by a "+" sign.

TABLE I

THE DATA MARKED WITH "+" WAS USED FOR GREENHOUSE GAS EMISSION ESTIMATION FOR THE UNITED STATES (USA) AND TURKEY (TUR)

Definition	Unit	USA	TUR
Total CO ₂ Emissions from Energy	Metric Tons of Carbon Dioxide	+	-
Greenhouse Gas Emissions	Mton CO ₂ e	-	+
Human Development Index	Index	+	+
Forest Area	Forest Land Area in km ²	+	+
Population	People	+	+
Gross Domestic Product - GDP	Base Year 2010=100 (USD per capita)	+	+
Net National Income	Base Year 2010=100 (USD per capita)	+	-
Gross National Income - GNI	Base Year 2010=100 (USD per capita)	+	+
Producer Price Index for All Commodities	Base Year 2010=100	+	+
Consumer Price Index	Base Year 2010=100	-	+
Financial Market Prices End-of-Period	Base Year 2010=100	+	-
Industrial Production Economic Activity Index	Base Year 2010=100	+	+
Long-term Investment Rates, Annual Percentage	Base Year 2010=100	+	-
Primary Energy	MLN_TOE	-	+
Renewable Energy	KTOE	-	+
Total Primary Energy Consumption	(Trillion Btu)	+	-
Total Renewable Energy Consumption	(Trillion Btu)	+	-

Greenhouse Gas Data: Greenhouse gas data includes all fossil CO₂ sources related to the combustion of fossil fuels, metal production processes, urea production, or agricultural solvent use. However, these data do not include emissions from savannah burning, forest fires, land use changes, forestry, and biomass burning. Emissions from fluorinated gases are based on country reports whenever possible, and if not available, they are included in the reports using data from the United Nations Environment Programme (UNEP), scientific literature, and expert opinions. For countries other than the United States, the studies were conducted based on greenhouse gas emission data available in the Emissions Database for Global Atmospheric Research (EDGAR) system. Table 2 presents the greenhouse gas emission values in Mton CO₂e for selected countries and sectors during the years 1970 and 1974.

TABLE II

GREENHOUSE GAS EMISSION VALUES IN MTONCO₂E FOR SOME COUNTRIES AND SECTORS FOR 1970 AND 1974 [13]

EDGAR Country Code	Country	1970	1971	1972	1973	1974
TUR	Turkey	103	108	116	122	126
GBR	United Kingdom	886	877	846	886	841
USA	United States	5791	5667	5934	6136	5966

Population Data: The work of the United Nations Statistics Division utilized data from country population records to compile the available information.

Human Development Index (HDI) data is obtained from the official website of the United Nations Development Programme (UNDP), which has been maintaining records on an annual basis since 1990 [14].

Gross National Income (GNI) data, which represents gross domestic product excluding production subsidies, net income from abroad, and net taxes, can be found in the inventory of economic data maintained by the Organisation for Economic Co-operation and Development (OECD). However, these values do not include income sent by foreigners in the country back to their own countries. Total annual Gross National Income values in terms of per capita dollars were used in this study [15].

Net National Income (NNI) is derived by subtracting the depreciation of fixed capital assets from gross national income and is included in the inventory of economic data for member countries maintained by the Organisation for Economic Co-operation and Development (OECD). In this study, the total annual Net National Income value in terms of per capita dollars was used [16].

Gross Domestic Product (GDP): The United Nations Statistics Division (United Nations, 2023) provides access to Gross Domestic Product (GDP) data, which represents the annual final goods and services for member states based on their statistical data. Per capita GDP data in terms of dollars for the respective countries in the year 2021 were used [17].

Financial Indicators: The International Monetary Fund (IMF) was established to meet the payment balance needs of its member countries [18]. The IMF utilizes various indicators, such as the consumer price index, producer price index, seasonally adjusted industrial production, industrial production economic activity index, and end-of-period financial market prices, to maintain inventories related to the financial conditions in countries. These indicators are evaluated in percentage units, with the data based on the 2010 figures as the baseline. The data utilized for these indicators are stored in the International Financial Statistics database.

The Organization for Economic Cooperation and Development (OECD) or the Organisation for Economic Co-operation and Development provides a wealth of data in the "Main Economic Indicators" (MEI) section on their website. These data cover various areas such as transportation, economic projections, finance, production, education, agriculture, and fisheries. Among these data, there is the indicator of "Long-term Investment Rates." With globalization, maturing markets, complex actors, advancing technologies, and evolving regulatory frameworks, financial indicators have gained importance. Data such as "Long-term Investment Rates" are used because they indicate the financial conditions of countries, which are crucial for achieving net-zero emission targets in greenhouse gas emissions through strong and evolving financial circumstances [19].

Primary energy sources are the natural forms of energy that are used directly. These sources include coal, oil, natural gas, nuclear energy, biomass, hydro power, solar energy, wind energy, wave energy, and tidal energy. These primary energy sources can be further processed or transformed into secondary energy sources. Secondary energy sources include electricity, gasoline, diesel, kerosene, secondary coal, coke, petroleum coke, air gas, and liquefied petroleum gas (LPG). Among renewable energy sources, there are hydro power, solar energy,

biomass, wind energy, geothermal energy, wave energy, tidal energy, and hydrogen. The increase in population, rise in living standards, and technological advancements lead to an increased energy demand. This growing energy demand can be met through planned use of non-renewable energy sources and greater utilization of renewable energy sources [20].

According to the Organisation for Economic Co-operation and Development (OECD) website, primary energy supply refers to the energy production needed, and in the data used, it is calculated based on the calorie content of energy products, expressed in metric tons of oil equivalent (toe). One metric ton of oil equivalent is equal to 107 kilocalories or 41.868 gigajoules [21].

According to the Organisation for Economic Co-operation and Development (OECD) website, renewable energy sources contribute to primary energy supply. Renewable sources include hydro power, geothermal energy, solar energy, wind energy, tidal energy, wave energy, hydrogen, and biofuels. These contribute to primary energy supply in terms of primary energy equivalents, except for pumped hydro storage method. Additionally, renewable energy includes bio-gasoline, biodiesel, biogas, renewable energy derived from urban waste, biomass (material obtained from living or recently living organisms) directly or indirectly produced fuels, wood, plant residues used for energy production, ethanol, animal materials or waste, sulfite liquor, and waste disposed of in a centralized location for heat and/or electricity production [22].

U.S. Primary and Renewable Energy Consumption with CO2 Emission Data: The U.S. Energy Information Administration (EIA) provides access to monthly CO2 emission data for total energy in the United States starting from January 1973 on their official website. Additionally, both Primary Energy Consumption and Renewable Energy Consumption data can be accessed in British Thermal Units (BTU) on an annual basis starting from January 1973 [23].

Afforestation: According to the official website of the World Bank, the organization collaborates with various countries and partners to promote sustainable forest management through informative programs related to the forest sector, strengthening countries' political commitments through long-term programs aimed at sustainable forest management. Forests contribute to national economies in areas such as employment, food, and energy, and play a significant role in addressing climate change. Particularly, wood-based fuels serve as an important energy source for Africa and offer an alternative to fossil fuels. Therefore, sustainable forest management is of great importance. Forests are also crucial ecosystems for soil fertility, water basins, and habitats for living beings. One of their most important features is their ability to absorb CO2 from the atmosphere, thus helping to mitigate climate change [24].

3.2. Data Organisation

For this study, January 1970 was established as the starting point, and December 2022 was used as the endpoint for data collection. During this timeframe, some data gaps were identified. These missing data points either pertained to periods before the initial recorded data or could be from periods preceding December 2022, which was the final data point. In such cases, missing data points were filled by extending the data from the initial recorded date in January 1970 up to the respective starting date of the missing data. Similarly, if the final recorded data date was earlier than December 2022, any missing data within that period was completed using the final

recorded data. Input data sets with extensive missing data were excluded from the study. This approach ensured that gaps resulting from missing data were addressed, rendering the data suitable for analysis.

For the United States, greenhouse gas emissions and primary and renewable energy source data were collected on a monthly basis. For Turkey, greenhouse gas emission data was obtained annually. These yearly data sets were transformed into monthly data points following a sinusoidal pattern for each year, considering the "Keeling Curve." Other data sources were retrieved from databases available on the official websites of the United Nations, IMF, OECD, and the European Union. Some economic or financial data were converted into percentage values based on the 2010 data, or they were used in their converted forms as provided by the data source organization. Yearly data for population and forest areas were maintained at constant values for each month within the respective year. In addition, for other input data, if yearly data were available, they were evenly distributed across each month.

3.3. Deep Learning (LSTM and CNN-RNN) and ANN

In the study that combines data such as greenhouse gas emissions, economic indicators, population, and afforestation for the purpose of deep learning, each data was individually evaluated and a single output was obtained by predicting future data that would encompass all the information in a single time series.

To achieve good performance in deep learning, it is essential to ensure an adequate amount of data. Additionally, in deep learning, networks can be observed during training to see how they adapt to the curve. The network continues training with iterations. Throughout the training process, corrected training accuracy curve, uncorrected training curve, and validation curve can be observed. Additionally, the loss training accuracy curve, uncorrected training curve, and validation curve can also be observed.

Initially, the LSTM Regression algorithm, which is one of the deep learning methods, was used. Then, a CNN-RNN hybrid method, another deep learning approach, was applied specifically to greenhouse gas emissions data of the relevant countries, and the results obtained from the LSTM Regression algorithm were compared for validation.

Each data was analyzed separately using the Deep Network Designer. The dataset used for analysis included known data from January 1970 to December 2022. Based on this study, predictions were made for the period from January 2023 to March 2028. The predicted data covered approximately 10% of the available information. Thus, predictions were made using 636 monthly data points for each data and 63 months of future predicted data were obtained. In total, a dataset of 699 monthly data points was generated.

Artificial Neural Network (ANN) with NARX modeling can be used for time series forecasting. With its feedback structure, it is a dynamic ANN model commonly used for nonlinear data inputs. In the predictions made using artificial neural networks, greenhouse gas emissions were selected as the target variable, and other data were used as input variables. The accuracy of the predictions was tested using a randomly selected 15% of the data with the Regression R-value. The NARX model based on the artificial neural network demonstrated successful prediction of greenhouse gas emissions at the country level with different input variables, confirming the relationships between the data [25].

3.3.1. Deep Learning with LSTM

Long Short-Term Memory (LSTM) is different from feedforward artificial neural networks; it has a recurrent structure. After the preliminary data preparation, the Deep Network Designer tool in Matlab was used for each data input. In the design of deep learning, a sequence was created using layers from the library. A Sequence-to-Sequence LSTM regression model with 5 different layers was chosen for prediction.

The first layer used a time series data sequence as input. In the second layer, "Long Short-Term Memory (LSTM)" was employed for predicting from time series or sequential data. The LSTM layer was trained, and the output data was obtained with only a single time series data input. 128 hidden units were chosen for the LSTM layer. The LSTM layer is a recurrent neural network (RNN) layer that learns long-term dependencies between data points based on the time series.

In the third layer, a "Dropout Layer" was used with a probability value of 0.5 to prevent overfitting and underfitting, aiming to improve the model's performance in deep learning tasks. In the fourth layer, a "Fully Connected Layer (FC Layer)" was used to connect to the neuron layer from the previous layer. Weight matrices and bias were included in the computations to enhance the outputs, and a single output was selected.

The final layer used a "Regression Layer" to calculate Mean Squared Error (MSE) for regression tasks. It provides an absolute value by calculating the average of the squared differences between the actual value from the model outcome and the target value, thus measuring the distance.

In the "Deep Network Designer," a network was created sequentially using single-row data input, consisting of an input layer, LSTM layer, a "drop" layer, a fully connected layer (FC) with a single output, and a regression layer. The analysis was performed using a 5-layered "Sequence-to-Sequence LSTM Regression model" without encountering any errors or warnings. The design and suitability of the model were verified after configuring the layers and settings in the "Deep Network Designer" in Matlab, as shown in Figure 2 in the research.

ANALYSIS RESULT				
	Name	Type	Activations	Learnables
1	input Sequence input with 1 dimensions	Sequence Input	1	-
2	lstm LSTM with 128 hidden units	LSTM	128	InputWeights 512×1 RecurrentWeights 512×1 Bias 512×1
3	drop 50% dropout	Dropout	128	-
4	fc 1 fully connected layer	Fully Connected	1	Weights 1×128 Bias 1×1
5	regressionoutput mean-squared-error	Regression Output	1	-

Figure 2. Stages of Deep Learning with LSTM

In deep learning, achieving good performance requires ensuring sufficient data size. Additionally, in the "Training Options" section of deep learning, options for training the network are observed. In the "Solver" section, options for optimizers such as Stochastic Gradient Descent with Momentum (SGDM), Root-mean-square Propagation (RMSProp), and Adaptive Moment Estimation (Adam) can be selected for training. With "Adam," different learning rates can be specified for different layers, and it performs well in terms of training speed. In this study, Adam was employed, enabling the setting of distinct learning rates for individual layers, resulting in enhanced training speed. A learning rate of 0.005

was chosen for this study. Additionally, "MaxEpochs" was set to 500, "Batch Size" to 128, "Gradient Threshold" to 1, and for weight decay, the "Gradient Threshold Method" was selected as "L2 norm."

3.3.2. Deep Learning with CNN-RNN

In this study, a hybrid approach combining CNN and RNN was employed to make predictions for future. CNN was used to extract features related to the given sequence in the time steps, while RNN was utilized to predict the values in the subsequent sequences over time.

Pre-trained CNN models have been found to expedite learning and enhance accuracy by leveraging weights from similar existing problems. In Inception pre-trained networks, operations are modularly processed in self-filtering and pooling layers simultaneously. Meanwhile, Xception networks, an extension of Inception, utilize smart depthwise and pointwise convolutions [26]. Recurrent Neural Networks (RNNs) are adept at handling time-series data like speech recognition, thanks to their ability to exhibit temporal dynamics by forming loops between nodes. Derived from feedforward neural networks, RNNs effectively process variable-length input sequences for tasks such as handwriting or speech recognition.

The study was conducted using the "Deep Learning Toolbox," one of the Matlab tools. In addition, in the example, the Xception network architecture was chosen, with 600 "MaxEpochs," a learning rate of 0.00611, feedforward learning, and the "adam" solver. Approximately 90% of the data was used for training purposes, and the remaining 10% was used for testing. Training was conducted using the "Deep Learning Toolbox" with Bayesian Optimization. After a correlation method based on sMAPE (Symmetric Mean Absolute Percentage Error) was used to verify the percentage error between the tested and predicted values, R-values were examined. Following these stages, predictions were made for future data, i.e., the steps after the last sequence, using the trained network [27].

In this study, which utilized a hybrid approach combining CNN-RNN algorithms, the results obtained with the LSTM algorithm, previously used for predicting the greenhouse gas emission levels of the United States and Turkey, for the next 63 months were compared. This comparison allowed for assessing the accuracy solely for the target data, thus providing a preliminary comparison for the next artificial neural network study.

3.3.3. Artificial Neural Networks (ANNs)

In this study, deep learning models were employed to make predictions about the future using data from the United States and Turkey. After this stage, predictions were made using a time-series neural network tool in an artificial neural network, and the accuracy of these predictions was evaluated.

Predictions regarding the future were made using deep learning, employing different data for the United States and Turkey. Subsequently, greenhouse gas emission predictions were conducted using the artificial neural network time series tool, utilizing relevant data for different countries. The greenhouse gas emission predictions obtained with ANN, considering data on energy, economic, developmental, population, and deforestation for each country, were compared and evaluated against the results obtained from LSTM and CNN-RNN studies.

For each dataset, Deep Network Designer was used separately to obtain data up to December 2022, which accounted for 10%

of the available data. In other words, predictions were made for the future from January 2023 to March 2028. Thus, for each dataset, predictions were made for the next 63 months using a total of 636 months of data, resulting in 699 months of data in total.

NARX modeling can be used for predictive purposes in time series data. It is a dynamic artificial neural network model typically employed for non-linear data inputs in feedback-used networks [28]. A network structure was created using the 'NARX Neural Network' in Matlab with the 'ntstool', as seen in Figure 3.

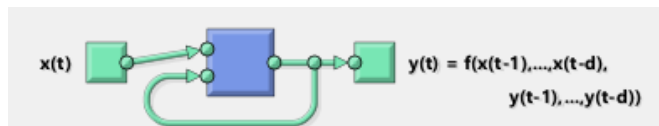


Figure 3. Illustrates the structure of the NARX (Nonlinear AutoRegressive with eXternal (eXogenous) Input) model ($x(t)$ input sequences, past values of $y(t)$, $y(t-d)$ prediction sequences)

Nonlinear AutoRegressive with eXternal (eXogenous) Input (NARX) modeling was used with random selections and Bayesian Regularization after data preprocessing. Performance measurement was done using Mean Squared Error (MSE) and the correlation coefficient (R). In Matlab's "ntstool," the NARX model was selected, and for the United States, "Total Energy CO₂ Emission" data was chosen as the output data, while the others were selected as input data. For the other countries, "Greenhouse Gas Emission" data was selected as the target data, and the other data were used as input.

In the random selections, 70% of the data was used for training purposes, 15% was used for validation, and the model was trained based on validation data. Once validation values were reached, the training was completed. The remaining 15% was used for testing.

The number of hidden layers to be used in the NARX neural network model and the "number of delays (d)" were selected. The network was set to "open loop."

In Figure 4, following the selection of the 'NARX Neural Network' application using Matlab's 'ntstool', details such as the number of input data, output data, hidden and output layer information, as well as output data counts, can be observed. Additionally, within the hidden layer, the circular shape indicates the time interval between input and output data. In the 'ntstool', the term 'number of delays (d)' represents the time interval between input and output data. This parameter determines the time interval over which past data will be used in predicting future values. A higher value of 'd' allows for predictions considering a longer time interval, while a lower value of 'd' results in predictions based on a shorter time interval. This parameter is crucial for making accurate predictions.

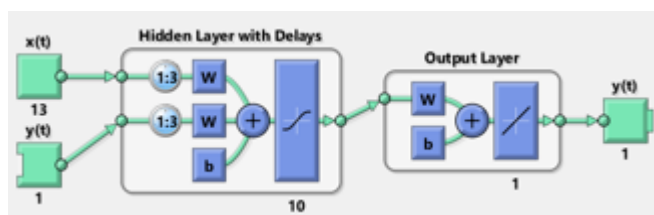


Figure 4. An example neural network model obtained from the Matlab application

Three training algorithms were available: "Levenberg-Marquardt," "Bayesian Regularization," and "Scaled Conjugate Gradient." Bayesian algorithm, although it may take

some time for datasets with noise and limited data, tends to provide good results as the R-value approaches 1. The goal of the training was to achieve results as close as possible to this outcome.

4. RESEARCH RESULTS AND DISCUSSIONS

4.1. Future Predictions with LSTM

In the prediction made for the United States, 14 features were used, and greenhouse gas emissions were selected as the target variable and others were used as input. For each feature, the "Deep Learning" LSTM algorithm was applied, resulting in RMSE values ranging from 0.3 to 0.1 and close-to-zero values for the loss curve. The graph Figure 5 illustrates the prediction data for the United States' "Total Energy CO₂ Emissions" after deep learning training, starting from January 2023 and covering a future period of 63 months.

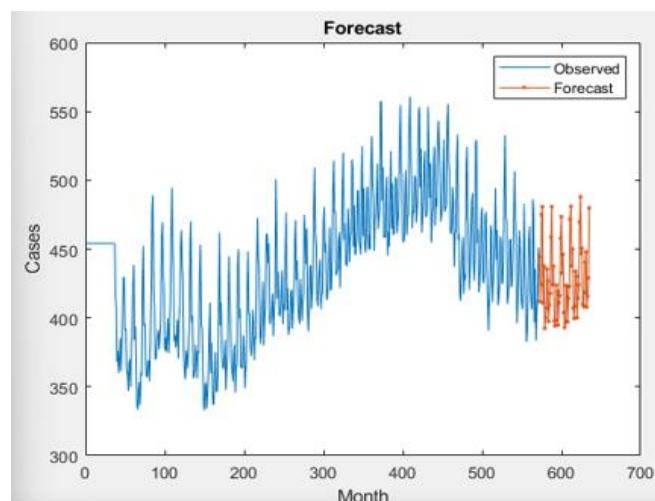


Figure 5. Predicted values for monthly "Total Energy CO₂ Emissions" in the United States using "Deep Learning" after training

In the prediction made for Turkey, 10 input variables were used, and one greenhouse gas emissions target was set. For each input variable, LSTM Regression algorithm was used in Deep Learning to perform the training. The RMSE values obtained during the training process range from 0.3 to 0.1, and the values on the "Loss" curve are close to 0. The graph Figure 6, depict the greenhouse gas emissions for Turkey and the corresponding prediction data for the future 63 months obtained through the training using deep learning.

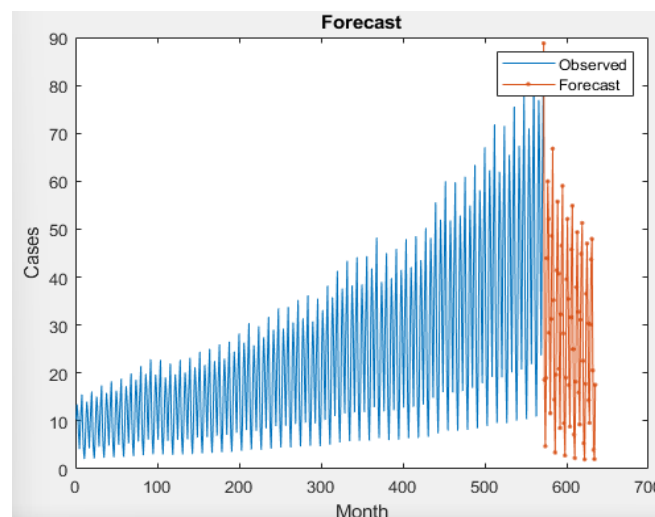


Figure 6. Predicted values for Turkey's annual "Greenhouse Gas Emissions" in the future after training using Deep Learning

The results obtained from the LSTM Deep Learning model for the mentioned data showed significantly low RMSE values compared to the highest values in the dataset. This indicates that the model has learned the data well and achieved low error values. The low RMSE values suggest that the model's predictions are close to the actual values and it performs well overall on the dataset. These results demonstrate that the LSTM Deep Learning model can effectively process the data and make reliable predictions. In the study conducted with Artificial Neural Networks (ANN), greenhouse gas emission values will be used as the target data, while the following data will be used as input data.

For the USA and Turkey, in Table 3 and Table 4, RMSE values and the ratios of RMSE values relative to the maximum value are observed to be below 5% and 8%, respectively.

TABLE III

THE RMSE VALUES FOR THE USA AND THE RATIOS OF RMSE VALUES RELATIVE TO THE MAXIMUM VALUE ARE OBSERVED

Definition	RMSE	The percentage ratios of RMSE relative to the maximum value
Total CO ₂ Emissions from Energy	27.56	4.914546071
Human Development Index	0.00	0.280473505
Forest Area	1717.50	0.055386253
Population	3026763.44	0.922620956
Gross Domestic Product - GDP	3.82	2.426800261
Net National Income	4.64	2.995560233
Gross National Income - GNI	2.969	2.226214247
Producer Price Index for All Commodities	1.72	1.255222449
Financial Market Prices End-of-Period	4.17	2.957979744
Industrial Production - Seasonably Adjusted	3.0039	2.629033725
Industrial Production Economic Activity Index	3.35	2.894096362
Long-term Investment Rates, Annual Percentage	0.21	1.338772846
Total Primary Energy Consumption	358.94	3.714064517
Total Renewable Energy Consumption	51.3992	4.282378073

TABLE IV

THE RMSE VALUES FOR TURKEY AND THE RATIOS OF RMSE VALUES RELATIVE TO THE MAXIMUM VALUE ARE OBSERVED

Definition	RMSE	The percentage ratios of RMSE relative to the maximum value
Greenhouse Gas Emissions	7.2559	7.713234463
Human Development Index	0.0044	0.520502626
Forest Area	902.44	0.407869972
Population	578260.00	0.680696704
Gross Domestic Product - GDP	1.4668	1.251027961
Gross National Income - GNI	1.9891	1.693839015
Producer Price Index for All Commodities	17.49	6.453204511
Consumer Price Index	72.15	11.54145272
Industrial Production - Seasonably Adjusted	17.56	8.306708832
Industrial Production Economic Activity Index	24.4698	10.25239306
Primary Energy	355.1154	2.692835215
Renewable Energy	1420200.00	7.288631733

The greenhouse gas values for the years 2020 to 2027 for two countries, as well as the estimated values using the LSTM Deep Learning model for 2023 and subsequent years, are shown in Table 5 in "Mton CO₂e" units.

TABLE V

ACTUAL VALUES FOR "GREENHOUSE GAS EMISSION" BEFORE 2022 IN 'MTONCO₂E' UNITS AND ESTIMATED VALUES FOR 2023 AND BEYOND USING LSTM DEEP LEARNING

	2020	2021	2022	2023	2024	2025	2026	2027
USA	4580	4903	4892	5136	5248	5028	4761	5033
Turkey	586	627	627	523	519	518	542	547

4.2. Greenhouse Gas Emissions - Future Prediction with CNN-RNN and Comparison with LSTM Results

In the context of future prediction using "Deep Learning," the CNN and RNN models were combined and the following regression value was obtained as seen in Figure 7 and 8 for the USA and Turkey, respectively.

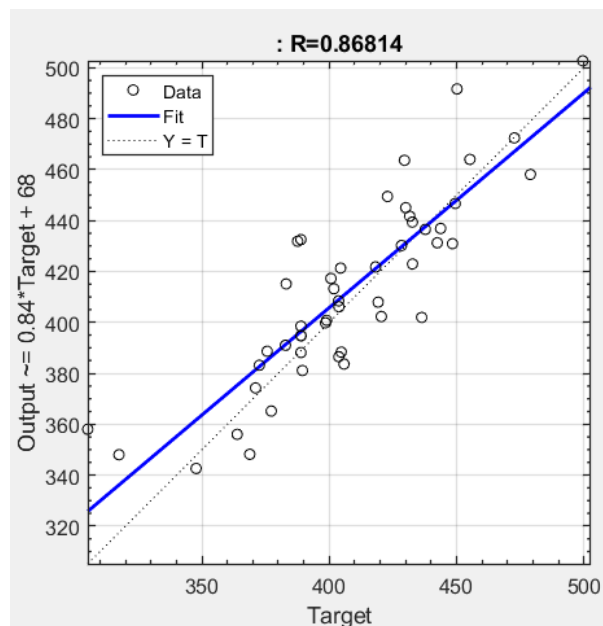


Figure 7. Regression value obtained using CNN and RNN models combined in a hybrid manner for the USA

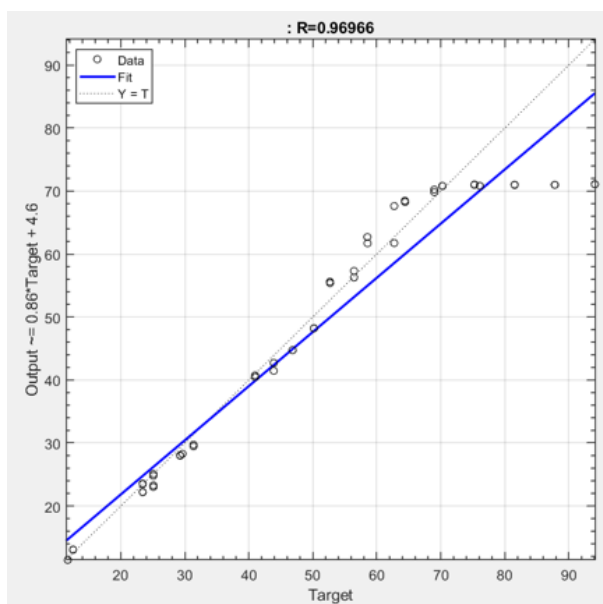


Figure 8. Regression value obtained from the hybrid use of CNN and RNN models for Turkey

The comparison of the R values obtained from the training with the Greenhouse Gas Emission data using the Deep Learning CNN-RNN hybrid model can be seen in Table 6. As observed, the values are close to 1, indicating the success of the training and suitability for prediction studies.

TABLE VI

THE R VALUES OBTAINED THROUGH MODELING WITH THE CNN-RNN HYBRID ALGORITHM IN DEEP LEARNING USING GREENHOUSE GAS EMISSION DATA FOR THE UNITED STATES AND TURKEY

	USA	Turkey
R Value	0,86814	0,96966

Table 7, along with Figures 9 and 10, compare the future greenhouse gas emission predictions obtained through the hybrid application of CNN-RNN using "Deep Learning" with the predictions obtained through LSTM using the Deep Learning method. As seen in the visualization, the results are close to each other.

TABLE VII

MONTHLY GREENHOUSE GAS EMISSION CNN-RNN AND LSTM PREDICTIONS (2025) FOR THE UNITED STATES AND TURKEY IN 'MTON CO₂E' UNITS WITH PERCENTAGE ERRORS

Month (2025)	USA			Turkey		
	CNN-RNN	LSTM	% Error	CNN-RNN	LSTM	% Error
1	422,5	434,2	2,76	17,2	18,299	-6,38
2	443,2	437,2	-1,37	14,44	7,5391	47,81
3	475,8	459,5	-3,42	30,05	26,077	13,23
4	506,8	480,1	-5,26	57,14	51,959	9,07
5	448,7	436,6	-2,69	68,1	75,239	-10,49
6	453,3	437,9	-3,40	55,54	50,567	8,95
7	408,9	407	-0,47	32,21	32,53	-0,99
8	414,2	386,8	-6,61	24,16	19,813	18,01
9	432	378,1	-12,48	52,65	43,071	18,20
10	461,5	390,2	-15,45	69,55	70,684	-1,64
11	454,6	386,3	-15,03	69,65	83,501	-19,89
12	419,2	394,7	-5,86	30,36	38,747	-27,62

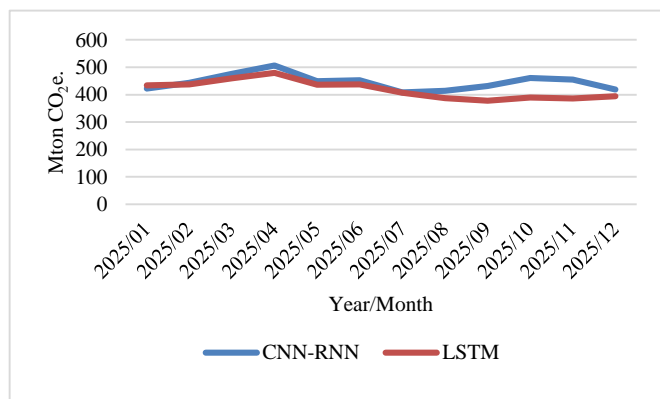


Figure 9. Comparison of Estimated Data for the Months of 2025 for the USA, Obtained with Deep Learning – CNN-RNN Hybrid (Blue Lines) and Obtained with Deep Learning - LSTM Algorithm (Red Line)

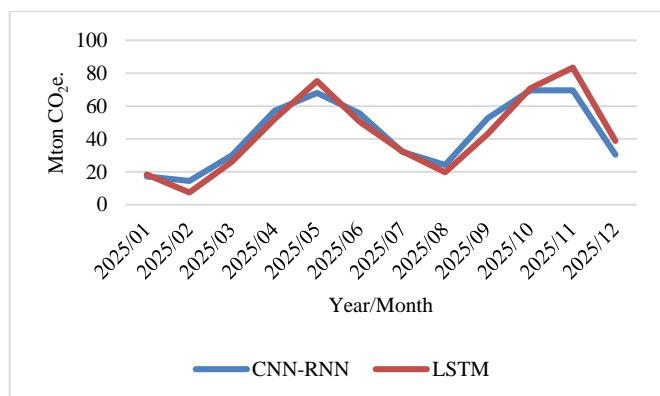


Figure 10. Comparison of Estimated Data for the Months of 2025 for Turkey, Obtained with Deep Learning – CNN-RNN Hybrid (Blue Lines) and Obtained with Deep Learning - LSTM Algorithm (Red Line)

In ANN, greenhouse gas emission values were used as the output data. Therefore, before using the LSTM prediction results for the years 2023 and beyond, the predictions made using the CNN-RNN Hybrid model through Deep Learning were compared with the prediction data obtained using the Deep Learning method. The comparisons yielded similar results, and the reliability of the LSTM Deep Learning method was tested prior to conducting the work with ANN. Table 8 presents the annual estimated greenhouse gas emission values, along with error values, for both the USA and Turkey. These values closely align with the total values.

TABLE VIII

ANNUAL GREENHOUSE GAS EMISSIONS FOR THE UNITED STATES AND TURKEY FOR THE YEARS 2023 AND BEYOND, CALCULATED USING DEEP LEARNING WITH CNN-RNN HYBRID AND LSTM MODELS (IN MTON CO₂E UNITS)

Year	USA			Turkey		
	LSTM	CNN-RNN	Percentage Difference	LSTM	CNN-RNN	Percentage Difference
2023	5094	5136	0,82	530	523	-1,32
2024	5236	5248	0,23	524	519	-0,95
2025	5341	5028	-5,86	521	518	-0,58
2026	5325	4761	-10,59	519	542	4,43
2027	5285	5033	-4,77	516	547	6,01

4.3. ANN results

The "ntstool" application available in the Matlab program was used to calculate future predictions for the country using the LSTM algorithm and Deep Learning method. These predictions were made using both the entire dataset and the target variable of greenhouse gas emissions. The aim is to effectively establish the relationship between the data variables that influence greenhouse gas emissions for the respective country. The Artificial Neural Network method utilized the Bayesian Regulation training algorithm with a time-series NARX neural network model.

For the USA, after selecting the 'NARX Neural Network' application with Matlab's 'ntstool,' the number of time-series input data used is 13, the number of time-series output data is 1, there are 12 hidden layers, and 1 output layer can be observed. The time interval or delay number between input and output data was set to 5, and prediction results were obtained. For Turkey, after selecting the 'NARX Neural Network' application with Matlab's 'ntstool,' the number of time-series input data used is 11, the number of time-series output data is 1, there are 10 hidden layers, and 1 output layer can be observed. The time interval or delay number between input and output data was set to 2, and prediction results were obtained. In the study conducted for the USA, when the number of hidden layers is chosen as 10 and the delay number is 2, an R value of 0.96974 is obtained, but the desired value is not achieved with an R value of 0.67255 for the test. However, different hidden layers and delay numbers can be tried. In this way, both training and test R values can be examined, and hidden layer and delay values can be selected for the research. Sample operations for different hidden layers and delay values can be seen in Table 9 for the USA. Of course, with repeated trials using similar data, different R values can be obtained, so the study can be concluded when the most suitable values are determined. In this study, for the USA, 15 hidden layers and 5 delay values were selected, and for Turkey, 10 hidden layer numbers and 2 delay numbers were preferred.

TABLE IX

THE R VALUES OBTAINED FOR THE TRAINING AND TESTING OF THE NARX BAYESIAN MODEL USED WITH THE ANN 'NTSTOOL' TOOL FOR THE USA

USA		R Values		Process Completion Reason
Hidden Layers	Delay Numbers (d)	Training	Test	
10	2	0.98882	0.91281	Mu Coefficient
10	5	0.96774	0.92773	Mu Coefficient
14	2	0.99650	0.92802	Mu Coefficient
14	5	0.97995	0.87176	Mu Coefficient
15	5	0.99616	0.93254	Mu Coefficient
15	2	0.96987	0.67255	Mu Coefficient
16	2	1.00000	0.86903	Mu Coefficient
16	5	0.98008	0.81632	Mu Coefficient
20	2	0.99972	0.96141	Mu Coefficient
20	5	1.00000	0.99525	Mu Coefficient

In Figure 11 for the USA and Figure 12 for Turkey, information regarding the training algorithms and processes is displayed. During the neural network training, the training concluded when the 'Mu' coefficient indicated that the weights in neurons had achieved their optimal performance and further improvement was not possible.

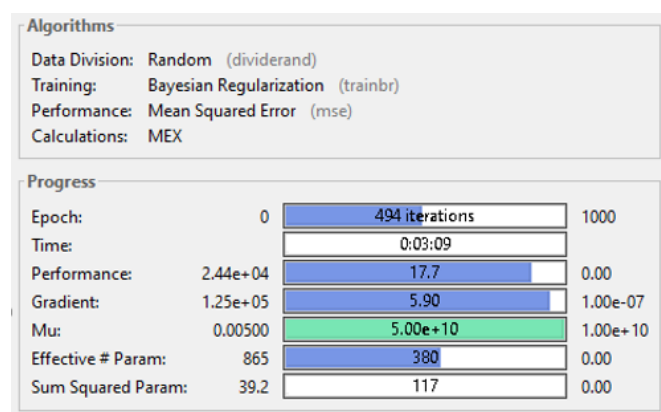


Figure 11. Information about the training algorithms and processes for the USA

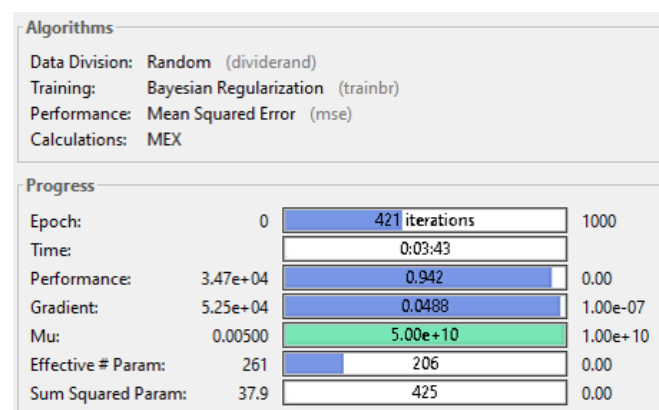


Figure 12. Information about the training algorithms and processes for the Turkey

The training process with "Artificial Neural Network" involves performing the training with 75% of the data, validation with 15% of the data, and testing with the remaining 15% of the data. The regression "R" value measures the correlation between the output data and the target data. A value close to 1 indicates a strong relationship between the two variables, while a value close to 0 indicates a random relationship. Figures 13 and 14 show the regression values obtained from the correlation between the output data and the target data used for training and testing.

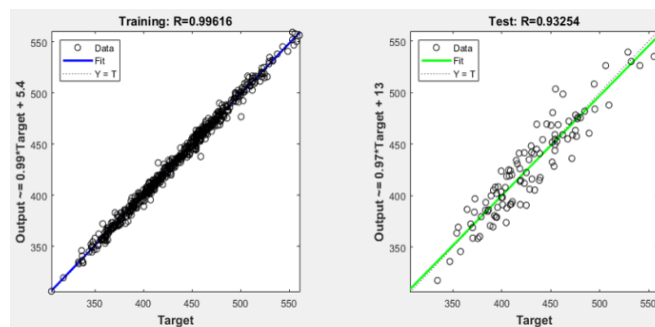


Figure 13. Regression values after training and testing using the NARX Neural Network model for the USA

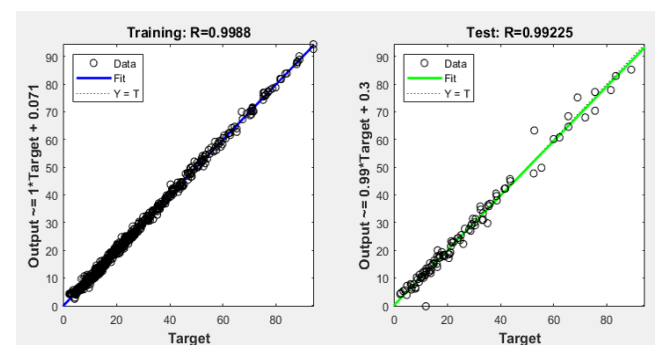


Figure 14. Regression values after training and testing the NARX neural network model for Turkey

The R values obtained from the Artificial Neural Network (ANN) modeling conducted using all the data for the USA and Turkey, along with the greenhouse gas emission predictions, are presented comparatively for both the training and testing processes in Table 10.

TABLE X

THE R-VALUES OBTAINED FOR BOTH TRAINING AND TESTING PHASES FROM THE GREENHOUSE GAS EMISSION DATA PREDICTION USING ALL AVAILABLE DATA FOR THE USA AND TURKEY

Country	Definition	R values
USA	R (Training)	0.99616
	R (Test)	0.93254
Turkey	R (Training)	0.9968
	R (Test)	0.99225

4.4. Comparison of Greenhouse Gas Emission Results between ANN and LSTM

Beginning in January 2023, predictive data was acquired using the LSTM algorithm in deep learning. This predictive dataset, spanning 63 months from January 2023 onwards, was subsequently integrated with the existing dataset. For the artificial neural network (ANN), greenhouse gas emission data were employed as output data within the "ntstool" environment, while all other data variables served as input for predictive modeling.

Comparing the predictions generated by the ANN-NARX model to the actual greenhouse gas emission data revealed close correspondence. These findings are visually represented in Figure 15 for the United States and Figure 16 for Turkey, with a focus on the data pertaining to the year 2010.

Additionally, Table 11 is provided, which includes error ratios depicting the comparison between the predictions generated by the ANN-NARX model and the actual greenhouse gas emission data. Specifically, for the year 2010, the error ratios between the actual values and the predictions obtained by the ANN-NARX model are also depicted.

TABLE XI

MONTHLY GREENHOUSE GAS EMISSION REAL VALUES AND ANN-NARX PREDICTIONS (2010) FOR THE UNITED STATES AND TURKEY IN 'Mton CO₂E' UNITS WITH PERCENTAGE ERRORS

Month (2010)	USA			Turkey		
	Actual Data	ANN-NARX	% Error	Actual Data	ANN-NARX	% Error
1	524,19	519,35	-0,92	42,26	43,10	-1,98
2	471,41	465,67	-1,22	54,94	54,75	0,35
3	469,02	469,80	0,17	46,49	46,85	-0,77
4	420,42	421,30	0,21	29,59	29,37	0,72
5	435,59	434,07	-0,35	16,91	17,20	-1,76
6	457,36	449,80	-1,65	38,04	37,32	1,88
7	484,43	507,67	4,80	50,72	50,12	1,17
8	490,64	485,72	-1,00	63,40	64,12	-1,14
9	441,76	448,68	1,57	33,81	34,33	-1,52
10	427,17	438,67	2,69	16,91	16,04	5,13
11	444,01	440,35	-0,82	8,45	8,45	0,08
12	527,56	515,03	-2,37	21,13	19,19	9,18

TABLE XII

MONTHLY GREENHOUSE GAS EMISSION LSTM AND ANN-NARX PREDICTIONS (2025) FOR THE UNITED STATES AND TURKEY IN 'Mton CO₂E' UNITS WITH PERCENTAGE DIFFERENCES

Month (2025)	USA			Turkey		
	LSTM	ANN-NARX	Percentage Difference	LSTM	ANN-NARX	Percentage Difference
1	434,2	430,4	-0,87	18,3	18,924	-3,42
2	437,2	435,2	-0,46	7,539	9,5837	-27,12
3	459,5	457,6	-0,41	26,08	26,309	-0,89
4	480,1	478,3	-0,39	51,96	53,095	-2,19
5	436,6	442,5	1,35	75,24	76,909	-2,22
6	437,9	464,5	6,07	50,57	50,838	-0,54
7	407	407,1	0,04	32,53	30,701	5,62
8	386,8	384,7	-0,53	19,81	20,536	-3,65
9	378,1	396,8	4,94	43,07	43,008	0,14
10	390,2	390,2	0,02	70,68	70,178	0,72
11	386,3	387,7	0,37	83,5	83,717	-0,26
12	394,7	395,5	0,22	38,75	38,313	1,12

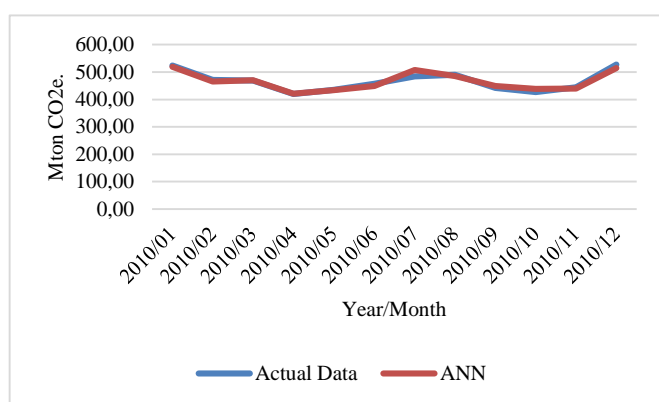


Figure 15. Comparison of actual and estimated greenhouse gas emission data for the United States by months for the year 2010, both before and after the ANN - NARX mode

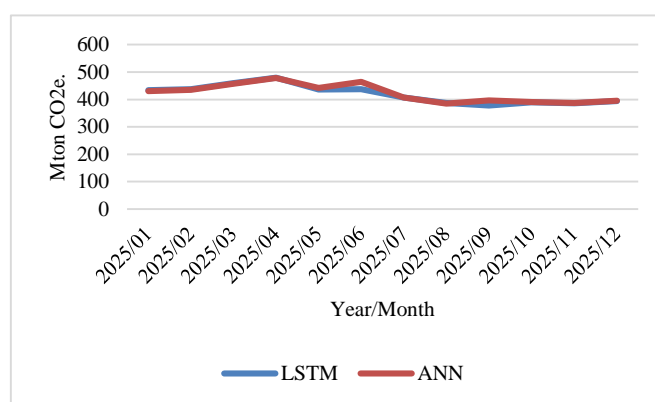


Figure 17. Comparison of Estimated Data for the Months of 2025 for the USA, Obtained with Deep Learning - LSTM Algorithm (Blue Lines) and Estimated Data for the USA Obtained with ANN Using "ntstool" (Red Line)

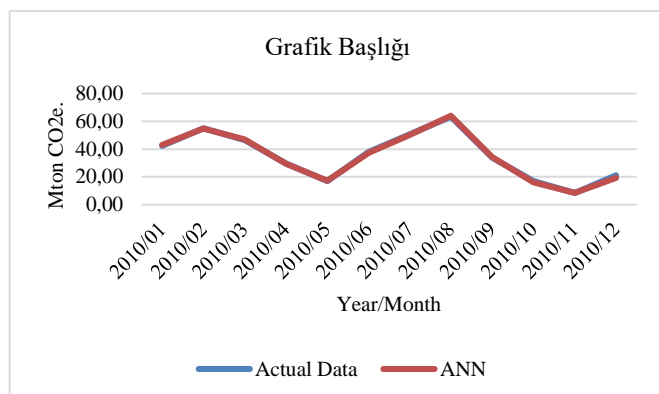


Figure 16. Comparison of actual and estimated greenhouse gas emission data for Turkey by months for the year 2010, both before and after the ANN - NARX mode

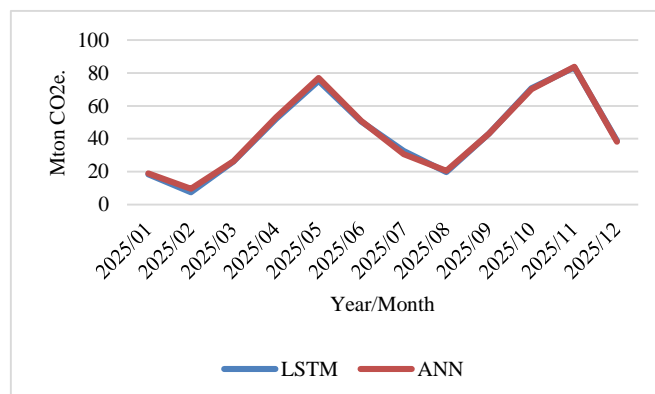


Figure 18. Comparison of Estimated Data for the Months of 2025 for Turkey, Obtained with Deep Learning - LSTM Algorithm (Blue Lines) and Estimated Data for Turkey Obtained with ANN Using "ntstool" (Red Line)

The modeling process, which involved incorporating predictive data from various sources into the ANN NARX model, resulted in greenhouse gas emission predictions that closely align with future greenhouse gas emission data obtained through the Deep Learning LSTM algorithm. When comparing the predictive data for the year 2025, as an example, the similarities between the two approaches are evident. This comparison is illustrated in Figure 15 for the United States and Figure 16 for Turkey. Additionally, in Table 12, the percentage differences between LSTM and ANN-NARX predictions can be observed.

When comparing the predicted data obtained from the LSTM algorithm and Deep Learning method for the future 63 months, with the input data obtained using "ntstool" in the ANN model, it can be observed from the graph below that there is a clear relationship between the input data and the Greenhouse Gas Emission.

The future prediction data obtained through LSTM algorithm and Deep Learning has been compared with the input data obtained through Artificial Neural Network (ANN) using "ntstool". Based on this comparison, it can be observed that a clear relationship can be established between the input data and the Greenhouse Gas Emissions. In Table 13, a comparison and

similarity between the annual actual greenhouse gas emission values and the estimated values, along with the corresponding percentage errors, obtained through the ANN-NARX model for the United States and Turkey from 2000 up to 2023 can be observed.

TABLE XIII

GREENHOUSE GAS EMISSION REAL VALUES AND ANN-NARX PREDICTIONS (2000-2022) FOR THE UNITED STATES AND TURKEY IN 'MTON CO₂E' UNITS

Year	USA			Turkey		
	Real Values	ANN	Percentage Error	Real Values	ANN	Percentage Error
2000	5889	5896	0,13	321,7	318,9	-0,87
2001	5778	5810	0,55	300	301,2	0,41
2002	5820	5812	-0,15	306	313,6	2,51
2003	5886	5881	-0,10	319,4	318,7	-0,23
2004	5994	5986	-0,12	323,7	320	-1,12
2005	6007	5988	-0,32	335	336,9	0,57
2006	5929	5969	0,67	370,5	370,3	-0,06
2007	6016	6004	-0,18	399,9	396,5	-0,84
2008	5823	5820	-0,05	398,6	397,1	-0,37
2009	5404	5476	1,33	406,3	411,6	1,30
2010	5594	5596	0,04	422,7	420,9	-0,43
2011	5455	5461	0,12	447,1	459,1	2,68
2012	5236	5323	1,65	479,1	467,9	-2,33
2013	5359	5360	0,02	476,9	475	-0,40
2014	5414	5433	0,35	503,7	495,7	-1,59
2015	5262	5222	-0,76	518,4	514,9	-0,67
2016	5169	5108	-1,17	546,2	546,3	0,03
2017	5131	5161	0,57	591,8	594,9	0,52
2018	5278	5241	-0,69	592,6	577,3	-2,59
2019	5147	5089	-1,12	585,3	582,3	-0,51
2020	4580	4629	1,08	585,6	598,9	2,28
2021	4903	4853	-1,02	627,1	623,1	-0,64
2022	4892	4865	-0,55	627,1	632,9	0,92

In Table 14, you can observe a comparison and proximity between the annual greenhouse gas emission values, along with percentage errors, for the United States and Turkey, starting from 2023 up to 2028, in relation to the ANN-NARX model and LSTM estimated values.

TABLE XIV

GREENHOUSE GAS EMISSION LSTM AND ANN-NARX PREDICTIONS (2023-2027) FOR THE UNITED STATES AND TURKEY IN 'MTON CO₂E' UNITS

Year	USA			Turkey		
	LSTM	ANN	Percentage Difference	LSTM	ANN	Percentage Difference
2023	5136	5143	0,13	522,7	520,8	-0,36
2024	5248	5183	-1,23	518,9	516,1	-0,55
2025	5028	5071	0,84	518	522,1	0,79
2026	4761	4775	0,29	541,5	532,1	-1,74
2027	5034	4985	-0,97	547,2	544,5	-0,48

For both the United States and Turkey, the predictive greenhouse gas emission values obtained through the ANN NARX model using the "ntstool" tool are depicted in Figure 19 for 5-year intervals, spanning from 1970 to 2025.

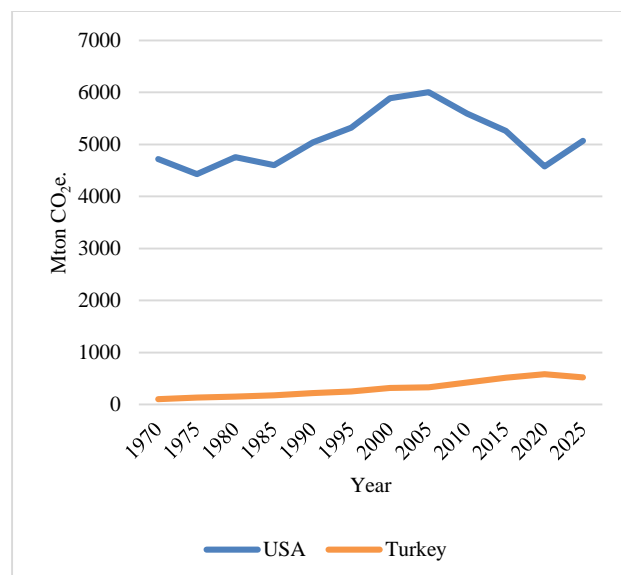


Figure 19. Actual Greenhouse Gas Emission Values and Predictive Values in "Mton CO₂e" for the United States and Turkey

During the research process, time series data were created by separately evaluating various data for each country, including greenhouse gas emissions, economic and financial conditions, primary and renewable energy supplies, population, and afforestation, in addition to factors like land use. Compared to previous studies, this research has introduced a multifactorial approach by incorporating a broader range of data, such as economic and financial indicators, alongside factors like afforestation.

5. RESULTS AND RECOMMENDATIONS

During the research process, time series data were created by separately evaluating various data for each country, including greenhouse gas emissions, economic and financial conditions, primary and renewable energy supplies, population, and afforestation, in addition to factors like land use. Compared to previous studies, this research has introduced a multifactorial approach by incorporating a broader range of data, such as economic and financial indicators, alongside factors like afforestation.

Upon examining the data from a methodological perspective, the utilization of deep learning methods, specifically LSTM, and the hybrid CNN-RNN approach, has yielded successful prediction results. Furthermore, the use of the NARX model with the MATLAB "ntstool" tool, where correlation values are close to 1, demonstrates the effectiveness of this study. When the predicted greenhouse gas emission values are compared with real data, it becomes evident that accurate predictions have been achieved.

Moreover, when the results are examined on a country-specific basis, it can be interpreted that Turkey experienced a reduction in greenhouse gas emissions, particularly during the pandemic period that began in 2019. This reduction can serve as an indicator of global economic challenges. In the case of the United States, the analysis of future predictions reveals that while there has been a decrease in greenhouse gas production compared to the 2000s, it has not fallen below the levels observed in the 1990s. Consequently, within the scope of this study, it is apparent that both the United States and Turkey have not reached the greenhouse gas production levels of the 1990s. This suggests a need for increased efforts in addressing climate change. Furthermore, it can be inferred that the

reductions in greenhouse gas emissions in these countries have led to heightened awareness regarding global warming. To achieve more comprehensive results in the analysis and prediction of climate change and greenhouse gas emissions, several recommendations can be made. In order to more accurately predict future greenhouse gas emissions, richer sources of data can be employed compared to previous research efforts. For instance, a broader range of parameters and data categories, including climate data, economic and financial indicators, population statistics, energy consumption data, urbanization rates, migration patterns, forest areas, environmental policies, and investments in renewable energy technologies, can be incorporated to construct a more comprehensive model. Given the success of advanced artificial intelligence techniques like "Deep Learning" and similar artificial neural network algorithms, it is reasonable to expect improved results with advanced AI techniques. Additionally, analyses based on various future scenarios can be conducted to formulate effective policies for greenhouse gas emissions. These analyses, rooted in machine learning, can provide policymakers with more efficient strategies for addressing climate change.

The increasing world population is increasing the demand for the industrial sector. Consequently, population growth and industrial demands make energy consumption essential. However, it is evident that primary energy sources contribute to greenhouse gas emissions and therefore are the main cause of global warming. Therefore, in order to prevent a global catastrophe, it is necessary to move away from primary energy sources as much as possible and shift towards renewable energy sources. The use of renewable energy sources seems achievable through increasing the utilization of sources such as hydropower, solar power, wind power, biomass, geothermal, wave, tidal, and hydrogen. By utilizing these sources, the need for renewable energy can be met by moving away from non-renewable energy sources.

REFERENCES

- [1] KORKMAZ, K., Küresel Isınma ve Tarımsal Uygulamalara Etkisi. Alatarım dergisi, 2007, 6.2: 43-49.
- [2] Levinson, D. (2020). Logistic Curve Models of CO2 Accumulation. Findings.
- [3] Ayyıldız, B. (2013). Ekolojik ekonomi yaklaşımı ile Türkiye'de çevresel etkinlik analizi (Master's thesis, Gaziosmanpaşa Üniversitesi, Fen Bilimleri Enstitüsü).
- [4] Şahin Ü., Tör O. B., Teimourzadeh S., Demirkol K., Künar A., Voyvoda E., Yeldan E., 2022, TÜRKİYE'NİN KARBONSUZLAŞMA YOL HARİTASI: 2050'DE NET SIFIR
- [5] Wikimedia Foundation, Inc., 2023, Access URL: https://en.wikipedia.org/wiki/Charles_David_Keeling, [Accessed: Feb. 15, 2023]
- [6] DİKEN, G. (2020). Antropojenik iklim değişikliğinin balıkçılık ve su ürünleri üzerine etki ve yönetim stratejilerine genel bir bakış. Journal of Anatolian Environmental and Animal Sciences, 5(3), 295-303.
- [7] United Nations Resmi Web Sitesi, 2022, Access URL: <https://www.un.org/en/climatechange/paris-agreement>, [Accessed: Jun. 08, 2022]
- [8] Aydın, S. G. ve Aydoğdu, G., 2022, Makine Öğrenmesi Algoritmaları Kullanılarak Türkiye ve AB Ülkelerinin CO2 Emisyonlarının Tahmini, Avrupa Bilim ve Teknoloji Dergisi, (37), 42-46.
- [9] Uzu, E., 2021, Estimates of Greenhouse Gas Emission in Turkey with Grey Wolf Optimizer Algorithm-Optimized Artificial Neural Networks, Neural Computing and Applications, 33(20), 13567-13585.
- [10] Acheampong, A. O. and Boateng, E. B., 2019, Modelling carbon emission intensity: Application of artificial neural network, Journal of Cleaner Production, 225, 833-856.
- [11] Ali, N., Assad, M. E. H., Fard, H. F., Jourdehi, B. A., Mahariq, I. and Al-Shabi, M. A., 2022, CO2 Emission Modeling of Countries in Southeast of Europe by Using Artificial Neural Network, In Sensing

for Agriculture and Food Quality and Safety XIV, Vol. 12120, 100-104.

- [12] Komeili Birjandi, A., Fahim Alavi, M., Salem, M., Assad, M. E. H. and Prabakaran, N., 2022, Modeling Carbon Dioxide Emission of Countries in Southeast of Asia by Applying Artificial Neural Network, International Journal of Low-Carbon Technologies, 17, 321-326.
- [13] European Union, Official Website, Access URL: https://edgar.jrc.ec.europa.eu/dataset_ghg70#p3, [Accessed: Feb. 24, 2023]
- [14] UNDP (United Nations Expanded Programme), 2023, Access URL: <https://hdr.undp.org/data-center/human-development-index#/indicies/HDI>, [Accessed: Feb. 17, 2023]
- [15] Organisation for Economic Co-operation and Development, 2023, Access URL: <https://stats.oecd.org/index.aspx?queryid=6779>, [Accessed: Feb. 20, 2023]
- [16] Organisation for Economic Co-operation and Development, 2023, Access URL: <https://data.oecd.org/natincome/net-national-income.htm>, [Accessed: Feb. 19, 2023]
- [17] Birleşmiş Milletler, 2023, Access URL: <https://unstats.un.org/unsd/snaama/Basic>, [Accessed: Feb. 19, 2023]
- [18] TUNALI, Ç. B., 2011, Uluslararası Para Fonu'nun Kredilendirme Mekanizması: Düşük Gelirli Ülkelere Yönelik Bir İnceleme. Maliye Araştırma Merkezi Konferansları, (56), 69-93.
- [19] Organisation for Economic Co-operation and Development, 2023, Access URL: <https://stats.oecd.org/index.aspx?queryid=6779>, [Accessed: Feb. 20, 2023]
- [20] Kaya, K., & Koç, E., 2015, Enerji Kaynakları-Yenilenebilir Enerji Durumu. Mühendis ve Makina, 56(668), 36-47.
- [21] Organisation for Economic Co-operation and Development, 2023, Access URL: <https://data.oecd.org/energy/primary-energy-supply.htm#:~:text=Primary%20energy%20supply%20is%20defined,plus%20or%20minus%20stock%20changes>, [Accessed: Feb. 21, 2023]
- [22] Organisation for Economic Co-operation and Development, 2023, Access URL: <https://data.oecd.org/energy/renewable-energy.htm#indicator-chart>, [Accessed: Feb. 21, 2023]
- [23] U.S. Energy Information Administration (EIA), 2023, Access URL: <https://www.eia.gov/totalenergy/data/monthly/index.php>, [Accessed: Feb. 20, 2023]
- [24] The World Bank, 2023, Access URL: <https://www.worldbank.org/en/topic/forests/forests-area#4>, [Accessed: Feb. 19, 2023]
- [25] Alizadeh, M. (2011). Yapay Sinir Ağları İle Fiyat Tahmin Analizi. İstanbul Üniversitesi. Fen Bilimleri Enstitüsü, Yüksek Lisans Tezi, İstanbul, 90s.
- [26] Dandil, E. & Serin, Z., 2020, Derin Sinir Ağları Kullanarak Histopatolojik Görüntülerde Meme Kanseri Tespiti, Avrupa Bilim ve Teknoloji Dergisi, 451-463.
- [27] Sanchez, H., 2023, Time Series Forecasting Using Hybrid CNN – RNN, MATLAB Central File Exchange, Retrieved April 24, 2023.
- [28] Alizadeh, M., 2011, Yapay Sinir Ağları İle Fiyat Tahmin Analizi, Yüksek Lisans Tezi, İstanbul Üniversitesi Fen Bilimleri Enstitüsü, İstanbul, 90s.

BIOGRAPHIES

Necmettin Sezgin graduated with a Bachelor of Science degree in Electrical and Electronics Engineering from Hacettepe University, Faculty of Engineering, in 2001. He completed his Master of Science in Electrical and Electronics Engineering at Dicle University, Graduate School of Natural Sciences, in 2003, and his PhD in the same field at İnönü University in 2011. In 2011, he joined Batman University as an Assistant Professor in the Department of Electrical and Electronics Engineering. In 2014, he was awarded the title of Associate Professor in Electrical and Electronics Engineering by the Turkish Interuniversity Board and continued his work at Batman University in the same department. In 2019, he became a Professor in the Department of Computer Engineering at Batman University, where he currently works. He has served in various editorial and peer-review roles for national and international journals. Additionally, he has held several administrative roles at the university, including Acting Dean, Vice Dean, Founding Department Head, Chair of the Department, Senate Member, University Board Member, and Faculty Board Member. His research interests include electronics, biomedical engineering, and signal processing.

Serkan Ertuğrul graduated with a Bachelor of Science in Electronics Engineering from Istanbul University in July 2002. He later earned a second bachelor's degree in Business Administration from Anadolu University's Faculty of Business in June 2018. He obtained his Master of Science degree in Electrical and Electronics Engineering from Batman University in July 2023 and is currently pursuing his PhD in the same field at Batman University. His research interests include control theory, machine learning, deep learning, and signal processing.

Microstructure and Mechanical Properties of Cold Metal Transfer Welded AA6013/SiC Metal Matrix Composites

Arzum Isitan^{1*} , Dirim Bartug Gokturk²  and Volkan Onar³ 

^{1*}Pamukkale University, Mechanical Engineering Department, 20160, Kınıklı, Denizli, Turkey. (e-mail: aisitan@pau.edu.tr).

²Pamukkale University, Automotive Engineering Department, 20160, Kınıklı, Denizli, Turkey. (e-mail: dream.gokturk@gmail.com)

³Pamukkale University, Mechanical Engineering Department, 20160, Kınıklı, Denizli, Turkey. (e-mail: vonar@pau.edu.tr).

ARTICLE INFO

Received: Sep., 44. 2023

Revised: Nov., 03. 2023

Accepted: Apr, 02. 2024

Keywords:

Composite

Welding

Cold Metal Transfer

Metal Matrix Composite

Heat Input

Corresponding author: *Arzum Isitan*

ISSN: 2536-5010 / e-ISSN: 2536-5134

DOI: <https://doi.org/10.36222/ejt.1365379>

ABSTRACT

This study aims to investigate the impact of varying heat input, achieved through changes in welding current, on the strength of cast composites. Three AA6013 matrix composites (AMCs) of varying SiC content (3, 6, and 9 wt.%) were prepared using the vortex-route method, with dimensions of 250x110x60 mm. Subsequently, the cast composites were sliced into 3.5x100x50 mm dimensions for butt welding. Welding operations were conducted at current intensities of 110 A, 120 A, and 130 A via the cold metal transfer (CMT) welding method. The microstructures and tensile strength of the welded composites were thoroughly analysed.

Results indicated that an increase in heat input led to a decrease in the strength values of welded composites by up to 10%. Furthermore, a notable enhancement in the mechanical properties of the reinforced composites, ranging from 19% to 32%, was observed when compared to the unreinforced alloy. In conclusion, the CMT method, which provides relatively less heat input compared to other welding methods, enables the welding of AMCs to achieve superior mechanical properties while maintaining a low reinforcement ratio.

1. INTRODUCTION

The strength of aluminum alloys tends to decrease at higher temperatures, despite their inherent benefits such as their high fracture toughness and lightweight design. Conversely, ceramic materials exhibit excellent creep resistance and high temperature strength but often lack thermal shock resistance and fracture toughness. To overcome these limitations and create materials with superior thermal and mechanical properties, aluminum matrix and ceramic-reinforced composite materials (AMCs) have been developed. These materials find extensive application areas, particularly in industries like automotive and defense [1].

AMCs, fortified with ceramic particles, outperform non-reinforced alloys in various aspects, including strength-to-weight ratio, dimensional stability, elevated creep and wear resistance, and robust mechanical load-carrying capability [1-4]. With the increasing utilization of AMCs, there is a growing emphasis on research into joining methods, particularly welding technology.

While traditional arc welding techniques remain prevalent due to their widespread use and cost-effectiveness, solid-state welding methods have proven successful in joining AMCs.

Despite its excellent metallurgical qualities, solid-state welding faces limitations in mass production, primarily due to constraints in component geometry [5]. This is where techniques like Tungsten Inert Gas (TIG), Metal Inert Gas (MIG), and laser welding come to the fore, offering cost-effectiveness, suitability for mass production, and flexibility with minimal component geometry restrictions. However, welding of AMCs reinforced with ceramic particles using these methods can lead to unintended consequences due to high heat input, particularly in the weld pool, and the substantial thermal expansion of aluminum [3,6].

In the contemporary landscape, Cold Metal Transfer (CMT), integrated into the MIG welding process, stands out as a solution that provides precise power supply control, minimizing thermal input. Unlike traditional MIG welding, where the wire electrode advances until a short circuit occurs, causing high heat input, CMT regulates material transfer using mechanically assisted methods while controlling the start and length of the short circuit. This technique is applicable to various metals and thicker materials, offering advantages in preventing undesired microstructure and precipitate formation caused by high heat input [7,8]. The fundamental principle behind CMT is the short circuit (immersion metal transfer),

patented by Fronius in 2004 [9]. It is envisioned using CMT, a large amount of heat input experienced with traditional arc welding is unlikely to result in a deterioration of the mechanical qualities in the welding area. Due to the minimal heat input, welding of thin sheets and plates together can provide high-quality results. The main distinction between CMT welding and conventional gas metal arc welding is that the latter uses an automation system to regulate the quantity of thermal input, arc length, current, and voltage, as well as the amount of metal transferred [10]. The primary novelty is that the servomotor included in the cannon retracts the wire electrode and aids in the transfer of drops. This servomotor can oscillate up to 70 Hz when a short circuit occurs and operates on alternating current. As a result, the temperature input is significantly reduced, and metal is moved to the weld pool without the use of electromagnetic force. The welding cycle continues after the drop transfer, the arc is ignited, and the wire electrode is advanced once more. Because of the short arc periods, the method's name uses the word "cold" to denote the fact that less heat is used than with MIG or MAG welding methods [9,10].

In the literature, there are very few studies on CMT welding of SiC-reinforced aluminum alloys. Liu et al. (2022) selected the ER5087 (Al-Mg4.5) wire as raw filler and 5A06 Al plate as substrate material. Four different SiC concentrations of Al-Mg alloy deposited on the 5A06 Al plate, and the mechanical properties of Al-Mg alloy improved [11]. Fan et al. (2023) investigated the effect of coating submicron sized La_2O_3 particles on the CMT welded joints of 6061 aluminum alloy [12]. Considering the potential and importance of the use of SiC-reinforced AMCs and the difficulties in the welded joints, there is a lack of studies on CMT welding of AMCs.

In this study, 3%, 6% and 9% in wt. SiC powder was added to the AA6013 alloy, respectively, and composites were produced by the vortex-route casting method. Welded joining processes were carried out by adjusting three different welding current intensities via the CMT method. The microstructures and mechanical properties of welded composite samples were investigated.

2. MATERIAL and METHODS

In this study, AA6013 alloy (AlMg1Si0.8CuMn) was chosen as the matrix material due to its medium strength, high corrosion resistance, good machinability, and widespread preference in welded joints [13]. Its selection was based on qualities such as good weldability, a wide range of industrial applications, and suitability for usage in the automotive sector. The alloy's chemical composition, as well as its physical and mechanical characteristics, are displayed in Tables I and II [14].

TABLE I

THE CHEMICAL COMPOSITION OF AA 6013 ALUMINUM ALLOY

Element	Si	Fe	Cu	Mn	Mg	Cr	Zn	Ti	Al
By weight (%)	0,8	0,25	0,85	0,5	1	0,05	0,12	0,05	Bal.

When creating composite materials with aluminum matrix and ceramic particle reinforcement, SiC is one of the most frequently used materials as the reinforcing ceramic particle. The choices made are significantly influenced by the

affordability of SiC particles and their superior wettability by aluminum alloys [1]. For these reasons, SiC ceramic particles with an F1000 size were used as a reinforcement in this study. The SiC powders were subjected to heating in an electric furnace at 200 °C for an hour to evaporate the particles' moisture.

TABLE II

PHYSICAL AND MECHANICAL PROPERTIES OF AA 6013

Symbol	Property	Value
ρ	Density	2,72 g/cm ³
T	Melting Temperature	579 °C
α	Coefficient of Thermal Expansion	21,7x10 ⁻⁶ K ⁻¹
E	Modulus of Elasticity	71 GPa
R_e	Yield Strength	350 MPa
R_m	Ultimate Strength	400 MPa
A	Elongation at Break	13 (%)
HV	Hardness	115 HV

AMCs can be produced using the same casting techniques that are typically used for aluminum alloys. One such method is vortex-route casting, intended to guarantee the uniform distribution of the reinforcing material in the molten matrix material. The density of the ceramic reinforcement material is higher than that of the aluminum matrix material (Al 2.7 g/cm³, SiC 3.2 g/cm³). A stainless-steel mixer combined with an induction furnace was used to prevent SiC particles from aggregating when wet by the aluminum material and to prevent the melt from settling at the bottom of the crucible. The mixing process was conducted slowly to avoid vortex formation.

AMCs were produced by melting the AA 6013 alloy, offered in rod and cylinder shapes, in the casting furnace. The amount of material to be melted is calculated by considering the volume of the model in the sand mold, the volume of the runner parts, and possible losses. Subsequently, the required quantity of AA 6013 alloy was placed into the ceramic crucible within the Nevola Efe series EVO 770 type induction furnace. After cleaning off the slag from the melt's surface and adding the degassing powder to the furnace, which was then heated to 750 °C, reinforcement material was added. A prolonged blending process was approximately 1 hour, was applied to combine SiC and molten aluminum alloy into a homogeneous slurry. Three different composites were obtained by adding 3%, 6% and 9% in wt. SiC powder separately in mixing processes.

Sand molding was used to create casting composite materials in the form of a billet with dimensions of 250x110x60 mm due to its simplicity, speed, and economic efficiency. Figure 1 illustrates the casting furnace, the sand mold, and the resulting cast composite.



Figure 1. The casting furnace, the sand mold, and the cast composite

After the composite billets were produced, a 5 mm layer of chips was removed from all surfaces using a milling machine.

Subsequently, the billets were cut into dimensions of 3.5x100x50 mm using a saw, obtaining the samples necessary for the welding process. Figure 2 represents the chip removal process during milling and cutting of the composite.



Figure 2. The chip removal process and cutting of the composites

The 3.5 mm thick samples were butt welded via CMT welding technique, a novel MIG welding method developed by Fronius International. Welding operations were carried out at Fronius International Istanbul. In the welding process, ER4043 (AlSi5) welding wire with a diameter of 1.2 mm was utilized. The chemical composition of the ER4043 welding wire is provided in Table III. Argon served as the shielding gas at a flow rate of 12 l/min.

TABLE III

THE CHEMICAL COMPOSITION OF ER4043 (AlSi5) WELDING WIRE

Element	Si	Fe	Cu	Mn	Zn	Ti	Al
By weight (%)	4.5-5.5	<0.5	<0.3	<0.05	<0.1	<0.01	Bal.

Three different current intensities, namely 110, 120, and 130 A, were applied to weld the samples reinforced with 3%, 6%, and 9% SiC. Heat input (H.I.) ($J \cdot mm^{-1}$) generated during the welding operations was calculated using Equation 1, where I is the current intensity (Amperes), V is the voltage (V), η is the arc efficiency (0.8 for CMT method operation), and FR is the feed rate ($mm \cdot min^{-1}$). The welding parameters of all the samples are detailed in Table 4.

$$HI = (60 \cdot I \cdot V) / (FR) \cdot h \quad (1)$$

TABLE IV
WELDING PARAMETERS

	Material	Current (A)	Voltage (V)	Heat input ($kJ \cdot mm^{-1}$)
1	AA6013	110	14.2	0.12
2	AA6013	120	14.4	0.13
3	AA6013	130	14.8	0.14
4	AA6013+3% SiC	110	14.2	0.12
5	AA6013+3% SiC	120	14.4	0.13
6	AA6013+3% SiC	130	14.8	0.14
7	AA6013+6% SiC	110	14.2	0.12
8	AA6013+6% SiC	120	14.4	0.13
9	AA6013+6% SiC	130	14.8	0.14
10	AA6013+9% SiC	110	14.2	0.12
11	AA6013+9% SiC	120	14.4	0.13
12	AA6013+9% SiC	130	14.8	0.14

Following the welding procedure, tensile test specimens were made by cutting flat bars measuring 3.5x20x140 mm into three pieces for each reinforcement ratio. Tensile tests were conducted in the Mechanical Engineering Materials Laboratory at Pamukkale University using a 30-ton Alşa brand tensile test machine, completed at a speed of 20 mm/min.

In the Metallography Laboratory of the Pamukkale University Mechanical Engineering, samples of non-reinforced alloy and reinforced composite materials, joined under different welding conditions, underwent examination. Their microstructure and macrostructure were analyzed using a microscope. The composites were further characterized using a Schottky Field Emission Scanning Electron Microscope (FESEM) in high vacuum mode (HV) (10^{-6} mbar) at the Pamukkale University Advanced Materials Research Center (ILTAM).

Phase analyses of the welded SiC reinforced composites were performed at Afyon Kocatepe University Technology Application and Research Center (TUAM) using a X-ray spectroscopy (XRD) Bruker D8 Advance diffractometer.

3. EXPERIMENTAL RESULTS

3.1. Tensile Test Results

Tensile strength (R_m) and yield limit (R_e) values of welded samples are shown in Table V. Almost all samples fractured at weld seam. The mechanical characteristics of the unreinforced as-cast AA 6013 alloy were determined to be $R_m=83.73$ MPa and $R_e=67$ MPa. The highest values after the welding process were obtained as $R_m=76.3$ MPa and $R_e=60.2$ MPa at 130 A for the unreinforced AA 6013 alloy. R_m and R_e both decreased by 9% and 11% in the specimen with welding process in order.

TABLE V

THE CHEMICAL COMPOSITION OF ER4043 (AlSi5) WELDING WIRE

	Material	Current (A)	Heat input ($kJ \cdot mm^{-1}$)	R_m (MPa)	R_e (MPa)
1	AA6013	110	0.12	70.6	57.8
2	AA6013	120	0.13	58.3	54.9
3	AA6013	130	0.14	76.3	60.2
4	AA6013+3% SiC	110	0.12	100.56	83.46
5	AA6013+3% SiC	120	0.13	95.09	80.9
6	AA6013+3% SiC	130	0.14	90.9	75.83
7	AA6013+6% SiC	130	0.14	73.88	60.3
8	AA6013+9% SiC	110	0.12	96.01	82.36
9	AA6013+9% SiC	120	0.13	95.19	80.9
10	AA6013+9% SiC	130	0.14	93.47	79.22

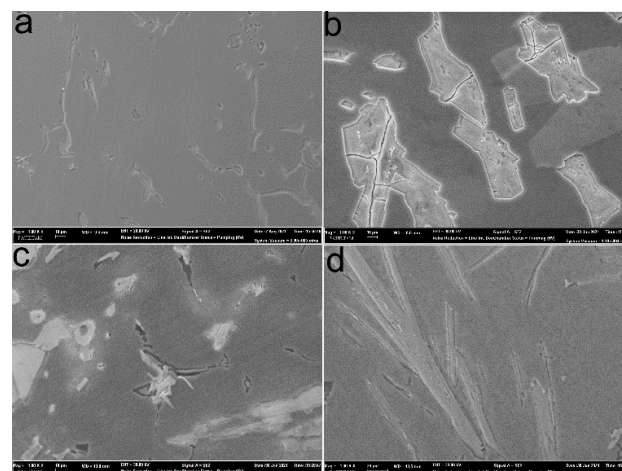


Figure 3. FESEM images of cast unreinforced alloy (a), 3% SiC (b), 6% SiC (c), and 9% SiC (d) reinforced composite materials

As a result of the tensile test, the highest average tensile strength value, $R_m=100.56$ MPa, was obtained at 110A welding current of AA6013+ 3% SiC composite. As the intensity of the current increased in the CMT method welding of AA6013+ 3% SiC composite, the strength values decreased by up to 10%.

Similar result is valid for 9% SiC reinforced composite. The highest average tensile strength value, $R_m=96.01$ MPa, was obtained at 110A welding current of AA6013+ 9% SiC composite. While the effect of heat input is more obvious in the 3% SiC reinforced composite, the reduction effect is less in the 9% SiC reinforced composite.

The tensile result values of welded joints of AA6013+ 6% SiC composite could not be obtained exactly. As can be seen in Figure 8, it is thought that the reason for this is the cracks and voids formed in the base metal alloy, transition zone, and welding area, which are caused by unsuitable casting conditions and the formation of a dendritic structure in the welding area.

In contrast to the unreinforced alloy, the mechanical values obtained at all reinforcement ratios decreased as the welding current and heat input increased.

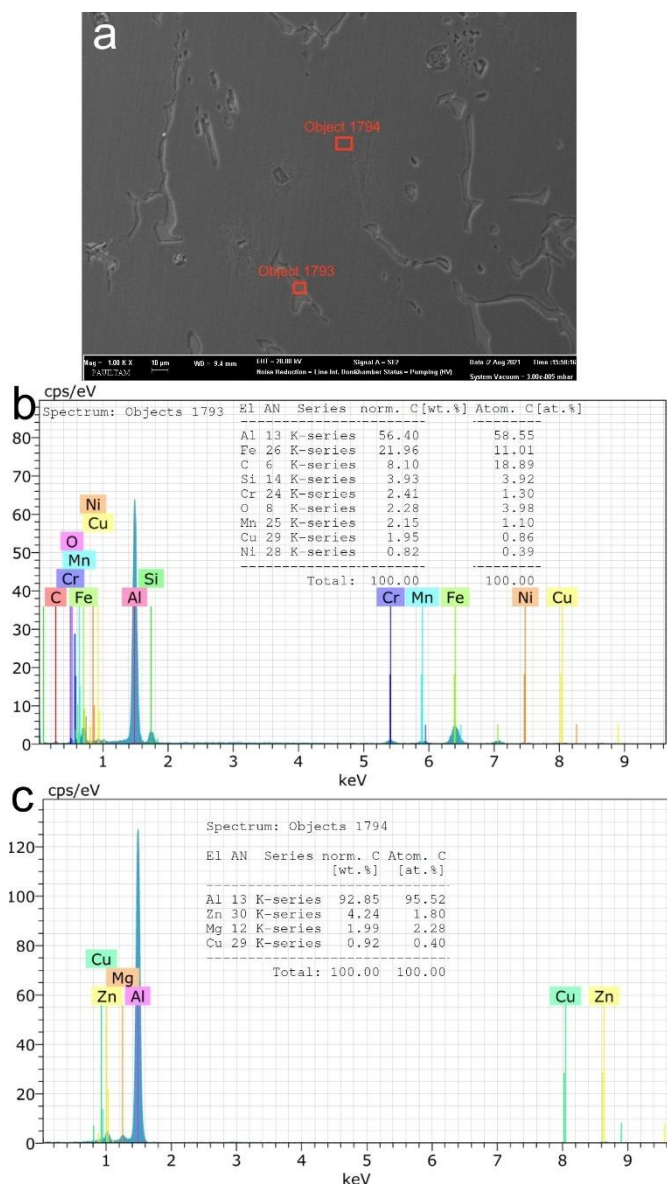


Figure 4. FESEM point analyses of unwelded AA6013 alloy

3.2. Macro and Microstructure Results

In Figure 3, FESEM images of cast unreinforced alloy (a), 3% (b), 6% (c), and 9% (d) reinforced composite materials can be shown, respectively.

Although there are alloying elements such as Si, Fe, Cu, Mn, Mg, Zn, and Ni in the AA 6013 alloy, as can be seen in Figure 4c, mainly Zn, Mg, and Cu were detected in the matrix structure in the FESEM point analysis (object 1794). In the point (object 1793) marked with red mark, Si, Fe, Cr, Cu, Mn, Mg, Zn, Ni, and C were detected (Figure 4b).

Gaps were detected in the weld seam and transition zone (HAZ) images of unreinforced AA 6013 alloy joined at 110 A (Figure 5). In the unreinforced AA 6013 alloy welded at 120 A, weld penetration was achieved as the welding current increased, and it was determined that there were fewer and smaller diameter gas voids compared to the sample joined with 110 A (Figure 6).

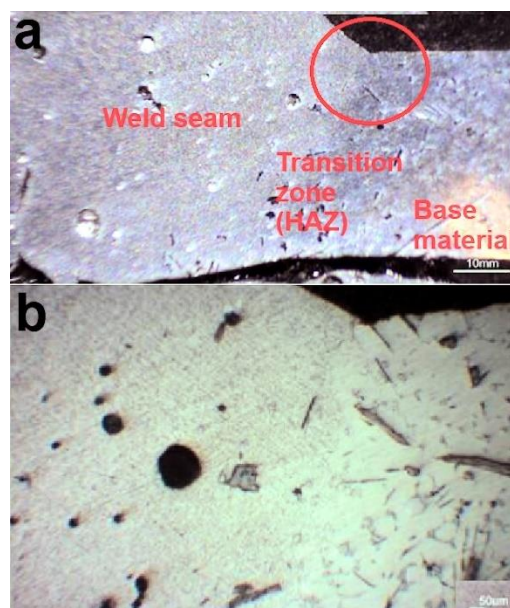


Figure 5. Macrostructure (a) and microstructure (b) images of unreinforced AA 6013 alloy joined at 110 A

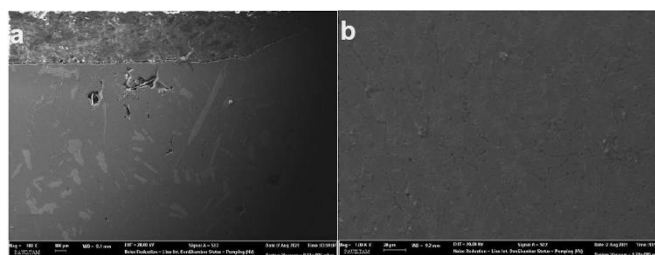


Figure 6. FESEM images of unreinforced AA 6013 alloy joined at 120 A: a) HAZ, b) Weld seam

Figure 7 shows the FESEM microstructure and point analysis of 3% SiC reinforced AMC as-cast condition. It was observed that SiC powders dispersed in all three composites without agglomeration. In Figure 7, red arrows indicate some of SiC particles. A point analysis of the structure (Figure 7b, Object 2431) shows that around the powders, thick rod-like structures consisting of Fe, C, O, Zn, Mg, and Si were formed. The thin and long rod-like structures, some of which are marked with a blue arrow, were observed to be β - Al_5FeSi platelets, similar to studies in the literature [15,16]. The primary silicon structures are marked with a green arrow, Mg_2Si structures are marked

with an orange arrow, and the purple arrow marks the Al_2Cu structures formed, similar to studies in the literature [16,17].

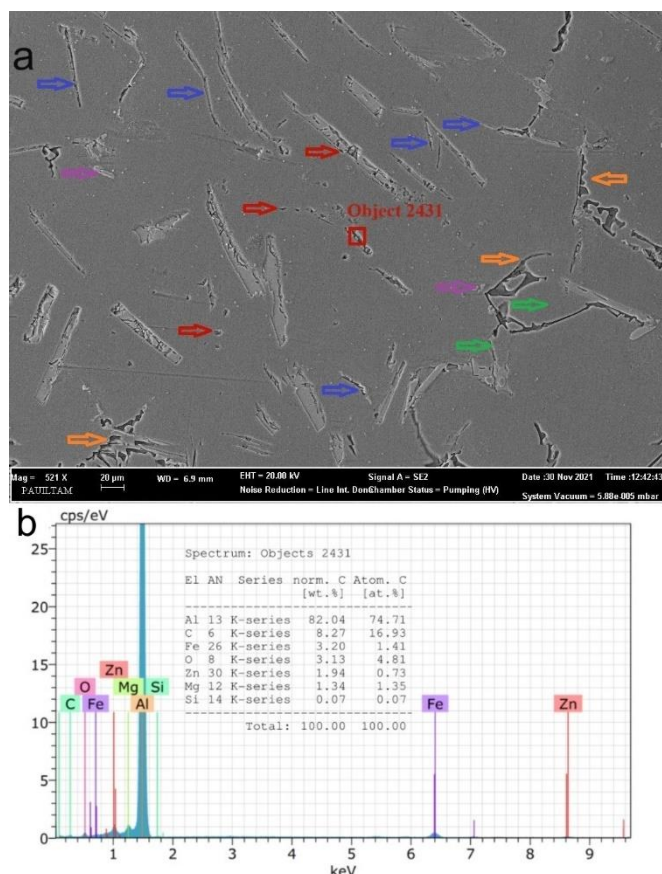


Figure 7. FESEM microstructure (a) and a point analysis (b) of 3% SiC reinforced alloy as-cast condition.

Since the highest tensile strength values were obtained at 110 A welding current, FESEM analysis of these specimens was performed for SiC reinforced composites. The microstructure image and FESEM line analysis of AA6013+ 3% SiC composite welded at 110 A welding current are shown in Figure 8. In the point analyses performed in the transition zone, the complex structures consisting of Fe, Cr, Mn, O, Mg, Mg, Zn, and Mn in the microstructure formed from the HAZ towards the weld seam were replaced by Al-Zn and SiC particles oriented towards the weld seam.

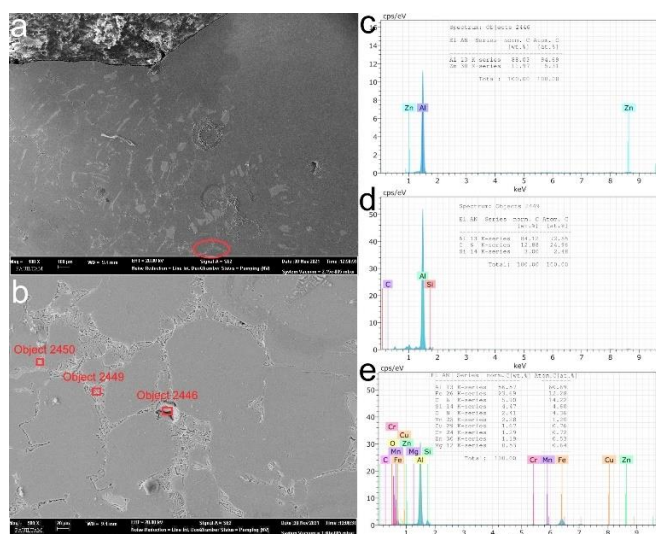


Figure 8. The FESEM microstructure images (a), (b), and FESEM point analyses (c), (d), and (e) of AA6013+ 3% SiC composite welded at 110 A

In the welded joints of AA6013+ 6% SiC composite, very large amount of cracks and gaps were detected in the base metal, transition zone, and welding area under all heat input values. Figure 9 presents of AA6013+ 6% SiC composite welded at 110 A FESEM microstructure of HAZ (Figure 9a), weld seam (Figure 9b), and FESEM weld seam area analysis. In the FESEM area analysis structures containing C, O, Zn, and Fe were predominantly detected in the unwelded samples, while O, Mg, Zn, Fe, Cr, and Si were predominantly detected in the transition zone line analysis of the welded samples (Figure 8a). In the point and area analyzes performed in the transition zone and source region, formations with Fe, C, Cr and Si contents were detected in the transition zone and dendritic formations with C, O, Fe, Si and Mg contents were detected in the source region (Figure 9c).

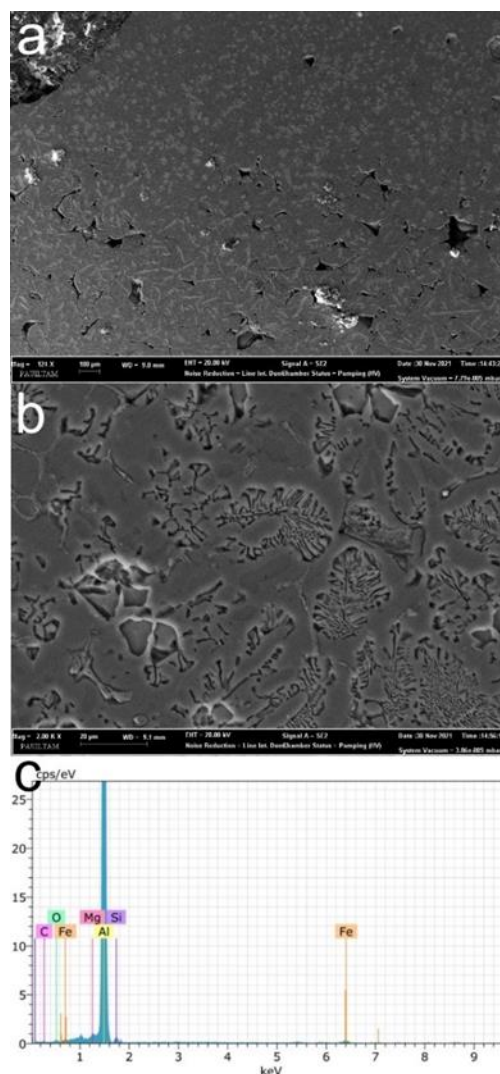


Figure 9. The FESEM HAZ image (a), weld seam microstructure image (b), and weld seam FESEM area analysis of AA6013+ 6% SiC composite welded at 110 A.

Gaps and cracks were detected in the weld and transition areas of AA6013+ 9% SiC composite. In the weld seam FESEM area analysis, structures containing C, O, Zn, Mg, and Si, were predominantly detected (Figure 10).

Following the obtained results, XRD analyzes were performed on the two samples showing the highest and lowest strength (Figure 11). The XRD analyses of (a) AA6013+ 3% SiC composite welded at 110 A, and (b) of AA6013+ 6% SiC composite welded at 130 A. It was found that $(\text{Al}_{26}\text{Si})_{0.148}$ and $\text{Al}_{0.985}\text{Cu}_{0.005}\text{Mg}_{0.01}$ were formed in the weld zones of both specimens. $(\text{Fe}_{97}\text{Mn}_3)_{0.02}$ was found to be formed differently in the 6% SiC reinforced

specimen. Considering the chemical composition of both the main material and the welding wire, it is normal to form of these structures.

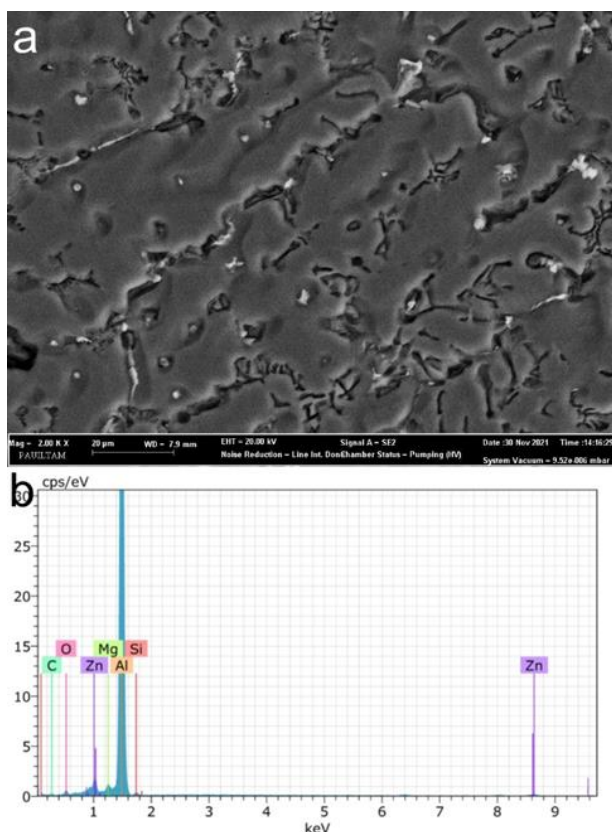


Figure 10. The FESEM microstructure image (a) and FESEM line analysis (b) of AA6013+ 9% SiC composite welded at 110 A

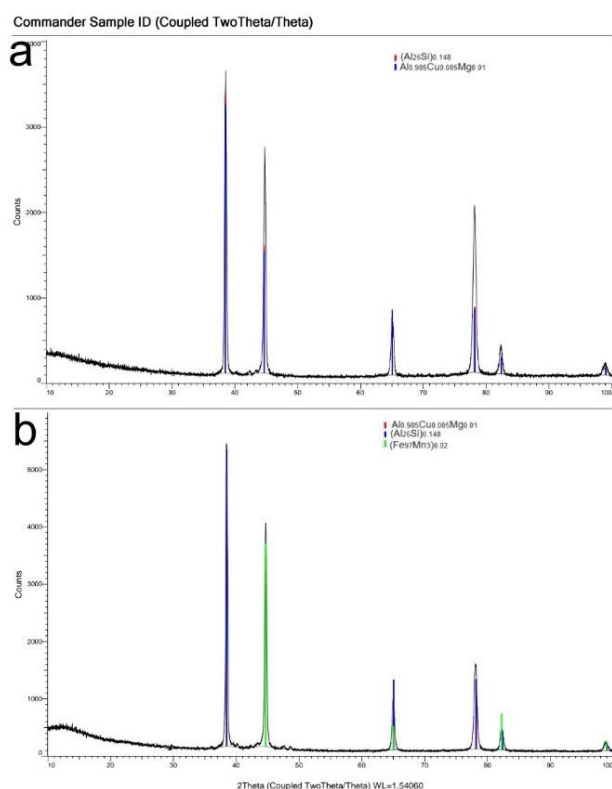


Figure 11. The XRD analyses of (a) AA6013+ 3% SiC composite welded at 110 A, and (b) of AA6013+ 6% SiC composite welded at 130 A.

4. DISCUSSION

Since the fusion zones frequently show coarse columnar grains as a result of the dominant heat conditions during the solidification of the weld metal, part strength reduces particularly as a result of fusion welding procedures. When compared to unwelded samples, welded samples' tensile strength can drop by up to 50% [18,19]. In this study, the mechanical characteristics of the unwelded and welded AA 6013 alloy under unreinforced and as-cast conditions, the tensile test results were close to each other. The mechanical property loss in welded samples was determined as 9.7% for Rm and 11.3% for Re. With the increase of heat input, the lowest values were obtained at 130 A welding current. These results show that the CMT method welding with current intensity and low heat input is suitable for unreinforced aluminum matrix composite.

When the mechanical properties of reinforced and welded composites were compared with the unreinforced and welded alloy, an increase in values ranging from 19% to 32% was obtained, except for the 6% SiC reinforced composite.

The porosity in a composite reinforced with coated Al_2O_3 particles was reduced by 15.45% in the work by Chandrasekar and Nagaraju [20] compared to the as-cast and unreinforced aluminum alloy. In addition, improvements of 15.2%, 23%, and 31.25% in hardness, tensile strength, and impact strength, respectively, were made. Aluminum 6063 MMCs reinforced with Al_2O_3 , TiO_2 , and SiC have higher tensile strength, hardness, and yield strength than pure AA 6063, and all these properties get better as the percentage of reinforcing particles increases, according to Shuvho et al. [21]. In this study, mechanical properties were improved with 3% and 9% SiC reinforcement. However, the most interesting result of the study is that welded with CMT while Rm and Re both decreased in the unreinforced specimens with welding process, except AA6013+6% SiC specimen, all welded SiC reinforced composites showed higher strength at all heat input values. This is a remarkable and innovative advancement. The mechanical properties did not increase in the welded samples with the increase of the reinforcement ratio. Considering the obtained results, it can be concluded that it is possible to obtain higher mechanical properties by keeping the reinforcement rate low with the CMT method which provides low heat input.

5. CONCLUSION

In this study, three distinct composites with aluminum AA 6013 matrix and 3%, 6%, and 9% SiC reinforcement by weight were produced using the vortex-route method. The cast samples were joined using CMT welding technique current intensities of 110, 120, and 130 A. The results of the studies carried out are summarized below:

With increasing heat input, the strength of the weld seam of the unreinforced material in the as-cast condition increased.

With increasing heat input, the strength of the weld seam of SiC reinforced AMCs decreased.

The CMT method resulted in higher weld seam strength than the unreinforced material.

As a result, strength values vary in different welding methods and different heat inputs, depending on the ratio of the

reinforcement material. By using 3% reinforcement material instead of 9%, more durable structures can be obtained at lower heat inputs.

ACKNOWLEDGEMENT

This study was supported by the Scientific Research Coordination Unit of Pamukkale University under project number 20FEBE041. The authors would like to thank Fronius Istanbul International for carrying out the welding operations.

REFERENCES

- [1] N. Chawla, K. K. Chawla, *Metal Matrix Composites*, 2nd ed., Springer, New York, 2013, pp. 336–350.
- [2] A. Ulukoy, M. Topçu, S. Tasgetiren, “Experimental investigation of aluminum matrix functionally graded material: Microstructural and hardness analyses, fretting, fatigue, and mechanical properties, Proceedings of the Institution of Mechanical Engineers, Part J: Journal of Engineering Tribology”, vol. 230, no. 2, pp. 143–155, 2016, DOI: <https://doi.org/10.1177/1350650115594405>.
- [3] A. Ulukoy, M. Topçu, S. Tasgetiren, “The effect of aging treatments on wear behavior of aluminum matrix functionally graded material under wet and dry sliding conditions”, *Materialwissenschaft und Werkstofftechnik*, vol. 42, no. 9, pp. 806–811, 2011, DOI: <https://doi.org/10.1002/mawe.201100784>.
- [4] M. Arumugam, M. S. Omkumar, M. Vinayagam, “Mechanical and Tribological characteristics of AA6082/ZrB₂ composites”, *Materials Testing*, vol. 63, no. 10, pp. 962–965, 2021, DOI: <https://doi.org/10.1515/mt-2020-0111>.
- [5] T. Singh, S. K. Tiwari, D. K. Shukla, “Mechanical and microstructural characterization of friction stir welded AA6061-T6 joints reinforced with nano-sized particles”, *Materials Characterization*, vol. 159, pp. 1–14, 2020, DOI: <https://doi.org/10.1016/j.matchar.2019.110047>.
- [6] P. Bassani, E. Capello, D. Colombo, B. Previtali, M. Vedani, “Effect of process parameters on bead properties of A359/SiC MMCs welded by laser”, *Composites Part A: Applied Science and Manufacturing*, vol. 38, no. 4, pp. 1089–1098, 2007, DOI: <https://doi.org/10.1016/j.compositesa.2006.04.014>.
- [7] C. G. Pickin, K. Young, “Evaluation of cold metal transfer (CMT) process for welding aluminium alloy, *Science and Technology of Welding and Joining*”, vol. 11, no. 5, pp. 583–585, 2006, DOI: <https://doi.org/10.1179/174329306X120886>.
- [8] S. Selvi, A. Vishvakshen, E. Rajasekar, “Cold metal transfer (CMT) technology-An overview”, *Defence technology*, vol. 14, no. 1, pp. 28–44, 2018, DOI: <https://doi.org/10.1016/j.dt.2017.08.002>.
- [9] P. Kah, R. Suoranta, J. Martikainen, “Advanced gas metal arc welding processes”, *Int J Adv Manuf Technol*, 67, 655–674, (2013).
- [10] F. Kahraman, G. M. Gençer, C. Yolcu, A. D. Kahraman, M. E. Dilbaz, “Soğuk metal transfer (CMT) ve darbeli soğuk metal transfer (darbeli CMT) kaynak işlemleri ile birleştirilmiş AA5754 alüminyum alaşımlarının mikroyapı ve mekanik özelliklerinin karşılaştırmalı olarak incelenmesi”, *DEU Mühendislik Fakültesi Fen ve Mühendislik Dergisi*, 20(59), 625–636, (2018).
- [11] K. Liu, X. Jiang, S. Chen, T. Yuan, Z. Yan, “Effect of SiC addition on microstructure and properties of Al–Mg alloy fabricated by powder and wire cold metal transfer process”, *Journal of Materials Research and Technology*, 17, 310–319, (2022).
- [12] Y. Fan, F. Chen, S. Cao, Y. Hu, R. Xie, “Effect of coating submicron-sized La₂O₃ particles on regulating grain structure and mechanical properties of 6061 aluminum alloy CMT welded joints”, *Materials Today Communications*, 107764, (2023).
- [13] E.F.A. Zeid, “Mechanical and electrochemical characteristics of solutionized AA 6061, AA6013 and AA 5086 aluminum alloys”, *Journal of Materials Research and Technology*, 8(2), 1870–1877, (2019).
- [14] S. Aytekin, “Analysis of the microstructure and hardness properties of aluminum matrix composite material reinforced with nano Al₂O₃ particles using different currents and forms of welding”, Master’s thesis, Pamukkale Üniversitesi Fen Bilimleri Enstitüsü, (2021).
- [15] J.A. Taylor, “The effect of iron in Al-Si casting alloys”, In 35th Australian Foundry Institute National Conference, Vol. 31, pp. 148–157, (2004).
- [16] C.T. Wu, S.L. Lee, M.H. Hsieh, J.C. Lin, “Effects of Cu content on microstructure and mechanical properties of Al–14.5 Si–0.5 Mg alloy”, *Materials Characterization*, 61(11), 1074–1079, (2010).
- [17] A. Uluköy, “Pulsed metall inert gas (MIG) welding and its effects on the microstructure and element distribution of an aluminum matrix reinforced with SiC composite material”, *Materialwiss Werks* (2017).
- [18] A.K. Lakshminarayanan, V. Balasubramanian, K. Elangovan, K. “Effect of welding processes on tensile properties of AA6061 aluminium alloy joints”. *The International Journal of Advanced Manufacturing Technology*, vol. 40, pp. 286–296, 2009, DOI: <https://doi.org/10.1007/s00170-007-1325-0>.
- [19] V. Balasubramanian, V. Ravisankar, G. Madhusudhan Reddy, “Effect of pulsed current welding on mechanical properties of high strength aluminum alloy”. *Journal of Advanced Manufacturing Technology*, 36, 254–262, 2008, DOI: <https://doi.org/10.1007/s00170-006-0848-0>.
- [20] P. Chandrasekar, D. Nagaraju, “The Effect of Electroless Ni–P-Coated Al₂O₃ on Mechanical and Tribological Properties of Scrap Al Alloy MMCs”. *International Journal of Metalcasting*, vol. 17, no. 1, pp. 356–372. (2022). <https://doi.org/10.1007/s40962-022-00779-9>.
- [21] M.B. Shuvho, M.A. Chowdhury, M. Kchaou, B.K. Roy, A. Rahman, M.A. Islam, “Surface characterization and mechanical behavior of aluminum based metal matrix composite reinforced with nano Al₂O₃, SiC, TiO₂ particles”. *Chemical Data Collections*, vol. 28, 100442, 2020). <https://doi.org/10.1016/j.cdc.2020.100442>.

BIOGRAPHIES

Arzum Işıtan has a B.S. degree in Mechanical Engineering from Yildiz Technical University, a M.S. degree and a PhD degree in Mechanical Engineering from Pamukkale University. She has worked in Pamukkale University since 2002.

Dirim Bartuğ Göktürk obtained his BSc degree in manufacturing engineering from Pamukkale University (PAU). He works on machining and welded construction.

Volkan Onar has a B.S. degree and M.S. degree in Faculty of Technical Education, Metal Teaching from Gazi University, a Ph.D. degree in Metallurgy and Materials Engineering from Sakarya University. He has worked in Pamukkale University since 2012.

Research Article

Analysis of Emotional Authenticity Displayed by Film Actors Using Image Processing Techniques

Burak Arslan^{1*} , Emrah Aydemir² 

^{1*}Sakarya University, Department of Management Information Systems, Faculty of Business, Sakarya, Turkey. (e-mail: burakarslan@sakarya.edu.tr).

²Sakarya University, Department of Management Information Systems, Faculty of Business, Sakarya, Turkey. (e-mail: emrahaydemir@sakarya.edu.tr).

ARTICLE INFO

Received: Jan., 24. 2024

Revised: Mar., 09. 2024

Accepted: Jul, 05. 2024

Keywords:

Image Processing Techniques

Local Binary Patterns

LBP

Feature Extraction

Cinema

Film Actor

Emotional Authenticity

Facial Expressions

Corresponding author: *Burak Arslan*

ISSN: 2536-5010 / e-ISSN: 2536-5134

DOI: <https://doi.org/10.36222/ejt.1425158>

ABSTRACT

This study analyzes a social phenomenon using technical methods to uncover the underlying reasons for the researched phenomenon. This study investigates the authenticity of facial expressions and emotional cues of well-known film actors in Turkish comedy cinema films. For the study, 480 video data samples related to the actors were collected from the social media platform YouTube. The videos were categorized into smile, surprise, and anger, with 120 samples analyzed for each category. The Kaggle database containing facial expressions of smile, surprise, and anger from regular individuals was utilized to compare the images.

The Local Binary Pattern (LBP) feature extraction technique was employed to extract features from the images. Machine learning models were then constructed using the extracted features. Based on the classification results, the accuracy values were 99.37% for the smile category, 97.19% for the surprise category, and 97.81% for the anger category.

The analysis results show that the emotional expressions of film actors and normal individuals differ. This study aims to develop a unique perspective by highlighting the distinctive characteristics of renowned actors through their emotional expressions.

1. INTRODUCTION

When people encounter any image, they can make a wide range of interpretations based on their experiences. Therefore, an image represents the meaning created by thousands of words coming together. From a computer's perspective, computers, despite lacking prior knowledge, can effectively identify and present the features that contribute to forming visual content through their semantic understanding capabilities. Thus, they are capable of efficiently detecting the features present within images. The features that constitute images are known to be color, texture, and size. Many images are formed based on these fundamental features [1].

Image processing is the process of using computer assistance to clean up noise or unwanted features in an image [2]. Image processing is also a technique that enables the manipulation of images obtained from different sources. Image processing can serve different purposes, such as object detection, object recognition, or enhancing image quality. For images to be comprehensible by computers, they need to be digitized. The digitization of images is achieved through the use of colors, a feature that constitutes images [3]. This allows images to be transferred into software languages and subjected to various types of research.

Image processing is widely applied in various fields such as defense, medicine, geographic information systems, robotics, and autonomous vehicles [4]. There are also studies that can identify individuals based on their handwriting style using image processing techniques [5]. The acquisition of images through cameras can stem from different sources. The remarkable advancement of technology in our present day has brought forth numerous diverse sources for accessing images. One of the most significant sources is social media channels. Social media platforms host an enormous amount of image data. Moreover, access to this data has become more convenient. It's known that platforms like YouTube contain millions of videos. Each of these videos comprises multiple images coming together to form moving visuals. The data obtained from these sources has given rise to various research opportunities.

YouTube hosts numerous films that feature important figures in the cinema industry. These iconic films continue to be watched by millions of users even today and are freely available for viewers on YouTube. What accounts for the repeated viewing of films by Kemal Sunal, a prominent figure in Turkish cinema? This phenomenon stems from the ability to authentically present the character's words, expressions, and behaviors in the films to the audience [6]. In other popular

Turkish cinema films, one can observe that other actors have successfully achieved this, winning the audience's affection. The skillful use of gestures and facial expressions by the characters in the films aims to create genuine behavior, inviting the viewers to become part of the movie experience [7]. Analyzing whether these expressions are unique to these actors can be accomplished through image processing techniques.

Feature extraction techniques play a crucial role in image processing, and they are particularly important for various applications such as person recognition and more. Feature extraction is the process of obtaining the most relevant information in the original data. It can also be seen as a specialized form of dimensionality reduction. This allows the acquired information to be represented in a lower-dimensional space. In other words, when data is raw, it can be of very high dimensionality. Feature vectors are defined as representations of the data that are more compact by selecting features with higher information content from the data. Transforming input data into a representation that summarizes information is generally referred to as feature extraction [8]. This process is vital for enabling various image processing applications related to person recognition and beyond.

Feature extraction can be categorized into different types based on applying different approaches. The most commonly used features in image processing are spectral, geometric, and structural. Processing an image's pixel matrix involves the use of spectral features. This allows each pixel within the image to be numerically represented in terms of color values and color changes. One of the advantages of leveraging spectral features is the ability to obtain features regardless of the image's size. The most fundamental type of spectral feature involves color space, which can be used to examine the distribution of colors on an image [9].

The feature extraction stage is not sufficient for detecting the investigated phenomenon. The obtained features are separated into their classes, and the prediction process takes place using machine learning or deep learning algorithms. Machine learning can be utilized for various problems, including face recognition or detecting facial expressions. Humans are emotional beings who reflect their emotions to others using facial expressions. Facial expressions are classified as binary (positive and negative), ternary (positive, neutral, negative), or 7-category (happy, sad, angry, disgust, fear, surprise, and neutral) within the scope of studies [10].

Facial expressions play a significant role in people's relationships with others. It is stated that facial expressions greatly influence viewers. Researchers have suggested that people's innate characteristics shape their emotions, and they demonstrate this through facial expressions. Facial expressions arise from sudden changes in the face due to the contraction of facial muscles, eyebrows, and lips. These changes reflect human emotions. Since the degree of muscle contraction in each person's face differs, some individuals can exhibit better or worse emotions [11].

In light of this information, extracting and analyzing the features of an image using image processing techniques is quite feasible. As previously mentioned, old Turkish films hold a unique place for the audience. Using images of veteran actors who appeared in these films, the actors' facial expressions can be separated into features using image processing techniques. Additionally, the actors' facial expressions are classified to depict different emotional states (smile, surprise, anger). This

would allow us to examine the uniqueness of the on-screen images portrayed by these talented actors.

2. RELATED WORK

Numerous studies related to image processing can be found when reviewing the literature. The studies analyzing emotion using image processing techniques have been reviewed in the first stage. When examining recent emotion analysis studies, it is observed that the focus is primarily on publicly shared datasets. Researchers have utilized these datasets to distinguish human emotions using classifier algorithms and have attempted to improve their performance. In one such study, [10] attempted to predict emotions using the FER-2013 and CK+ datasets shared as open-source on the Kaggle website. They employed a CNN algorithm with tuned parameters as the classifier. The same classifier was utilized to categorize human faces into three categories (positive, neutral, negative) and seven categories (happy, angry, sad, disgust, fear, surprise, neutral) within the same dataset. The CNN algorithm exhibited better performance in the emotion class containing three categories. In a similar study, [11] conducted their research on different datasets shared as open-source. They attempted to detect seven different emotional states (happiness, sadness, surprise, disgust, anger, fear, neutral) using both traditional machine learning algorithms and deep learning algorithms. They employed a Histogram of Oriented Gradients (HOG) as the feature extraction method during the image processing stage. The analysis results indicated that deep learning algorithms like CNN provided better results across three different datasets compared to classical machine learning algorithms. Consequently, they attempted to identify performance differences between algorithms through emotion analysis. Another study aimed at more accurately detecting emotional states by combining different classification models. In this study by [12], they attempted to predict seven different emotions (happy, surprise, sad, disgust, anger, fear, and neutral). As a result, they found that combined classifiers performed better for positive and neutral emotional states, while singular classifiers performed better for emotions like anger and sadness. This study demonstrates that the classifier with higher performance for the investigated emotional state can be utilized for emotion prediction.

It is also possible to come across practical studies conducted on emotion analysis. From such studies, [13] claimed in their research that people's negative emotional states affect their driving behaviors. They attempted to detect seven different emotional states (happy, sad, neutral, angry, disgusted, surprised, and afraid) by capturing facial images of drivers at certain moments. They used CNN and derivative algorithms during the feature extraction stage from the images and successfully distinguished emotions with 96.63% accuracy. Thus, they aimed to develop a system capable of detecting drivers' negative emotional states and alerting them accordingly.

Emotion analysis is conducted using image processing techniques, with studies directly focusing on the human face. In a study by [14], they attempted to calculate the charisma score of the human face. They aimed to determine the visual attractiveness of celebrities by using both celebrities and non-celebrities. They utilized a dataset consisting of 6000 images of celebrities and 6000 images of non-celebrities. By employing the ResNet-50 deep learning algorithm, they

achieved a performance score of 95.92%. Regarding facial features, they found that factors such as disproportionate face width, baby face shape, and thin chin are distant from celebrity charisma. At the same time, larger eyes and darker skin tones are closer to celebrity charisma.

In another study, [15] mentioned that aging human faces is an inevitable consequence of human structure and characteristics. This phenomenon holds significant importance in biometric systems as they developed a new method capable of predicting age from facial images. Their dataset included photos of 1002 individuals aged between 0 and 69 and 1046 individuals aged between 18 and 93. They obtained features using a combination of the Local Binary Pattern (LBP) and Binary Similarity-Independent Features (BSIF) techniques for feature extraction. For classification, they employed the Support Vector Regression (SVR) algorithm. Using the developed model, they estimated the age of the provided image data. As a result, they achieved prediction accuracy ranging from 82% to 83%. In a different study, [16] highlighted that individuals have been recognized throughout history based on their inclusion in different ethnic groups. Exploiting these ethnic differences, they performed ethnic origin classification using facial images, as human faces exhibit diverse characteristics. They conducted the study using the Convolutional Neural Network (CNN) algorithm, a deep learning technique widely used in various face recognition applications. They obtained a dataset of 3105 images with different ages and ethnicities from sources like Google, Facebook, and others. The acquired images were selected in various sizes and resolutions. They used 3052 images for the training and 53 for the testing phases. Since each original image had different dimensions, all images were standardized to a size of 64x64. Utilizing the CNN algorithm, they managed to create a model that achieved an accuracy of 84.91%.

In another area of application for image processing techniques, [17] emphasized the significant importance of classifying malicious viruses in the field of cybersecurity. Departing from the traditional approach of virus identification, they aimed to classify viruses using binary images of the viruses. They obtained their dataset from a source containing 12,000 binary virus images of 32 different types. They applied the Local Binary Pattern (LBP) feature extraction technique to these images. Through training models using the K-Nearest Neighbors (KNN) classification algorithm, they achieved a prediction accuracy of 85.93%. Moreover, using the Support Vector Machine (SVM) algorithm, they reached a prediction accuracy of 87.88% for the models they created.

The related literature shows that image-processing techniques have been applied in various interdisciplinary studies. Simultaneously, the literature review demonstrates the existence of studies utilizing image processing techniques for both emotion analysis and extracting the characteristic features of the human face. Past research indicates that investigation into emotional authenticity has not been the focus. Therefore, the relationship between human emotion and the uniqueness of facial characteristics is considered an open topic for investigation.

In this study, image-processing techniques have been implemented in the cinema industry to contribute a novel perspective to the literature by applying image-processing techniques and exploring the authenticity of emotions.

3. METHODOLOGY

The data for this study was obtained from old Turkish films on the social media platform YouTube. The study focuses on determining the authenticity of emotions displayed by actors in Turkish films using image processing techniques. For analysis, images of four veteran film actors who had appeared in comedy films, namely Kemal Sunal, Şener Şen, Münir Özkul, and Adile Naşit, were utilized. Images were collected from various films for each actor, capturing their emotional expressions [18]. These emotional states consist of smiles, surprise, and anger. For each actor, there are 40 images depicting each of these emotions, resulting in 120 images representing four different emotional states. 480 emotion-related images were used for analysis across the four actors. As shown in Figure 1, only the part of the film frame that displays the emotional expression was cropped and used as data. The study aims to determine the authenticity of emotional expressions by seasoned actors. To enable comparison, a database of images containing smiles, surprise, and anger expressions from different individuals was obtained from the Kaggle website [19][20].

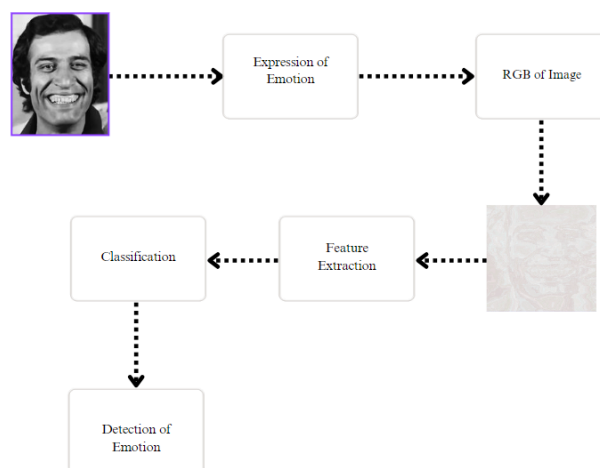


Figure 1. The Process of Detecting Emotion Expression from Image

3.1. Data Preprocessing

The data obtained undergoes several preprocessing steps for use in subsequent stages [21]. Initially, images are cropped from the film frames to include only the relevant facial expressions of the actors. As shown in Figure 1, once the facial expression image is obtained, it is converted into grayscale. In image processing and machine learning processes, images need to be transformed into a numerical format. Converting the image to grayscale yields the form seen in Figure 1, containing RGB numerical values of the image. Since each image may have different dimensions, all images are standardized to a consistent size. This size is 50x50 to reduce computation time during the machine learning phase. Standardized images then proceed to the feature extraction stage to obtain their characteristics.

3.2. Feature Extraction

There are various methods for extracting features from images. In this study, the features of the images were obtained using the Local Binary Pattern (LBP) method. LBP, a popular technique among feature extraction methods, initially emerged

for texture classification. The discovery of different application areas has also become commonly used in fields such as facial expression detection, face recognition, and fingerprint recognition [22]. The LBP method is applied to each pixel within an image. The LBP method considers the relationship between each pixel and its surrounding neighbor pixels. This relationship is based on whether the pixel is greater or smaller than its neighboring pixel. This results in a binary structure in binary notation, where the pixel is represented as 1 if greater and 0 if smaller. These binary values are combined from left to right to obtain a new value in decimal notation [23].

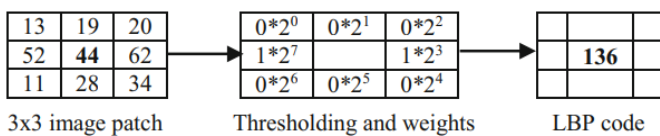


Figure 2. LBP Technique [24]

Following this approach, local LBP histograms were computed. The calculated local histograms form the feature vector. A machine learning model was constructed with the created feature vector, and the introduced images to the model were classified using multiple classification algorithms.

3.3. Classification Algorithms

3.3.1. HistGradientBoostingClassifier

It is an adaptation of the GradientBoosting classifier algorithm. Unlike the GradientBoosting algorithm, this algorithm offers a histogram-based approach. As a result, it learns faster and uses less memory than the GradientBoosting algorithm does [25].

3.3.2. LinearSVC

Support Vector Machines (SVM) is a machine learning algorithm for regression analysis and data classification. It is applied to datasets with two or more classes. LinearSVC is an adapted version of Support Vector Classification (SVC). LinearSVC aims to maximize the margin between classes, which it achieves by trying to find a linear hyperplane [26].

3.3.3. AdaBoostClassifier

Adaboost aims to create a stronger classifier by combining weak classifiers, such as decision trees. This process is applied on top of a base classifier. It focuses on reducing the error in the new classifier by increasing the weights of the points where the previous classifier has made mistakes [27].

3.4. Performance Evaluation Metric

In binary classification problems, the degree of separation between the two classes can be observed in the Confusion Matrix table. In the Confusion Matrix table, tp and tn represent the correctly classified data, while fp and fn indicate the misclassified data in the classification outcome [28].

	Actual Positive Class	Actual Negative Class
Predicted Positive Class	True positive (tp)	False negative (fn)
Predicted Negative Class	False positive (fp)	True negative (tn)

Figure 3. Confusion Matrix Binary Classification [28]

In Figure 3, evaluation metrics are used to assess the performance of the classifier algorithm. Accuracy indicates the

ratio of correctly predicted emotional expressions of actor and normal classes within the total dataset. Accuracy is the most commonly preferred evaluation metric in binary or multiclass classification problems [28].

$$\text{Accuracy (acc)} = \frac{tp+tn}{tp+fp+tn+fn} \quad (1)$$

Precision is a ratio that shows how accurately the samples predicted as a player class is predicted due to classification.

$$\text{Precision (p)} = \frac{tp}{tp+fp} \quad (2)$$

Recall is a ratio that shows how successfully the instances belonging to the actual player class are predicted.

$$\text{Recall (r)} = \frac{tp}{tp+fn} \quad (3)$$

F-Measure, or F-score, is the harmonic mean of Recall and Precision values. It provides a balanced assessment of both Recall and Precision in a classification setting [29].

$$\text{F-Measure (FM)} = \frac{2 \cdot p \cdot r}{p+r} \quad (4)$$

4. EXPERIMENTS

The confusion matrix for each emotion expression after the classification process is shown in Figure 4.

TABLE 1
RESULTS OF EMOTION OF SMILE

Method	Accuracy	F-Score	Recall	Precision
ensemble.HistGradientBoostingClassifier	0.9937	0.9938	0.9938	0.9938
XGBoost	0.9937	0.9937	0.9938	0.9941
ensemble.RandomForestClassifier	0.9906	0.9906	0.9906	0.9915
ensemble.GradientBoostingClassifier	0.9875	0.9875	0.9875	0.9886
naiveBayes.BernoulliNB	0.9875	0.9875	0.9875	0.9886
ensemble.AdaBoostClassifier	0.9844	0.9843	0.9844	0.9856
linear_model.LogisticRegressionCV	0.9844	0.9843	0.9844	0.9862
linear_model.LogisticRegression	0.9844	0.9843	0.9844	0.9862
neural_network.MLPClassifier	0.9813	0.9810	0.9813	0.9841
ensemble.VotingClassifier	0.9813	0.9810	0.9813	0.9841

Based on the classification results in Tables 1, 2, and 3, the highest accuracy value for the "smile" category is calculated as 99.37% with the HistGradientBoostingClassifier. For the "surprise" category, the highest accuracy is 97.19% with the LinearSVC, and for the "anger" category, the highest accuracy is 97.81% with the AdaBoostClassifier. The lowest performances for the algorithms are determined as follows: VotingClassifier with an accuracy of 98.37%, SGDClassifier with an accuracy of 94.38%, and BaggingClassifier with an accuracy of 95.31%.

TABLE 2
RESULTS OF EMOTION OF SUPRISE

Method	Accuracy	F-Score	Recall	Precision
svm.LinearSVC	0.9719	0.9718	0.9719	0.9737
linear_model.LogisticRegression	0.9719	0.9718	0.9719	0.9741

linear_model.LogisticRegressionCV	0.9656	0.9656	0.9656	0.9671
linear_model.PassiveAggressiveClassifier	0.9594	0.9593	0.9594	0.9620
neural_network.MLPClassifier	0.9594	0.9593	0.9594	0.9619
linear_model.Perceptron	0.9563	0.9561	0.9563	0.9590
ensemble.AdaBoostClassifier	0.9469	0.9466	0.9469	0.9512
ensemble.BaggingClassifier	0.9438	0.9436	0.9438	0.9467
svm.SVC	0.9438	0.9436	0.9438	0.9467
linear_model.SGDClassifier	0.9438	0.9434	0.9438	0.9491

TABLE 3
RESULTS OF EMOTION OF ANGRY

Method	Accuracy	F-Score	Recall	Precision
ensemble.AdaBoostClassifier	0.9781	0.9781	0.9781	0.9797
linear_model.LogisticRegressionCV	0.9750	0.9750	0.9750	0.9761
neural_network.MLPClassifier	0.9750	0.9750	0.9750	0.9761
svm.LinearSVC	0.9688	0.9687	0.9688	0.9702
linear_model.LogisticRegression	0.9688	0.9687	0.9688	0.9705
ensemble.HistGradientBoostingClassifier	0.9688	0.9687	0.9688	0.9705
XGBoost	0.9656	0.9655	0.9656	0.9683
ensemble.RandomForestClassifier	0.9594	0.9593	0.9594	0.9619
linear_model.PassiveAggressiveClassifier	0.9563	0.9559	0.9563	0.9622
ensemble.BaggingClassifier	0.9531	0.9530	0.9531	0.9570

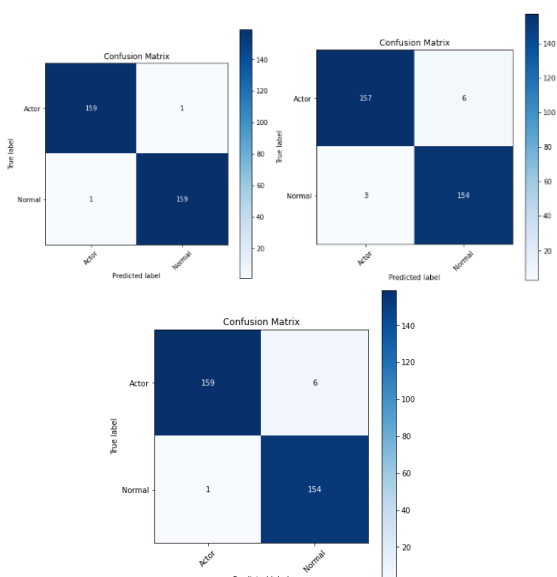


Figure 4. Confusion Matrix (Emotion of Smile, Surprised and Angry, respectively)

5. DISCUSSION

This study aims to analyze a social phenomenon using technical methods to uncover the underlying reasons behind the investigated phenomenon. The research examines the uniqueness of facial expressions and emotional states of renowned film actors in Turkish comedy movies. The analysis confirms that the actors' expressions significantly differ from those of regular individuals. Tables 1, 2, and 3 present the results obtained through machine learning. The algorithm with the highest accuracy rate for the "smile" category is the "HistGradientBoosting" with an accuracy of 99.37%. For the "surprise" category, the highest accuracy is achieved by the "LinearSVC" with 97.19%, and for the "anger" category, the "AdaBoostClassifier" performs the best with an accuracy of 97.81%.

A similar previous study by [14] attempted to identify the features that distinguish the facial characteristics of celebrities. They constructed their datasets from facial images of both celebrities and non-celebrities. Similar to this study, the ResNet-50 algorithm they used accurately classified celebrities and non-celebrities with a success rate of 95.92%. Other image processing studies have also achieved good results using similar algorithms. From these studies, [30] developed a machine-learning model using AdaboostClassifier on 355 brain images to differentiate brain tumors. Their model achieved 100% accuracy using 155 test images. In another study, [31] developed a machine-learning model to distinguish diseased leaves from leaf images. Similarly, they used LBP and HOG techniques for feature extraction and employed multiple algorithms for classification. The HistGradientBoosting algorithm yielded the highest accuracy of 89.11% among the tested algorithms. Another study by [32] focused on predicting seven different facial expressions from the KDEF_RaFD dataset. Their model achieved the highest F-score using the LinearSVC algorithm. These reviewed studies demonstrate that comparable performance results can be obtained using the machine learning algorithms employed in this study. Although the topics investigated in image processing vary, the results sought to be achieved are similar. Studies demonstrating the distinct facial characteristics of celebrities also support this research.

In this study, the emotional expressions of four master actors in comedy films were obtained, focusing on happiness, surprise, and anger. The data collection phase posed challenges in obtaining emotional expression data related to the actors. Therefore, analysis was conducted using three emotional expressions and four cinema actors. This limitation could be considered in the study. In future studies, the diversity of emotional expressions and the number of actors can be expanded to conduct further analyses.

6. CONCLUSION

The analysis of this study revolves around the unique nature of emotional expressions displayed by master actors in Turkish films using image processing and machine learning techniques. The study attempted to demonstrate the distinctiveness of famous actors' emotional states compared to existing similar studies. Being the first study to evaluate the subject from this perspective indicates its originality. The study aims to uncover whether the emotional expressions of these actors are distinctive and contribute to their enduring popularity and have resonance with audiences even today. The emotional expressions of regular individuals and actors were utilized to achieve this analysis. The findings suggest that machine learning models effectively differentiate between the emotional expressions of regular individuals and those of actors. This outcome implies that the gestures and facial expressions of master actors are indeed unique to them. The immense popularity of films featuring these master actors can be attributed to this uniqueness. Furthermore, emerging actors in the film industry can be evaluated using this approach, providing insight into how closely their expressions align with those of veteran actors. In future research, an application can be designed for this system, enabling artificial intelligence to serve as a decision-support element in actor selection within the film industry. The study also provides opportunities for future research. The analysis phase of the study was conducted

using traditional machine learning algorithms with a limited data set. Subsequent studies could expand the data set and test the findings using deep learning algorithms to enhance the research. Additionally, the study used only images of Turkish film actors for analysis. Future research could broaden the scope of the investigation by using images of renowned actors from different countries worldwide to make the findings more generalizable.

REFERENCES

- [1] D. Ping Tian, "A review on image feature extraction and representation techniques" *International Journal of Multimedia and Ubiquitous Engineering*, vol. 8, no. 4, pp. 385-396, 2013.
- [2] B. Chitradevi and P. Srimathi, "An overview on image processing techniques" *International Journal of Innovative Research in Computer and Communication Engineering*, vol. 2, no. 11, pp. 6466-6472, 2014.
- [3] A. Eldem, H. Eldem, and A. Palali, "Görüntü işleme teknikleriyle yüz algılama sistemi geliştirme" *Bitlis Eren Üniversitesi Fen Bilimleri Dergisi*, vol. 6, no. 2, pp. 44-48, 2017.
- [4] S. Solak and U. Altınışık, "Görüntü işleme teknikleri ve kümeleme yöntemleri kullanılarak fındık meyvesinin tespit ve sınıflandırılması" *Sakarya University Journal of Science*, vol. 22, no. 1, pp. 56-65, 2018.
- [5] S. Ağduk and E. Aydemir, "Classification of Handwritten Text Signatures by Person and Gender: A Comparative Study of Transfer Learning Methods" *Acta Informatica Pragensia*, vol. 2022, no. 3, pp. 324-347, 2022.
- [6] A. K. Sunal, TV ve sinemada Kemal Sunal güldürüsü. Marmara Üniversitesi (Turkey), 1998.
- [7] Z. OKRAY and C. A. MEVLANA, "Selvi Boylum Al Yazmalım Filminin Göstergebilimsel Yöntem Bilimiyle Analizi" *Uluslararası Beşeri Bilimler ve Eğitim Dergisi*, vol. 5, no. 12, pp. 1216-1244, 2019.
- [8] G. Kumar and P. K. Bhatia, "A detailed review of feature extraction in image processing systems" in *2014 Fourth international conference on advanced computing & communication technologies*, 2014: IEEE, pp. 5-12.
- [9] M. Kunaver and J. Tasic, "Image feature extraction-an overview" in *EUROCON 2005-The International Conference on "Computer as a Tool"*, 2005, vol. 1: IEEE, pp. 183-186.
- [10] Meena, G., et al. (2023). "Identifying emotions from facial expressions using a deep convolutional neural network-based approach." *Multimedia Tools and Applications*: 1-22.
- [11] Aksoy, O. E. and S. Güney (2022). "Sentiment analysis from face expressions based on image processing using deep learning methods." *Journal of Advanced Research in Natural and Applied Sciences* 8(4): 736-752.
- [12] Moun, E. G., et al. (2022). "Ensemble-based face expression recognition approach for image sentiment analysis." *Int. J. Electr. Comput. Eng* 12(3): 2588-2600.
- [13] Gite, S., et al. (2024). "Real-Time Driver Sentiment Analysis Using Hybrid Deep Learning Algorithm." *International Journal of Intelligent Systems and Applications in Engineering* 12(6s): 735-748.
- [14] Feng, X. F., et al. (2021). "An AI method to score celebrity visual potential from human faces." Shunyuan and Liu, Xiao and Srinivasan, Kannan and Lamberton, Cait Poyner, An AI Method to Score Celebrity Visual Potential from Human Faces (May 1, 2021).
- [15] S. E. Bekhouche, A. Ouafi, A. Taleb-Ahmed, A. Hadid, and A. Benlamoudi, "Facial age estimation using bsif and lbp" *arXiv preprint arXiv:1601.01876*, 2016.
- [16] T. I. Baig et al., "Classification of human face: Asian and non-Asian people" in *2019 International Conference on Innovative Computing (ICIC)*, 2019: IEEE, pp. 1-6.
- [17] J.-S. Luo and D. C.-T. Lo, "Binary malware image classification using machine learning with local binary pattern" in *2017 IEEE International Conference on Big Data (Big Data)*, 2017: IEEE, pp. 4664-4667.
- [18] Arslan, B., & Aydemir, E. (2023). Turkish Cinema Faces– Data set. Kaggle.
<https://www.kaggle.com/datasets/147e6c63e2bcb13f22ebbad54601e9a59c1556d85ed1251fdb6b9c6ecfc94f3d>
- [19] Chazzer (2022). Smiling or Not– Data set. Kaggle.
<https://www.kaggle.com/datasets/chazzer/smiling-or-not-face-data?resource=download>
- [20] Vaidya (2020). Natural Human Face Images for Emotion Recognition – Data set. Kaggle.
<https://www.kaggle.com/datasets/sudarshanvaidya/random-images-for-face-emotion-recognition>
- [21] Dalgın, G. T., & Daş, R. Sinema verilerinin Neo4j çizge veritabanı ile modellenmesi ve analizi. Dicle Üniversitesi Mühendislik Fakültesi Mühendislik Dergisi, 15(1), 1-13.
- [22] P. Kral and L. Lenc, "LBP features for breast cancer detection" in *2016 IEEE international conference on image processing (ICIP)*, 2016: IEEE, pp. 2643-2647.
- [23] A. Gunay and V. V. Nabiye, "Automatic age classification with LBP" in *2008 23rd international symposium on computer and information sciences*, 2008: IEEE, pp. 1-4.
- [24] Karanwal, S. and M. Diwakar (2023). "Triangle and orthogonal local binary pattern for face recognition." *Multimedia Tools and Applications* 82(23): 36179-36205.
- [25] Brownlee, J. (2020, April 27). Histogram-Based Gradient Boosting Ensembles in Python.
<https://machinelearningmastery.com/histogram-based-gradient-boosting-ensembles/>
- [26] C.-C. Chang and C.-J. Lin, "LIBSVM: a library for support vector machines" *ACM transactions on intelligent systems and technology (TIST)*, vol. 2, no. 3, pp. 1-27, 2011.
- [27] Y. Freund and R. E. Schapire, "A decision-theoretic generalization of on-line learning and an application to boosting" in *European conference on computational learning theory*, 1995: Springer, pp. 23-37.
- [28] M. Hossin and M. N. Sulaiman, "A review on evaluation metrics for data classification evaluations" *International journal of data mining & knowledge management process*, vol. 5, no. 2, p. 1, 2015.
- [29] H. Dalianis and H. Dalianis, "Evaluation metrics and evaluation" *Clinical Text Mining: secondary use of electronic patient records*, pp. 45-53, 2018.
- [30] R. Sonavane and P. Sonar, "Classification and segmentation of brain tumor using Adaboost classifier" in *2016 International Conference on Global Trends in Signal Processing, Information Computing and Communication (ICGTSPICC)*, 2016: IEEE, pp. 396-403.
- [31] M. B. Devi and K. Amarendra, "Machine Learning-Based Application to Detect Pepper Leaf Diseases Using HistGradientBoosting Classifier with Fused HOG and LBP Features" in *Smart Technologies in Data Science and Communication: Proceedings of SMART-DSC 2021*, 2021: Springer, pp. 359-369.
- [32] N. V. Smirnov and A. S. Chernyshov, "Emotion recognition from facial images" in *2022 International Russian Automation Conference (RusAutoCon)*, 2022: IEEE, pp. 116-121.

BIOGRAPHIES

Emrah Aydemir received the M.S. degrees in computer teaching from the University of Elazığ Firat, in 2012 and the Ph.D. degree in informatics from Istanbul University, Turkey, TR, in 2017. From 2012 to 2015, he was an Expert with the Istanbul Commerce University. Since 2017, he has been an Associate Professor with the Management Information Systems Department, Sakarya University. His research interests include artificial intelligence, microcontroller, knowledge management systems, database and software.

Burak Arslan obtained his BSc degree in electrical and electronics engineering from Sakarya University (SAU) in 2016. He received the MSc. diploma in Business Administration from the Pamukkale University in 2021. He continues his PhD. in management information systems at Sakarya University. His research interests are data analysis, data mining, business intelligence, business analytics and artificial intelligence.

Research Article

The Impact of Locally Available Materials on Architectural Heritage: Preliminary Findings from the Güzelşeyh Pavilion, Türkiye

Felat Dursun^{1,2*} ^{1*}Department of Conservation and Restoration of Cultural Heritage, Izmir Institute of Technology, Izmir, Türkiye²Department of Mining Engineering, Dicle University, Diyarbakir, Türkiye (e-mail: felatdursun@gmail.com; felatdursun@iyte.edu.tr)

ARTICLE INFO

Received: Sep., 30. 2024

Revised: Nov., 03. 2024

Accepted: Nov., 08. 2024

Keywords:

Basalt

Limestone

Local material

Stone conservation

Güzelşeyh Pavilion

Corresponding author: *Felat Dursun*

ISSN: 2536-5010 | e-ISSN: 2536-5134

DOI: <https://doi.org/10.36222/ejt.1558833>

ABSTRACT

Understanding how local stones shaped material selection in historical structures is crucial for preserving architectural heritage and guiding conservation strategies. The current study examines the role of local materials in the construction and preservation of the Güzelşeyh Pavilion (GP), situated in the Çınar district of Diyarbakır, Türkiye. GP is unique not only for its use of basalt and limestone but also for combining these locally sourced stones into its architectural elements. This preliminary research assesses the pavilion's current condition and proposes possible stone sources for conservation. Located at the meeting point of volcanic rocks and Eocene limestones, the pavilion uses basalt for load-bearing elements and limestone for both decorative and structural components. The contrast between dark basalt and light limestone enhances its aesthetic appeal, while their combined application strengthens its durability. Fieldwork and laboratory studies, including mineralogical, petrographic, and geochemical analyses, were conducted to investigate the materials and their sources. Site investigations revealed that the pavilion, now largely in ruins, has suffered different forms of decay, particularly in its limestone components compared to the basalt. The analysis suggests nearby volcanic units as a probable source for the basalt, reflecting characteristics that closely match those of the region. Similarly, the limestone appears to align with materials sourced from quarries in Bağacık village, suggesting these quarries as a possible source for the pavilion's limestone. By identifying these sources, the study offers practical guidance for conservation architects working to ensure the long-term preservation of the site.

1. INTRODUCTION

Using locally available materials in historic structures has long been an essential architectural practice, reflecting cultural identity, sustainability, and environmental adaptability across diverse regions [1–3]. These materials (often known as locally sourced, locally extracted, locally quarried) are typically resources either naturally found or produced from raw materials within the region. For centuries, communities have utilized local resources to construct functional structures that reflect regional traditions and respond to environmental conditions. Materials like stone, timber, wood, bamboo, brick, and adobe have been valued not only for their durability and aesthetic properties but also for their ability to resist local environmental pressures while enhancing sustainability across various regions [4–9].

It is known that ancient builders did not simply choose these materials for convenience; their selections were guided by a deep understanding of the materials' behavior under different environmental and structural loads. This expertise, refined

over generations, informed construction techniques that maximized the resilience and efficiency of structures [17–20]. Generations of accumulated knowledge allowed communities to create building techniques specifically suited to their local environment. As a result, their shelters, religious structures, and monuments were durable and designed to work in harmony with the region's climate and geological conditions. Stone holds a unique position among building materials, not only for its durability, strength, and adaptability but also as one of the most abundant resources available on the Earth's surface. Its role in architecture is unmatched, as it not only provides structural stability but also contributes to the cultural identity of civilizations across time [10–12]. Their accessibility often dictated architectural choices, with stones sourced from nearby quarries to minimize transportation challenges. However, the use of stone was not based solely on practical considerations; it also reflected the cultural values of the communities. This deep connection between material and heritage is evident across numerous ancient cultures, where stone became the foundation of their architectural

achievements. For example, the Nabataeans expertly carved the city of Petra into the red sandstone cliffs of modern-day Jordan, using the soft but strong stone to create impressive facades that have lasted through centuries of weathering [13–14]. Similarly, the city of Mardin in southeastern Türkiye is renowned for its distinctive limestone architecture, where locally quarried limestone, well-suited to the semi-arid climate, provides both insulation and durability for historic buildings [15]. In Italy, Roman structures like the Colosseum were built primarily with local stones like travertine and volcanic tuff, indicating the Romans' skill in using these materials for both strength and aesthetic appeal [16].

The relationship between natural stone and architectural heritage extends beyond material availability. Abundant local stone fostered a tradition of skilled craftsmen, including stone carvers and masons. In Mardin, the skilled stone carving traditions reflect the community's deep knowledge of limestone's workability and weathering properties, enabling artisans to create buildings that are both durable and artistically impressive [15].

Sourcing building stones for conservation projects has long been a challenge. Conservation architects frequently consult geologists on how and where to obtain compatible materials [3]. Even when suitable stones are locally available, factors like urbanization, industrialization, or legal protections can limit extraction. Despite these obstacles, the geology of a region still plays a key role in shaping the landscape and determining stone availability. Variations in rock types—igneous, sedimentary, metamorphic—along with morphology, petrography, tectonic activity, topography, and durability, provide diverse materials that influence architectural practices.

Considering the locally available stone materials, the convergence of different geological units—refers to the meeting or interaction of distinct rock formations, such as volcanic, sedimentary, or metamorphic units, within a specific region—not only shapes the surface topography but also allows for the formation of different natural stone types within proximity. This practice is particularly evident in structures built near geological boundaries, where the proximity of different geological units allowed for the use of various stone types. In this context, the Güzelşeyh Pavilion (GP), located between Diyarbakır and Mardin, serves as a unique example of how local geology influenced material choices.

This study aims to define how the local availability of different lithological units is reflected in the GP's architecture and suggest proper material sources for its conservation.

2. STUDY AREA

The subject of this study is the GP, located in the Çınar district of Diyarbakır province, Turkey. The pavilion has been officially protected by the Diyarbakır Regional Board for the Conservation of Cultural Heritage since June 6, 1990 [21]; however, notable work on the site has been limited. Aside from Meltem-Tekin's [22] conservation-focused documentation and Yariş's [23] study on ornamentations, the site has received little significant attention to date. There is no clear documentation identifying the exact date of construction or the builders of the GP [24–27]. However, the Diyarbakır Regional Board suggests that the pavilion was built approximately 150 years ago by Assyrian stonemasons from Mardin, though the evidence supporting this claim remains uncertain. An Ottoman-period document from 1898, cited by

[26], indicates that the building was used as both a madrasa and a pavilion in the early 20th century. Another perspective is proposed by art historians, including [23–24], who suggest that considering the ornamentations and construction techniques, it was likely built during the Ottoman period and initially served as an inn or postal relay station. All the evidence suggests that the structure has existed since at least 1855 [22], [26].

The structure, originally constructed using traditional masonry techniques, has unfortunately fallen into a state of partial ruin over time due to prolonged neglect (Figure 1). The pavilion consists of the ground floor and the first floor. The ground floor was used as a madrasa, and the upper floor was used as a pavilion [23]. The ground floor, rectangular and aligned east-west, is accessed through two entrances in the same direction. These entrances lead to a central corridor flanked by 16 rooms. While the rooms on the west side remain relatively intact, those on the east side have collapsed in places with damage extending to the foundation level (Figure 1). The first floor, oriented perpendicular to the ground floor, was originally accessed by a staircase, which has since been demolished. This floor consists of two rooms in a rectangular form along the north-south axis and a central space [23]. The upper cover of the rooms has been completely demolished (Figure 1), and portions of the floor have also collapsed. This transition is significant as it reveals how the building's original fabric changed over time.

Basalt served as the foundational material on the ground floor, used on the flooring and in load-bearing walls due to its strength. On the first floor, dressed limestone became the dominant material, contributing to the building's decorative carvings, ornamentation, and arches, which enhanced its aesthetic value. The most common ornamentations in the building are those with plant and geometric patterns. Although these decorative elements are concentrated on the first floor, it is possible to see remarkable ones carved in limestone on the exterior facades (especially on corner borders, portals, arches, windows, and hood molds) [22–23] (Figure 1).

3. MATERIALS AND METHODS

This preliminary study was conducted in two primary phases: field surveys and laboratory analyses. The fieldwork involved site inspections and material sampling. During the site inspections, the geological context of the site and its surrounding areas were investigated by examining the distribution, boundaries, and characteristics of geological units. Accessible outcrops were visited to assess the sources of construction materials. Additionally, the conservation state of the pavilion was assessed to determine the application of natural building stones and identify major forms of decay. To characterize and identify the materials used in the construction of the pavilion, four representative locations were selected for sampling.

A total of 5 samples were collected, including one basalt sample from the pavilion (Sample 1), one sample from the basalt quarry near the pavilion (sample 2), one limestone sample from the pavilion (Sample 3), one limestone sample from the Bağacık Village (Sample 4) and one limestone sample from the Zerzevan Castle outcrops (Sample 5). The second phase focused on laboratory analyses, which included mineralogical, petrographic, and chemical characterization of the collected samples.



Figure 1. Façade views and principal construction materials of the GP (Bottom right image sourced from [22])

Five thin sections were prepared for petrographic examination of the limestone and basalt samples collected from the pavilion and potential material sources. An optical microscope equipped with a camera system was used to perform modal analysis and assess grain size, texture, and rock classification. The major oxide compositions were determined through X-ray Fluorescence (XRF) analysis. All petrographic and chemical analyses were conducted at the Institute of Mineral Research and Exploration (MTA) Laboratories in Ankara, Türkiye.

4. GEOLOGICAL SETTINGS

The GP is located in the transition zone between volcanic and sedimentary terrains. Understanding this geological setting is crucial for contextualizing the site's location and construction materials. Figure 2 provides geological maps of the region and site derived from those prepared by the Mineral Research and Exploration General Directorate [26–28]. These maps illustrate the distribution and age of rock units, enhancing our understanding of the geological composition and the location of the GP.

The study area is situated along the northern margin of the “Arabian Platform” (Figure 2 a), characterized by a Paleozoic succession with clastic and carbonate layers and a Mesozoic succession predominantly composed of carbonates. This platform is tectonically overlain by northward-verging ophiolitic nappes [29–30]. A distinct structural feature in the region is the presence of numerous east-west trending fold axes aligned parallel to the northern thrust fault. These structural sequences are unconformably overlain by Neogene to Quaternary sedimentary and volcanic layers. Figure 2 b illustrates the local geology near the study area, where exposed

rock units include Eocene limestones and continental sedimentary deposits from the Neogene to Quaternary periods, interlayered with volcanic rocks. Among these, only the Eocene limestones and volcanic rocks have been used as building materials in the GP. The following sections detail these two units.

Eocene Limestone: This limestone is the oldest exposed unit within the study area and represents the youngest layer of the Arabian Platform sequence (Figure 2 b). The limestone appears in shades ranging from light cream to beige and is generally massive, with medium to thick bedding; however, in some areas, it also exhibits a porous structure. The unit includes thin to thick layers of cream and beige dolomite and several levels of cherty limestone. Widespread across southeastern Turkey, this unit has a thickness exceeding 300 meters [27]. The Eocene limestone, used as a building stone in the construction of the GP, is also found in the Roman castrum of Zerzevan Castle, located approximately 20 km south of the pavilion. This same limestone was used for the fortifications and other structures within the castrum [31]. However, this unit can show color and textural variations even in areas close to the study location.

Volcanic Rocks: The second type of building stone used in the GP is volcanic in origin and dates to the Neogene-Quaternary period. These volcanic rocks belong to the Karacadağ volcanic complex, which has been widely studied for its mineralogical, petrographic, and geochemical properties [32–36]. Karacadağ volcanism, characterized by basaltic formations with a shield-like morphology, covers a broad area in southeastern Türkiye.

Ercan et al. [33] proposed a volcano-stratigraphic scheme dividing the Karacadağ volcanic activity into three main phases. According to this scheme:

- The first phase, known as the Siverek volcanic complex, dates to the Late Miocene based on K-Ar dating and extends over an area of approximately 10,000 square kilometers to the south and west of Diyarbakır. This phase covers over 80% of the volcanic complex and provides the possible building stones quarried for the GP.
- The second phase, referred to as the Karacadağ volcanics, represents the main formation of the Karacadağ Mountain, which reaches an elevation of 1,957 meters. These volcanics cover around 15% of the complex and include the basalt layers beneath the Diyarbakır City Wall (Figure 2 b).
- The third and most recent phase, known as the Ovabağ volcanics, consists of fresh-looking basalts along the southeastern and eastern margins of the complex. These rocks are distinguished by their dark color, sparse vegetation, and well-preserved morphology, including Aa and Pahoe-hoe lava flows, lava tubes, and prominent scoria cones on the eastern slopes.

Other exposed units in the area include semi-consolidated to unconsolidated sedimentary deposits, largely of fluvial origin and formed in a continental environment. The alluvial deposits of the Tigris River currently form the eastern boundary of the Karacadağ volcanic complex.

5. RESULTS AND DISCUSSION

5.1. Field observations

Field observations revealed that the pavilion is situated on a hill at an elevation of 686 meters, offering a commanding view over the surrounding plain. The geological characteristics of this location have played a significant role in the choice of the site. The nearby village of Altınakar, to which the pavilion is connected, lies on the floodplain of the Tigris River at a lower elevation of 650 meters (Figure 2). In contrast, the pavilion is located approximately 3 km northwest of Altınakar village, within the basalt outcrops. As shown in Figure 2, this area marks the endpoint of a basalt lava flow. The basaltic landscape, offering a more stable foundation than the floodplain's alluvial deposits, seems to have been a deliberate technical decision in the pavilion's site selection.

The primary building materials of the pavilion are basalt and limestone. The ground floor is mainly constructed from rubble or semi-dressed basalt, with walls varying in thickness from 95 to 105 cm. Limestone is primarily used on the first floor and for specific architectural elements such as wall edges, door frames, floor moldings, and windows. The limestone walls on the upper floor are slightly thinner, with a thickness ranging from 60 to 80 cm, reflecting limestone's unique properties and load-bearing requirements [22].

The basalt blocks in the masonry are irregularly shaped, with average dimensions of 22 cm in height, 25 cm in width, and 20 cm in depth. However, these dimensions can vary significantly depending on their position within the wall and specific

structural demands. In contrast, the limestone blocks on the upper floor are typically larger and more uniform, averaging 35 cm in height, 50 cm in width, and 35 cm in depth. These measurements are approximate, as stone sizes often vary due to the adaptive construction techniques applied.

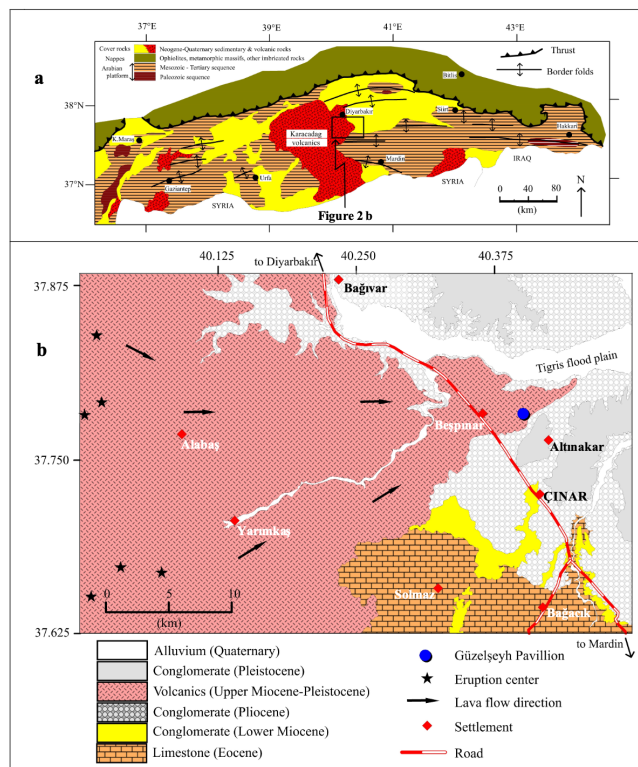


Figure 2. Geological map of the area around the GP [26-28]

The most likely source of the basalt used in the construction of the pavilion is thought to be the basalt units observed in its immediate vicinity. In addition to basalt, the region and its surroundings offer limestone units that are well-suited for use as building materials. Notably, limestone outcrops in Bağacık Village, located about 15 km south of the site (Figure 2,6), and the historically significant Zerzevan Castle, situated roughly 20 km southeast, stand out as prominent sources of stone for construction. As mentioned in previous sections, field studies revealed that basalt and limestone were applied in different forms in the structure (i.e., as rubble and cut stone). The primary reason for employing limestone as cut stone is its suitability for carvings and motifs that enhance the building's aesthetic and historical value. Additionally, limestone is easier and more efficient to work with than basalt, offering advantages in terms of both time and labor.

Early written and photographic documents from the registration records confirm that basalt was extensively used for the ground floor during the original construction. However, in later periods, certain sections of the building were modified with the addition of limestone, particularly in areas where basalt had originally been used. These changes, likely made during repairs and renovations, introduced limestone for architectural features such as door and window frames, wall edges, and sections of the vaults. Limestone was also added to parts of the ground floor, especially at the portal and the corners of the walls. Meltem-Tekin and Oğuz [22] also noted these modifications, pointing out the repeated use of limestone in various parts of the structure during different renovation phases.

The type, extent, and distribution of decay forms were analyzed as part of the field studies. Although the current abandoned state of the building limits a comprehensive assessment, an attempt was made to describe the weathering forms observed in the remaining standing sections (Figure 3). It was observed that the basalt, especially in areas in contact with the ground, showed signs of decay, including discoloration, chipping, and blistering due to water exposure. On the other hand, the limestone exhibited more severe deterioration, primarily characterized by significant material loss.

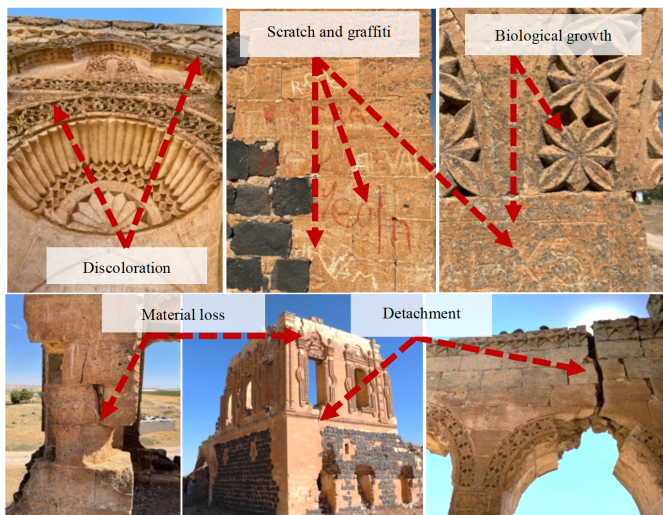


Figure 3. Some of the decay forms observed in Güzelşeyh (Bottom right image sourced from [22])

Additionally, the limestone showed signs of chipping, fading, erosion, discoloration, deposits, fractures, cracks, scratching, and biological colonization (Figure 3). Although less common, efflorescence was also noted at certain lower elevations. The forms of decay observed affected not only the building stones but also the iconic reliefs. Damage from both human activities and atmospheric conditions has accelerated the deterioration process. Today, this damage combines with other forms of decay, further threatening the surviving parts of the structure.

5.2. Mineralogical, petrographic and geochemical characteristics

Based on the field studies and petrographic investigations, the materials used in the GP are classified as basalt (massive and vesicular) and limestone. The thin section images, illustrating the textural and structural characteristics of the samples, are shown in Figure 4. At the same time, the XRF results, detailing the major oxide composition (in weight percent, wt%), are summarized in Table 1.

In the hand specimen, Sample 1 (basalt from the structure) shows some local signs of weathering, while Sample 2 (basalt from a nearby quarry) appears unaltered. Both samples display a dark grey to black color, typical of basalt, with a fine-grained, dense texture and no visible large crystals, consistent with the characteristics of massive basalt.

The thin sections of the basalts (Figure 4 a, b) reveal a mineral composition primarily made up of plagioclase, pyroxene, and olivine. Plagioclase forms the dominant groundmass in the form of lath-shaped microlites. However, Sample 1, taken from the structure, shows some signs of alterations, particularly in the forms of iddingsite and carbonatization.

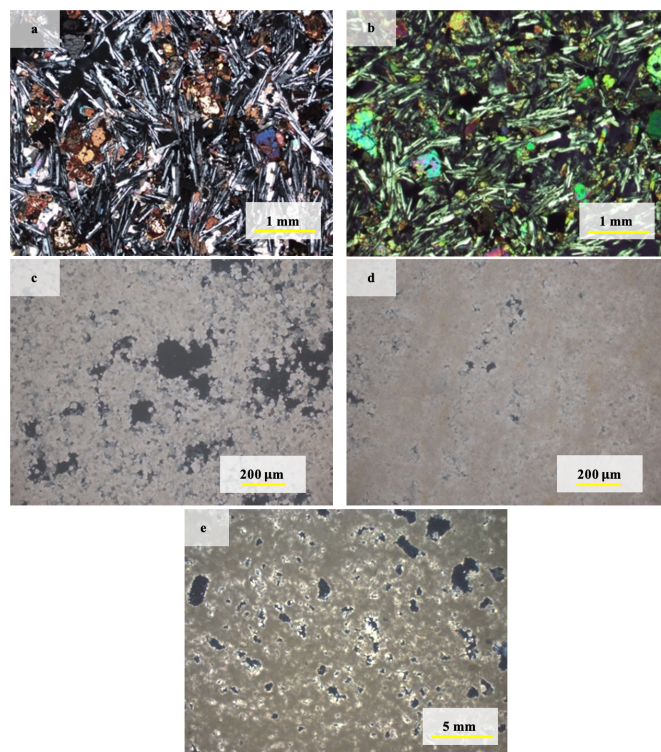


Figure 4. Photomicrograph illustrating the mineralogical and textural characteristics of (a) sample 1: basalt used in the structure, (b) sample 2: basalt sampled from the quarry, (c) sample 3: limestone used in structure, (d) sample 4: limestone sample from Bağacık Village, (e) sample 5: limestone sample from the vicinity of Zerzevan Castle (under cross-polarized light (XPL))

Iddingsite formation, a process where olivine transforms into iron oxides and clay minerals, occurs when olivine is exposed to moisture and oxygen over time. During this transformation, magnesium is typically removed from the olivine structure as part of the alteration process, leading to a reduction in the original magnesium content of the rock [37–38]. In addition, carbonatization is observed, which involves the chemical alteration of the basalt whereby carbonate minerals form in the voids and spaces between plagioclase laths (Figure 4 a, b). This process occurs when calcium interacts with carbon dioxide (CO_2) and water, forming calcium carbonate (CaCO_3), which can precipitate within the rock [39]. Limestone, which naturally contains calcium carbonate, likely accelerated the carbonatization of the basalt by providing a ready source of calcium, especially in the presence of moisture and environmental CO_2 [40–41]. Sample 2, while showing fewer signs of alteration compared to Sample 1.

The XRF analysis (Table 1) aligns partially with these petrographic observations, highlighting the chemical differences between Sample 1 and Sample 2. Sample 1 shows a higher CaO content (11.9 wt%) compared to Sample 2 (7.27 wt%), reflecting the presence of carbonates introduced during the carbonatization process. This process is likely influenced by the combined use of limestone and basalt as building materials, where the calcium content of the limestone accelerates the carbonatization of basalt. The interaction between these materials, especially in the presence of moisture and CO_2 , has promoted faster carbonate formation within Sample 1.

Here, it is worth noting that, due to the preliminary nature of this study and the limited number of samples, these findings require further validation. Therefore, attributing the observed CaO variation solely to this combination of materials does not

fully capture the complexity of the differences noted. While alteration clearly contributes to the CaO increase, the variation also likely reflects primary magmatic characteristics of Karacadağ Volcanism, which is known for its CaO variability [42]. This suggests that both alteration processes and the original magmatic composition play a significant role in the CaO levels observed in Sample 1.

TABLE 1. Chemical composition (wt%) of samples analyzed by XRF

Oxides (wt%)	Sample 1	Sample 2	Sample 3	Sample 4	Sample 5
Al ₂ O ₃	12.6	13.72	0.4	0.3	0.2
CaO	11.9	7.27	29.2	30.2	33.7
Fe ₂ O ₃	14.6	14.41	0.1	0.1	0.1
K ₂ O	1.1	1.08	<0.1	0.1	<0.1
MgO	8.5	9.63	21.1	20.4	18.7
MnO	0.2	0.17	<0.1	<0.1	<0.1
Na ₂ O	2.6	3.3	0.2	0.1	0.4
P ₂ O ₅	0.4	0.33	<0.1	<0.1	<0.1
SiO ₂	42.4	47.68	1.8	2.1	0.6
TiO ₂	2.5	2.4	<0.1	<0.1	<0.1
LoI	2.75	-0.1	46.9	46.5	45.8

In terms of MgO, Sample 1 has a slightly lower content (8.5 wt%) compared to Sample 2 (9.63 wt%). While the MgO reduction in Sample 1 may indicate alteration of olivine through iddingsite formation, the difference between Sample 1 and Sample 2 (nearly 5%) suggests that primary magmatic variations may also contribute, rather than alteration alone. The MgO content in Karacadağ basalts varies significantly based on magmatic origin [42], which should be considered alongside alteration effects. Both samples display similar Fe₂O₃ content (14.6 wt% and 14.41 wt%), indicating the stability of iron-bearing minerals like pyroxene and olivine. The SiO₂ content is higher in Sample 2 (47.68 wt%) than in Sample 1 (42.4 wt%), suggesting that Sample 2, having undergone less alteration, still holds more of its original silica-rich composition. The Loss on Ignition (LOI) is considerably higher in Sample 1 (2.75 wt%), confirming the presence of volatile components, such as carbonates formed during the alteration process. The results suggest that Sample 1 and Sample 2 likely originate from the same volcanic source. However, their varying degrees of alteration, influenced by both environmental factors and primary magmatic composition, set them apart.

The petrographic analyses of the three limestone samples collected from the structure (Sample 3), Bağacık Village (Sample 4), and a quarry close to the Zerzevan castle (Sample 5) indicate considerable similarities as carbonate rocks, yet certain variations are observed in terms of texture and mineral content (Figure 4 c, d, e). In both the hand specimens, Samples 3 and 4 show more remarkable similarity to each other compared to Sample 5. Samples 3 and 4 hand specimens are more compact, with fewer visible voids and a massive appearance than Sample 5. Both share a light-yellow color and a fine-grained texture; in contrast, Sample 5 is visibly more porous and lighter in color, with a yellowish-white tone and a slightly different texture in the hand specimen.

The petrographic analysis of the three samples reveals that all of them are classified as limestone. Despite this shared classification, minor differences in texture and mineral content are observed across the samples. Samples 3 and 4 exhibit a clastic texture with fine-grained carbonate minerals and

micritic cement as a binder (Figure 4 c, d). The voids present in these two samples are related to dissolution processes, with Sample 3—taken from a structure—showing a higher degree of porosity. This is likely due to long-term environmental exposure and weathering (Figure 4 c). Dolomite is present in both samples as scattered grains within the micritic matrix, with Sample 3 displaying more visible alteration features than Sample 4. In contrast, Sample 5 is also a limestone but differs due to its cryptocrystalline to microcrystalline texture and a more porous appearance. Some of these voids are partially filled with secondary carbonate minerals (Figure 4 e). This suggests that Sample 5 has undergone a different diagenetic process compared to the first two samples, with more calcite crystallization occurring in its pore spaces. Additionally, Sample 5 is noted for its lighter color and visibly more porous hand specimen, setting it apart from the more compact appearance of Samples 3 and 4.

The XRF analysis provides further insight into the composition of the samples and helps to clarify the differences observed in the petrographic study (Table 1). Samples 3 and 4 both contain significant amounts of CaO and MgO, indicative of substantial dolomitization. Sample 3 has 29.2 wt% CaO and 21.1 wt% MgO, while Sample 4 contains 30.2 wt% CaO and 20.4 wt% MgO. These values align with the petrographic evidence of dolomite in both samples, further supported by the clastic texture and the fine distribution of dolomite grains within the micritic matrix. The slightly higher MgO content in Sample 3 reflects its greater dolomite presence, which corresponds to the higher degree of alteration observed in the petrographic analysis. The XRF results reinforce these observations by showing similar CaO and MgO concentrations in Samples 3 and 4, further supporting their close relationship in terms of mineral content and dolomitization (Table 1). Sample 5, however, diverges both petrographically and chemically, with higher calcite content, fewer dolomite phases, and greater porosity, indicating a different diagenetic history. Thus, when considering both the petrographic and XRF analyses, it is clear that Samples 3 and 4 exhibit a much closer relationship to each other in terms of texture, mineral content, and diagenesis, while Sample 5 stands apart due to its calcite-rich composition, greater porosity, and different textural features.

5.3. Possible sources for stone materials

Selecting the most appropriate stone materials is crucial for any conservation or repair work on the GP. Even when replacing a single stone, it is essential that the new material aligns perfectly with the original in terms of texture, color, and composition. This careful matching is vital to preserve both the aesthetic and structural integrity of the pavilion, as mismatched materials can lead to further deterioration or compromise the historical authenticity of the structure. Following established practices in heritage conservation, the identification of suitable stone sources becomes a key element in ensuring the long-term sustainability of conservation efforts [43-44].

Based on the mineralogical, petrographic, and geochemical characteristics of the stone samples, two primary stone groups emerge as possible candidates for conservation works. For the basalt used in the pavilion, geological investigations confirm that the structure is built upon a basalt unit from the Karacadağ volcanism, the only source of basalt in the region.



Figure 5. Limestone-built structures and potential quarry sources in Bağacık village

Petrographic and geochemical analyses have revealed that Sample 2, collected from the massive basalt layers of the Siverek phase of the Karacadağ volcanic complex, shows similar characteristics to the basalt used in the pavilion. The dense, fine-grained texture and mineral composition—primarily plagioclase, pyroxene, and olivine—indicate that the basalt in the pavilion is likely derived from the same volcanic activity phase, making it a possible option for future repairs.

The limestone used in the pavilion is part of a widespread Eocene-aged carbonate formation in the region. However, despite the formation's overall continuity, the sediments display lateral variations. In this context, two specific levels with building stone potential were identified—one near Zerzevan Castle and the other in Bağacık Village. Petrographic and geochemical analyses identified Sample 4 from Bağacık as a potential match for the pavilion's limestone. This sample shares key characteristics, such as color, texture, and mineral composition—including dolomite content—making it a possible choice for future repairs. Moreover, field observations confirm the presence of quarries in Bağacık that historically supplied building stones for local structures, like the village houses (Figure 5).

6. CONCLUSION

This study examined the role of locally sourced materials in shaping the architectural features of the GP, located in the Çınar district of Diyarbakır, Türkiye. The primary objectives were to investigate the influence of the region's geology on the selection of building materials, assess the current condition of the pavilion, and propose potential stone sources for future conservation efforts. Situated at the intersection of volcanic and sedimentary terrains, the pavilion reflects the practical use of basalt and limestone in its construction. Field observations revealed that basalt was primarily used for structural elements such as the foundation and walls, while limestone was selected as the principal building material for the upper floor and decorative elements. Field studies identified various types and distributions of decay affecting the building's basalt and limestone components. Basalt, particularly near the ground, exhibited decay in the form of discoloration, chipping, and blistering due to water exposure. At the same time, the limestone showed more extensive damage, including material

loss, erosion, and biological colonization. Human activities and atmospheric conditions have accelerated these decay processes, posing additional risks to both the building stones and carved reliefs. The combined effects of these factors continue to endanger the remaining parts of the structure. Mineralogical and geochemical analyses suggested that the basalt used in the pavilion may originate from basalt units of Karacadağ Volcanism, while the limestone resembles samples from Bağacık Village, indicating potential sources for the pavilion's limestone. However, these findings are preliminary and require further validation due to the limited number of samples and analyses. Findings from this study reveal the need to use compatible materials in conservation efforts to preserve the pavilion's structural stability and historical integrity. By identifying possible sources of basalt and limestone, future research can provide essential recommendations for local authorities, architects, and conservators tasked with maintaining the site. Comprehensive investigations involving systematic sampling (both from the structures and geological units) and advanced analytical techniques, including isotope analyses, will enhance our understanding and support more effective conservation strategies.

ACKNOWLEDGEMENT

The author sincerely thanks the Zerzevan Castle Excavation Team for their invaluable guidance and support in discovering this structure during a field study. The author is also grateful to Prof. Dr. Vedat Toprak (METU) for his valuable contributions to the development of the geological section of this study. Special appreciation is extended to the anonymous reviewers, whose thoughtful feedback and suggestions significantly enhanced the quality of this manuscript.

REFERENCES

- [1] F. Hafner, "On the perspective of the availability of ornamental rocks for the conservation of monuments," *Zeitschrift der Deutschen Gesellschaft für Geowissenschaften*, vol. 158, no. 4, pp. 695–700, 2007.
- [2] R. Přikryl and Á. Török, "Natural stones for monuments: their availability for restoration and evaluation," *Geological Society, London, Special Publications*, vol. 333, no. 1, pp. 1–9, 2010.
- [3] G. Lott, "Sourcing stone for the conservation and repair of historical buildings in Britain," *Quarterly journal of engineering geology and hydrogeology*, vol. 46, no. 4, pp. 405–420, 2013.
- [4] O. A. Nwoke and B. O. Ugwuishi, "Local bamboo and earth construction potential for provision of affordable structures in Nigeria," *International Journal of Sustainable Construction Engineering and Technology*, vol. 2, no. 2, 2011.
- [5] H. Danso, "Building houses with locally available materials in Ghana: benefits and problems," *International Journal of Science and Technology*, vol. 2, no. 2, pp. 225–231, 2013.
- [6] M. Gomez-Heras, B. J. Smith, and H. A. Viles, "Oxford stone revisited: causes and consequences of diversity in building limestone used in the historic centre of Oxford, England," *Geological Society, London, Special Publications*, vol. 333, no. 1, pp. 101–110, 2010.
- [7] A. Devos, G. Fronteau, O. Lejeune, C. Sosson, E. Chopin, and V. Barbin, "Influence of geomorphological constraints and exploitation techniques on stone quarry spatial organisation: Example of Lutetian underground quarries in Rheims, Laon and Soissons areas," *Engineering Geology*, vol. 115, no. 3–4, pp. 268–275, 2010.
- [8] M. García-Rodríguez, M. García-Rodríguez, and M. Gomez-Heras, "Sierra de Guadarrama (Madrid, Spain): bridging the gap between geology and architecture," *Special Publications*, vol. 416, no. 1, pp. 101–112, 2016.

- [9] F. Diri Akyıldız, N. Şahin Güçhan, and Y. D. Aktaş, "Construction processes and techniques in traditional Birgi houses: a typical Ottoman settlement," *Journal of Architectural Conservation*, vol. 30, no. 1, pp. 77-102, 2024.
- [10] J. R. Senior, "The selection of dimension and ornamental stone types used in some northern monasteries—the exploitation and distribution of a natural resource," In: R. Gilchrist and H. Mytum (Eds.), *Archaeology of Rural Monasteries*, British Archaeological Reports (British Series), vol. 203.i, pp. 223–237, 1989.
- [11] D. Ergenç, E. Caner Saltık, and T. Topal, "Antique stone quarries in Turkey: a case study on tuffs in the Temple of Apollon Smintheus," *Geological Society, London, Special Publications*, vol. 416, no. 1, pp. 133-144, 2016.
- [12] A. Almssad, A. Almusaed, and R. Z. Homod, "Masonry in the context of sustainable buildings: A review of the brick role in architecture," *Sustainability*, 14(22):14734. <https://doi.org/10.3390/su142214734>, 2022
- [13] C. R. Orloff, "The water supply and distribution system of the Nabataean city of Petra (Jordan), 300 BC–AD 300," *Cambridge Archaeological Journal*, vol. 15, no. 1, pp. 93-109, 2005.
- [14] S. M. Rababeh, *How Petra Was Built: An analysis of the construction techniques of the Nabataean freestanding buildings and rock-cut monuments in Petra, Jordan*, BAR Publishing, 2005.
- [15] F. Dursun, "From quarry to monument: considering Mardin stone (SE, Türkiye) as the symbol of architectural and cultural heritage," *Geoheritage*, vol. 16, no. 3, pp. 1-19, 2024.
- [16] L. C. Lancaster, "The process of building the Colosseum: the site, materials, and construction techniques," *Journal of Roman Archaeology*, vol. 18, pp. 57-82, 2005.
- [17] J. P. Protzen, "Stonemasonry of the Incas," in *Encyclopaedia of the History of Science, Technology, and Medicine in Non-Western Cultures*, H. Selin, Ed., Dordrecht: Springer, 2014.
- [18] D. Jackson, J. Fleming, and A. Rowe, "Enabling the transfer of skills and knowledge across classroom and work contexts," *Vocations and Learning*, vol. 12, no. 3, pp. 459-478, 2019.
- [19] M. Vatan, "Evolution of construction systems: Cultural effects on traditional structures and their reflection on modern building construction," in *Cultural Influences on Architecture*, IGI Global, 2017, pp. 35-57.
- [20] R. Bellopede and A. Quartulli, *Natural Stone and World Heritage: Itria Valley and Alberobello, Apulia Region, Italy*, CRC Press, 2024.
- [21] Diyarbakır Regional Board, *Archive of Registration Records*, Diyarbakır Regional Board for the Conservation of Cultural Heritage, 1990.
- [22] M. Tekin Bayram, *The Conservation and Restoration Proposal of Diyarbakır Güzelşeyh Pavilion*, M.Sc. thesis, Dept. of Architecture, Dicle Univ., 2022.
- [23] S. Yariş, "Ornament features of Güzelşeyh Pavilion," *Palmet Dergisi*, vol. 2, pp. 106-128, 2022.
- [24] İ. Yıldız, Z. Erdal, and D. Yıldız, "Cultural assets in Çınar district," in *A District at the Crossroads of Civilisations: Çınar*, Y. K. Haspolat, Ed., Çınar District Governorship Publications, 2015.
- [25] M. Tekin Bayram and G. Oğuz, "Documentation of the Güzelşeyh Pavilion in Çınar, Diyarbakır," in *Built Environment Assessments*, H. Demir Kayan, Ed., Nobel Publications, 2022.
- [26] S. Bağırşakçı et al., "Diyarbakır-Ergani ve Çınar Alanın Jeolojisi," Ankara, 1995.
- [27] E. Yılmaz and O. Duran, "Lexicon: A guide for stratigraphic nomenclature of the autochthonous and allochthonous units in the southeast Anatolian region," *Turkish Petroleum Corporation Educational Publication*, 1997.
- [28] MTA, "1:100.000 scale geological maps of Turkey, Sheet No: M44, Report No: 68," General Directorate of Mineral Research and Exploration, Geology Department, 2008.
- [29] Y. Yılmaz, "New evidence and model on the evolution of the southeast Anatolian Orogen," *Geological Society of America Bulletin*, vol. 105, pp. 251–271, 1993.
- [30] A. I. Okay, "Geology of Turkey: a synopsis," *Anschnitt*, vol. 21, pp. 19–42, 2008.
- [31] F. Dursun, E. D. Oğuz-Kırca, V. Toprak, and A. Coşkun, "Reconstruction of an ancient hill used as an On-Site quarry: Castrum Zerzevan (SE-Türkiye)," *Int. J. Architectural Herit.*, pp. 1–19, 2023. Available: <https://doi.org/10.1080/15583058.2023.2268015>
- [32] A. Haksal, "Petrographie und Geochemie des Schildvulkans Karacadağ," Ph.D. dissertation, Hamburg University, 1981. (Unpublished)
- [33] T. Ercan, F. Şaroğlu, N. Turhan, J. I. Matsuda, T. Ui, T. Fujitani, ... and H. Gürler, "Karacadağ volkanitlerinin jeolojisi ve petrolojisi," *Türkiye Jeoloji Bülteni*, vol. 6, pp. 118-133, 1991.
- [34] R. Westaway, H. Guillou, A. Seyrek, T. Demir, D. Bridgland, S. Scaillet, and A. Beck, "Late Cenozoic Surface Uplift, Basaltic Volcanism, and Incision by the River Tigris Around Diyarbakır, SE Turkey," *Int. J. Earth Sci.*, vol. 98, no. 3, pp. 601–625, 2009.
- [35] M. Lustrino, M. Keskin, M. Mattioli, V. A. Lebedev, A. Chugaev, E. Sharkov, and O. Kavak, "Early activity of the largest Cenozoic shield volcano in the circum-Mediterranean area: Mt. Karacadağ, SE Turkey," *European Journal of Mineralogy*, vol. 22, no. 3, p. 343, 2010.
- [36] F. Koçbulut, Z. Akpınar, O. Tatar, J. D. Piper, and A. P. Roberts, "Palaeomagnetic study of the Karacadağ Volcanic Complex, SE Turkey: monitoring Neogene anticlockwise rotation of the Arabian Plate," *Tectonophysics*, vol. 608, pp. 1007–1024, 2013.
- [37] P. Gay and R. W. LeMaitre, "Some Observations on Iddingsite," *The American Mineralogist*, vol. 46, pp. 92-111, 1961.
- [38] R. A. Eggleton, "Formation of Iddingsite Rims on Olivine: A Transmission Electron Microscope Study," *Clays and Clay Minerals*, vol. 32, no. 1, pp. 1-11, 1984.
- [39] A. Raza, M. Mahmoud, M. Murtaza, M. Arif, A. Hassan, G. Glatz, ... and A. Al-Karnos, "Experimental investigation of mafic rocks for carbon mineralization prospect," *Energy & Fuels*, vol. 37, no. 8, pp. 5976-5985, 2023.
- [40] D. Goldberg and A. L. Slagle, "A global assessment of deep-sea basalt sites for carbon sequestration," *Energy Procedia*, vol. 1, no. 1, pp. 3675-3682, 2009.
- [41] H. T. Schaefer, B. P. McGrail, and A. T. Owen, "Carbonate mineralization of volcanic province basalts," *International Journal of Greenhouse Gas Control*, vol. 4, no. 2, pp. 249-261, 2010.
- [42] M. Lustrino, M. Keskin, M. Mattioli, and O. Kavak, "Heterogeneous mantle sources feeding the volcanic activity of Mt. Karacadağ (SE Turkey)," *Journal of Asian Earth Sciences*, vol. 46, pp. 120-139, 2012.
- [43] P. López-Arce, J. García-Guinea, D. Benavente, L. Tormo, and E. Doehne, "Deterioration of dolostone by magnesium sulphate salt: An example of incompatible building materials at Bonaval Monastery, Spain," *Construction and Building Materials*, vol. 23, no. 2, pp. 846-855, 2009.
- [44] J. Martínez-Martínez, A. Pola, L. García-Sánchez, G. Reyes Agustín, L. S. Osorio Ocampo, J. L. Macías Vázquez, and J. Robles-Camacho, "Building stones used in the architectural heritage of Morelia (México): quarries location, rock durability and stone compatibility in the monument," *Environmental Earth Sciences*, vol. 77, pp. 1-16, 2018

BIOGRAPHY

Felât Dursun is a graduate of Çukurova University (CU), Geological Engineering. He received his master's degree in Mining Engineering at Dicle University (DU) and earned his Ph.D. in Geological Engineering from Middle East Technical University (METU). His Ph.D. thesis was awarded "*The Best Thesis of the Year*" in 2017 by the METU Graduate School of Natural and Applied Sciences. During his doctoral studies, he received a grant to conduct research on historic building materials as a visiting scientist at the Getty Conservation Institute in Los Angeles, USA, from 2014 to 2015. He later received a postdoctoral research grant from TÜBİTAK to continue his research at University College London (UCL), London, UK, between 2022 and 2023. Dr. Dursun specializes in stone conservation, geoarchaeology, site selection, and the physicochemical characterization of stones used in historic buildings. Dr. Dursun has experience leading both national and international research projects. He is involved in several boards and organizations, including ICOMOS, the Ministry of Culture and Tourism's Scientific Committee, and different archaeological excavation teams. Currently, he serves as an Assistant Professor at Dicle University and as a visiting scholar at İzmir Institute of Technology.

Research Article

Agricultural Waste-Based Composite Materials: Recycling Processes, Technical Properties, and Industrial Applications

Izham Kılınç^{1*}  and Mustafa Korkmaz² 

^{1*} Batman University, Department of Design, Interior Design, Vocational School of Technical Sciences, Batman, Türkiye (e-mail: izham.kilinc@batman.edu.tr)

² Department of Wood Products Industrial Engineering, Faculty of Forestry, Düzce University, Düzce, Türkiye (e-mail: mustafakorkmaz@duzce.edu.tr)

ARTICLE INFO

Received: Nov., 01, 2024

Revised: Dec., 07, 2024

Accepted: Dec., 10, 2024

Keywords:

Agricultural waste-based composites

Environmental sustainability

Biodegradable materials

Wood based composites

Recycling processes

Corresponding author: [İzham Kılınç](mailto:izham.kilinc@batman.edu.tr)

ISSN: 2536-5010 / e-ISSN: 2536-5134

DOI: <https://doi.org/10.36222/ejt.1577864>

ABSTRACT

The transformation of agricultural waste into eco-friendly, lightweight, durable, and biodegradable composite materials supports sustainable production processes and presents new opportunities as alternatives to traditional materials. These composites offer significant advantages, particularly in terms of energy savings, low cost, and minimizing environmental impact. Widely used in industrial applications, these composites contribute to sustainable development goals by serving as insulation materials in construction, interior components and body panels in the automotive industry, biodegradable packaging materials, decorative elements and outdoor furniture in the furniture industry, and plant pots and mulch in agriculture. The broader adoption of agricultural waste-based composites in industrial applications not only offers potential solutions to waste management challenges but also represents a critical step toward enhancing environmental sustainability. This study aims to examine the potential of agricultural waste-based composite materials across various industrial applications. Within this scope, the uses of biodegradable composite materials, recycled from agricultural waste, are detailed across sectors such as construction, automotive, packaging, furniture, and agriculture.

1. INTRODUCTION

The production of composite materials from agricultural waste has garnered significant interest in recent years due to the benefits of waste valorization and the development of sustainable materials. Abundant and often underutilized agricultural residues can be employed as effective reinforcing agents in composite formulations, thereby enhancing the mechanical, thermal, and acoustic properties of the composites. The use of agricultural waste in composite production stems from the growing demand for sustainable materials that can serve as alternatives to traditional materials. Agricultural by-products such as corn stalks, rice husks, and sugar beet pulp are rich in lignocellulosic fibers. Utilizing these materials enables the creation of composites that exhibit improved mechanical properties, thermal insulation, and biodegradability [1]. In comparison to traditional materials, agricultural waste-based composites offer several advantages, such as lower environmental impact due to their renewable and biodegradable nature, as well as a reduction in production costs. These materials also contribute to a circular economy by reducing waste and promoting resource efficiency. The incorporation of such agricultural waste in composite production not only prevents resource waste but also enhances various characteristics of the composites [2]–[4]. For instance, it has been reported that wood-plastic composites (WPC)

produced from branches and leaves obtained from the pruning of citrus trees, combined with low-density polyethylene (LDPE), achieve improved compatibility between materials through surface modification with enzymes [3]. It has been reported that this modification enhances the water-repellent properties of the wood-derived fibers, allowing for better adhesion to the plastic matrix. This enzymatic process not only improves the mechanical properties of the composite material but also increases its biodegradability, making it a more environmentally friendly option. The thermal properties of composites produced from agricultural waste have also been extensively studied. One study indicated that due to their low thermal conductivity and lightweight structure, these composites hold significant potential as thermal insulation materials, offering advantages for various applications in the construction and automotive industries [4]. In another study, the mechanical properties of composites made from polyester and corn stalks were evaluated. This research concluded that the incorporation of agricultural fibers into the composite production process significantly enhances the mechanical strength and thermal stability of the resulting materials [2]. Additionally, it has been noted that composites reinforced with pineapple leaf fibers can be utilized in the production of unmanned aerial vehicles (UAVs), as their lightweight and strong characteristics contribute positively to UAV

performance [5], [6]. These findings also highlight the versatility of agricultural waste composites in providing effective insulation solutions, particularly in the context of promoting sustainability.

In addition to thermal insulation properties, the acoustic characteristics of agricultural waste composites have been studied, particularly in terms of sound absorption. Koçak et al. (2022) reported that polyurethane composites reinforced with alkali-treated agricultural waste fibers exhibit excellent acoustic properties, making these fibers suitable for noise reduction applications [7]. This characteristic is becoming increasingly important in today's context, where noise pollution poses a growing environmental issue. In addition to their sound-absorbing capabilities, the lightweight and cost-effective nature of these composites makes them a significant alternative to traditional sound insulation materials.

Various methods, such as compression molding, injection molding, and extrusion, can be employed for the production of agricultural waste composites, each exhibiting significant differences [8]. These techniques allow for the customization of composite properties to meet specific application requirements.

Mycelium-based composites represent a novel approach to valorizing agricultural waste through a process where fungal mycelium is cultivated on lignocellulosic substrates to form bio-composite materials. A study examining these types of composites noted that their lightweight and biodegradable structures suggest potential applications in the construction and packaging sectors [9]. The innovative use of biological processes in material production exemplifies the interdisciplinary interaction between biotechnology and materials science. The mechanical properties of composites derived from agricultural waste can be further enhanced by incorporating various additives and treatments. For instance, the addition of agricultural waste fibers as a filler in polylactic acid (PLA) composites improves the material's viscoelastic properties by increasing its degree of crystallinity [10]. These enhancements are of significant importance for applications in sectors such as automotive and aerospace, where there is a demand for high strength-to-weight ratios. Furthermore, the use of agricultural waste as reinforcement not only improves the performance of composites but also reduces production costs, making them more economically viable alternatives compared to traditional materials [11], [12].

The use of bio-based binders such as alginate and starch in the production of composite materials from agricultural by-products enhances the mechanical performance of the composites while also contributing to the preservation of environmental sustainability [13]. This trend towards utilizing renewable resources in composite material production aligns with the principles of a circular economy, which aim to reduce dependence on fossil fuels and promote circular usage.

The environmental benefits of utilizing agricultural waste in composite production are also significant. By repurposing these materials, industries can mitigate waste disposal issues and more easily achieve their sustainability goals [14]. The integration of agricultural waste into composite production promotes resource efficiency and reduces the carbon footprint associated with material manufacturing.

In conclusion, this study has examined the various production processes, properties, and application areas of composites derived from agricultural waste. By highlighting the innovative methods used in their production and the potential benefits they

offer across different sectors, a comprehensive perspective has been provided to the literature in this field.

2. SUSTAINABILITY and ENVIRONMENTAL IMPACTS OF AGRICULTURAL WASTE

2.1. Types and Sources of Agricultural Waste

Composites produced from agricultural waste have emerged as a significant resource in the quest for sustainable and environmentally friendly alternatives to traditional materials. Various types of agricultural waste, including fibers and by-products, are employed to enhance the mechanical and thermal properties of composites, making them suitable for a wide range of applications. Among the primary types of agricultural waste used in composite material production are lignocellulosic fibers derived from crops such as rice, corn, and wheat. These fibers are renowned for their superior mechanical properties and biodegradability, which render them ideal candidates for reinforcing polymer matrices. Additionally, fruit and vegetable peels, leaves, stems, flowers, and by-products generated during their processing can also be utilized as raw materials in the production of diverse composites. Table 1 provides information on the transformation of various agricultural wastes into materials and products across different industries.

TABLE I
UTILIZATION OF AGRICULTURAL WASTE IN VARIOUS INDUSTRIES

Biomass Waste	Products
Pineapple leaves, sugarcane residues	Animal feed, industrial absorbents, beverage additives, and biocomposites
Wheat straw	Pelletized polypropylene (PP) feedstock, fertilizer, biocomposites
Rice husk	Silica, metal coatings, water-soluble oils, and synthetic lubricants
Sugarcane bagasse	Wood materials, biocomposites, paper and packaging materials, paper goods
Abaca leaves	Fiber crafts, rope, textiles and fabrics, pulp, and specialty papers
Coconut husk	Coconut fiber rope and twine, brooms and brushes, mats, carpets, mattresses, and upholstery, often rubber-coated coconut pads
Sugar factory boiler ash (from bagasse)	Filtration materials and absorbent products
Oil palm fruit residues	Biodegradable packaging materials, construction, pulp and paper, automotive components
Kenaf fibers, jute fibers	Sound insulation systems, thermal insulators, automotive components, electronics, pharmaceuticals
Abaca leaves	Abaca leaf sheath, aerospace, maritime, and electronics
Coconut fibers	Coconut ropes
Banana pseudostems	Banana fibers, biocomposites, pulp, and paper
Flax	Biodegradable bags and covers, energy sports equipment

Biomass, constituting a significant category of agricultural waste, can be derived from various crops and possesses the potential to be processed into lightweight composites [15]. The utilization of excess biomass derived from agricultural waste not only reduces waste volume but also contributes to decreasing dependence on non-renewable resources, thereby promoting ecological sustainability. Composites produced

from agricultural waste, such as rice husks and wheat straw, have been found to possess favorable thermal insulation properties, making them suitable for use in construction applications [4]. These findings are consistent with the results of another study that explored the use of rice husks and other agricultural fibers for the development of sustainable thermal insulation bio-composites [9].

2.2. Sustainability and mitigation of environmental impacts

The utilization of agricultural waste in the production of composite materials plays a significant role in mitigating environmental impacts. This practice not only prevents agricultural waste from harming the environment as part of waste management strategies but also reduces dependence on fossil fuel-based materials. The production of agricultural waste-based composites leads to a substantial decrease in carbon footprint and greenhouse gas emissions. Furthermore, the manufacturing processes for these materials consume less water and energy compared to traditional materials. Consequently, composites derived from agricultural waste contribute to the enhancement of environmental sustainability [16], [17].

The use of agricultural waste in composite materials has arisen primarily from the need to reduce environmental pollution and promote sustainability goals. Despite their abundance, agricultural wastes such as rice husks, corn stover, and bagasse is often underutilized. This presents a significant opportunity for recycling and sustainable production processes. For instance, utilizing agricultural waste to reinforce metallic matrix composites not only reduces costs but also contributes to waste reduction. It has been noted that the incorporation of agricultural wastes, such as rice husk granules and corn cob granules, plays a crucial role in this context [18]. Similarly, the use of agricultural waste as a reinforcement material in aluminum matrix composites (AMCs) has been noted to replace traditional reinforcements, thereby reducing environmental impacts and enhancing sustainability [19].

Composites derived from agricultural waste play a vital role in promoting sustainability and supporting the circular economy. These materials are recognized for their suitability for use in various sectors, including automotive, packaging, and construction, offering cost-effectiveness along with superior mechanical properties [15], [20]. Agricultural waste composites contribute to the effective utilization of waste by reducing dependence on non-renewable resources [15], [20], [21]. For instance, various studies have reported that agricultural wastes, such as tomato peels, enhance the properties of biodegradable composite materials and align with the principles of sustainable waste management. Additionally, agricultural waste offers eco-friendly alternatives for 3D printing, contributing to the circular economy [22], [23]. Moreover, the use of by-products such as rice husks in metallic matrix composites has been reported to improve material properties while also reducing pollution [18]. Furthermore, the conversion of agricultural wastes such as cocoa bean shells into biocomposites contributes to sustainable material production by reducing the carbon footprint [20], [24]. This approach is essential for resource efficiency and the reduction of environmental impacts [25]. Table 2 presents the annual production and sources of agricultural waste-based natural fibers [26]. The source of the fibers indicates which part of the plant they are derived from, while the production quantities worldwide are expressed in thousand tons (103 tons).

TABLE II

ANNUAL PRODUCTION OF AGRICULTURAL WASTE-BASED NATURAL FIBERS

Fiber Source	Global Production (10 ³ Tons)	Source
Bamboo	10,000	Stem
Oil Palm Fruit	23,500	Fruit
Sugarcane Bagasse	75,000	Stem
Banana	200	Fruit
Coconut Fiber	100	Stem
Wood	1,750,000	Stem
Pineapple	1,200	Leaf
Rice Straw	28,900	Stem
Rice Husk	26,750	Seed
Jute	2,500	Stem
Kenaf	770	Stem
Flax	810	Stem
Sisal	380	Stem
Abaca Fiber	70	Stem
Kapok Fiber	100	Stem

3. THE UTILIZATION OF AGRICULTURAL WASTE IN THE PRODUCTION OF COMPOSITE MATERIALS

The valorization of agricultural waste as composite materials is a significant process for sustainability and involves a comprehensive production line comprising several stages (Figure 1). Initially, suitable agricultural residues must be collected and cleansed of impurities. Following this, the waste undergoes a grinding process to achieve specific dimensions and is subsequently classified to attain the desired granulometric distribution. These steps are critical for rendering the waste suitable for composite material fabrication.

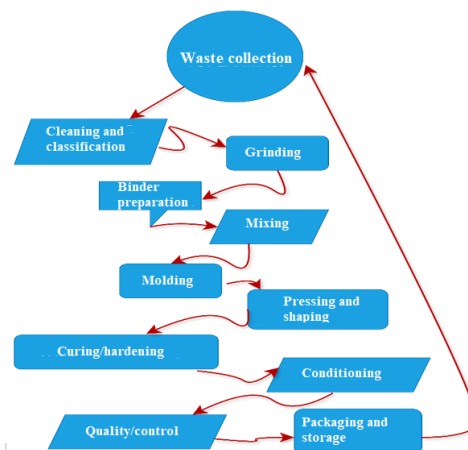


Figure 1. Schematic representation of composite material production from agricultural waste.

The ground agricultural waste must be combined with a binder, or matrix, material. The matrix material determines the final properties of the composite and facilitates the integration of the waste with the matrix [27]. Matrix materials employed in this stage typically include thermoplastics, thermosetting resins, and natural polymers [28]–[30]. Thermoplastics (e.g., polypropylene (PP), polyethylene (PE), and polyvinyl chloride (PVC)) can be melted and reshaped under heat. Thermosetting resins (e.g., epoxy, phenolic resins) are known to provide permanent hardness and strength under high temperature and pressure [31], [32]. Furthermore, natural polymers are also favored in composite production due to their environmentally

friendly and biodegradable properties [33]–[35]. The subsequent stage involves the pressing process. Among the pressing methods are:

- Hot pressing, which facilitates the strong bonding of waste materials with the matrix, resulting in a durable composite material.
- Extrusion, employed for the production of continuous lengths of profiles, sheets, and pipes by homogeneously mixing agricultural waste with a polymer matrix.
- Injection molding, an ideal method for the mass production of small products with complex shapes.
- Filament winding, which enables the creation of cylindrical structures and robust composite products by coating agricultural fibers with resin and winding them around a mandrel.

To determine the performance and durability of the composite materials, various testing and analysis methods are employed. Mechanical tests measure the tensile, compressive, flexural, and impact strength of the material, while thermal tests evaluate its stability at elevated temperatures. Microstructural analyses (e.g., scanning electron microscopy (SEM) and X-ray diffraction (XRD)) examine the fiber-matrix interaction and internal structure. Chemical analyses (e.g., Fourier transform infrared spectroscopy (FTIR) and energy-dispersive X-ray spectroscopy (EDX)) assess the chemical composition of the composite material and any potential alterations.

These comprehensive processes enable the transformation of agricultural waste into sustainable and high-performance composite materials, offering significant contributions both environmentally and economically. Table 3 provides information on some agricultural wastes used as reinforcement in composite material production.

TABLE III

UTILIZATION OF AGRICULTURAL WASTE AS REINFORCEMENT IN COMPOSITE MATERIAL PRODUCTION

Waste Type	Matrix	Method	Pros	Cons
Corn Cob	PP, Epoxy, PES	Injection, Compression	Cheap, abundant	Short fibers, low strength
Rice Husk	PLA, Epoxy	Injection, Compression	High area, light	Weak bonding
Wheat Straw	PP, PE	Compression, Extrusion	Light, biodegradable	Hard to mix evenly
Coconut Shell	Epoxy, PES	Compression, Pultrusion	Hard, durable	Hard to process
Sugarcane Bagasse	PP, PLA	Extrusion, Compression	Abundant, cheap	Low fiber quality
Flax Fiber	PA, PP	Pultrusion, Vacuum	Strong, low density	Costly, hard to process
Bamboo Fiber	Epoxy, PES	Pultrusion, Injection	Strong, fast growth	Low density, hard to process
Hazelnut Shell	Epoxy, PU	Compression, Pultrusion	Hard, wear-resistant	Varying quality
Walnut Shell	PES, Epoxy	Injection, Compression	Hard, durable	Hard to process
Apricot Pit Shell	PP, Epoxy	Injection, Compression	Light, recyclable	Low fiber quality

4. PROPERTIES of AGRICULTURAL WASTE BASED COMPOSITES

Agricultural waste-based composites have garnered significant attention due to their technical attributes, often exhibiting advantages such as enhanced mechanical strength, thermal stability, and biodegradability. A study on polyester/corn stalk composites reported that such materials demonstrate excellent water and oxygen barrier properties, rendering them suitable for diverse applications in the construction and automotive industries [2], [36]. Furthermore, research has highlighted the potential of agricultural waste derived composites as effective thermal insulators owing to their low thermal conductivity [4]. This aligns with the findings of [9], which indicated that composites fabricated from rice husk and wood fibers exhibit favorable thermal insulation properties, offering promising results for industrial applicability.

The utilization of agricultural waste in the fabrication of composite materials presents significant potential within the context of recycling, often involving various treatments to enhance the properties of the resultant composites. For instance, a study focusing on epoxy-based polymer matrix composites, incorporating waste materials such as coconut and walnut shells, emphasized the improvement of mechanical properties and the optimization of flexural and physical behavior through the application of Taguchi techniques [37]. Further research on alkali-treated oil palm leaf waste demonstrated its capacity to significantly augment interfacial adhesion in polylactic acid composites, thereby enhancing mechanical performance [38].

4.1. Mechanical Properties

The mechanical properties of agricultural waste-based composites have garnered increasing attention in recent years due to their potential to provide sustainable and environmentally friendly alternatives. Agricultural residues, such as rice husk, corn stalk, walnut shell, hazelnut shell, and coconut shell, are employed as reinforcement materials in composite production. These materials not only enhance mechanical strength but also offer environmental benefits by reducing waste and promoting a circular economy. The integration of these residues into composite matrices contributes to the improvement of mechanical properties, including tensile strength, flexural strength, and impact resistance [39], thereby facilitating their application in diverse industries such as construction, automotive, and consumer goods [9].

Studies have revealed that the mechanical performance of agricultural waste based composites varies depending on the type of waste employed, the matrix material, and the processing techniques implemented [40], [41]. For instance, composites reinforced with rice husk ash have been shown to exhibit superior mechanical properties compared to their counterparts lacking such reinforcement [42]. Specifically, the incorporation of rice husk ash into aluminum matrix composites has been reported to enhance tensile strength and wear resistance, rendering these materials suitable for applications in automotive and structural components [43], [44]. Similarly, the utilization of corn stalk fibers in polyester composites has been shown to contribute to increased mechanical strength, dimensional stability, and thermal resistance, highlighting the

remarkable versatility of agricultural waste as a reinforcement material [2].

The optimization of mechanical properties in agricultural waste-based composites can be achieved through various processing techniques. For example, the Taguchi method has been employed to optimize the flexural and physical behavior of epoxy-based composites reinforced with agricultural waste, demonstrating that careful selection of processing parameters significantly improves mechanical performance [37]. Furthermore, alkali treatment has been shown to enhance fiber-matrix interfacial adhesion during the processing of agricultural fibers, yielding composites with superior mechanical properties [7].

4.2. Physical Properties

Agricultural waste based composites, derived from various agricultural byproducts, offer numerous advantages, particularly in the construction, automotive, and packaging sectors, due to their physical properties and environmental sustainability [9], [39]. A primary benefit of these composites lies in their low density and lightweight structure. The utilization of low-density agricultural residues, such as coconut shells, palm leaves, and corn stalks, significantly reduces material weight, facilitating ease of handling and application while simultaneously lowering costs [37], [38]. Despite their lightweight nature, these materials offer sufficient mechanical strength, enabling their effective use in structural and automotive applications. Another notable physical attribute of agricultural waste composites is their excellent thermal insulation capacity. Natural fibers like corn stalk, rice husk ash, and coconut shell, when incorporated into composite matrices, not only enhance mechanical durability but also provide superior thermal insulation, positioning these materials as a sustainable alternative to conventional insulation products [4], [37]. Especially in the context of increasing demand for sustainable building materials, such composites are deemed invaluable for enhancing energy efficiency and mitigating environmental impact [45].

The physical durability of agricultural waste-based composites, notably their resistance to fluctuations in humidity and temperature, is particularly remarkable. Studies have demonstrated the dimensional stability of these materials, confirming their capacity to maintain structural integrity in the face of environmental variations [2], [46], [47]. Furthermore, fiber treatment methods, such as alkali treatment, are reported to enhance fiber-matrix interfacial adhesion, thereby augmenting the composites' physical durability and long-term performance [38], [48]. Agricultural waste, readily integrable with polymer matrices, not only elevates the physical properties of the resultant composites but also fosters environmental sustainability by mitigating reliance on synthetic materials [49], [50]. Table 4 provides a comparative analysis of the mechanical properties of composites derived from various agricultural residues.

The fundamental parameters presented in Table 4, such as density, tensile strength, and Young's modulus, offer valuable insights into the potential applications and durability of these fibers. In particular, the high tensile strength exhibited by sources like oil palm and rice straw enhances their suitability for composite material fabrication. Furthermore, fiber density plays a crucial role in material selection [51], [52]. This table provides a valuable reference for bioengineering and

sustainable materials research regarding agricultural waste fibers.

TABLE IV
SELECTED PHYSICAL AND MECHANICAL PROPERTIES OF COMPOSITES
FABRICATED FROM VARIOUS AGRICULTURAL WASTE FIBERS.

Fiber Source	Density (g/m ³)	Tensile Strength (MPa)	Young's Modulus (GPa)	References
Oil Palm	0.7–1.55	227.5–278.4	2.7–3.2	[53], [54]
Bagasse	0.31–1.25	257.3–290.5	15–18	[55]
Banana	0.65–1.36	51.6–55.2	3.00–3.78	[56], [57]
Coconut	0.67–1.15	173.5–175.0	4.0–6.0	[56], [57]
Pineapple	1.25–1.60	166–175	5.51–6.76	[46]
Rice Straw	0.86–0.87	435–450	24.67–6.33	[58], [59]
Jute	1.3–1.45	300–700	20–50	[60], [61]
Kenaf	0.15–0.55	295–955	23.1–27.1	[62], [63]
Bamboo	0.6–1.1	360.5–590.3	22.2–54.2	[64]
Sisal	1.45–1.5	300–500	10–30	[60], [61]
Abaca	1.42–1.65	879–980	38–45	[61]
Kapok	0.68–1.47	80.3–111.5	4.56–5.12	[65], [66]

As shown in Table 4, agricultural waste materials offer superior mechanical properties compared to traditional materials, such as high tensile strength and Young's modulus. Additionally, their low density provides advantages in terms of reduced weight and ease of transport. Being environmentally friendly and renewable resources, they contribute to sustainability, while their low cost and local availability offer economic benefits. With these characteristics, agricultural waste materials hold great potential as an alternative to traditional materials in the production of construction materials and composites.

4.3. Environmental and Economic Characteristics

The environmental and economic attributes of agricultural waste-based composites offer significant advantages in terms of sustainability and cost-effectiveness. These composites present valuable solutions for waste management, energy conservation, and the mitigation of environmental impact. By repurposing agricultural waste, manufacturers can substantially diminish the environmental footprint associated with waste disposal and raw material extraction. The utilization of agricultural waste in composites not only addresses waste management challenges but also promotes sustainability by providing renewable and biodegradable materials [37], [67]. Moreover, employing locally sourced agricultural waste yields economic benefits through cost savings in material procurement and processing. This renders the production of such composite materials a financially viable option [2].

5. CONTEMPORARY APPLICATIONS of AGRICULTURAL WASTE-BASED COMPOSITES

5.1. Application in the Construction Industry

Agricultural waste-based composites have emerged as a sustainable alternative in the construction industry, offering the potential to address both environmental concerns and the need for innovative building materials. A key application of agricultural waste composites in construction lies in the development of lightweight, high-strength materials. For instance, bio-composites derived from agricultural residues, such as durian peel fibers combined with poly(lactic acid) (PLA), have been shown to exhibit enhanced tensile and thermal properties, rendering them suitable for various

structural applications [68]. The incorporation of these natural fibers into composite matrices augments the overall material performance, proving particularly advantageous in applications where weight reduction is critical, such as prefabricated building components [69]. Furthermore, mycelium-based composites, which utilize agricultural waste as a substrate for fungal growth, have demonstrated promising results in construction applications. These composites exhibit excellent mechanical properties and can be molded into diverse forms, making them suitable for use as insulation panels or structural elements [70]. Mycelium's ability to bind agricultural waste into a cohesive material not only provides a sustainable building solution but also contributes to carbon sequestration, mitigating the effects of climate change [71]. The durability and weather resistance of agricultural waste composites are also noteworthy. Studies have revealed that composite materials bonded with methylene diphenyl diisocyanate (MDI) and reinforced with bamboo or other agricultural fibers maintain their structural integrity under natural weathering conditions [72]. This characteristic is paramount for construction materials, which must withstand fluctuating environmental conditions over time. Beyond their mechanical and durability advantages, agricultural waste composites contribute to a circular economy by utilizing materials that would otherwise be considered waste. The use of cocoa pod husks in polypropylene composites, for example, not only offers a sustainable material option but also addresses the issue of agricultural waste accumulation [73]. This approach aligns with the growing trend towards eco-conscious construction practices, where the entire life cycle of materials, from production to disposal, is considered. Moreover, the integration of biocomposites into the construction sector is further bolstered by advancements in additive manufacturing technologies. The ability to 3D print using materials derived from agricultural waste allows for innovative designs tailored to specific structural requirements, opening new avenues for customized building solutions [74]. This technology enhances the versatility of agricultural waste composites, making them an attractive option for modern construction needs.

5.2. Application in the Automotive Industry

The industrial applications of agricultural waste-based composite materials are remarkably diverse, encompassing sectors such as construction, automotive, furniture, packaging, and thermal insulation. The lightweight nature and specific strength of these composites make them particularly appealing for automotive applications, where minimizing vehicle weight is crucial for enhancing fuel efficiency and reducing emissions. In this context, the potential of green materials, including agricultural waste, as reinforcement in aluminum matrix composites, and their role in lightweighting strategies, is underscored [24]. These composites are employed in vehicles to achieve reductions in weight, improvements in fuel economy, and a diminished carbon footprint (Figure 2).

5.3. Applications in the Packaging Industry

The utilization of agricultural waste-based composite materials in the packaging sector has gained significant momentum in recent years, driven by a growing interest in biodegradable and environmentally friendly alternatives. The detrimental environmental impact of conventional plastic packaging materials, and their persistence in the environment for extended periods, has rendered biodegradable composites

derived from agricultural waste an attractive solution. These composite materials offer both environmental and economic benefits, particularly in addressing waste management and plastic pollution.



Figure 2. Agricultural waste-based composite components utilized in automotive interiors [75].

The viability of agricultural waste as a packaging material is intrinsically linked to several key advantages inherent in these composite materials. Primarily, their inherent biodegradability ensures environmentally benign decomposition after use, aligning perfectly with the burgeoning demand for biodegradable packaging solutions. For instance, agricultural residues such as corn cobs, wheat straw, rice husks, and coconut shells can be combined with polymer matrices to create biodegradable packaging materials [50]. These materials possess the potential to replace conventional plastic packaging, thereby significantly reducing the environmental footprint of the packaging industry. Furthermore, the use of biopolymer-based composites derived from agricultural waste promotes sustainability by mitigating reliance on non-renewable resources. Agricultural waste, being a recyclable and renewable resource, readily integrates into sustainable production processes. This not only minimizes environmental impact but also facilitates more efficient utilization of local resources [20]. For example, composites produced from combining waste materials like rice husks and corn stalks with biopolymers offer durable, lightweight, and environmentally friendly solutions for the packaging sector (Figure 3). Moreover, biodegradable composites from agricultural waste enhance functional performance within the packaging industry. These materials can exhibit desirable packaging characteristics such as moisture resistance, oxygen barrier properties, and high tensile strength. Biodegradable composites used in food packaging, in particular, provide the necessary barrier properties to maintain product freshness while simultaneously undergoing environmentally benign decomposition at the end of their lifespan [76]. This underscores the considerable environmental sustainability advantage of biodegradable composites over their plastic counterparts.

5.4. Applications in the Furniture Industry

The utilization of agricultural waste-based composites in the furniture industry is attracting increasing attention due to their potential to create sustainable, eco-friendly products while addressing waste management challenges. These composites, often incorporating materials such as wheat straw, pineapple fibers, and mycelium, offer a range of mechanical and aesthetic properties suitable for diverse furniture applications. A significant example of agricultural waste utilization in furniture design is the incorporation of wheat

straw into composite materials. Research indicates that composites reinforced with chopped wheat straw can be effectively combined with various plastics, such as polyethylene and polypropylene, to produce materials with enhanced mechanical properties [78]. These composite materials offer a sustainable alternative to traditional wood-based materials, contributing to the mitigation of environmental impacts associated with furniture production. Mycelium-based composite materials, employing fungal growth on agricultural waste substrates, represent another innovative approach in furniture manufacturing. These materials stand out due to their inherent fire-resistant properties and adaptability to specific applications, making them suitable for various furniture designs [79]. Mycelium's ability to bind agricultural waste into a cohesive material enables the creation of lightweight and durable furniture products capable of satisfying the aesthetic and functional demands of modern consumers. Additionally, the use of pineapple leaf fibers in furniture design has been explored as a means of upcycling agricultural waste. Pineapple cultivation generates substantial waste, and research demonstrates that these fibers can be transformed into composite materials exhibiting favorable mechanical properties [80], [81]. Such innovations foster sustainable practices within the furniture industry and contribute to the circular economy by enhancing the value of agricultural by-products. The development of bio-composite boards from straw fibers has also garnered significant interest in the furniture sector. Produced from readily available agricultural waste, these boards find applications in various uses (Figure 4-5), including cabinets and decorative elements [82].



Figure 3. The biodegradable materials in packaging applications [77].

5.5. Applications in Agriculture and Horticulture

Agricultural waste-based composite materials utilized in agriculture and horticulture promote environmental sustainability while offering functional advantages. Composites derived from waste such as rice husks, corn stalks, and coconut shells exhibit organic fertilizer properties and function as soil amendment materials, enhancing water retention capacity. These composites are known to improve soil structure and nutrient content, contributing to healthy plant root development. Furthermore, they offer lightweight and durable materials for horticultural landscaping, providing water-conserving and aesthetically pleasing solutions. The application of agricultural waste-based composites contributes to achieving sustainability goals within this sector, while simultaneously reducing costs and promoting efficient natural resource utilization and waste management.

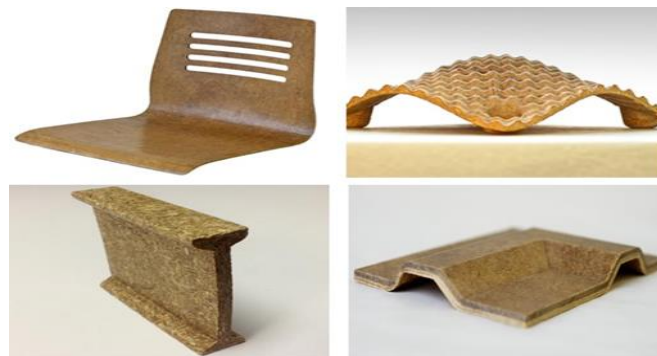


Figure 4. Bio-based wood composites from sugarcane bagasse [83].

The growing demand for biodegradable and sustainable materials has driven research to optimize the properties of these bio-composites and ensure they meet the performance standards required for furniture applications. Furthermore, the integration of waste textile materials into furniture design has emerged as a viable strategy for sustainability. By recycling waste textiles into composite materials, manufacturers can create products that are not only environmentally friendly but also economically viable [84]. This approach highlights the potential for innovation in material sourcing and product design, addressing the dual challenge posed by textile waste and the need for sustainable furniture solutions.



Figure 5. Fiberboard from Rice Straw for Furniture and Furniture Manufacturing [85].

6. CONCLUSIONS

This study has highlighted the significance of agricultural waste-based composite materials from the perspective of environmental sustainability, elucidating their production processes, properties, and potential for industrial applications. Findings demonstrate that these materials, offering advantages such as low cost, lightweight properties, biodegradability, and energy efficiency, can be considered viable sustainable alternatives in sectors including construction, automotive, furniture, packaging, and agriculture. However, certain improvements are necessary to facilitate wider adoption. Specifically, research and development investment is crucial for advancing biodegradable binders and processing technologies, implementing surface modification techniques to enhance fiber-matrix compatibility, and quantifying environmental benefits through life cycle analyses. Furthermore, public policies incentivizing wider adoption of these materials, coupled with industry education on sustainability, will significantly increase sector awareness. The study's conclusions indicate that the efficient utilization of agricultural waste contributes to the circular economy and strengthens industrial sustainability.

REFERENCES

- [1] R. Y. Venkataravanappa, A. Lakshmikanthan, N. Kapilan, M. P. G. Chandrashekarappa, O. Der, and A. Ercetin, "Physico-Mechanical Property Evaluation and Morphology Study of Moisture-Treated Hemp-Banana Natural-Fiber-Reinforced Green Composites," *J. Compos. Sci.*, vol. 7, no. 7, 2023, doi: 10.3390/jcs7070266.
- [2] O. Anozie and N. Ifeanyi, "Evaluation of the Physico-Mechanical Properties of Polyester/Corn Stalk Composite," *Poljopr. Teh.*, 2022, doi: 10.5937/poljtehd22030090.
- [3] A. M. Youssef, M. S. Hasanin, M. E. A. El-Aziz, and O. M. Darwesh, "Green, Economic, and Partially Biodegradable Wood Plastic Composites via Enzymatic Surface Modification of Lignocellulosic Fibers," *Heliyon*, 2019, doi: 10.1016/j.heliyon.2019.e01332.
- [4] H. Serin, G. Güzel, U. Kumlu, and M. A. Akar, "Potential of Using Agricultural Waste Composites as Thermal Insulation Material," *Macromol. Symp.*, 2022, doi: 10.1002/masy.202100409.
- [5] G. A. K. Gürdil, M. Mengstu, and A. Kakarash, "Utilization of Agricultural Wastes for Sustainable Development," *Black Sea Journal of Agriculture*. 2021. doi: 10.47115/bsagriculture.953415.
- [6] F. S. Shahar, M. T. H. Sultan, A. Łukaszewicz, and R. A. Grzejda, "A Review on Agricultural Wastes and Pineapple Leaf Fibers in UAVs Airframe Manufacturing," *Preprints*, 2023, doi: https://doi.org/10.20944/preprints202307.1813.v1.
- [7] D. Koçak, H. Olcay, and Z. Yildiz, "Mechanical and Acoustic Properties of Alkali Treated Agricultural Waste Reinforced Sustainable Polyurethane Composites," *Journal of Reinforced Plastics and Composites*. 2022. doi: 10.1177/07316844221147641.
- [8] U. I. A. B. M. Adnan, F. R. Wong, M. F. Morni, A. H. Abdullah, A. A. Rashid, and S. K. Yong, "Mechanical Properties of Rice Husk-Recycled Polypropylene Composite," *J. Mech. Eng.*, vol. 12, no. 1, pp. 45–61, 2023, doi: 10.24191/JMECHE.V12I1.24637.
- [9] R. Muthuraj, C. Lacoste, P. Lacroix, and A. Bergeret, "Sustainable Thermal Insulation Biocomposites From Rice Husk, Wheat Husk, Wood Fibers and Textile Waste Fibers: Elaboration and Performances Evaluation," *Industrial Crops and Products*. 2019. doi: 10.1016/j.indcrop.2019.04.053.
- [10] L. Yang, D. Park, and Z. Qin, "Material Function of Mycelium-Based Bio-Composite: A Review," *Front. Mater.*, 2021, doi: 10.3389/fmats.2021.737377.
- [11] C. Nyambo, A. K. Mohanty, and M. Misra, "Polylactide-Based Renewable Green Composites From Agricultural Residues and Their Hybrids," *Biomacromolecules*. 2010. doi: 10.1021/bm1003114.
- [12] A. M. Nermin and D. E. El-Nashar, "The Influence of Using Agriculture Wastes as Reinforcing Fillers on Hybrid Biocomposites Properties," 2019. doi: 10.21825/autex.63876.
- [13] G. U. Raju and S. Kumarappa, "Experimental Study on Mechanical and Thermal Properties of Epoxy Composites Filled With Agricultural Residue," *Polymers From Renewable Resources*. 2012. doi: 10.1177/204124791200300303.
- [14] S. Manivannan, R. Venkatesh, M. Kubendiran, C. R. Kannan, N. Karthikeyan, and S. Naveen, "Conservation of Waste Melon Shell and Fly Ash Utilized as Reinforcements for Aluminum Alloy Matrix in Terrestrial Ecosystem Acquired Green Hybrid Composites," *Environmental Quality Management*. 2023. doi: 10.1002/tqem.21990.
- [15] C. H. S. N. G. Velmurugana, Jasgurpreet Singh Chohan, M. Abhilakshmi, S. Harikaran, M. B. Shakti dharshini, "A Short Review on the Growth of Lightweight Agronomic Surplus Biomass Composites for Ecological Applications Using Biopolymers," *Int. Res. J. Multidiscip. Technovation*, vol. 6, no. 1, pp. 140–154, Jan. 2024, doi: 10.54392/irjmt24111.
- [16] Y. Altunkaynak and M. Canpolat, "Use of Orange Peel Waste in Removal of Nickel(II) Ions from Aqueous Solutions: Equilibrium, Kinetic and Thermodynamic Studies," *J. Adv. Res. Nat. Appl. Sci.*, vol. 8, no. 2, pp. 322–339, Jun. 2022, doi: 10.28979/jarnas.1000133.
- [17] Y. Altunkaynak and M. Canpolat, "Removal of Manganese (II) Ions from Aqueous Solutions with Raw Orange Peel: Equilibrium, Kinetic and Thermodynamic Studies," *Afyon Kocatepe University Journal of Sciences and Engineering*, vol. 22, no. 1, pp. 45–56, 2022. doi: 10.35414/akufemubid.1032148.
- [18] O. O. Joseph and K. O. Babaremu, "Agricultural waste as a reinforcement particulate for aluminum metal matrix composite (AMMCs): A review," *Fibers*, vol. 7, no. 4, 2019, doi: 10.3390/fib7040033.
- [19] I. Peter P, M. Oki, and A. Adekunle A, "A review of ceramic/bio-based hybrid reinforced aluminium matrix composites," *Cogent Eng.*, vol. 7, no. 1, 2020, doi: 10.1080/23311916.2020.1727167.
- [20] Y. G. Yashas, S. Ballupete Nagaraju, M. Puttegowda, A. Verma, S. M. Rangappa, and S. Siengchin, "Biopolymer-Based Composites: An Eco-Friendly Alternative from Agricultural Waste Biomass," *J. Compos. Sci.*, vol. 7, no. 6, 2023, doi: 10.3390/jcs7060242.
- [21] D. Puglia, D. Pezzolla, G. Gigliotti, L. Torre, M. L. Bartucca, and D. Del Buono, "The Opportunity of Valorizing Agricultural Waste, Through Its Conversion Into Biostimulants, Biofertilizers, and Biopolymers," *Sustainability*. 2021. doi: 10.3390/su13052710.
- [22] S. Pemas, D. Gkiliopoulos, C. Samiotaki, D. N. Bikiaris, Z. Terzopoulou, and E. M. Pechlivani, "Valorization of Tomato Agricultural Waste for 3d-Printed Polymer Composites Based on Poly(lactic Acid)," *Polymers*. 2024. doi: 10.3390/polym16111536.
- [23] D. Fico, D. Rizzo, V. De Carolis, and C. Esposito Corcione, "Bio-Composite Filaments Based on Poly(Lactic Acid) and Cocoa Bean Shell Waste for Fused Filament Fabrication (FFF): Production, Characterization and 3D Printing," *Materials*. 2024. doi: 10.3390/ma17061260.
- [24] A. O. Ibhade, "Engine Lightweighting: Use of Green Materials as Reinforcement in Aluminum Metal Matrix Composites." 2023. doi: 10.5772/intechopen.108273.
- [25] N. Bandara and K. Gajasinghe, "Insights of Circular Economics Practices in Rice Cultivation and Processing - A Review," *Journal of Agriculture and Value Addition*. 2023. doi: 10.4038/java.v6i2.79.
- [26] R. Dungani et al., *Bionanomaterial from agricultural waste and its application*. Elsevier Ltd, 2017. doi: 10.1016/B978-0-08-100957-4.00003-6.
- [27] E. Chiellini, P. Cinelli, S. H. Imam, and L. Mao, "Composite Films Based on Biorelated Agro-Industrial Waste and Poly(vinyl alcohol). Preparation and Mechanical Properties Characterization," *Biomacromolecules*, vol. 2, no. 3, pp. 1029–1037, Sep. 2001, doi: 10.1021/bm010084j.
- [28] A. G. de Souza, R. F. S. Barbosa, and D. S. Rosa, "Nanocellulose from Industrial and Agricultural Waste for Further Use in PLA Composites," *J. Polym. Environ.*, vol. 28, no. 7, pp. 1851–1868, Jul. 2020, doi: 10.1007/s10924-020-01731-w.
- [29] R. Hsissou, R. Seghiri, Z. Benzekri, M. Hilali, M. Rafik, and A. Elharfi, "Polymer composite materials: A comprehensive review," *Compos. Struct.*, vol. 262, p. 113640, Apr. 2021, doi: 10.1016/j.compstruct.2021.113640.
- [30] W. Obade, C. M. Ó Brádaigh, and D. Ray, "Continuous fibre-reinforced thermoplastic acrylic-matrix composites prepared by liquid resin infusion – A review," *Compos. Part B Eng.*, vol. 215, p. 108771, Jun. 2021, doi: 10.1016/j.compositesb.2021.108771.
- [31] J.-M. Raquez, M. Deléglise, M.-F. Lacrampe, and P. Krawczak, "Thermosetting (bio)materials derived from renewable resources: A critical review," *Prog. Polym. Sci.*, vol. 35, no. 4, pp. 487–509, Apr. 2010, doi: 10.1016/j.progpolymsci.2010.01.001.
- [32] X. Liu et al., "Ultrastrong and High-Tough Thermoset Epoxy Resins from Hyperbranched Topological Structure and Subnanoscaled Free Volume," *Adv. Mater.*, vol. 36, no. 9, Mar. 2024, doi: 10.1002/adma.202308434.
- [33] G. Rajeshkumar et al., "Environment friendly, renewable and sustainable poly lactic acid (PLA) based natural fiber reinforced composites – A comprehensive review," *J. Clean. Prod.*, vol. 310, p. 127483, Aug. 2021, doi: 10.1016/j.jclepro.2021.127483.
- [34] L. Yu, K. Dean, and L. Li, "Polymer blends and composites from renewable resources," *Prog. Polym. Sci.*, vol. 31, no. 6, pp. 576–602, Jun. 2006, doi: 10.1016/j.progpolymsci.2006.03.002.
- [35] E. Chiellini, P. Cinelli, F. Chiellini, and S. H. Imam, "Environmentally Degradable Bio-Based Polymeric Blends and Composites," *Macromol. Biosci.*, vol. 4, no. 3, pp. 218–231, Mar. 2004, doi: 10.1002/mabi.200300126.
- [36] M. S. Bulut, M. Ordu, O. Der, and G. Basar, "Sustainable Thermoplastic Material Selection for Hybrid Vehicle Battery Packs in the Automotive Industry: A Comparative Multi-Criteria Decision-Making Approach," *Polymers (Basel)*, vol. 16, no. 19, 2024, doi: 10.3390/polym16192768.
- [37] R. Kumar, K. N. Bairwa, and T. K. Sharma, "Optimization in Flexural and Physical Behavior of Agricultural Waste Reinforced Epoxy Based Polymer Matrix Composite by Taguchi Technique," *Evergreen*, vol. 10, no. 4, pp. 2607–2613, 2023, doi: 10.5109/7160916.
- [38] N. Hongsriphan, J. Subsanga, P. Suebsai, S. Sitthipong, and P. Patanathabutr, "Use of oil palm frond waste to reinforce poly(lactic acid) based composites with the improvement of interfacial adhesion by alkali treatment," *J. Met. Mater. Miner.*, vol. 32, no. 1, pp. 134–143, 2022, doi: 10.55713/jmmm.v32i1.1244.
- [39] A. Ashori and A. Nourbakhsh, "Bio-based composites from waste

- agricultural residues," *Waste Manag.*, vol. 30, no. 4, pp. 680–684, Apr. 2010, doi: 10.1016/j.wasman.2009.08.003.
- [40] M. Suffo, M. de la Mata, and S. I. Molina, "A sugar-beet waste based thermoplastic agro-composite as substitute for raw materials," *J. Clean. Prod.*, vol. 257, p. 120382, Jun. 2020, doi: 10.1016/j.jclepro.2020.120382.
- [41] M. Barczewski, K. Sałasińska, and J. Szulc, "Application of sunflower husk, hazelnut shell and walnut shell as waste agricultural fillers for epoxy-based composites: A study into mechanical behavior related to structural and rheological properties," *Polym. Test.*, vol. 75, pp. 1–11, May 2019, doi: 10.1016/j.polymertesting.2019.01.017.
- [42] M. A. Suhot, M. Z. Hassan, S. A. Aziz, and M. Y. Md Daud, "Recent Progress of Rice Husk Reinforced Polymer Composites: A Review," *Polymers (Basel)*, vol. 13, no. 15, p. 2391, Jul. 2021, doi: 10.3390/polym13152391.
- [43] Z. Seikh, M. Sekh, S. Kunar, G. Kibria, R. Haque, and S. Haidar, "Rice Husk Ash Reinforced Aluminium Metal Matrix Composites: A Review," *Mater. Sci. Forum*, vol. 1070, pp. 55–70, 2022, doi: 10.4028/p-u8s016.
- [44] P. P. Kulkarni, B. Siddeswarappa, and K. S. H. Kumar, "A Survey on Effect of Agro Waste Ash as Reinforcement on Aluminium Base Metal Matrix Composites," *Open J. Compos. Mater.*, vol. 09, no. 03, pp. 312–326, 2019, doi: 10.4236/ojcm.2019.93019.
- [45] K. Anitha and S. Senthilselvan, "Agricultural Waste Materials Applications in Building Industry – An Overview," *Ecs Transactions*. 2022. doi: 10.1149/10701.2371ecst.
- [46] N. C. Amulah, A. M. El-Jumma, A. A. Hammajam, and U. Ibrahim, "Experimental Investigation on the Thermal Properties of Gypsum Plaster-Rice Husk Ash Composite," *Open Journal of Composite Materials*. 2022. doi: 10.4236/ojcm.2022.124010.
- [47] A. E. Eladawi and A. H. Rajpar, "Investigation of Mechanical Properties for Reinforced Polyester Composites With Palm Fronds," *Journal of Materials Science and Chemical Engineering*. 2020. doi: 10.4236/msce.2020.83006.
- [48] U. V. Akhil, N. Radhika, B. Saleh, S. A. Krishna, N. Noble, and L. Rajeshkumar, "A Comprehensive Review on Plant-based Natural Fiber Reinforced Polymer Composites: Fabrication, Properties, and Applications," *Polymer Composites*. 2023. doi: 10.1002/pc.27274.
- [49] W. Liu *et al.*, "Properties of poly(butylene adipate-co-terephthalate) and sunflower head residue biocomposites," *Journal of Applied Polymer Science*, vol. 134, no. 13, 2017. doi: 10.1002/app.44644.
- [50] P. Cinelli, M. Seggiani, N. Mallegni, V. Gigante, and A. Lazzeri, "Processability and Degradability of PHA-Based Composites in Terrestrial Environments," *International Journal of Molecular Sciences*. 2019. doi: 10.3390/ijms20020284.
- [51] M. Noryani, S. M. Sapuan, M. T. Mastura, M. Y. M. Zuhri, and E. S. Zainudin, "Material Selection of a Natural Fibre Reinforced Polymer Composites using an Analytical Approach," *J. Renew. Mater.*, vol. 7, no. 11, pp. 1165–1179, 2019, doi: 10.32604/jrm.2019.07691.
- [52] A. Karimah *et al.*, "A review on natural fibers for development of eco-friendly bio-composite: characteristics, and utilizations," *J. Mater. Res. Technol.*, vol. 13, pp. 2442–2458, Jul. 2021, doi: 10.1016/j.jmrt.2021.06.014.
- [53] H. P. S. Abdul Khalil, M. Siti Alwani, R. Ridzuan, H. Kamarudin, and A. Khairul, "Chemical Composition, Morphological Characteristics, and Cell Wall Structure of Malaysian Oil Palm Fibers," *Polym. Plast. Technol. Eng.*, vol. 47, no. 3, pp. 273–280, Feb. 2008, doi: 10.1080/03602550701866840.
- [54] A. H. Hemmasi, H. Khademi-Eslam, S. Pourabbasi, I. Ghasemi, and M. Talaiepour, "Cell morphology and physico-mechanical properties of HDPE/EVA/Rice hull hybrid foamed composites," *BioResources*, vol. 6, no. 3, pp. 2291–2308, 2011, doi: 10.15376/biores.6.3.2291-2308.
- [55] C. Driemeier, W. D. Santos, and M. S. Buckeridge, "Cellulose crystals in fibrovascular bundles of sugarcane culms: orientation, size, distortion, and variability," *Cellulose*, vol. 19, no. 5, pp. 1507–1515, 2012, doi: 10.1007/s10570-012-9743-z.
- [56] M. S. Alwani, H. P. S. A. Khalil, N. Islam, O. Sulaiman, A. Zaidon, and R. Dungani, "Microstructural Study, Tensile Properties, and Scanning Electron Microscopy Fractography Failure Analysis of Various Agricultural Residue Fibers," *J. Nat. Fibers*, vol. 12, no. 2, pp. 154–168, Mar. 2015, doi: 10.1080/15440478.2014.905216.
- [57] M. Sakthivel and S. Ramesh, "Mechanical properties of natural fibre (banana, coir, sisal)," *Sci Park*, vol. 1, no. 1, pp. 1–6, 2013.
- [58] M. Bouasker, N. Belayachi, D. Hoxha, and M. Al-Mukhtar, "Physical Characterization of Natural Straw Fibers as Aggregates for Construction Materials Applications," *Materials (Basel)*, vol. 7, no. 4, pp. 3034–3048, 2014, doi: 10.3390/ma7043034.
- [59] N. Reddy and Y. Yang, "Properties of High-Quality Long Natural Cellulose Fibers from Rice Straw," *J. Agric. Food Chem.*, vol. 54, no. 21, pp. 8077–8081, Oct. 2006, doi: 10.1021/jf0617723.
- [60] C. Alves, P. M. C. Ferrão, M. Freitas, A. J. Silva, S. M. Luz, and D. E. Alves, "Sustainable design procedure: The role of composite materials to combine mechanical and environmental features for agricultural machines," *Mater. Des.*, vol. 30, no. 10, pp. 4060–4068, 2009, doi: https://doi.org/10.1016/j.matdes.2009.05.015.
- [61] S. Sathees Kumar, B. Sridhar Babu, C. N. Chankravarthy, and N. Prabhakar, "Review on natural fiber polymer composites," *Mater. Today Proc.*, vol. 46, no. 2, pp. 777–782, 2021, doi: 10.1016/j.matpr.2020.12.599.
- [62] P. Wambua, J. Ivens, and I. Verpoest, "Natural fibres: can they replace glass in fibre reinforced plastics?," *Compos. Sci. Technol.*, vol. 63, no. 9, pp. 1259–1264, 2003, doi: https://doi.org/10.1016/S0266-3538(03)00096-4.
- [63] S. S. Munawar, K. Umamura, and S. Kawai, "Characterization of the morphological, physical, and mechanical properties of seven nonwood plant fiber bundles," *J. Wood Sci.*, vol. 53, no. 2, pp. 108–113, 2007, doi: 10.1007/s10086-006-0836-x.
- [64] A. R. Rathod, "Analysis of Physical Characteristics of Bamboo Fabrics," *Int. J. Res. Eng. Technol.*, vol. 03, no. 08, pp. 21–25, 2014, doi: 10.15623/ijret.2014.0308004.
- [65] S. Chairrekij, A. Apirakchaiskul, K. Suvarnakich, and S. Kiatkamjornwong, "Kapok I: Characteristics of kapok fiber as a potential pulp source for papermaking," *BioResources*, vol. 7, no. 1, pp. 475–488, 2012, doi: 10.15376/biores.7.1.475-488.
- [66] L. Y. Mwaikambo and M. P. Ansell, "The determination of porosity and cellulose content of plant fibers by density methods," *J. Mater. Sci. Lett.*, vol. 20, no. 23, pp. 2095 – 2096, 2001, doi: 10.1023/A:1013703809964.
- [67] B. Babu, J. Bensam Raj, R. Jeya Raj, and X. Roshan Xavier, "Investigation on the mechanical properties of natural composites made with Indian almond fiber and neem seed particulates," *Proc. Inst. Mech. Eng. Part C J. Mech. Eng. Sci.*, vol. 237, no. 17, pp. 3908–3915, Apr. 2023, doi: 10.1177/09544062231167018.
- [68] M. C. Lee *et al.*, "Properties of Poly(lactic Acid)/Durian Husk Fiber Biocomposites: Effects of Fiber Content and Processing Aid," *Journal of Thermoplastic Composite Materials*. 2019. doi: 10.1177/0892705719831734.
- [69] R. Phiri, M. R. Sanjay, S. Siengchin, O. P. Oladijo, and H. N. Dhakal, "Development of Sustainable Biopolymer-Based Composites for Lightweight Applications From Agricultural Waste Biomass: A Review," *Advanced Industrial and Engineering Polymer Research*. 2023. doi: 10.1016/j.aiepr.2023.04.004.
- [70] E. Elsacker, S. Vandeloek, A. Van Wylick, J. Ruytinx, L. De Laët, and E. Peeters, "A Comprehensive Framework for the Production of Mycelium-Based Lignocellulosic Composites," *The Science of the Total Environment*. 2020. doi: 10.1016/j.scitotenv.2020.138431.
- [71] Y. K. Abdallah and A. T. Estévez, "Biowelding 3d-Printed Biodegradable Brick of Seashell-Based Biocomposite by *Pleurotus Ostreatus* Mycelium," *Biomimetics*. 2023. doi: 10.3390/biomimetics8060504.
- [72] D. Lestari *et al.*, "Durability to Natural Weathering of Methylene Diphenyl Diisocyanate-Bonded Bamboo Oriented Strand Board," *Jurnal Sylva Lestari*. 2024. doi: 10.23960/jsl.v12i1.839.
- [73] S. C. Koay and S. Husseinsyah, "Agrowaste-Based Composites From Cocoa Pod Husk and Polypropylene," *Journal of Thermoplastic Composite Materials*. 2016. doi: 10.1177/0892705714563125.
- [74] A. M. Rahman, A. Bhardwaj, J. G. Vasselli, Z. Pei, and B. D. Shaw, "Three-Dimensional Printing of Biomass-Fungi Biocomposite Materials: The Effects of Mixing and Printing Parameters on Fungal Growth," *Journal of Manufacturing and Materials Processing*. 2023. doi: 10.3390/jmmp8010002.
- [75] R. V. Patel, A. Yadav, and J. Winczek, "Physical, Mechanical, and Thermal Properties of Natural Fiber-Reinforced Epoxy Composites for Construction and Automotive Applications," *Appl. Sci.*, vol. 13, no. 8, p. 5126, Apr. 2023, doi: 10.3390/app13085126.
- [76] C. Maraveas, "Production of sustainable and biodegradable polymers from agricultural waste," *Polymers (Basel)*, vol. 12, no. 5, 2020, doi: 10.3390/POLYM12051127.
- [77] Christyanne Faye San Juan, "Sustainable Packaging Solutions for Eco-Conscious Consumers and Businesses," *Paper Mart*, 2023.
- [78] D. Bolcu, M. M. Stănescu, and C. M. Mitițoiu, "Some Mechanical Properties of Composite Materials With Chopped Wheat Straw Reinforcer and Hybrid Matrix," *Polymers*. 2022. doi:

- 10.3390/polym14153175.
- [79] M. P. Jones *et al.*, “Waste-derived Low-cost Mycelium Composite Construction Materials With Improved Fire Safety,” *Fire and Materials*. 2018. doi: 10.1002/fam.2637.
- [80] N. S. F. Azman and Z. Romli, “Alternative Pineapple Fibre Advancement in Furniture Design,” *Environment-Behaviour Proceedings Journal*. 2024. doi: 10.21834/e-bpj.v9isi17.5434.
- [81] X. Hanyue, M. T. H. Sultan, M. I. Najeeb, and F. S. Shahar, “A Short Review on the Recent Progress and Properties of Pineapple Leaf Fiber Reinforced Composite,” *E3s Web of Conferences*. 2024. doi: 10.1051/e3sconf/202447700096.
- [82] J. T. Aladejana, Z. Wu, and M. Fan, “Key Advances in Development of Straw Fibre Bio-Composite Boards: An Overview,” *Materials Research Express*. 2020. doi: 10.1088/2053-1591/ab66ec.
- [83] Ş. Yıldızhan, A. Çalık, M. Özcanlı, and H. Serin, “Bio-composite materials: a short review of recent trends, mechanical and chemical properties, and applications,” *European Mechanical Science*, 2018.
- [84] Y. Wang, C. Liu, X. Zhang, and S. Zeng, “Research on Sustainable Furniture Design Based on Waste Textiles Recycling,” *Sustainability*. 2023. doi: 10.3390/su15043601.
- [85] G. Singh, M. K. Gupta, S. Chaurasiya, V. S. Sharma, and D. Y. Pimenov, “Rice straw burning: a review on its global prevalence and the sustainable alternatives for its effective mitigation,” *Environ. Sci. Pollut. Res.*, vol. 28, no. 25, pp. 32125–32155, Jul. 2021, doi: 10.1007/s11356-021-14163-3.

BIOGRAPHIES (HELVETICA 10P BOLD)

Izham KILINÇ obtained his bachelor's degree from the Furniture and Decoration Teaching Department at Karabük University in 2010. He began his master's education in the Department of Furniture and Decoration Education at Karabük University the same year and completed it in 2013. During his master's studies, he served as a scholarship holder in the TÜBİTAK Agricultural and Forestry Foundation project. In 2014, he started working as a lecturer in the Interior Design Program at Batman University's Technical Sciences Vocational School. He began his doctoral studies in 2018 in the Department of Interdisciplinary Composite Material Technologies at Düzce University and completed his doctorate in 2023. During his doctoral education, he was also a scholarship holder in the TÜBİTAK 1005 project. He currently serves as a lecturer and doctor at Batman University, continuing his research in interior design and composite material technologies.

Mustafa Korkmaz obtained his Bachelor of Science degree in Furniture and Decoration Teaching from Karabük University in 2010. He subsequently received his Master of Science and Doctor of Philosophy degrees in the same department from Karabük University in 2012 and 2018, respectively. His research interests include wood materials, non-destructive testing (NDT) of wood, and wood modification. In 2013, he joined the Faculty of Technology at Düzce University as a research assistant and is currently serving as an assistant professor.

Research Article

Speed Control of a Single-Phase Induction Motor Using a Fuzzy Logic Based Hysteresis Band PWM

Ece Yilmaz^{1*}, Sencer Unal², Mehmet Ozdemir³

^{1*}Firat University, Electrical and Electronics Engineering Department, Elazığ, Turkey. (21113112@firat.edu.tr).

²Firat University, Electrical and Electronics Engineering Department, Elazığ, Turkey. (sencerunal@firat.edu.tr).

³ Firat University, Electrical and Electronics Engineering Department, Elazığ, Turkey. (mozdemir@firat.edu.tr).

ARTICLE INFO

Received: Mar., 14, 2024

Revised: July, 30, 2024

Accepted: Aug., 15, 2024

Keywords:

Single Phase Induction Motor

Hysteresis Band PWM

Fuzzy Logic

Corresponding author: Ece Yilmaz

ISSN: 2536-5010 / e-ISSN: 2536-5134

DOI: <https://doi.org/10.36222/ejt.1452899>

ABSTRACT

Single-phase asynchronous motors are preferred in the industry due to their significant features such as robust construction, easy maintenance, and ability to operate in different ambient conditions. They are widely used in various types of automated control systems, cooling and ventilation appliances, and household appliances. Although the structure of the single-phase induction motors is quite simple, modeling and speed control of them are very difficult due to their nonlinear structure. Since traditional speed control methods are not sufficient in nowadays, various methods are being investigated for the speed control of these motors. One of them is to control the speed of a single-phase induction motor by changing the voltage waveform via the power electronic components. In addition to this method, fuzzy logic controller can be preferred in the systems that are difficult to analyze and it does not require a mathematical model. For this reason, in this study, a PWM controlled AC chopper circuit and fuzzy logic controller, which is one of the faster and cheaper methods, are proposed for the speed control of a single phase induction motor. Thus, better results are obtained from the fuzzy logic controller. The system is modeled by MATLAB/Simulink simulations and the results are validated.

1. INTRODUCTION

3-phase induction motors are the most widely used motors in the industry. On the other hand, single-phase induction motors are also commonly preferred in low power drive systems. The speed of the induction motors varies very little based on the load. While the speed of direct current motors can be varied within wide limits, the speed of an induction motor can only be increased or decreased to a limited extent by conventional control methods. Induction motors are cheaper in all respects, require less periodic maintenance and do not produce electric arcs during operation. Because of these features, three-phase and single-phase induction motors are the most widely utilized motors in the industry [1]. Despite these advantages, single-phase induction motors have some drawbacks which are being nonlinear and fifth-order, and the complex modeling. Although conventional speed control methods are proper for the linear applications, they are not adequate for the single-phase induction motors, which have a nonlinear structure [2]. Since single-phase induction motors provide a wider speed range for load torques that vary with the square of the speed, Alternating Current (AC) chopper is considered as a suitable solution [3]. In the literature, some studies carried out in this area are handled. Firstly, Zigirkas and Kalomiros propose an asymmetric PWM technique and

fuzzy logic controller for the voltage control of a single phase induction motor [4]. Bouzidi, Harrouz, and Mansouri present a fuzzy logic control of an induction motor based on the variation of the rotor resistance and control of the rotational speed [5]. Agyare, Asiedu, and Biney study a fuzzy logic controller to monitor the behavior of the induction motor based on the amplitude characteristics of the stator currents [6]. Mekrini and Seddik design a fuzzy logic based controller to improve the direct torque control and provide desired torque and flux in the machine [7]. Maghfiroh, Saputro, Fahmizal, and Baballe use the fuzzy logic and PI controllers together for the speed control of the induction motor. Since PID performances degrade when system conditions change, a fuzzy logic is used as a tunable algorithm to change the PID gain [8]. Gobimohan and Murali focus on the design of a closed-loop control for a capacitor-driven asynchronous motor drive with pulse width modulated AC chopper control using a bacteria collection based optimization algorithm. A linearized boost model for the PWM AC chopper is shown for a specific functional point of the drive [9]. Ariff and his/her friends address the problem of the speed control for indirect field steering of an induction motor in the designed system. The problems in the speed control cause the performance degradation of the induction motor in high performance applications. Takagi-Sugeno type fuzzy logic controller is

used as a speed controller to reduce the speed distortion [10]. In the paper, Ahmed and Soliman present the modeling of a motor fed by a pulse width modulated, voltage controlled AC chopper circuit. The advantages of the system are high power factor and low total harmonics in the motor current [11]. Mohan, Pathak, and Dwivedi propose a reactive power based speed control of an induction motor drive for wide speed range applications. This approach involves the control of the reactive power curve entering and leaving the motor for the speed control of the induction motor using a fuzzy logic method. The main advantage of this approach is to achieve the desired power factor operation [12]. Daoudi, Lazrak, Ouanjli, and Lafkih develop a fuzzy direct torque control for a two-level inverter driven induction motor drive. The aim of them is to improve the system performance by reducing the electromagnetic torque and stator flux fluctuations while improving stator current waveforms. A comparative study between direct torque control based on the fuzzy logic and nonlinear sliding mode direct torque control is performed by using MATLAB/Simulink [13]. Muthamizhan, Shivaj, and Aijaz control the speed of the induction motor in the study by using the V/f control technique via three phase multilevel inverters. The multilevel inverter used are 7, 9, and 11 level diode clamped multilevel inverters. The V/f control system is based on a fuzzy logic controller which replaces the conventional closed loop proportional integral controller for the induction motor drive. The study is realized by a MATLAB/Simulink software including a multilevel inverter with a V/f control [14]. As mentioned above, AC chopper circuit, PWM signals, and fuzzy logic are the preferred and studied methods for the speed control of a single phase induction motor. These methods, which are also easy to implement, are open to improvement.

In this paper, hysteresis band PWM controlled AC circuit and fuzzy logic controller are studied for the speed control of a single phase induction motor. The high-speed power switches used in the AC chopper circuit are preferred to control the speed of the single-phase induction motor by changing the voltage waveform of the motor. PWM signals generated by the hysteresis band are used to trigger the power electronics elements. Depending on this control method, a fuzzy logic controller is used to get better results especially in the speed graph. With the fuzzy logic method, which is widely preferred in complex systems, a closed loop is created and the model gives better results.

The methods used in the design are explained in the Sections 2, 3, 4 and 5 of the study. Sections 6 and 7 present the design and results.

2. A SINGLE PHASE INDUCTION MOTOR MODEL

A single-phase induction motor with auxiliary winding is used in the model.

2.1. Auxiliary Winding Motors

A motor consisting of two different stator windings placed at 90° to each other as shown in Figure 1 is called an auxiliary winding motor. When the motor speed reaches 75-80% of the synchronous speed, the start switch disables the auxiliary winding. This switch is opened by the centrifugal force. The rotor of this type motor is a squirrel cage. In the starting process, the two windings are connected in parallel to each other and also to the supply source [15].

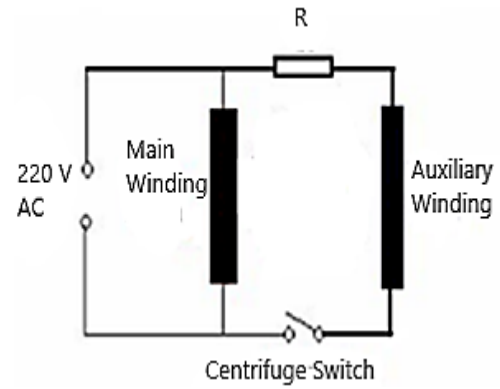


Figure 1. Equivalent circuit of a single phase induction motor with auxiliary winding.

2.2. Mathematical Model of a Single Phase Induction Motor

In order to analyze a single-phase asynchronous motor, a mathematical model is required. With the help of the equivalent circuit given in Figure 2, the d-q model is created and can be analyzed in this way [16]. In the equations, V , λ , I , R , and L are the voltage, flux, current, resistance, and inductance value for the d-q axis, respectively. $d\theta/dt$ is the rotor angular speed, T_m is the motor torque, T_y is the load torque, ω is the angular speed and j is the coefficient of the inertia. Sub-indexes s , r , d , and q represent the stator, rotor, d-axis, and q-axis, respectively.

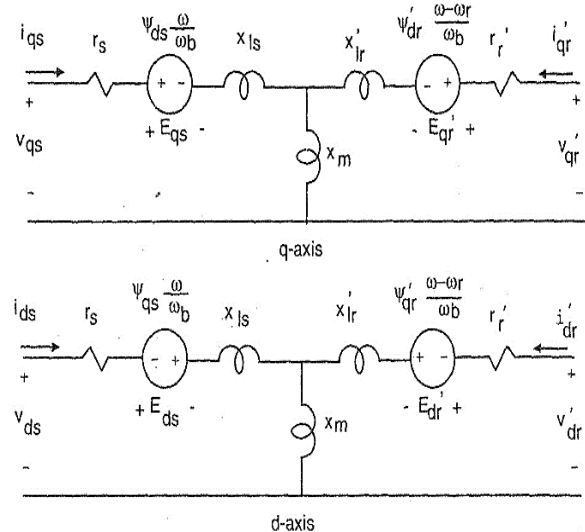


Figure 2. Circuit of a single phase induction machine [16].

The voltage equations are given below.

$$V_{qs} = R_{qs} * I_{qs} + \frac{d\lambda_{qs}}{dt} \quad (1)$$

$$V_{ds} = R_{ds} * I_{ds} + \frac{d\lambda_{ds}}{dt} \quad (2)$$

$$V_{qr} = R_r * I_{qr} - \lambda_{dr} * \frac{d\theta_r}{dt} + \frac{d\lambda_{qr}}{dt} \quad (3)$$

$$V_{dr} = R_r * I_{dr} + \lambda_{qr} * \frac{d\theta_r}{dt} + \frac{d\lambda_{dr}}{dt} \quad (4)$$

The fluxes can be obtained from the voltage equations as follows

$$\lambda_{qs} = \int (V_{qs} - R_{qs} * I_{qs}) dt \quad (5)$$

$$\lambda_{ds} = \int (V_{ds} - R_{ds} * I_{ds}) dt \quad (6)$$

$$\lambda_{qr} = \int (V_{qr} - R_r * I_{qr} + \lambda_{dr} * \frac{d\theta_r}{dt}) dt \quad (7)$$

$$\lambda_{dr} = \int (V_{dr} - R_r * I_{dr} - \lambda_{qr} * \frac{d\theta_r}{dt}) dt \quad (8)$$

The flux equations can be given as follows

$$\lambda_{qs} = L_{lqs} * I_{qs} + L_{mq} * (I_{qs} + I_{qr}) \quad (9)$$

$$\lambda_{ds} = L_{lds} * I_{ds} + L_{md} * (I_{ds} + I_{dr}) \quad (10)$$

$$\lambda_{qr} = L_{lrr} * I_{qr} + L_{mq} * (I_{qs} + I_{qr}) \quad (11)$$

$$\lambda_{dr} = L_{lrr} * I_{dr} + L_{md} * (I_{ds} + I_{dr}) \quad (12)$$

The current equations can be written as follows

$$I_{qs} = \frac{1}{L_{lqs}} * (\lambda_{qs} - L_{mq} * (I_{qs} + I_{qr})) \quad (13)$$

$$I_{ds} = \frac{1}{L_{lds}} * (\lambda_{ds} - L_{md} * (I_{ds} + I_{dr})) \quad (14)$$

$$I_{qr} = \frac{1}{L_{lrr}} * (\lambda_{qr} - L_{mq} * (I_{qs} + I_{qr})) \quad (15)$$

$$I_{dr} = \frac{1}{L_{lrr}} * (\lambda_{dr} - L_{md} * (I_{ds} + I_{dr})) \quad (16)$$

The motion equation of the system is given below.

$$T_m = \frac{P}{2} * (\lambda_{qr} * I_{dr} - \lambda_{dr} * I_{qr}) \quad (17)$$

$$j * \frac{d\omega_r}{dt} = T_m - T_y \quad (18)$$

3. PWM Controlled AC Chopper

3.1. PWM Controlled AC Chopper

AC voltage choppers are widely used in the speed control of 3-phase and single-phase induction motors, especially for load torques that vary with the square of the speed. The control methods used in these choppers cause non-uniform waveforms in the supply voltages and load currents. The single-phase pulse width modulation controlled AC chopper proposed by Kwon has high power factor, low harmonic input current, and high efficiency. In the PWM controlled AC Chopper for motor speed control, power switches are used to interrupt the source voltage. This method causes the pulse width of the AC voltage waveform to change. Therefore, this AC voltage control method is called symmetrical pulse width modulation. The circuit diagram of the system is given in Figure 3 [17].

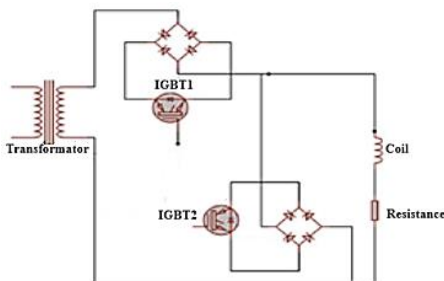


Figure 3. Symmetric PWM AC chopper circuit diagram [17].

3.2. Hysteresis Band PWM

Hysteresis band current control to obtain the power switching signal in a way that reduces the current error [18]. As a result of this technique, a significant improvement is provided in the quality of the load current in the system simulation. The advantages of the system are its ease of industrial implementation, cost, and reliability [19]. This

PWM method is commonly used in the current-controlled PWM applications. A feedback loop is utilized to measure the inrush value of the motor current. A sinusoidal current reference is monitored within a defined hysteresis band as shown in Figure 4. When the actual current exceeds the upper hysteresis band, the upper switch on one leg of the drive is cut off and the lower switch conducts. This is a current reduction state. If the current falls below the hysteresis band, the upper switch conducts and the lower switch cuts. When a positive voltage is applied to the phase, the current increases. Hysteresis band PWM is used to keep the motor current within the hysteresis band. This is an easy method to implement the PWM and since the response time of the controller is very fast, the controller does not need any other parameter other than the value of the current. Besides these advantages, this modulation method also has some disadvantages. The first one is that the PWM switching frequency does not have a fixed value, however, it varies within a frequency band. When the current ripple is not desired, the hysteresis band is narrowed, resulting in more switching per period (switching losses also increase at high switching frequency) [20].

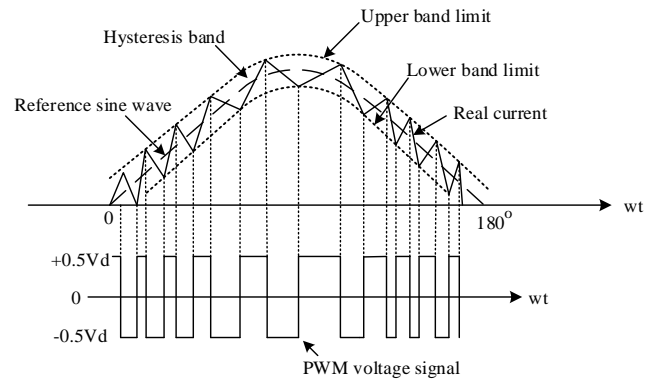


Figure 4. Principle schematic of the hysteresis band PWM [20].

3.3. Fuzzy Logic Controller

A fuzzy logic is an expert system that works from a knowledge representation based on the set theory. It consists of a database that counts all the information about the process and it allows us to define the membership functions and fuzzy rules of the fuzzy system [21]. Fuzzy logic controllers are preferred in the control of time-varying and nonlinear systems which mathematical model cannot be determined precisely. The concept of them had been first introduced by Lutfi A. Zadeh. In the fuzzy logic structure, the relationships between concepts are represented by verbal or numerical expressions. In the control process, there is a linguistic control structure created by an expert persons [22]. The fuzzy logic system has been proven to give better results and better torque response compared to classical methods for evaluating speed control performance [23]. Hence fuzzy logic speed controller is preferred due to its simplicity and low implementation cost. In addition, it exhibits strong performance in nonlinear controller systems without designing any mathematical model [24]. A fuzzy logic controller consists of three basic parts which are fuzzification, rule-based inference mechanism, and stabilization as shown in Figure 5 [25].

4. EXPERIMENTS

4.1. System Design

The system model is realized with MATLAB/Simulink package program. In the designed model, the speed control of a single-phase induction motor with AC chopper controlled by asymmetric PWM signals generated from hysteresis band.

The tag values of the single-phase induction motor are given in Table 1. When the motor speed reaches 75% of the synchronous speed, the auxiliary winding is removed from the circuit.

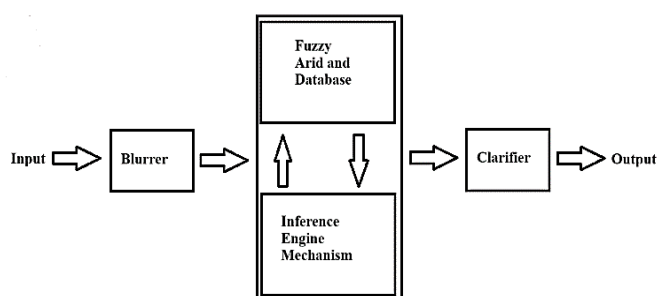


Figure 5. Block diagram of a fuzzy logic controller [25].

TABLE I

LABEL INFORMATION FOR SINGLE PHASE INDUCTION MOTOR.

Symbol	Engine Information	Numeric Values
W	motor power	8.98 W
V	voltage	230 V
Hz	frequency	50 Hz
Ω	Main winding resistance(stator)	149.5 Ω
H	Main winding inductance(stator)	0.58001 H
Ω	Main winding resistance(rotor)	162.5 Ω
H	Main winding inductance(rotor)	0.58001 H
H	Main winding common inductance	3.1344 H
Ω	Auxiliary winding resistance	1625 Ω
H	Auxiliary winding inductance	0.029 H
j	Moment of inertia	0.0146 kg*m ²
N_s/N_r	Winding ratio	1.18
p	Number of poles	4

4.2. Research Findings

In this study, it is aimed to create a fuzzy logic closed-loop model to prevent the speed drop when a load is connected to

the shaft of the single-phase induction motor. In the previous model, the torque generated by the motor is used for the input of the hysteresis band. However, here, the input of the hysteresis band is changed. Firstly, a closed loop is created with a fuzzy logic controller. In the first input of the fuzzy logic controller designed with two inputs and one output, the speed error signals obtained from comparing the speed of the motor and the reference speed are used. The reference speeds are chosen as 1000-1200-1300 and 1400 rpm. The model is re-run for each reference speed value. For the second input, the derivative of the speed error signals is taken and the speed error change signals are obtained. The torque change signals obtained from the output of the fuzzy logic controller are summed with the torque signals produced by the motor and used for the input of the block where the hysteresis band is generated. Thus, only the input signal of the hysteresis band generation block is changed, the shape and values of the reference signal are used for the hysteresis band and the values of the relay are not changed. As shown in Figure 6, seven different load values (0.05-0.055-0.06-0.065-0.065-0.07-0.75-0.08 Nm) are gradually connected to the motor shaft incrementally starting from the 25th second.

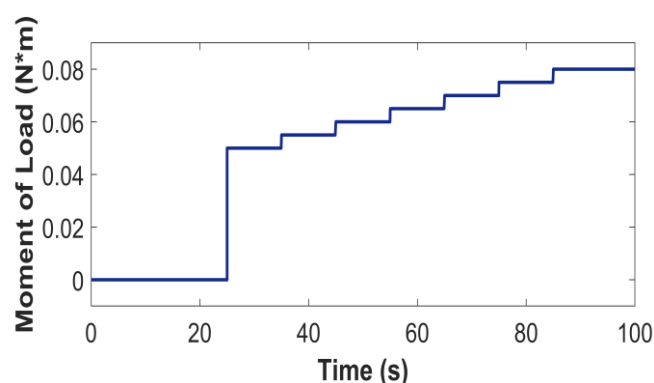


Figure 6. Load values connected to the motor.

The designed model is given in Figure 7. The model is designed using a fuzzy logic controller. This consists of two inputs, one output, and seven membership functions.

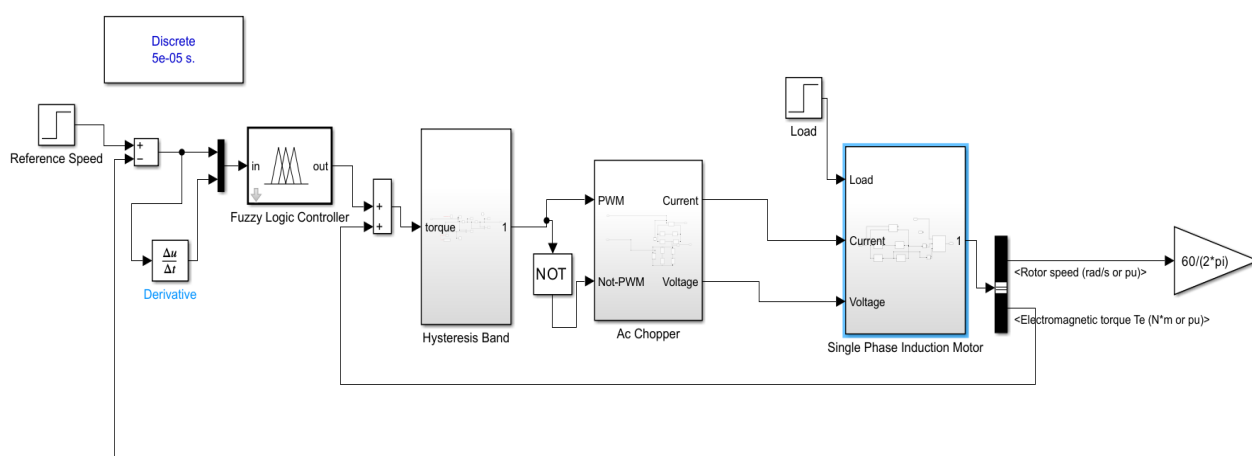


Figure 7. Model for the speed control of a single phase induction motor using hysteresis band PWM with a fuzzy logic controller.

The model is tested for different reference speed values and the same controller is used for these speed values. The rule surface of the fuzzy logic controller is given in Figure 8.

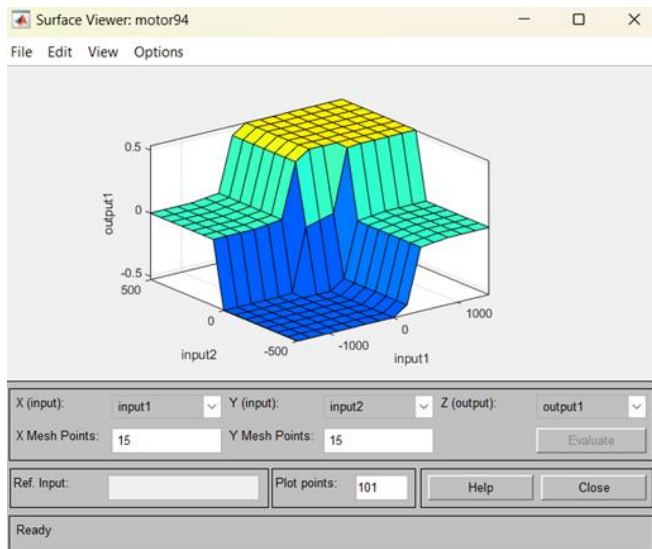


Figure 8. Rule surface.

The speed graph of the single-phase induction motor controlled by an asymmetric PWM without a fuzzy logic controller is given in Figure 9 and Figure 10 for unloaded and loaded conditions.

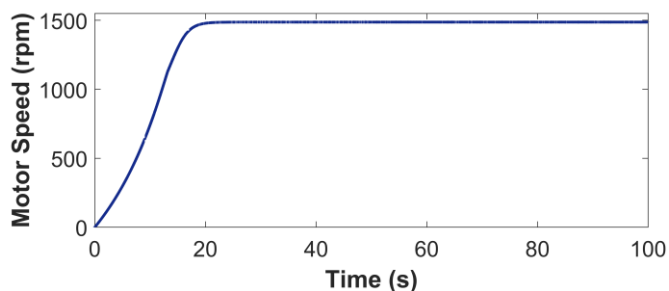


Figure 9. Speed graph for no-load condition.

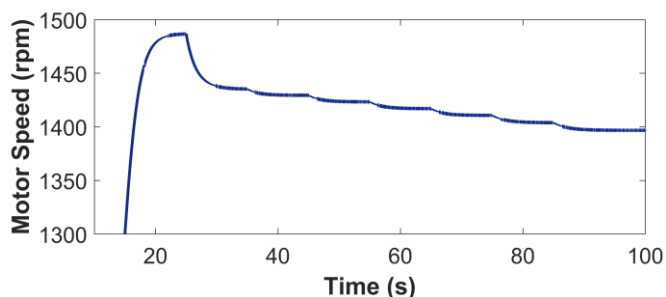


Figure 10. Speed graph for loaded state.

After the control system is created by the fuzzy logic controller, the graphical results obtained for some reference speeds which are 1000-1200-1300, and 1400 rpm and different load values are given as below.

By using 1000 rpm reference speed value and load values given in Figure 6, the speed, voltage, current, and torque curves produced by the motor are given in Figures 11-14.

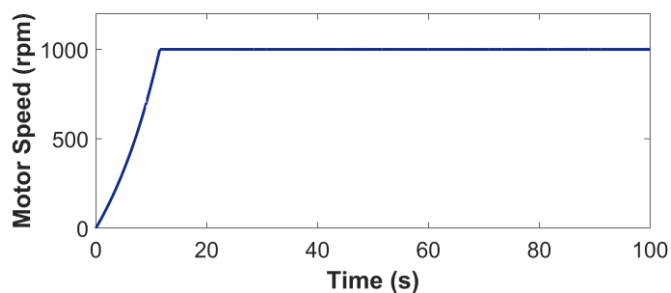


Figure 11. Speed curve of the motor for 1000 rpm reference speed value.

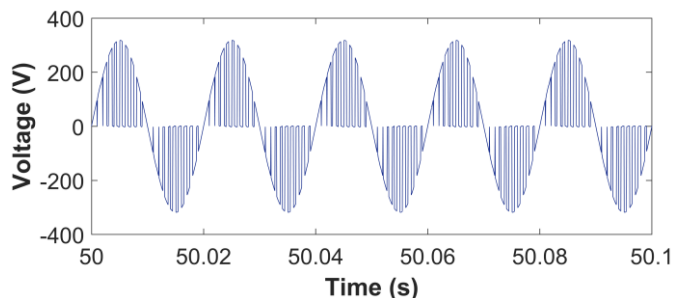


Figure 12. Voltage curve of the motor for 1000 rpm reference speed value.

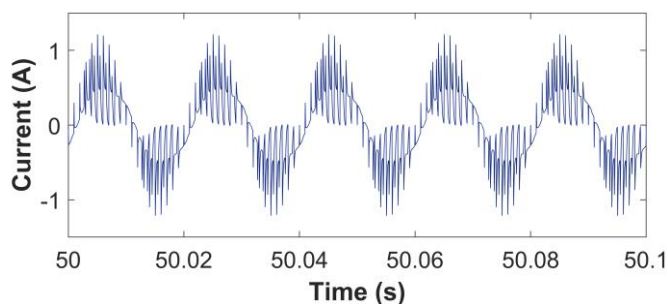


Figure 13. Current curve of the motor for 1000 rpm reference speed value.

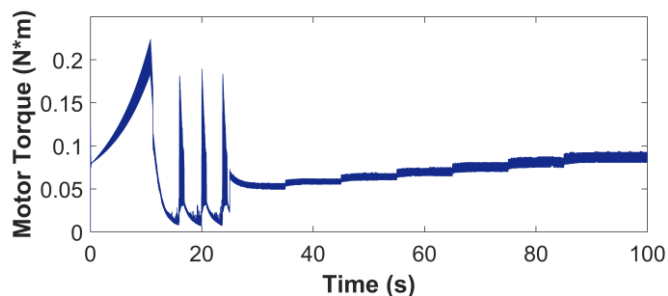


Figure 14. Torque curve produced by the motor for 1000 rpm reference speed value.

By using 1200 rpm reference speed value and the load values given in Figure 6, the speed, voltage, current, and torque curves produced by the motor are shown in Figures 15-18.

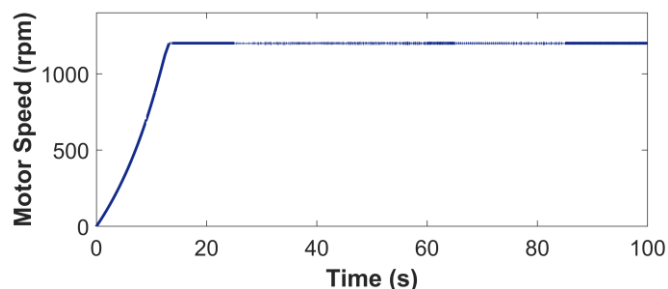


Figure 15. Speed curve of the motor for 1200 rpm reference speed value.

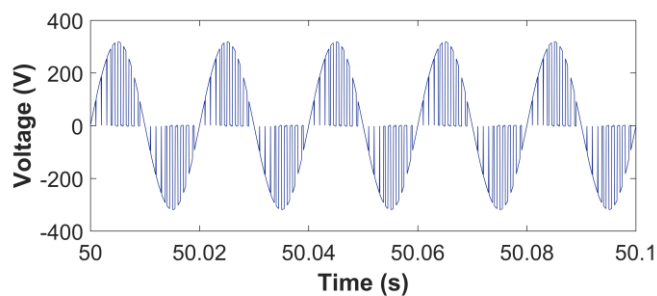


Figure 16. Voltage curve of the motor for 1200 rpm reference speed value.

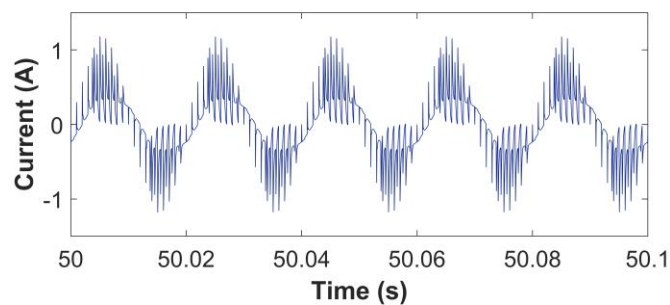


Figure 21. Current curve of the motor for 1300 rpm reference speed value.

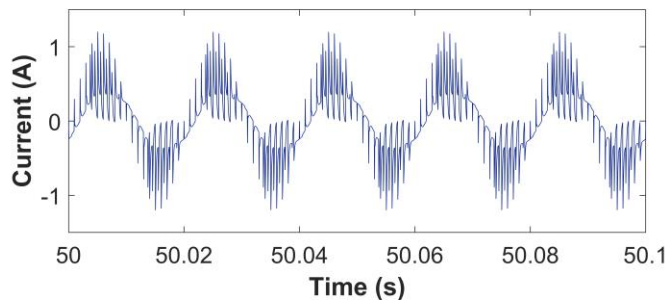


Figure 17. Current curve of the motor for 1200 rpm reference speed value.

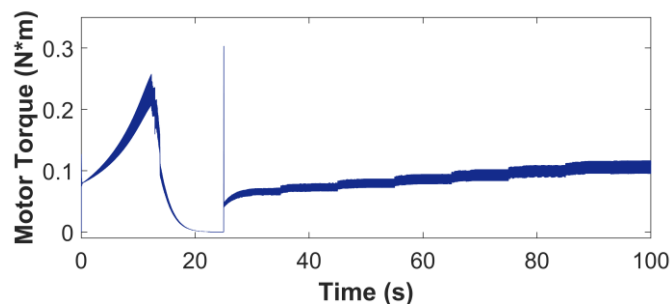


Figure 22. Torque curve produced by the motor for a reference speed of 1300 rpm.

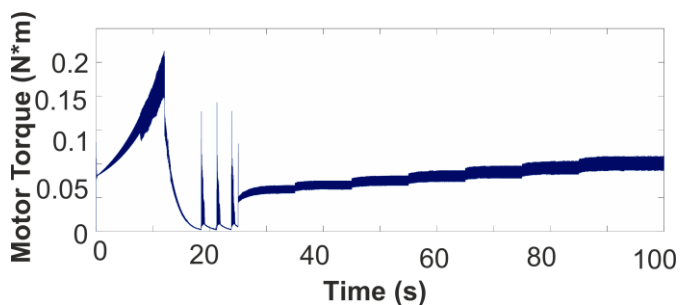


Figure 18. Torque curve produced by the motor for 1200 rpm reference speed value.

By using the reference speed of 1300 rpm and load values given in Figure 6, the speed, voltage, current and torque curves produced by the motor are drawn in Figures 19-22.

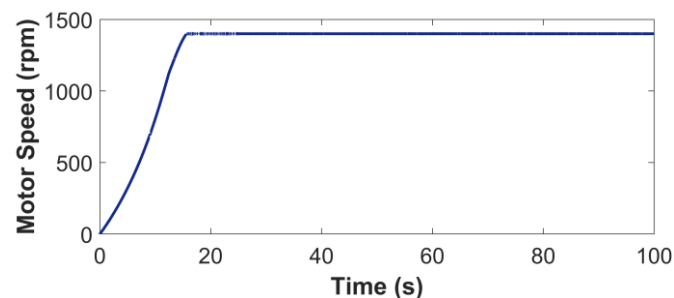


Figure 23. Speed curve of the motor for 1400 rpm reference speed value.

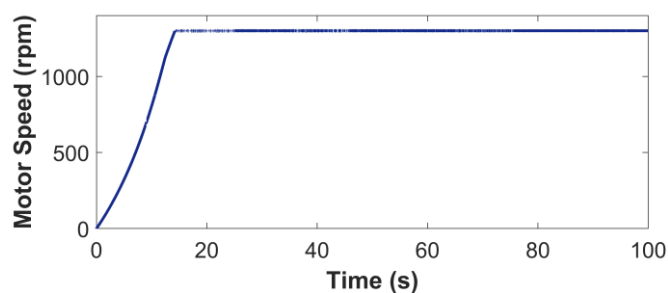


Figure 19. Current curve of the motor for 1300 rpm reference speed value.

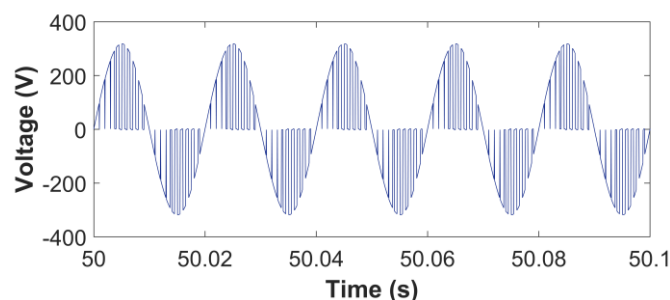


Figure 24. Voltage curve of the motor for 1400 rpm reference speed value.

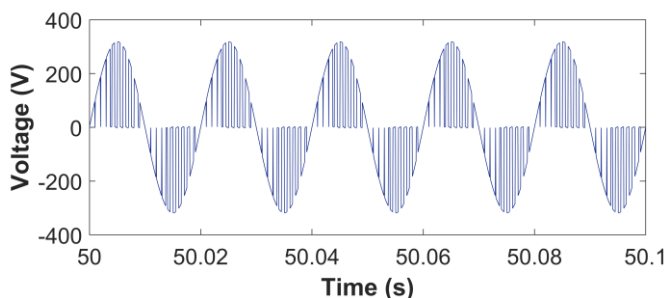


Figure 20. Voltage curve of the motor for 1300 rpm reference speed value.

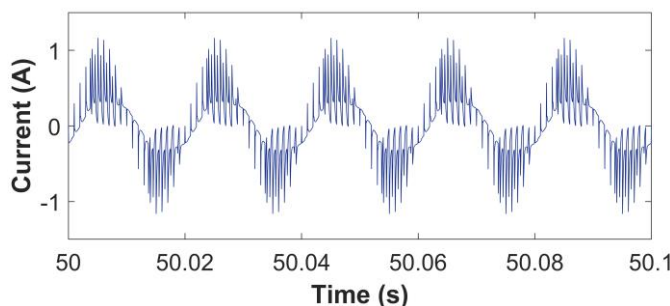


Figure 25. Current curve of the motor for 1400 rpm reference speed value.

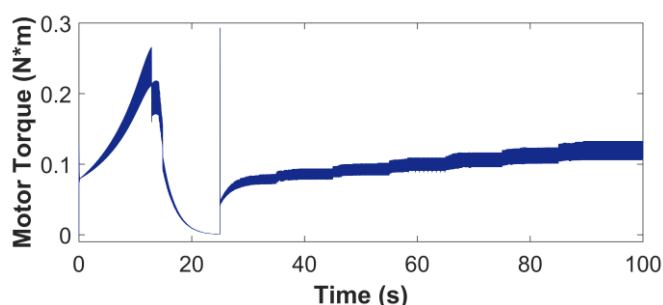


Figure 26. Torque curve produced by the motor for a reference speed of 1400 rpm.

5. CONCLUSION

In this paper, a solution method for the speed control problem of the single-phase induction motors which is one of the biggest problems of these motors is proposed. Thus, it is aimed to increase the usage areas of these motors. The speed control of the motor is achieved by the help of an AC chopper that changes the voltage waveform applied to the motor. A hysteresis band is created for triggering the power electronics elements. For the inputs of the hysteresis band, the torque generated by the motor and the reference signal are used. A saw tooth is also chosen for the reference signal. The PWM signals obtained by comparing the motor torque and reference signal are utilized for triggering the power electronics switches. The speed control of the motor is carried out, however, when a load is connected to the motor shaft, a fall is observed in the speed curve.

A closed loop system is created by using a fuzzy logic controller to prevent the drops in the speed curves. At this stage, the torque input produced by the motor used for the hysteresis band is changed. For the first input of the fuzzy logic controller, the speed error is obtained by the difference between the reference speed value and the motor speed. For the second input, the derivative of the speed error value is taken to obtain the speed error change. The torque values obtained from the output of the fuzzy logic controller and the produced by the motor are summed and used as the new input of the hysteresis band. Thus, power electronics switches are triggered with the new PWM signals obtained. As a result, it is observed that the proposed fuzzy logic speed controller method gives successful results in the closed loop system.

REFERENCES

- [1] A. H. Saçkan, "Asenkron Motorlar," Birsan Yayınevi, 1994.
- [2] J. Holtz, "Speed Estimation and Sensorless Control of Drives," Proc. IEEE Int. Conf. On Ind.Elec.Cont. And Intr. (IECON'93), November 1993, Maui, Book of Proceedings : 649-654 .
- [3] N. Jain, N. H. Funde, N. P. Meshram, S. Shrikant, "Speed Control of Single Phase Induction Motor Using AC Chopper by Asymmetrical PWM Technique," *GRD Journal for Engineering*, vol. 3, no. 10, 2019.
- [4] G. Zigirkas, J. Kalamiros, "Voltage Control of Single-Phase Induction Motors Using Asymmetrical PWM and Fuzzy Logic," *5 th International Conference on Modern Circuits and Systems Technologies*, 2016.
- [5] M. Bouzidi, S. Harrouz, S. Mansori, "Control and Automation of Asynchronous Motor Using Fuzzy Logic," *Algerian Journal of Renewable Energy and Sustainable Development*, vol. 1, no. 2, pp. 12415-12422, 2014.
- [6] O. R. Agyare, A. B. Asiedu-Asante, A. R. Biney, "Fuzzy Logic Based Condition Monitoring of a 3-Phase Induction Motor".
- [7] Z. Mekrini and S. Bri, "Fuzzy Logic Application for Intelligent Control of An Asynchronous Machine," *Indones. J. Electr. Eng. Comput Sci.*, vol. 7, no. 1, p. 61, 2017.

- [8] H. Maghfiroh, J. Slamet Saputro, F. Fahmizal, and M. Ahmad Baballe, "Adaptive Fuzzy-PI for Induction Motor Speed Control," *jfsc*, vol. 1, no.1, pp. 1-5, 2023.
- [9] G. M. Sivasubramanian and M. NArayanamurthy, "Implementation of PWM AC Chopper Controller for Capacitor Run Induction Motor Drive Via Bacterial Foraging Optimization Algorithm," *Int. J. Reconfigurable Embed. Syst. (IJRES)*, vol. 9, no.3, pp. 169-177, 2020.
- [10] R. M. Ariff, D. Hanafi, W. M. Utomo, N. M. Zin, S. Y. Sim, and A. A. Bohari, "Takagi-Sugeno Fuzzy Perpose as Speed Controller in Indirect Field Oriend Control of Induction Motor Drive," *IAES Int. J. Artif. Intell. (IJ-AI)*, vol. 5, no. 4, p.149, 2015.
- [11] M. M. R. Ahmed, M. Soliman, "Speed Control of AC Series Motor Using AC Chopper Voltage Control," *IEEE Electrical Power &Energy Conference*, 2010.
- [12] H. Mohan, M. K. Pathak, and S. K. Dwivedi, "Reactive Power Based Speed Control of Induction Motor Drive using Fuzzy Logic for Industrial Application," in *2020 IEEE International Conference on Power Electronics, Smart Grid and Renewable Energy (PESGRE2020)*, 2020.
- [13] S. El Daoudi, L. Lazrak, N. El Ouanjli, M. Ait Lafkih M, "Sensorless Fuzzy Direct Torque Control of Induction Motor With Sliding Mode Speed Controller," *Computer and Electrical Engineering*, vol. 96, no. 107490, p.107490, 2021.
- [14] T. Muthamizhan, B. Shivaji, M. Aijaz, "Fuzzy Logic Controller Based Multilevel Inverters Integrated Speed Control of Induction Motors," in *2022 3rd International Conference for Emerging Technology(INCET)*, 2022.
- [15] G. Bal, *Özel Elektrik Makinaları*, Seçkin Yayıncılık, 2011.
- [16] S. Ünal, M. Özdemir, S. Sünter, "Voltage and Frequency Control of a Single-Phase Self-Excited Generator," *International Aegean Conference on Electrical Machines and Power Electronics*, Istanbul-Turkey, pp.509-514, May 2004.
- [17] Bashi S.M., Mailah N. F., Cheng W.B., (2008). "Development of a Single Phase AC Controller", *Pertanika J.Sci&Technol*. Vol 16, No.2, pp.119-127, 2008.
- [18] R. R. Duvvuru, T. S. K. Manoj, A. V. S. Reddy, R. R. Duvvuru, C. N. Kumar, and C. R. Reddy, 2021. "Fuzzy Logic Controller Based Three-Phase PWM AC Chopper Fed Induction Motor Drive With HBCC Technique," *International Journal of Electrical Engineering and Technology(IJEET)*, vol. 12, no. 5, 2021.
- [19] N. Çatalbaş, C. Çatalbaş, S. Sunter, "Design and Implementation of a Hysteresis Band Current Controller Three-Phase AC Chopper System," *International Journal of Renewable Energy Research*, June, 2020.
- [20] H. Çelik, H. Kürüm, "Düzenli Örneklemeli Sinüzoidal PWM'in Asenkron Motorun Hız Kontrolündeki Etkileri," *Elektrik-Elektronik-Bilgisayar Mühendisliği 11. Ulusal Kongresi ve Fuarı Bildirileri*, 2005.
- [21] A. Herizi, A. Bouguerra, S. Zeghlache, R. Rouabhi, R. Mahmoudi, H. E. Smaini, 2020. "Type-2 Sugeno Fuzzy Logic Inference System for Speed Control of a Doubly-Fed Induction Motor," in *2020 1st International Conference on Digitization and its Application (ICDA'2020)*, 2020.
- [22] İ. Alışkan, S. Ünsal, "Farklı Çıkarım Yöntemlerine Sahip Bulanık Mantık Denetleyicileri Kullanılarak Kalıcı Mıknatıslı Senkron Motorun Hız Denetimi," *Pamukkale Üniversitesi Mühendislik Bilimleri Dergisi*, 24(2), 185-191, 2018.
- [23] H. Maghfiroh, J. S. Saputro, F. Adriyanto, A. Sujono, R. L. Lambang, 2020. "Performance Evaluation of Fuzzy-PID in Speed Control of Three Phase Induction Motor," *ICIMECE*, 2020.
- [24] M. A. Hannan, J. A. Ali, M. S. H. Lipu, A. Mohamed, P. J. Ker, T. M. I. Mahlia, M. Mansor, A. Hussain, K. M. Muttaqi, Z. Y. Dong , "Role of Optimization Algorithms Based Fuzzy Controller in Achieving Induction Motor Performance Enhancement," *Nature Communications*, vol. 11, no. 1, p. 3792, 2020.
- [25] G. Kamalapur, M. S. Aspalı "Direct Torque Control and Dynamic Performance of Induction Motor Using Fractional Order Fuzzy Logic Controller," *International Journal of Electrical and Computer Engineering(IJECE)*, vol.13, no.4, pp.3805-3816, 2023.

BIOGRAPHIES

Ece Yılmaz received her bachelor's degree in Electrical and Electronics Engineering from Firat University in 2020. She started her master's degree in electrical and electronics engineering at Firat University in 2021. She is currently a graduate student at Firat University, Department of Electrical and Electronics Engineering. His research interests are electric machines and drive systems.

Sencer Ünal born in 1978 in Elazig-Turkey. Received B.Sc., M.Sc. and Ph.D degrees in Electrical Engineering from Firat University (Elazig-Turkey) in 1999, 2002 and 2009, respectively. He is currently Assistant Professor in the Electrical and Electronic Dept. of Firat University. His area of interest is Electrical Machines and Power Electronics.

Mehmet Özdemir born in 1958 in Elazig-Turkey. Received B.Sc., M.Sc. and Ph.D degrees in Electrical Engineering from Firat University (Elazig-Turkey) in 1980, 1984 and 1993, respectively. He is currently Associate Professor in the Electrical and Electronic Dept. of Firat University. His area of interest is Electrical Machines and Drives. He retired in 2024.

Research Article

Effect of Cutting Parameters in Turning of AISI 1015 Steel: Comparison of Dry and MQL Conditions

Bahar Sayin Kul^{1*} ¹Selçuk University, Mechanical Engineering Department, Konya, Turkey. (e-mail: bsayin@selcuk.edu.tr).

ARTICLE INFO

Received: June, 05, 2024

Revised: July, 20, 2024

Accepted: July, 20, 2024

Keywords:

AISI 1015 Steel
Machinability
Turning
MQL

Corresponding author: *Bahar Sayin Kul*

ISSN: 2536-5010 / e-ISSN: 2536-5134

DOI: <https://doi.org/10.36222/ejt.1496244>

ABSTRACT

This study is about turning AISI 1015 steel with coated carbide inserts in dry and MQL environments. In the experimental procedure built according to the full factorial experimental design, cutting parameters such as cutting speed (90,135 m/min), feed rate (0.2, 0.40 mm/rev) and cutting depth (0.1, 0.2 mm) on surface roughness, cutting force and cutting temperature were investigated. The experiments were carried out in two different environmental conditions, aiming to compare the machining performances in both environments and to determine the cutting parameters that make the biggest contribution to each output parameter. The main findings of the study are as follows: In turning operations performed under dry and MQL conditions, the worst surface quality (with surface roughness values of 2.509 μm and 2.114 μm respectively) was obtained at the lowest cutting speed, feed and depth of cut values. Increasing the cutting speed was manifested by the average 20.1% decrease in surface roughness for both environmental conditions. While cutting temperature and cutting force increased as the cutting speed increased at low feed rates, both decreased at high feed rates. Increasing the cutting depth caused an average 40% increase in cutting forces. Moreover, the surface roughness, cutting temperature, and cutting force data obtained under MQL conditions were on average 16.9%, 2%, and 29.8% lower than those obtained under dry conditions, respectively.

1. INTRODUCTION

The machinability is a multifaceted process that is affected by both the composition, microstructure and strength of the material being processed, and operational factors such as cutting speed, feed rate, cutting dept, cutting fluid and cutting tool material. Making the appropriate selection for operational factors is important to avoid consequences such as tool wear and/or breakage, workpiece deterioration, and the process resulting in a poor-quality surface [1-4].

In engineering processes, where the bar is raised with the development of technology, the term quality, which is reduced to surface quality when evaluating the processing of the material, continues to be a critical feature that cannot be compromised.

It is possible to talk about the simultaneous effect of many factors on roughness during processing. While this is the case subjecting different cutting parameters, material and cutting tool combinations, to experimental studies is a necessary procedure to better understand the parameters affecting surface roughness and optimize the process [5-7].

To date, various studies have been carried out on the machinability of many materials, one of which is steel, and academic outputs have been obtained [8-15] can be given as examples of machinability studies carried out in recent years

and these examples can be multiplied. Within the scope of this paper, studies on AISI 1015 steel have been exemplified below and it has aimed to give readers an idea about the place of this material in the literature. Then, studies on the machinability of it were discussed in some more detail. Apay and Gulenc [16] have coated AISI 1015 steel with an alloy welding wire by micro laser, and microstructure of the samples was examined by being evaluated in terms of microhardness and wear tests, SEM and XRD analysis. Gnanamoorthy and Reddy [17] carried out a study on the plain and fretting fatigue of AISI 1015. The study, Makhatha, et al. [18] carried out, the variation on corrosion, hardness and wear properties of laser alloyed Al-Sn dual coatings on AISI 1015 steel were reported. Namdev, et al. [19] developed dual phase steel by inter-critical heat treatment followed by water quenching using AISI 1015 to analyze its mechanical properties such as tensile and hardness behavior and wear properties by comparing that of with other varieties of plain low carbon steel properties. During CNC turning of AISI 1015 steel with cathodic arc evaporation coated TiAlN/WC-C tungsten carbide cutting tool, cutting parameters, namely cutting depth, feed rate, spindle speed, cutting fluid flow rate and number of layers accumulated on the surface, on roughness and flank wear were examined in the study belongs to Moganapriya, et al. [20]. Gökkaya and Nalbant [21] have examined the variation in surface quality using four different

cemented carbide cutting tools in the turning process of AISI 1015 steel. Experiments carried out for 5 different cutting speeds and 2 different feed rates, the most positive effect on surface roughness was obtained with 3-layer coated tool coated outermost with TiN. Increasing the cutting speed and keeping the feed rate low resulted in better surface quality. Sahu, et al. [22] investigated the effects of cutting parameters such as spindle speed, feed rate, cutting depth and air pressure on surface roughness, cutting temperature and metal removal rate during hard machining of AISI 1015 steel using carbide insert in dry and spray impact cooling environment. Moganapriya, et al. [23] evaluated coated carbide inserts for surface roughness and flank wear during turning of AISI 1015 steel and determined optimum levels of five parameters, for which three levels of each were tested. It was concluded that the most optimum combination was the speed of 500 rpm, cutting depth of 1 mm, the feed rate of 0.05 mm/rev, the cutting fluid flow rate at a high level, and the use of a TiAlN/WC-C coated insert.

The main motivation for the preparation of this study is that when the literature is examined, it is seen that studies on turning AISI 1015 steel are limited and there is no sufficient and satisfactory information about the material/process. This situation has revealed the need for a study investigating the effects of machining parameters on turning. Therefore, in the study carried out by turning AISI 1015 steel with a TiAl coated carbide insert under different cutting parameters/levels, it was aimed to investigate the effect of cutting speed, feed rate, cutting depth on the variation in cutting temperature, surface roughness and cutting force. Traditional machining processes, especially those conducted under dry conditions, can lead to high surface roughness, increased cutting forces, and elevated cutting temperatures. These factors not only affect the quality of the machined parts but also lead to increased tool wear and energy consumption. Although dry cutting conditions are considered the cheapest and cleanest process for chip removal, it is necessary to test more environmental methods, due to the difficulty of removing chip under these conditions and the difficulty of controlling the heat occurring during the process. The study aims to explore the potential benefits of using Minimum Quantity Lubrication (MQL) as an alternative to dry machining and to compare machining performances in both environments and identify cutting parameters that make greater contributions to each output parameter compared to others. At the same time, it aims to lay the foundation for future studies on the machinability of AISI 1015 and to contribute to the existing literature.

2. MATERIALS AND METHODS

In this study, AISI 1015 steel with a machining length of 100 mm and a diameter of 70 mm was used as the sample, while TiAl-coated carbide insert was preferred as the cutting edge. Chemical composition of it has presented in Table 1. The machining parameters in the form of cutting speed, feed rate and cutting depth, which were prepared according to the full factorial experimental design and each consisted of two different levels, are detailed in Table 2. Full factorial experimental design is an experimental method used to examine the effects of combinations of multiple factors (independent variables) and all possible levels (values) of each factor [24, 25]. The reason why this design method is preferred is that it ensures that the experimental results are more

comprehensive and reliable since it includes all possible combinations. Machining parameters were selected by examining the studies in the existing literature and according to the hypothesis established in accordance with the purpose of the experiment, taking into account both material properties and the recommendations of the cutting tool company. The schematic view of the experimental setup, in which the entire experimental study was carried out and consisting of elements such as a universal lathe (De Lorenzo S547-8899), AISI 5115 workpiece, TiN coated carbide cutting tool, a type of cutting tool commonly used in high-performance machining applications (CCMT-09T308-304), perthometer (Mahr), InGaAs (Telc) radiation sensors, is presented in Figure 1. Following the experiments carried out under dry conditions, all were repeated in an MQL environment with the lubrication support of oil-based (olive oil) cutting fluid. In the experiments where measurements were repeated 3 times, temperature and force data were also taken. Statistical analysis was applied to see the contribution of the cutting parameters on each of the output factors, such that signal to noise ratio and variance analysis were used for evaluation.

TABLE 1.
CHEMICAL COMPOSITION OF AISI 1015 STEEL [19]

wt. %	% C	% Mn	% P	% S
	0.15	0.3-0.6	0.04	0.05

TABLE 2. Machining parameters for experiments.

Machining Parameters/Levels	Cutting speed (m/min)	Feed rate (mm/dev)
	90-135	0.2-0.4
	Cutting depth (mm)	Regime
	0.1-0.2	Dry-MQL

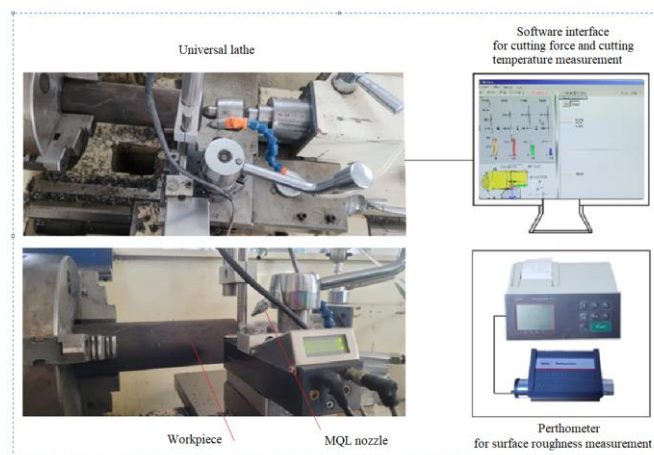


Figure 1. The schematic view of the experimental setup.

3. RESULTS AND DISCUSSION

This study provides an evaluation of the effects of both cutting parameters and cutting environment (regime) on the surface roughness, cutting force and cutting temperature of AISI 1015 steel. Below, the effects of cutting parameters on each output parameter are examined under separate headings.

3.1. Surface Roughness

As can be seen from figure 2, during the turning process performed both in dry conditions and in the MQL environment, the worst surface quality was obtained in the experimental

conditions where the cutting speed, feed rate and cutting depth had the lowest values. In dry conditions, increasing the cutting speed at both cutting depth levels, both at low feed speed and high feed speed, resulted in a decrease in surface roughness. Namely higher cutting speeds (90 m/min) generally produce better surface roughness to lower speeds (60 m/min) under both dry and MQL conditions. The range where this decrease is more pronounced (with a difference of 0.785 (μm)) is where the cutting speed increases from 90 to 135 for low feed rate and cutting dept. It is reported in the literature that cutting speed is an effective parameter on surface roughness and causes changes in the mechanical properties of the workpiece and chip formation [26-28]. It is possible to make similar evaluations in the case of MQL. This can be explained by the decrease in the hardness of the material with increasing cutting speeds [5]. For the same combination of cutting speed, feed rate and cutting depth, in terms of surface roughness, those obtained under dry conditions always had higher values than those obtained under MQL conditions. This difference varies between 6.1 % (for 90/04/02 experiment) and 31.5% for 135/04/02 experiment). Thus, it can be said that MQL cutting environment conditions are better in terms of surface roughness compared to dry conditions.

To sum up, regardless of the feed rate and cutting depth, increasing the cutting speed caused the surface roughness to decrease. Study belongs to Gökkaya and Nalbant [21] is an example of studies in which the relationship between cutting speed and surface roughness is similar to the one here. The decrease in surface roughness as the cutting speed increases is associated with the removal of less material from the sample surface as a result of the increase in the volume of the cutting edge in relation to the amount of sample removed per unit time in the literature [29-31]. In addition, the decrease in surface roughness with the increase of cutting speed can be attributed to the fact that the increase in cutting speed causes the temperature to increase and subsequently causes the workpiece to be easily deformed.

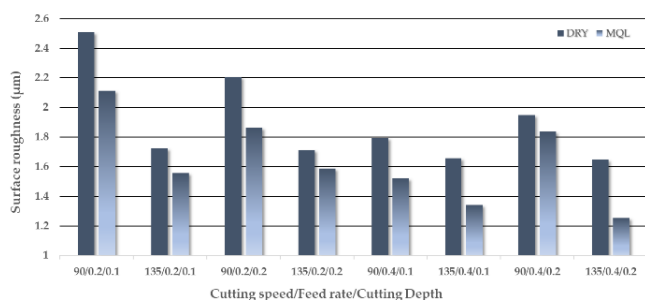


Figure 2. Variation of surface roughness versus cutting parameters.

Env.	Exp.	Surface Roughness (μm)	SR vs CS	Exp.	Surface Roughness (μm)	SR vs CD	Exp.	Surface Roughness (μm)	SR vs FR
DRY	90/0.2/0.1	2.509		90/0.2/0.1	2.509		90/0.2/0.1	2.509	
	135/0.2/0.1	1.724		90/0.2/0.2	2.206		90/0.4/0.1	1.795	
	90/0.2/0.2	2.206		90/0.4/0.1	1.795		90/0.2/0.2	2.206	
	135/0.2/0.2	1.711		90/0.4/0.2	1.948		90/0.4/0.2	1.948	
	90/0.4/0.1	1.795		135/0.2/0.1	1.724		135/0.2/0.1	1.724	
	135/0.4/0.1	1.659		135/0.2/0.2	1.711		135/0.4/0.1	1.659	
MQL	90/0.2/0.2	1.948		135/0.4/0.1	1.659		135/0.2/0.2	1.711	
	135/0.4/0.2	1.65		135/0.4/0.2	1.65		135/0.4/0.2	1.65	
	90/0.2/0.1	2.114		90/0.2/0.1	2.114		90/0.2/0.1	2.114	
	135/0.2/0.1	1.556		90/0.2/0.2	1.863		90/0.4/0.1	1.521	
	90/0.2/0.2	1.863		90/0.4/0.1	1.521		90/0.2/0.2	1.863	
	135/0.2/0.2	1.587		90/0.4/0.2	1.836		90/0.4/0.2	1.836	
MQL	90/0.4/0.1	1.521		135/0.2/0.1	1.556		135/0.2/0.1	1.556	
	135/0.4/0.1	1.343		135/0.2/0.2	1.587		135/0.4/0.1	1.343	
	90/0.4/0.2	1.836		135/0.4/0.1	1.343		135/0.2/0.2	1.587	
135/0.4/0.2	1.255	135/0.4/0.2		1.255	135/0.4/0.2		1.255		
SR: Surface roughness CS: Cutting speed CD: Cutting Depth FR: Feed Rate									

Figure 3. An additional figure for variation of surface roughness.

It cannot be said that the effect of feed rate on surface roughness is affected much by the variation in cutting speed and cutting depth, either in dry conditions or in MQL conditions. This situation is thought to be due to keeping the difference between the levels of the parameters small. In other words, increasing the feed rate reduced the surface roughness in both dry and MQL cases. Reducing the feed rate mentioned as a well-known practice for improving surface roughness makes the results here reasonable [21, 32-36].

Although increasing the cutting depth mostly has a decreasing effect on the surface roughness, it is not possible to make a generalization. When the 90/04/01 experiment is compared with the 90/04/02 experiment in both dry and MQL cases, it is seen that the decreasing trend is disrupted. Under MQL conditions, the same effect is also seen between the 135/02/01 experiment and the 135/02/02 experiment. In other words, the effect of low cutting speed combined with high feed rate and similarly the effect of high cutting speed combined with low feed rate resulted in an increase in surface roughness.

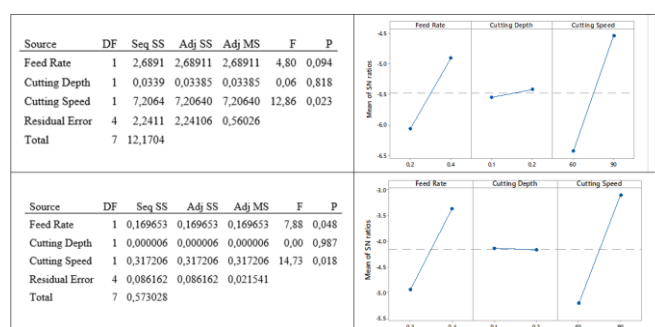


Figure 4. Anova tables and S/N ratios for surface roughness under dry and MQL cases respectively.

The value of $p < 0.05$, which indicates the significance level of each parameter in Figure 4a), shows that cutting speed has a significant effect on surface roughness in dry conditions. In MQL conditions, two parameters, cutting speed and feed rate, have a significant effect on the surface roughness. The order of importance of cutting parameters on surface roughness is as follows; cutting speed > feed rate > cutting depth.

Signal-to-noise ratio symbolizes the ratio of the signal (S) to the background noise factor (N), which are exemplified by ambient temperature and humidity, and are the source of variability in responses [37, 38]. As can be seen from Figure 4 b), the cutting depth has almost no effect on the S/N ratio, while high levels of cutting speed and feed rate serve to reduce surface roughness. These results are also compatible with ANOVA tables.

3.2. Cutting Temperature

In Figure 5 and Figure 6, where the effect of cutting parameters on the cutting temperature is seen, a trend is observed between the experiments conducted in dry and MQL environments for the same cutting parameters/levels, where the cutting temperature obtained in the MQL condition is lower than that obtained in the other. This decrease is approximately 2% on average and the inherent cooling effect of oil-based lubrication.

While the increase in cutting speed causes an effect that increases the cutting temperature at low feed rates, the opposite trend is observed at high feed rates. In experiments carried out under MQL conditions, increasing the shear rate has a relatively similar effect to that in dry conditions. Again,

increasing the cutting depth decreased the cutting temperature at low feed speeds and caused it to increase at high feed speeds. This situation is similar for MQL conditions, ignoring the change between 90/04/01 and 90/04/02. The increasing effect of feed rate generally increased the cutting temperature regardless of cutting speed and cutting depth.

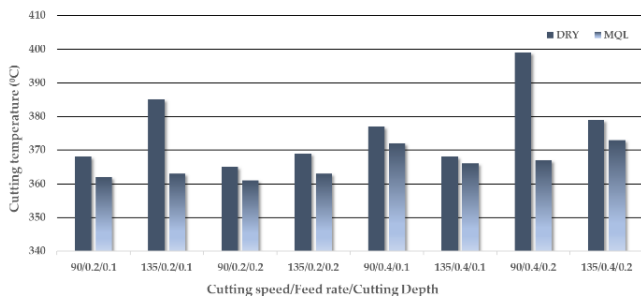


Figure 5. Variation of cutting temperature versus cutting parameters.

Env.	Exp.	Cutting Temperature (°C)	CT vs CS	Exp.	Cutting Temperature (°C)	CT vs CD	Exp.	Cutting Temperature (°C)	CT vs FR
DRY	90/0.2/0.1	368	↗	90/0.2/0.1	368	↗	90/0.2/0.1	368	↗
	135/0.2/0.1	385	↗	90/0.2/0.2	365	↘	90/0.4/0.1	377	↗
	90/0.2/0.2	365	↘	90/0.4/0.1	377	↗	90/0.2/0.2	365	↘
	135/0.2/0.2	369	↗	90/0.4/0.2	399	↗	90/0.4/0.2	399	↗
	90/0.4/0.1	377	↗	135/0.2/0.1	385	↗	135/0.2/0.1	385	↗
	135/0.4/0.1	368	↘	135/0.2/0.2	369	↗	135/0.4/0.1	368	↘
	90/0.4/0.2	399	↗	135/0.4/0.1	368	↘	135/0.2/0.2	369	↗
	135/0.4/0.2	379	↘	135/0.4/0.2	379	↘	135/0.4/0.2	379	↘
MQL	90/0.2/0.1	362	↗	90/0.2/0.1	362	↗	90/0.2/0.1	362	↗
	135/0.2/0.1	363	↗	90/0.2/0.2	361	↘	90/0.4/0.1	372	↗
	90/0.2/0.2	361	↘	90/0.4/0.1	372	↗	90/0.2/0.2	361	↘
	135/0.2/0.2	362	↗	90/0.4/0.2	367	↗	90/0.4/0.2	367	↗
	90/0.4/0.1	372	↗	135/0.2/0.1	363	↘	135/0.2/0.1	363	↘
	135/0.4/0.1	366	↘	135/0.2/0.2	362	↘	135/0.4/0.1	366	↘
	90/0.4/0.2	367	↗	135/0.4/0.1	366	↘	135/0.2/0.2	362	↘
	135/0.4/0.2	373	↗	135/0.4/0.2	373	↗	135/0.4/0.2	373	↗

CT:Cutting temperature CS:Cutting speed CD: Cutting Depth FR:Feed Rate

Figure 6. An additional figure for variation of cutting temperature.

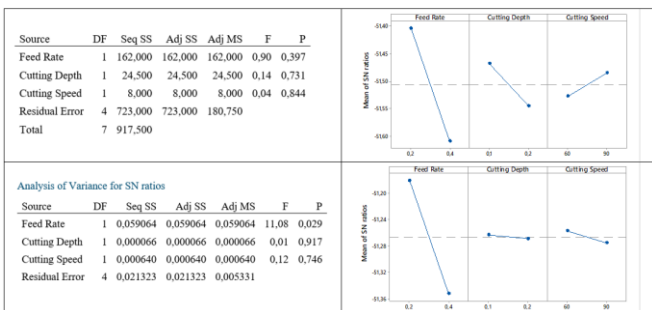


Figure 7. Anova tables and S/N ratios for cutting temperature under dry and MQL cases respectively.

Considering the statistical evaluation for cutting temperature given in Figure 7, the fact that p values of all variables are greater than 0.05 in dry conditions shows that the effect of cutting parameters on cutting temperature is not statistically significant. In the MQL condition, only the feed rate has a significant effect on the cutting temperature. This situation reveals the necessity of making new experimental designs by changing the parameter levels and perhaps even the parameters. It can also be seen from the graph that the lower feed rate, corresponding to the higher value of the S/N ratio, serves to minimizing the cutting temperature.

3.3. Cutting Forces

Low cutting forces are a desired condition for high machining performance and efficiency [23]. Figures 8 and 9 show how cutting forces, another output parameter, are

affected by variation in cutting conditions. The cutting force had its lowest value at 50 N in dry conditions and 44 N in MQL conditions for the lowest levels of all cutting parameters. The cutting force peaked at 156 N in dry conditions and 120 N in MQL conditions with low cutting speed and high feed rate and cutting depth. For the same combinations of cutting speed, feed rate and cutting depth, there is an average difference of 29.8% between the test results under dry conditions and those under MQL conditions. The difference in force data obtained in experiments performed at a high level of feed rate is more evident than in those performed at a low level of feed rate.

At low feed rates and for both levels of cutting depth, the increase in cutting speed resulted in an increase in cutting force. This trend is like this for both dry and MQL conditions.

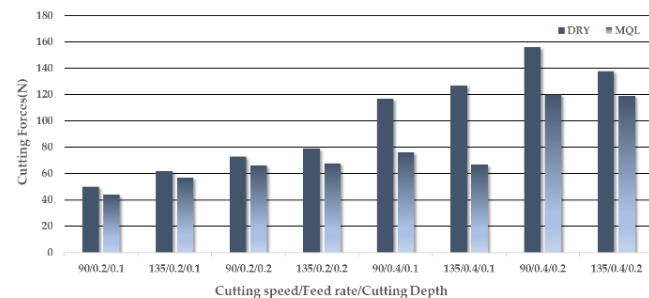


Figure 8. Variation of cutting temperature versus cutting forces.

Env.	Exp.	Cutting Forces (N)	CF vs CS	Exp.	Cutting Forces (N)	CF vs CD	Exp.	Cutting Forces (N)	CF vs FR
DRY	90/0.2/0.1	50	↗	90/0.2/0.1	50	↗	90/0.2/0.1	50	↗
	135/0.2/0.1	62	↗	90/0.2/0.2	73	↗	90/0.4/0.1	117	↗
	90/0.2/0.2	73	↗	90/0.4/0.1	117	↗	90/0.2/0.2	73	↗
	135/0.2/0.2	79	↗	90/0.4/0.2	156	↗	90/0.4/0.2	156	↗
	90/0.4/0.1	117	↗	135/0.2/0.1	62	↗	135/0.2/0.1	62	↗
	135/0.4/0.1	127	↗	135/0.2/0.2	79	↗	135/0.4/0.1	127	↗
	90/0.4/0.2	156	↗	135/0.4/0.1	127	↗	135/0.2/0.2	79	↗
	135/0.4/0.2	138	↗	135/0.4/0.2	138	↗	135/0.4/0.2	138	↗
MQL	90/0.2/0.1	44	↗	90/0.2/0.1	44	↗	90/0.2/0.1	44	↗
	135/0.2/0.1	57	↗	90/0.2/0.2	66	↗	90/0.4/0.1	76	↗
	90/0.2/0.2	66	↗	90/0.4/0.1	76	↗	90/0.2/0.2	66	↗
	135/0.2/0.2	68	↗	90/0.4/0.2	120	↗	90/0.4/0.2	120	↗
	90/0.4/0.1	76	↗	135/0.2/0.1	57	↗	135/0.2/0.1	57	↗
	135/0.4/0.1	67	↗	135/0.2/0.2	68	↗	135/0.4/0.1	67	↗
	90/0.4/0.2	120	↗	135/0.4/0.1	67	↗	135/0.2/0.2	68	↗
	135/0.4/0.2	119	↗	135/0.4/0.2	119	↗	135/0.4/0.2	119	↗

Figure 9. An additional figure for variation of cutting forces

Among the combinations where high feed rate is combined with high cutting depth, the effect of increasing cutting speed on reducing cutting force stands out. It is seen that increasing the cutting depth increases cutting forces, regardless of changes in cutting speed and feed rate. This effect is similar and stable for both cutting media. Again, it is seen that the increase in feed rate increases the cutting forces, regardless of the cutting speed and cutting depth. Although this increase seems to be independent of the cutting conditions in terms of quality, the difference is evident in terms of quantity, so that, as stated at the beginning, an average difference of 1 in 3 is observed between the cutting forces by assuming the other conditions are constant and changing the cutting environment only.

The ANOVA table in Figure 10 shows that feed rate and cutting depth are significant factors affecting the S/N ratio, with feed rate being the most significant. Cutting speed, on the other hand, does not significantly affect the S/N ratio in both cases. This conclusion is supported by the high F-statistics and low p-values for feed Rate and cutting depth, indicating their strong influence on the response variable. Considering the S/N ratios, it was observed that lower cutting forces occurred when the sample was turned with a low feed rate and low cutting depth.

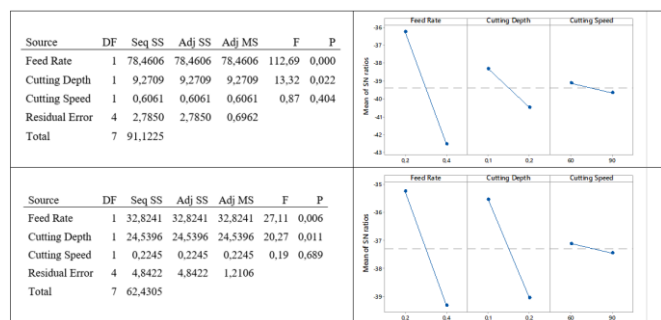


Figure 10. Anova tables and S/N ratios for cutting force under dry and MQL cases respectively.

4. CONCLUSION

This study, which experimentally demonstrates the positive effects of the minimum quantity lubrication (MQL) method on performance compared to dry cutting conditions, serves the purpose of using more environmentally friendly and efficient methods in manufacturing processes. The findings of this study, which investigated the relationship between cutting parameters and output parameters such as surface roughness, cutting temperature and cutting force during the machining of AISI 1015 steels, are summarized below.

Surface roughness;

- In turning operations performed under dry and MQL conditions, the worst surface quality was obtained at the lowest cutting speed, feed rate and depth of cut values.
- As the cutting speed increased, the surface roughness decreased in both conditions.
- Surface roughness values obtained under MQL conditions were between 6.1% and 31.5% lower than those obtained under dry conditions.
- According to ANOVA analysis, cutting speed has a significant effect on surface roughness in dry conditions, and both cutting speed and feed rate have a significant effect on surface roughness in MQL conditions.

Cutting Temperature;

- Cutting temperature was on average 2% lower under MQL conditions than under dry conditions.
- As the cutting speed increased at low feed rates, the cutting temperature increased, and at high feed rates it decreased.
- According to ANOVA analysis, cutting parameters have no significant effect on cutting temperature in dry conditions, while only feed rate has a significant effect in MQL conditions.
- When the signal-to-noise ratio was evaluated, it was seen that low feed rate minimized the cutting temperature.

Cutting Forces;

- Cutting forces were on average 29.8% higher in dry conditions than in MQL conditions.
- As the cutting speed increased at low feed rates, the cutting force increased, and at high feed rates it decreased.
- According to ANOVA analysis, feed rate and depth of cut have a significant effect on cutting forces, while cutting speed has no significant effect.

- When signal-to-noise was evaluated, it was seen that low feed rate and depth of cut resulted in lower cutting forces.
- This study, which experimentally demonstrates the positive effects of the minimum quantity lubrication (MQL) method on performance compared to dry cutting conditions, serves the purpose of using more environmentally friendly and efficient methods in manufacturing processes.

In line with these findings, the following recommendations can be made for future studies: In addition to diversifying the input parameters (such as cooled/uncooled machining conditions) or output parameters (such as tool wear, vibration), examining the parameters in a wider range to detail the simultaneous effects of the parameters can help obtain more comprehensive results. The environmental impacts and cost effectiveness of the MQL method can be evaluated in terms of sustainable production, and the machinability of the material can also be tested in different cutting environments.

REFERENCES

- [1] R. Binali, M. Kuntoğlu, D. Y. Pimenov, Ü. A. Usca, M. K. Gupta, and M. E. Korkmaz, "Advance monitoring of hole machining operations via intelligent measurement systems: A critical review and future trends," *Measurement*, vol. 201, p. 111757, 2022.
- [2] R. Binali, S. Yaldız, and S. Neşeli, "Investigation of power consumption in the machining of S960QL steel by finite elements method," *European Journal of Technique (EJT)*, vol. 12, no. 1, pp. 43-48, 2022.
- [3] M. Günay, M. E. Korkmaz, and N. Yaşar, "Performance analysis of coated carbide tool in turning of Nimonic 80A superalloy under different cutting environments," *Journal of Manufacturing Processes*, vol. 56, pp. 678-687, 2020.
- [4] M. K. Gupta, P. Niesłony, M. Sarıkaya, M. E. Korkmaz, M. Kuntoğlu, and G. Królczyk, "Studies on geometrical features of tool wear and other important machining characteristics in sustainable turning of aluminium alloys," *International Journal of Precision Engineering and Manufacturing-Green Technology*, vol. 10, no. 4, pp. 943-957, 2023.
- [5] M. Kuntoğlu, A. Aslan, D. Y. Pimenov, K. Giasin, T. Mikolajczyk, and S. Sharma, "Modeling of cutting parameters and tool geometry for multi-criteria optimization of surface roughness and vibration via response surface methodology in turning of AISI 5140 steel," *Materials*, vol. 13, no. 19, p. 4242, 2020.
- [6] H. Yurtkuran, M. E. Korkmaz, and M. Günay, "Modelling and optimization of the surface roughness in high speed hard turning with coated and uncoated CBN insert," *Gazi University Journal of Science*, vol. 29, no. 4, pp. 987-995, 2016.
- [7] R. Binali, H. Demirpolat, M. Kuntoğlu, and E. Salur, "Different aspects of machinability in turning of AISI 304 stainless steel: a sustainable approach with MQL technology," *Metals*, vol. 13, no. 6, p. 1088, 2023.
- [8] S. Kolomy *et al.*, "Machinability of extruded H13 tool steel: Effect of cutting parameters on cutting forces, surface roughness, microstructure, and residual stresses," *Alexandria Engineering Journal*, vol. 99, pp. 394-407, 2024.
- [9] S. Hassan, S. A. Khan, R. Naveed, S. Anwar, and M. U. Farooq, "Finish dry turning of DC53 tool steel via modified carbide inserts: a study of machining dynamics," *The International Journal of Advanced Manufacturing Technology*, pp. 1-19, 2024.
- [10] O. G. Ehibor, M. S. Abolarin, M. B. Ndaliman, and A. A. Abdullahi, "Evaluation and Multi-Objective Optimisation of Cutting Parameters in Turning of AISI 1020 Mild Steel using Formulated Cutting Fluid," *ABUAD Journal of Engineering Research and Development*, vol. 7, no. 1, pp. 131-143, 2024.
- [11] A. Das, A. Kumar, S. Padhan, S. R. Das, M. P. Satpathy, and S. K. Patel, "Hard turning of AISI H10 steel using AlTiN and AlTiSiN coated carbide tools: comparative machining performance evaluation and economic assessment," *Journal of the Brazilian Society of Mechanical Sciences and Engineering*, vol. 46, no. 5, pp. 1-34, 2024.
- [12] M. E. Korkmaz *et al.*, "Prediction and classification of tool wear and its state in sustainable machining of Bohler steel with different machine learning models," *Measurement*, vol. 223, p. 113825, 2023.
- [13] M. Kuntoğlu, "Measurement and analysis of sustainable indicators in machining of Armox 500T armor steel," *Proceedings of the Institution*

- of Mechanical Engineers, Part C: Journal of Mechanical Engineering Science, vol. 236, no. 13, pp. 7330-7349, 2022.
- [14] R. Binali, "Experimental and machine learning comparison for measurement the machinability of nickel based alloy in pursuit of sustainability," *Measurement*, vol. 236, p. 115142, 2024.
 - [15] M. Gupta *et al.*, "Potential use of cryogenic cooling for improving the tribological and tool wear characteristics while machining aluminum alloys," *Tribology International*, vol. 183, p. 108434, 2023.
 - [16] S. Apay and B. Gulenc, "Wear properties of AISI 1015 steel coated with Stellite 6 by microlaser welding," *Materials & Design*, vol. 55, pp. 1-8, 2014.
 - [17] R. Gnanamoorthy and R. R. Reddy, "Fretting fatigue in AISI 1015 steel," *Bulletin of Materials Science*, vol. 25, pp. 109-114, 2002.
 - [18] M. Makhatha, O. Fatoba, and E. Akinlabi, "Effects of rapid solidification on the microstructure and surface analyses of laser-deposited Al-Sn coatings on AISI 1015 steel," *The International Journal of Advanced Manufacturing Technology*, vol. 94, pp. 773-787, 2018.
 - [19] A. Namdev, A. Telang, R. Purohit, and A. Kumar, "The effect of inter critical heat treatment on mechanical and wear properties of AISI 1015 steel," *Advances in Materials and Processing Technologies*, vol. 8, no. sup2, pp. 434-444, 2022.
 - [20] C. Moganapriya, R. Rajasekar, K. Ponappa, P. S. Kumar, S. K. Pal, and J. S. Kumar, "Effect of coating on tool inserts and cutting fluid flow rate on the machining performance of AISI 1015 steel," *Materials Testing*, vol. 60, no. 12, pp. 1202-1208, 2018.
 - [21] H. Gökkaya and M. Nalbant, "The effects of cutting tool coating on the surface roughness of AISI 1015 steel depending on cutting parameters," *Turkish J. Eng. Env. Sci.*, vol. 30, pp. 307-316, 2006.
 - [22] S. K. Sahu, P. C. Mishra, K. Orra, and A. K. Sahoo, "Performance assessment in hard turning of AISI 1015 steel under spray impingement cooling and dry environment," *Proceedings of the Institution of Mechanical Engineers, Part B: Journal of Engineering Manufacture*, vol. 229, no. 2, pp. 251-265, 2015.
 - [23] C. Moganapriya, R. Rajasekar, P. Sathish Kumar, T. Mohanraj, V. Gobinath, and J. Saravanakumar, "Achieving machining effectiveness for AISI 1015 structural steel through coated inserts and grey-fuzzy coupled Taguchi optimization approach," *Structural and Multidisciplinary Optimization*, vol. 63, pp. 1169-1186, 2021.
 - [24] J. Antony, "6 - Full factorial designs," in *Design of Experiments for Engineers and Scientists*, J. Antony Ed. Oxford: Butterworth-Heinemann, 2003, pp. 54-72.
 - [25] R. Binali, S. Yaldiz, and S. Neşeli, "Finite element analysis and statistical investigation of S960ql structure steel machinability with milling method," *Journal of the Brazilian Society of Mechanical Sciences and Engineering*, vol. 46, no. 5, p. 260, 2024.
 - [26] M. Mia *et al.*, "Taguchi S/N based optimization of machining parameters for surface roughness, tool wear and material removal rate in hard turning under MQL cutting condition," *Measurement*, vol. 122, pp. 380-391, 2018.
 - [27] M. Kuntoglu, "Machining induced tribological investigations in sustainable milling of Hardox 500 steel: A new approach of measurement science," *Measurement*, vol. 201, p. 111715, 2022.
 - [28] M. Kuntoglu, M. K. Gupta, A. Aslan, E. Salur, and A. Garcia-Collado, "Influence of tool hardness on tool wear, surface roughness and acoustic emissions during turning of AISI 1050," *Surface Topography: Metrology and Properties*, vol. 10, no. 1, p. 015016, 2022.
 - [29] S. H. Musavi, M. Sepehriki, B. Davoodi, and S. A. Niknam, "Performance analysis of developed micro-textured cutting tool in machining aluminum alloy 7075-T6: assessment of tool wear and surface roughness," *The International Journal of Advanced Manufacturing Technology*, vol. 119, no. 5, pp. 3343-3362, 2022/03/01 2022, doi: 10.1007/s00170-021-08349-9.
 - [30] İ. Asiltürk, M. Kuntoglu, R. Binali, H. Akkuş, and E. Salur, "A comprehensive analysis of surface roughness, vibration, and acoustic emissions based on machine learning during hard turning of AISI 4140 steel," *Metals*, vol. 13, no. 2, p. 437, 2023.
 - [31] M. Uzun, Ü. A. Usca, M. Kuntoglu, and M. K. Gupta, "Influence of tool path strategies on machining time, tool wear, and surface roughness during milling of AISI X210Cr12 steel," *The International Journal of Advanced Manufacturing Technology*, vol. 119, no. 3, pp. 2709-2720, 2022.
 - [32] H. Demirpolat, R. Binali, A. D. Patange, S. S. Pardeshi, and S. Gnanasekaran, "Comparison of tool wear, surface roughness, cutting forces, tool tip temperature, and chip shape during sustainable turning of bearing steel," *Materials*, vol. 16, no. 12, p. 4408, 2023.
 - [33] S. Şap, Ü. A. Usca, M. Uzun, M. Kuntoglu, and E. Salur, "Performance evaluation of AlTiN coated carbide tools during machining of ceramic reinforced Cu-based hybrid composites under cryogenic, pure-minimum quantity lubrication and dry regimes," *Journal of Composite Materials*, vol. 56, no. 22, pp. 3401-3421, 2022.
 - [34] R. Binali, A. D. Patange, M. Kuntoglu, T. Mikolajczyk, and E. Salur, "Energy saving by parametric optimization and advanced lubri-cooling techniques in the machining of composites and superalloys: A systematic review," *Energies*, vol. 15, no. 21, p. 8313, 2022.
 - [35] Ü. A. Usca, S. Şap, and M. Uzun, "Evaluation of machinability of Cu matrix composite materials by computer numerical control milling under cryogenic LN2 and minimum quantity lubrication," *Journal of Materials Engineering and Performance*, vol. 32, no. 5, pp. 2417-2431, 2023.
 - [36] N. S. Ross, M. Ganesh, D. Srinivasan, M. K. Gupta, M. E. Korkmaz, and J. Krolczyk, "Role of sustainable cooling/lubrication conditions in improving the tribological and machining characteristics of Monel-400 alloy," *Tribology International*, vol. 176, p. 107880, 2022.
 - [37] R. Binali, "Parametric optimization of cutting force and temperature in finite element milling of AISI P20 steel," *J. Mater. Mechatron. A*, vol. 4, pp. 244-256, 2023.
 - [38] S. Neşeli, S. Yaldiz, and E. Türkes, "Optimization of tool geometry parameters for turning operations based on the response surface methodology," *Measurement*, vol. 44, no. 3, pp. 580-587, 2011.

BIOGRAPHIES

Bahar Sayın Kul obtained his BSc degree in Atatürk University, Mathematics / Mechanical Engineering Department in 2010/2012. In 2014 and 2020, she received her Master's and PhD degrees, respectively, from Selçuk University, Institute of Science, Department of Mechanical Engineering. Commencing her academic journey as a research assistant in 2012, she now holds the position of assistant professor in the Mechanical Engineering Department at the Faculty of Technology, Selçuk University.

Research Article

The Effect Of Thin Film CrC Coating On Microstructure And Microhardness Properties Of Manganese Steel Surface

Musa Kilic^{1*} ^{1*}Batman University, Metallurgy and Materials Engineering Department, Batman, Turkey. (e-mail: musa.kilic@batman.edu.tr).

ARTICLE INFO

Received: July., 08. 2024

Revised: Sep., 03. 2024

Accepted: Sep. 03. 2024

Keywords:

CrC (Chromium Carbide)

TRD (Thermo Reactive Diffusion)

Microstructure

Microhardness

Coating

Corresponding author: *Name Surname*

ISSN: 2536-5010 / e-ISSN: 2536-5134

DOI: <https://doi.org/10.36222/ejt.1512398>

ABSTRACT

In this study, the microstructure and microhardness properties of manganese steel coated with chromium carbide (CrC) using Thermo Reactive Diffusion (TRD) method at 900°C and 1100°C for 4 hours were investigated. The surface morphology of the coating was characterized by scanning electron microscopy (SEM), elemental distribution, X-ray spectroscopy (EDS). Microhardness properties were determined using the Vickers method. Microstructural properties and microhardness results were characterized. The microstructure results showed that the coating process at 1100°C was metallurgically more uniform. The minimum coating thickness was 14.95 μm at 900°C and the maximum thickness was 24.1 μm at 1100°C. In EDS measurements, while CrC was dense in the coating region, Fe density increased towards the substrate. In the microhardness measurements, the highest value was measured as 2371 HV0.5 in the sample coated at 1100°C. Based on these results, it is thought that CrC coating forms a better coating layer especially at high temperatures.

1. INTRODUCTION

Especially in the machinery and manufacturing industry, metal parts are faced with negativities such as wear and corrosion depending on the environment in which they are used. One method of extending the service life of the parts is the improvements to be made on the surface. These improvements on the surface are applied to improve one or more properties such as mechanical and chemical properties such as hardness, fatigue, wear and corrosion [1]. Under these conditions, various surface coating methods have been developed to provide the desired surface performance of the materials [2]. Laser, TIG (Tungsten Inert Gas), PAW (Plasma Arc Welding), HVOF (high-velocity oxygen fuel), plasma spray, CVD (Chemical Vapor Deposition) methods are frequently used by researchers in coating studies [3-7]. Among these methods, especially Laser and CVD methods have limited their use due to their expensive equipment and special environment requirements. In the TRD method process, the coating process is more convenient, cost-effective and suitable for industrial use compared to other methods [8]. Coatings containing VC, NbC and CrC in thicknesses of 1-15 μm , created on the surface with TRD, provide surfaces with high hardness and good wear resistance [9-10].

In previous applications, it was determined that the amount of coating attached to the surface increases with increasing temperature [11].

It has been stated by the authors that increasing the coating time and temperature increased the coating thickness by 311.40% [12].

However, an important point in this method is that the C content of the steel-based substrate to be coated must be at least 0.3% or higher for the TRD process to take place [13].

In this study, the surface of manganese steel was coated with CrC by TRD method. Microstructure characterization was performed after coating. Microhardness measurements of the coating layer were made and the results were characterized by microstructure.

2. MATERIAL AND METHOD

Diffusion thin film coating of manganese steel surface with CrC using TRD method. Manganese steel (%C: 1.375, %P: 0.047, %Si: 0.356, %S: 0.005, %Mo: 0.261, %Ni: 0.104, %Cu: 0.110, %V: 0.047, %Mn: 17.590, %Al: 0.013, %Cr: 0.977, %B: 0.002 and Fe) were cut to 12x12mm. The surface was polished with 1200 mesh SiC sandpaper before coating. The polished samples were cleaned from dirt and impurities on the surface in an ethanol bath. 45%CrC 45%Al₂O₃ and 10% NH₄Cl were

used as coating powder. Al_2O_3 as inert filler and NH_4Cl as activator were used to prevent the powders from sintering with each other during the coating process. Al_2O_3 was used as plastering material before the coating powders into the crucible. After the plastering process was completed, the mixture powder was poured into the crucible and then the samples were buried in the mixture powder. After placing the samples in the crucible, the crucible was tightly closed and the outer wall was plastered with heat resistant paste. The process steps are shown in Figure 1.



Figure 1. Processing steps

The crucibles were placed in the oven at 900°C and 1100°C and kept for 4 hours. After the completion of the process, the crucibles were removed from the oven and cooled in water. After cooling, the scale on the surface of the coating material was removed. The coating samples were subjected to metallographic processes for optical microscope, SEM and EDS analysis. Coating surfaces were rough polished with 400-1200 mesh SiC abrasives and final polishing was carried out with a fine polisher. After polishing, the prepared 4% nital etchant was dipped. After the etching process was completed, the coating microstructure and elemental distribution were examined by optical microstructure with an image system consisting of a Nikon Eclipse MA 100 type light microscope mounted with a Clemex type digital camera, SEM and EDS examinations were performed using SEM JEOL JSM-5600 device. Microhardness measurements were performed using Future Tech FM-700 model digital hardness tester.

3. RESULT AND DISCUSSION

3.1. Microstructure

The optical microstructures of CrC coating on manganese steel surface at 900°C and 1100°C for 4 hours are shown in

Figure 2. In Figure 2a and 1b optical images of the coating at 900°C , there is a clear contrast difference between the coating and the substrate. The veneer layer is lighter while the substrate is darker. The veneer layer is indented and protruding in tooth form. There is a homogeneous bond between the veneer and the substrate. No pores and discontinuities were observed. The minimum coating thickness was $14.96\mu\text{m}$ and the maximum was $20.72\mu\text{m}$. Figure 2 (2a,2b) coating made at 1100°C was homogeneous and non-porous. There is a distinct color difference between the veneer and the substrate. The plating layer is lighter while the substrate is darker. The reason for the marked color difference between the coating layer and the substrate at the interface is attributed to the ability of iron in the matrix to dissolve chromium [14]. The lowest coating thickness was $22.39\mu\text{m}$ and the highest was $24.1\mu\text{m}$. When the coating thicknesses were compared, the highest thickness value was obtained in the sample made at 1100°C . It was determined that the coating temperature has a significant effect on the thickness. In the coating studies carried out by different researchers with TRD method, it was observed that the coating thickness increased with increasing temperature [15].

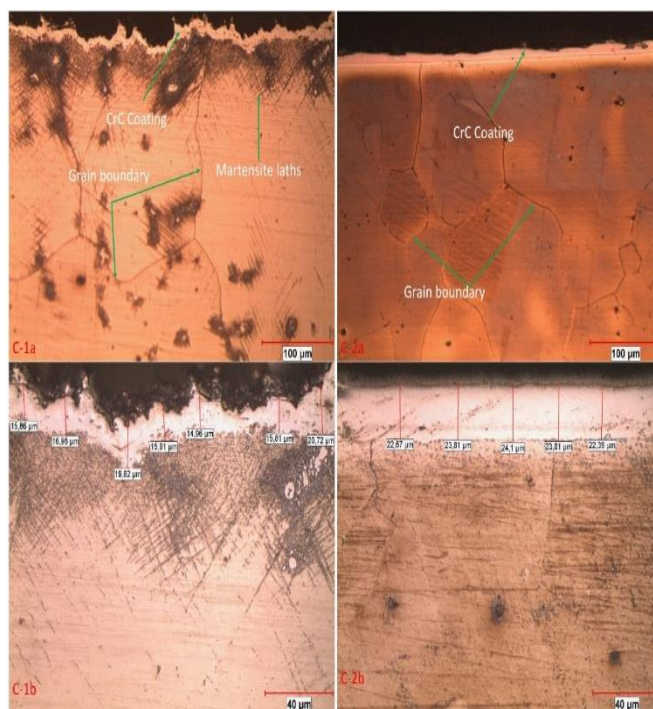


Figure 2. Optical microstructure image of CrC (1a, b) coating performed at 900°C for 4 hours and CrC (2a, b) coating performed at 1100°C for 4 hours

Figure 3 shows the SEM-EDS images and results of the sample coated at 900°C . There is a homogeneous bonding between the coating and the substrate. The coating layer is dispersedly bonded to the substrate. The upper part of the coating layer looks like a cloud. As you go towards the substrate, slats similar to martensite slats are formed. When the EDS results were evaluated, it was determined that the ratio of carbon and chromium decreased and iron increased as you move towards the bottom layer of the coating. At the 1st point, the network was analyzed as 11.93% C, 61.15 Cr, 26.95 Fe, at the 2nd point as 27.88% C, 46.74 Cr, 25.38 Fe, and at the 3rd point as 9.48% C, 8.49 Cr, 82.04 Fe. When the mapping results of the coating sample at 900°C are evaluated in Figure 4, it is observed that the color concentration of C and Cr decreases from the coating to the substrate while Fe increases.

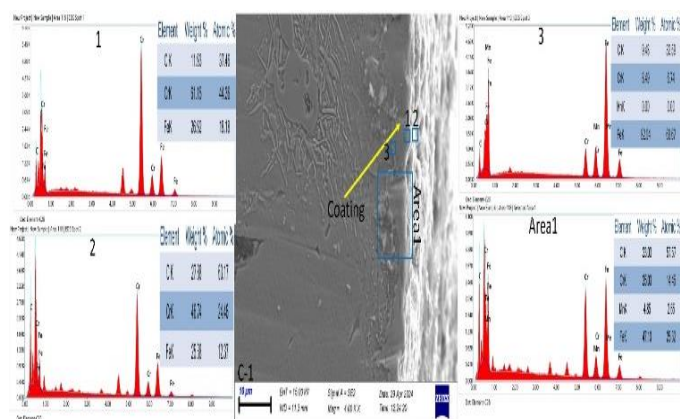


Figure 4. SEM-EDS images of CrC coating performed at 900 °C for 4 hours

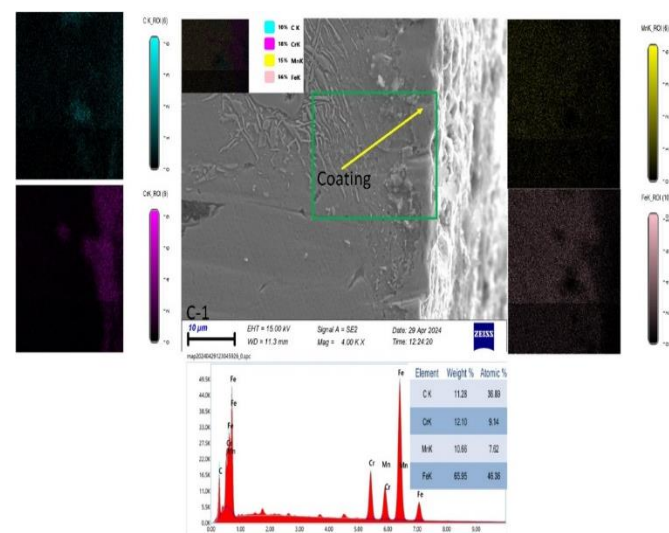


Figure 3 Mapping image of CrC coating performed at 900 °C for 4 hours

these compounds. Depending on the values in EDS analysis, he stated that it may indicate CrxCy type carbides [19].

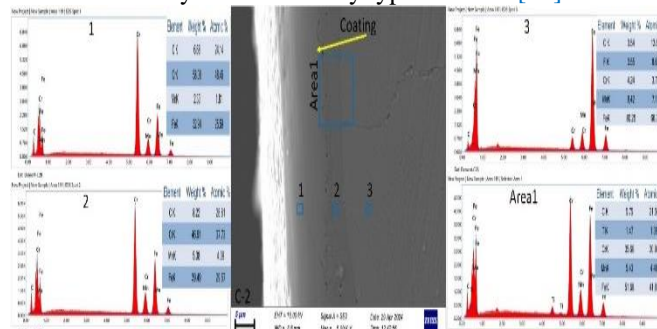


Figure 5. SEM-EDS images of CrC coating performed at 1100 °C for 4 hours

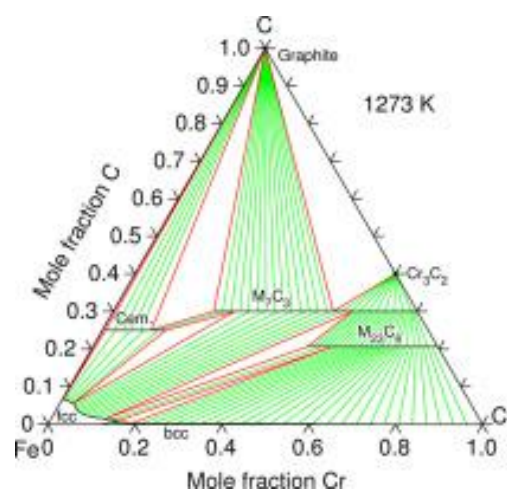


Figure 6. Fe-Cr-C triple phase diagram [20].

3.2. Microhardness

The hardness change table and graph of the coated samples depending on the process temperature are given in Figure 7. In both samples, it is seen that the hardness increases significantly as you go from the coating to the substrate. The lowest hardness value measured at 900°C was 673 HV0.5 in the substrate and the highest value was 1823 HV0.5 in the coating layer. In the sample coated at 1100°C, the lowest hardness value was measured as 789 HV0.5 in the substrate, while the hardness value reached 2371 HV0.5 in the coating layer. The hardness value increased about 2.5 times in the coating layer compared to the substrate. In addition, a change in hardness measurement values with temperature change was also determined in the light of the data obtained. Based on these results, it can be concluded that the temperature-dependent diffusion in the TRD method is better and leads to the formation of harder carbide phases. Najari et al. investigated the possibility of chromium carbide layer formation on the surface of AISI W1 cold work tool steel by TRD method. They successfully obtained compact, adhesive, uniform and crack-free chromium carbide coatings ranging in thickness from 5.14 to 18.06 μm , mainly composed of Cr_7C_3 , Cr_{23}C_6 and Cr_3C_2 on the substrate at 900°C and 1000°C. The hardness of the coatings was in the range of 771 to 1600 HV, depending on the process conditions [21]. Ganji et al. used carbide coatings to extend the life of dies used for hot and cold forging, extrusion and powder metallurgy. They stated that a hardness value of

1782 HV was obtained in the chromium carbide layer after the process [22]. When compared with the results we obtained in the light of the literature, similarly high hardness measurements were obtained in the coating layer compared to the substrate.

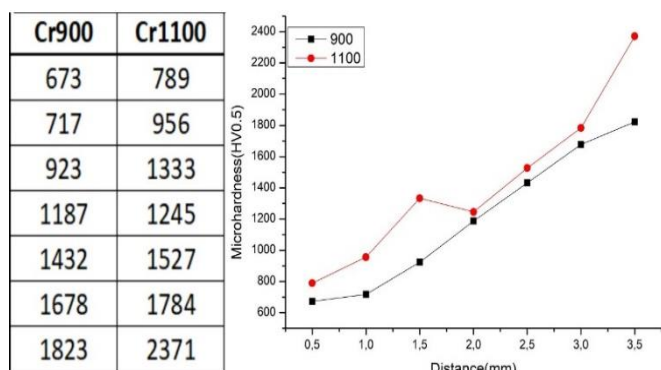


Figure 7. Hardness table and graphic table of microhardness values of the coating

4. CONCLUSION

The manganese steel surface was coated with CrC using the TRD method. The following results were obtained after microstructure analysis and hardness measurements after the coating process.

1. In the microstructure results, the coating process at 1100°C temperature was metallurgically more uniform.
2. The lowest coating thickness was 14.95µm at 900°C and the highest thickness was 24.1µm at 1100°C.
3. In EDS measurements, while CrC was dense in the coating region, Fe density increased towards the substrate.
4. In the microhardness measurements, the highest value was measured as 2371 HV0.5 in the sample coated at 1100°C.
5. Based on these results, it is thought that CrC coating forms a better coating layer especially at high temperatures.

REFERENCES

- [1] Ş. Ertürk, F. Erzincanlı, "Investigation of Coating Properties and Machining Capability of Boron and Titanium Coated AISI D2 Cutting Tools by Thermochemical Method." DUBITED 8.1: 1095-1109, 2020.
- [2] S. Özel, "Yüzey Kaplama İşlemlerinde Kullanılan Isıl Püskürtme Yöntemleri." Bitlis Eren University Journal of Science 2.1: 88-97, 2013.
- [3] Ç. Dindar, M. Altay, & H. Aydın, "Laser Cladding Process and Process Parameters: A Review Uludağ University Journal of The Faculty of Engineering 26.2: 723-736, 2021
- [4] M. Kilic, A. Imak, & I. Kirik, "Surface modification of AISI 304 stainless steel with NiBSi-SiC composite by TIG method." JMEPEG 30.2: 1411-1419, 2021.
- [5] M. Akkaş, "The mechanical and corrosion properties of WCCo-Al coatings formed on AA2024 using the HVOF method." Materials Research Express(MRX) 7.7: 076515, 2020.
- [6] H. Durmuş, M. Türkmen, & U. Çalığüllü, "Wear Resistances of X6Cr17 Ferritic Stainless Steel Surfaces Coated with Al2O3 Powders Using Thermal Spray Method." DUJE 11.3: 1167-1173, 2020.
- [7] A. Aytac, & U. Malayoglu, "Comparison of PVD and JVD / DVD Thin Film Coatings by Physical Vapor Deposition Methods and a Conceptual, Academic and Theoretical Analysis on Industrial Applications of DVD Coating Technology." Journal of Defense Sciences 17.1: 131-164, 2018.
- [8] M. Kılıç, & E. Korkmaz, " Effect of Parameters on Coating Thickness." Batman University Journal of Life Sciences 13.2: 28-35, 2024.
- [9] B. Kurt, Y. Küçük, and M.S. Gök, Microabrasion wear behavior of VC and CrC coatings deposited by thermo-reactive diffusion technique, Tribol. Trans., 57, No. 2, pp. 345, 2014.
- [10] A. Toru, "Thermoreactive deposition/diffusion process for surface hardening of steels." Steel Heat Treating Fundamentals and Processes. ASM International, 725-740, 2013.

- [11] M. Kilic, (2020). "TiC coatings on an alloyed steel produced by thermal diffusion". Materials Testing, 62(9), 909-912, 2020.
- [12] Çelik, Y. H., Ertem, M., Gür, A. K., Kurt, B., Caligulu, U., Özyay, Ç., & Yildiz, T. (2021). Investigation Of Microstructure Properties Of Nbc-B Coated Hardox 400 Steel By Trd Method And Evaluation Of Wear Behavior By Taguchi Method. Surface Review and Letters, 28(12), 2150115.
- [13] S. Buytoz, B. Yılmaz, " Investigation of microstructural properties of TiC coating obtained by thermoreactive diffusion process on AISI4140 steel." Firat University Journal of Engineering Sciences 31.2: 473-480, 2019.
- [14] B. Kurt, Y. Küçük, & M.S. Gök, "Microabrasion wear behavior of VC and CrC coatings deposited by thermoreactive diffusion technique." Tribology Transactions 57.2: 345-352, 2014.
- [15] Y. Karaca, "Investigation of VC Coatability Of 1.2344 Hot Work Tool Steel With Box Cementation Method." Nevşehir Journal of Science and Technology 106-110, 2019.
- [16] M. Kilic, "TiC coatings on an alloyed steel produced by thermal diffusion." Materials Testing 62.9: 909-912, 2020.
- [17] F. E. Castillejo, D. M. Marulanda, J. J. Olaya & J. E. Alfonso, "Wear and corrosion resistance of niobium–chromium carbide coatings on AISI D2 produced through TRD." Surface and Coatings Technology 254: 104-111, 2014.
- [18] A. Ghadi, H.Ebrahimnezhad-Khaljiri, & R. Gholizadeh, "A comprehensive review on the carbide-base coatings produced by thermo-reactive diffusion: microstructure and properties viewpoints." Journal of Alloys and Compounds, 171839, 2023.
- [19] S. Özel, " Microstructure and hardness investigation of fe matrix carbide layers alloyed by TIG welding method." KSU Journal of Engineering Sciences 27.2: 311-324, 2024.
- [20] A. V. Khvan, B.Hallstedt, & C. Broeckmann, "A thermodynamic evaluation of the Fe–Cr–C system." Calphad 46: 24-33, 2014.
- [21] M. R. Najari, S. A. Sajjadi, & O. Ganji, " Microstructural evolution and wear properties of chromium carbide coating formed by thermo-reactive diffusion (TRD) process on a cold-work tool steel " Results in Surfaces and Interfaces 8: 100059, 2022.
- [22] O. Ganji, S. A. Sajjadi, Z. G.Yang, M. Mirjalili, & M. R. Najari, "On the formation and properties of chromium carbide and vanadium carbide coatings produced on W1 tool steel through thermal reactive diffusion (TRD)" Ceramics International 46.16: 25320-25329, .

BIOGRAPHIES

Musa KILIÇ obtained his BSc degree in metal teaching from Firat University in 2004. He received the MSc diploma in Metallurgy and materials training from the Firat University and Phd degree in Graduate School of Science from Firat University. His research interests are welding and coating. In 2014 he joined the Faculty of Technology, Batman University as a assistant professor doctor, where he is presently a Associate Professor.

Automated Fault Classification in Solar Panels Using Transfer Learning with EfficientNet and ResNet Models

Rojbin Akinca¹ , Hüseyin Firat²  and Mehmet Emin Asker^{3,*} 

¹ Dicle University, Department of Renewable Energy Resources, Diyarbakır, Türkiye. (e-mail: rojbin.akinca@dicle.edu.tr).

² Dicle University, Department of Computer Engineering, Diyarbakır, Türkiye. (e-mail: huseyin.firat@dicle.edu.tr).

^{3,*} Dicle University, Department of Electricity and Energy, Diyarbakır, Türkiye. (e-mail: measker@dicle.edu.tr).

ARTICLE INFO

Received: Aug., 15. 2024

Revised: Nov., 05. 2024

Accepted: Nov., 09. 2024

Keywords:

Solar panel
Transfer learning
EfficientNet
ResNet
Fault classification

Corresponding author: Mehmet Emin Asker

ISSN: 2536-5010 / e-ISSN: 2536-5134

DOI: <https://doi.org/10.36222/ejt.153783>

ABSTRACT

Classifying and detecting faults in solar panels using deep learning methods is crucial to ensuring their efficiency and longevity. In this study, we propose a model that concatenates ResNet and EfficientNet to classify faults in solar panel images. ResNet's advantage lies in its residual connections, which help mitigate the vanishing gradient problem and improve training of deep networks. EfficientNet is known for its scalability and efficiency, providing a balanced trade-off between accuracy and computational cost by optimizing network depth, width, and resolution. Together, these models enhance fault classification accuracy while maintaining efficiency. To evaluate the performance of the proposed model, experimental studies were conducted using a solar panel dataset with six classes: bird-drops, covered snow, dusty, clean, electrical and physical damage on the surfaces of solar panels. The results demonstrated that the ResNet101 + EfficientNetB1 concatenation achieved superior performance, with an accuracy of 87.55%, F1-score of 88.13%, recall of 88.75%, and precision of 87.92%. This concatenation provided significant improvements in fault classification metrics compared to individual models.

1. INTRODUCTION

Recently, the reduction in fossil fuel reserves and the impact of global warming have driven a greater focus on sustainable, clean, and renewable energy (RE) sources such as geothermal energy, hydroelectric, solar, and wind [1,2]. Among RE sources, solar energy is one of the most powerful and is being used increasingly often [3]. Solar panels (SPs) are key to producing solar energy efficiently [4]. The performance and durability of SPs are closely connected to identifying and fixing potential issues. Therefore, early detection of faults in SPs is crucial for ensuring uninterrupted energy production and reducing maintenance costs [5-8].

The SP faults result from a combination of electrical irregularities and environmental factors. Various issues, such as physical damage, electrical damage, hot spots, bird droppings, dust, and panel deformation due to external conditions, can cause disruptions in energy production [9-12]. Traditional machine learning methods for detecting these faults tend to be both costly and time-consuming. However, fault detection methods based on manual inspections and remote monitoring tools have been significantly improved recently with the advent of deep learning (DL) models [1,6]. The DL

involves artificial intelligence techniques capable of recognizing and learning complex patterns from large datasets [13]. Convolutional neural networks (CNNs) and DL-based feature extractors are particularly effective in extracting precise information from image data and identifying faults [11,14]. Using DL methods to detect faults in SPs provides several advantages. Early fault detection can extend the lifespan of panels, reduce energy production losses, and make maintenance processes more efficient, thereby increasing the reliability of solar energy systems [15,17].

In the literature, there are various studies on fault detection from SP images using DL models. Some of these studies are as follows. Espinosa et al. [5] introduced an automated technique for classifying faults in SP images by employing CNNs for both classification and semantic segmentation based on RGB images. The method achieved an average accuracy 70% for categorizing four classes: dust, shadows, cracks, no-fault, and 75% for distinguishing between no-fault and fault categories. Le et al. [6] introduced a CNN framework that combines a residual network method with ensemble method to identify faults in photovoltaic modules. Following the method, they applied various transformations to augment the dataset, aiming to achieve the highest classification performance. Additionally,

they determined the optimal number of filters by evaluating both the augmented datasets and raw with different filter configurations. The ensemble method achieved an accuracy of 94.40% for the 2-class problem and 85.90% for the 12-class problem. Duranay [11] examines using infrared images of solar modules for detecting defects via DL, aiming to improve solar energy system efficiency. The dataset included 20,000 images across 12 classes, with classification performed using an EfficientNetB0 model and SVM classifier. The method achieved strong results, with average accuracy of 93.93%, F1-score of 89.82%, precision of 91.50%, and sensitivity of 88.28%. Mahmud et al. [12] conducted fault detection on SP images using the VGG16 and VGG19 models. Their dataset, besides clean panels, included five additional classes: Snow-Covered, Physical damage, Electrical damage, Bird-drops, and Dusty. Their experimental results showed a prediction accuracy of 72.88% with VGG16 and 86.44% with VGG19. Alves et al. [18] introduced a CNN architecture for classifying faults in photovoltaic modules. They created a balanced dataset by applying oversampling and undersampling techniques. To analyze the classification effectiveness of their proposed approach, they examined different scenarios. The overall classification criterias for the 2-class problem were reported as 92.50% for accuracy (Acc), 92.00% for F1-score (F1s), recall (R), and precision (P). Additionally, They noted that the proposed approach acquired an Acc of 66.43% for the 11-class problem. Lee et al. [19] introduces LIRNet, a lightweight inception residual convolutional network designed for detecting faults in SPs. LIRNet leverages DL and hierarchical learning, consisting of two phases: data preprocessing using K-means clustering to refine the dataset, followed by model training to enhance fault detection accuracy and processing speed.

In this study, we propose concatenating ResNet and EfficientNet models to classify faults in SP images. ResNet is known for its ability to effectively train deep neural networks using residual connections, which help prevent issues like vanishing gradients. EfficientNet, on the other hand, optimizes accuracy and efficiency by scaling depth, width, and resolution systematically. By concatenating these models, the proposed approach benefits from ResNet's depth and learning capabilities and EfficientNet's balanced performance, resulting in improved fault classification accuracy. To test the effectiveness of the proposed model, a dataset containing images of SPs with six classes was used. Experimental results on this dataset showed that among the ResNet models, ResNet152 acquired the best performance with an Acc of 84.15%, P of 85.72%, R of 82.84%, and F1s of 83.97%. For the EfficientNet models, the best results were obtained with EfficientNetB2, achieving an Acc of 82.64%, P of 83.96%, R of 83.54%, and F1s of 83.67%, and with EfficientNetB4, achieving an Acc of 83.40%, P of 83.68%, R of 83.45%, and F1s of 83.41%. The concatenation of different versions of the two models resulted in the best performance with the ResNet101 + EfficientNetB1 model, achieving an Acc of 87.55%, P of 87.92%, R of 88.75%, and F1s of 88.13%. This concatenation showed improvements in classification metrics compared to the closest models by 3.4% in Acc, 2.2% in P, 5.21% in R, and 4.16% in F1s.

In the other sections of the paper, Section 2 covers the dataset containing solar panel images, the proposed model, and the models that make up the proposed model. Section 3 discusses the experimental setup, evaluation metrics, and

experimental results in detail. The final section, Section 4, provides a general summary of the study's findings.

2. MATERIALS AND METHODS

2.1. Solar Panel (SP) Dataset

The presence of bird drops, snow, dust etc. on SP surfaces decreases their efficiency and the energy they generate. Thus, it is essential to monitor and clean these panels regularly. Creating an effective process for monitoring and cleaning SPs is crucial to enhance their efficiency, lower maintenance costs, and minimize resource usage.

In this study, a dataset containing publicly available SP images from the Kaggle platform was used [20]. This dataset consists of images of clean, dusty, and various damaged panels, categorized into six different classes. The classes are as follows: snow-covered, physical damage, electrical damage, bird drops, dusty, and clean. The original dataset includes a total of 885 SP images. Among these images, 193 are clean, 190 are dusty, 103 have electrical damage, 69 have physical damage, 123 are snow-covered, and 207 contain bird drops. The sample panel images in the dataset are shown in Figure 1.

The aim of utilizing this dataset is to evaluate the effectiveness of various machine learning classifiers in accurately classifying bird drops, snow, dust, as well as electrical and physical damage on the surfaces of SPs.



Figure 1. Sample images of solar panels

2.2. Transfer Learning

Transfer learning (TL) is an effective method in DL that involves utilizing a model trained for one specific task as the foundation for a model aimed at a different but related task [21]. This approach is particularly beneficial in DL, as it allows models to leverage features learned from large datasets, reducing the amount of data and training time required for new tasks [22]. The primary concept involves transferring knowledge from one domain (source) to another (target), where the source domain contains a large amount of data, while the target domain has only a small amount of data available.

The TL involves utilizing feature extraction from a model that has already been pre-trained, thereby avoiding the necessity for developers to train a model from scratch [21]. Typically, a TL model is trained on a large dataset such as ImageNet [23]. The learned parameters from this model can then be applied to a CNN-based model for a different but related application. Such models can be directly employed for

making predictions on new tasks or integrated into the training processes of related applications [21,22].

In summary, the TL is a versatile and efficient approach to developing deep learning models, allowing the reuse of existing knowledge to solve new problems. It accelerates the training process, improves performance, and is particularly useful when working with limited data. By leveraging pre-trained models and applying techniques like feature extraction and fine-tuning, transfer learning can effectively address a wide range of tasks across different domains.

In this study, EfficientNet [24] and Residual Network (ResNet) [25], two important pre-trained models available in the Keras library, are used for classifying faults in solar panels.

2.3. Residual Network (ResNet) Model

Residual networks, or ResNets, are a type of deep CNN architecture introduced to address the challenges associated with training very deep networks. The key innovation of ResNets is the concept of residual learning (RL), which helps overcome issues like vanishing gradients and difficulty in training deep models [25].

The RL is a technique in deep learning designed to address the difficulties associated with training very deep CNN. Instead of learning the entire transformation directly from input to output, the RL focuses on learning the residual, or the difference between the desired output and the input [25].

In practice, this means that if the aim of the network is to learn a mapping $H(x)$, it learns $F(x)=H(x)-x$ instead. Here, $H(x)$ is the desired mapping, x is input, and $F(x)$ represents the residual function. The final output of the network is then obtained by adding this residual to the original input, resulting in $F(x)+x$ (Figure 2). This method simplifies the learning process by allowing the network to concentrate on the residuals, which are often easier to model than the complete transformation [25].

The RL is implemented through residual blocks, which are the core components of ResNets. Each block consists of several convolutional layers followed by a skip connection that adds the input of the block directly to its output (Figure 2). These shortcut or skip connections, ensure that the learning focuses on the residuals and help maintain the flow of gradients during training, thus mitigating the vanishing gradient problem. In addition, the benefits of the RL are substantial. It makes the training of very deep networks more manageable by simplifying the optimization process. By enabling the effective training of deeper models, the RL enhances feature extraction capabilities and overall model accuracy [25].

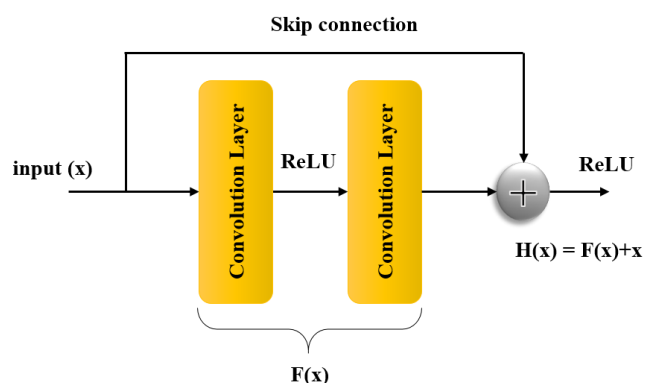


Figure 2. Block of residual learning

ResNets can be quite deep, with common variants including ResNet50, ResNet101, and ResNet152 where the number indicates the number of layers. This depth enables the network to learn more complex features and achieve high accuracy in various tasks [25]. ResNet50 model has 50 layers and is known for its balance between performance and computational efficiency. It is commonly used for various image recognition tasks. Suitable for applications where computational resources are limited, and real-time performance is needed. With 101 layers, ResNet101 model provides increased depth compared to ResNet50, allowing it to capture more complex features and achieve higher accuracy on image classification tasks. Ideal for tasks requiring more detailed feature extraction and where additional computational resources are available. It can be a good choice for medium to large-scale image classification tasks. The deepest among the three, with 152 layers, ResNet152 offers even greater accuracy, making it suitable for more demanding image recognition tasks. However, it requires more computational resources and longer training times. Best for high-performance applications that require the utmost accuracy, such as medical imaging and large-scale visual recognition [25].

2.4. EfficientNet Model

EfficientNet is a family of CNNs designed for image classification tasks, introduced by Google researchers. The key innovation in EfficientNet is its use of a compound scaling approach that uniformly scales all dimensions of resolution, width, and depth. This approach ensures EfficientNet models to acquire higher accuracy and efficiency compared to previous models [24].

The EfficientNet family comprises models named from EfficientNetB0 to EfficientNetB7, each increasing in size and complexity. EfficientNetB0 is the smallest and simplest model in the family, serving as the base model. It has approximately 5.3 million parameters and performs about 0.39 billion floating-point operations (FLOPs). EfficientNetB1 is slightly larger than EfficientNetB0, with around 7.9 million parameters and approximately 0.70 billion FLOPs. EfficientNetB2 continues this trend, being larger than EfficientNetB1, with roughly 9.2 million parameters and about 1.0 billion FLOPs. EfficientNetB3 increases the size and complexity even further, containing around 12 million parameters and performing approximately 1.8 billion FLOPs. EfficientNetB4, significantly larger than B3, has around 19 million parameters and about 4.2 billion FLOPs. EfficientNetB5 is larger still, with approximately 30 million parameters and 9.9 billion FLOPs, offering very high accuracy suitable for high-end applications with substantial computational resources. EfficientNetB6, larger than B5, contains around 43 million parameters and performs approximately 19 billion FLOPs. It provides extremely high accuracy, making it suitable for applications demanding the highest performance and having ample computational power. At the top of the scale is EfficientNetB7, the largest model in the family, with around 66 million parameters and approximately 37 billion FLOPs [24].

The fundamental building block used in EfficientNet models is the MBConv block, which stands for Mobile Inverted Bottleneck Convolution [26]. This block is optimized for both performance and efficiency, making it well-suited for deep neural networks used in mobile and resource-constrained environments. EfficientNet models use a varying number of MBConv blocks in their models, depending on the specific

model variant (B0 to B7). The number of MBConv blocks increases with the model size, contributing to the depth and complexity of the network [24,26].

The MBConv block combines several methods to achieve high computational efficiency and powerful feature extraction, as shown in Figure 3. These methods in the structure of the MBConv block are as follows.

Inverted Bottleneck: Traditional bottleneck layers in neural networks reduce the dimensionality of the data before processing it further. In contrast, the inverted bottleneck layer in MBConv expands the dimensionality of the input features (i.e., increases the number of channels) before applying further convolutions. This expansion allows the network to capture more complex features and then compress them back to a lower-dimensional space efficiently [27].

Depthwise Convolution (DC): This convolution operation applies a single filter to each input channel separately, as opposed to using multiple filters across all channels. This significantly reduces the computational complexity and the number of parameters required [28].

Pointwise Convolution (PC) (1x1 Convolution): After the DC, a PC is used to combine the outputs of the DC. This step effectively mixes information across different channels and compensates for the reduced computational complexity of the DC [28].

Squeeze-and-Excitation (SE) Block: The SE block is integrated within the MBConv block to enhance the representational power of the network. It consists of two main steps: *Squeeze*: Global average pooling is applied to each channel of the feature map to produce a channel descriptor, reducing each feature map to a single value. *Excitation*: These descriptors are passed through two fully connected (FC) layers with a Swish activation in between, generating a set of weights that are used to scale the original input channels. This process helps the network focus on the most important features by recalibrating the feature maps [29].

Residual Connections: Residual connections are used to add the input of the MBConv block directly to its output. This skip connection helps in mitigating the vanishing gradient problem, making it easier to train deeper networks. It also enables the network to learn residual mappings, which are often more straightforward to optimize than learning the complete transformation [25].

The working steps of the MBConv block given in Figure 3 are as follows:

- The process starts with an input tensor, which is a set of features with a certain number of channels. The first step is to expand this input tensor by increasing the number of channels. This is done using a pointwise convolution (1x1 convolution). This expansion allows the network to capture more detailed and complex features from the input data.
- After expanding the number of channels, the next step is to apply a DC. Unlike a regular convolution that operates across all channels, a DC applies a separate filter to each channel. This means that each channel is processed independently. This step is computationally efficient because it decreases the number of parameters and operations compared to a full convolution.
- The output from the DC is then passed through a squeeze-and-excitation block.
- After the SE block has re-weighted the channels, another PC (1x1 convolution) is implemented to decrease the number of channels back to the original count. This step

compresses the expanded and processed features back to a manageable number of channels, making the output tensor easier to handle.

- Dropout is used in MBConv blocks to prevent overfitting and improve generalization by randomly deactivating a subset of neurons during training.
- If the dimensions of the input tensor and the output tensor after the compression phase (second PC) are the same, a residual connection is used. This means the original input tensor is added to the output tensor, helping the network learn better by preserving the original input information.
- Batch normalization (BN) is performed after each convolution operation in the network. BN is used to stabilize and speed up the training process of deep neural networks in MBConv blocks. In addition, the activation function used in this network is Swish. The EfficientNet model uses the Swish activation function, which has been shown to improve performance compared to traditional activation functions like ReLU (Rectified Linear Unit).

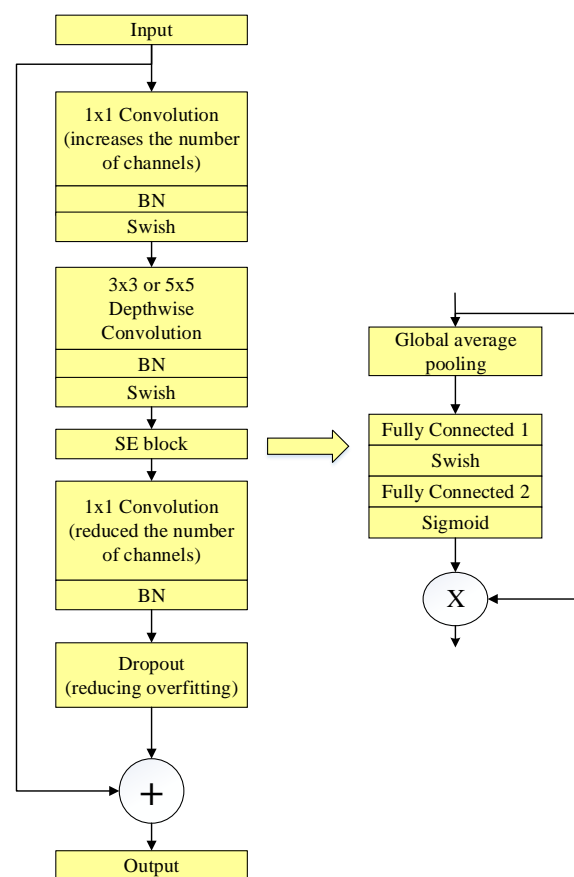


Figure 3. Structure of MBConv

2.5. Proposed Model

In this study, a concatenation of ResNet and EfficientNet models is proposed for automated classification of faults in solar panels. The proposed model is a concatenation of ResNet101 and EfficientNetB1 models as shown in Figure 4. The reasons for using ResNet101 in the proposed model are as follows: (1) ResNet101's depth allows it to capture more detailed features than ResNet50, making it more effective for tasks that require distinguishing between fine-grained classes. (2) ResNet101 strikes a balance between the number of layers and computational efficiency, making it suitable for tasks that are not too simple but also not extremely complex. (3) Compared to ResNet152, ResNet101 is less prone to overfitting

on small datasets, which is crucial for maintaining good generalization performance. In summary, ResNet101 outperformed ResNet50 and ResNet152 because it provides the right depth and complexity for the task at hand. It is deep enough to capture complex patterns in the solar panel images, but not so deep that it overfits on the relatively small dataset, making it the best choice for achieving high accuracy. The reasons for using the EfficientNetB1 model in the proposed model are as follows: (1) EfficientNetB1 has more parameters and a higher resolution input size compared to EfficientNetB0, allowing it to capture more detailed features and improve classification accuracy. (2) Compared to EfficientNetB0, The additional layers and width in EfficientNetB1 help in learning more complex patterns and subtle differences, which is crucial for tasks like fault detection in solar panels where fine details matter. (3) EfficientNetB1 has significantly fewer parameters and FLOPs compared to larger models (EfficientNetB2 to B7), making it more efficient and suitable for environments with limited computational resources.

The proposed model starts with an input image. The size of the input solar panel image is $224 \times 224 \times 3$. Then, this input image is given to the input of ResNet101 and EfficientNetB1 models separately and feature extraction is performed. A detailed description of the layer steps of the ResNet101 model when performing feature extraction on the $224 \times 224 \times 3$ input image is as follows. Following the input layer, the image is passed through the first convolutional layer, which applies 64 filters, each of size 7×7 , with a stride of 2. This operation increases the depth of the feature maps and reduces the spatial dimensions, resulting in an output of size $112 \times 112 \times 64$. This initial convolutional layer is crucial for capturing low-level features, such as edges and textures, in the input image. The output from the convolutional layer is then normalized using a batch normalization layer, which stabilizes and accelerates the training process by normalizing the inputs to each layer. After batch normalization, a ReLU activation function is implemented to introduce non-linearity into the model, enabling it to learn more complex representations. Next, a max pooling layer with a filter size of 3×3 and a stride of 2 further reduces the spatial dimensions, yielding an output of size $56 \times 56 \times 64$. This pooling operation helps to down-sample the feature maps and reduce computational complexity, while also retaining important features. ResNet101 is primarily built using bottleneck residual blocks, each consisting of three convolutional layers: 1×1 , 3×3 , and 1×1 . The network contains several groups of these blocks, organized to gradually reduce the spatial dimensions while increasing the depth, allowing the network to learn increasingly abstract features. The bottleneck residual blocks in the ResNet101 model are as follows:

Conv2x Stage (3 Blocks): The first set of residual blocks, known as Conv2x, begins with a bottleneck block that comprises three key layers: 1×1 Convolution Layer uses 64 filters to reduce the dimensionality of the input, making the computation more efficient. 3×3 Convolution Layer (the main processing layer), which employs 64 filters to perform convolutions and extract features. 1×1 Convolution Layer restores the dimensionality using 256 filters, preparing the output for the next stage. Within each bottleneck block, a residual connection adds the input to the output, creating a shortcut path that enables gradients to flow more easily during

backpropagation. This mechanism is central to the success of residual networks, as it alleviates the vanishing gradient problem. The Conv2_x stage contains three of these bottleneck blocks, each maintaining an output size of $56 \times 56 \times 256$.

Conv3x Stage (4 Blocks): The next stage, Conv3x, introduces the first bottleneck block with downsampling, which reduces the spatial dimensions while increasing the depth. 1×1 Convolution Layer utilizes 128 filters to reduce dimensions. 3×3 Convolution Layer continues processing with 128 filters. 1×1 Convolution Layer increases dimensions using 512 filters. The Conv3_x stage consists of four bottleneck blocks, resulting in an output size of $28 \times 28 \times 512$.

Conv4x Stage (23 Blocks): The Conv4x stage is the deepest stage, consisting of 23 bottleneck blocks, each further refining the feature maps. 1×1 Convolution Layer employs 256 filters for dimensionality reduction. 3×3 Convolution Layer applies 256 filters for feature extraction. 1×1 Convolution Layer restores dimensions with 1024 filters. The Conv4x stage maintains an output size of $14 \times 14 \times 1024$.

Conv5x Stage (3 Blocks): The final set of blocks, Conv5x, consists of three bottleneck blocks that further distill the features. 1×1 Convolution Layer uses 512 filters for dimensionality reduction. 3×3 Convolution Layer processes with 512 filters. 1×1 Convolution Layer expands dimensions with 2048 filters. The output from this stage has a size of $7 \times 7 \times 2048$. After the final convolutional stage, ResNet101 employs a global average pooling (GAP) layer. This layer reduces each feature map to a single value by averaging, resulting in a 2048-dimensional feature vector. This vector effectively summarizes the learned features from the input image.

A detailed description of the layer steps of the EfficientNetB1 model when performing feature extraction on the $224 \times 224 \times 3$ input image is as follows. Following the input layer, the image is passed through the first convolutional layer, which applies 32 filters, each of size 3×3 , with a stride of 2. The output size obtained at the end of this process is $112 \times 112 \times 32$. MBConv blocks in the EfficientNetB1 model are applied to the obtained output feature map. EfficientNetB1 consists of seven MBConv blocks. These are depth separable convolutions that are efficient and help to decrease the number of parameters and computations while maintaining performance. The blocks are organised as follows: Block 1 includes two MBConv 3×3 layers. Block 2 includes three MBConv 3×3 layers. Block 3 includes three MBConv 5×5 layers. Block 4 includes four MBConv 3×3 layers. Block 5 includes four MBConv 5×5 layers. Block 6 includes five MBConv 5×5 layers. Block 7 includes two MBConv 3×3 layers. The output from all MBConv block has a size of $7 \times 7 \times 2560$. After the final MBConv block, EfficientNetB1 employs the GAP layer. This layer reduces each feature map to a single value by averaging, resulting in a 2560-dimensional feature vector. After performing feature extraction using both ResNet101 and EfficientNetB1 models, the obtained feature maps are passed through a GAP layer, and then the two models are concatenated. The concatenated model results in a 4608-dimensional feature vector. Subsequently, a FC layer with 128 neurons is applied. After the FC layer, batch normalization is applied, followed by a dropout layer with a dropout rate of 0.3. Finally, classification is performed using a softmax classifier.

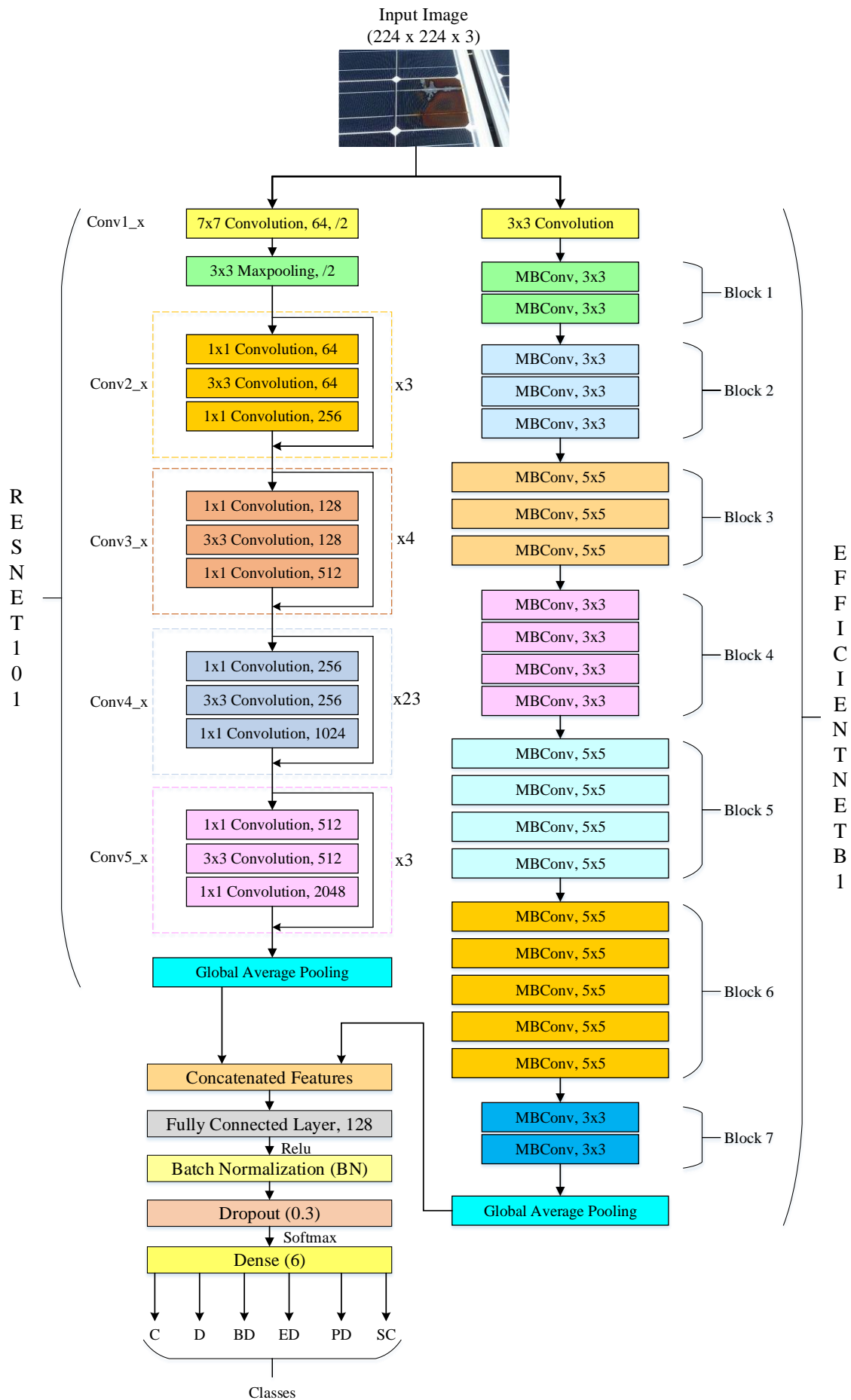


Figure 4. Structure of proposed model

3. EXPERIMENTS

3.1. Experimental Setup

In the experimental studies, the python programming language and Keras-TensorFlow libraries were used. All python code was written on the Kaggle notebook platform. For training the proposed model on the Kaggle platform, a GPU P100 was used as the execution environment. The hyperparameters used are as follows: batch size 64, learning rate 0.0001, and the number of epochs was set to 150. The Adam optimization method was used. The input image dimensions were set to 224x224x3. The dataset containing 885 solar panel images was split into training and test datasets as 70% and 30%, respectively. That is, 620 images were used for training and 265 images for testing. Sparse Categorical Crossentropy (SCC) loss function is used to train the proposed model. The SCC is a loss function that is particularly advantageous for multi-class classification problems where labels are available as integers rather than one-hot encoded vectors. This loss function is efficient because it directly uses integer labels, reducing memory and computational overhead compared to Categorical Crossentropy, which requires one-hot encoded labels. It is well-suited for tasks where each instance belongs to a single class among many, providing a straightforward probabilistic interpretation of predictions through integration with the softmax activation function. This efficiency and compatibility make the SCC an ideal choice for training models with a significant number of classes, as in our solar panel image classification task [30-32].

3.2. Evaluation Metrics

Different evaluation metrics were used to compare the performance of the proposed model. The following four metrics are commonly used when observing various criteria of a classifier.

Accuracy represents the ratio of correct predictions to the total number of predictions made by the model. Accuracy is calculated as in Equation (1) [33].

$$Accuracy (Acc) = \frac{TP + TN}{TP + FP + TN + FN} \quad (1)$$

In the context of multi-class classification, precision is a metric that evaluates the accuracy of positive predictions made by a model for each class. Precision measures how many of the examples predicted as positive actually belong to the class. It is defined as shown in Equation (2) [33].

$$Precision (P) = \frac{TP}{TP + FP} \quad (2)$$

Recall is a metric used in classification to evaluate a model's ability to correctly identify all relevant examples (true positives) from the total actual positive examples (true positives + false negatives). In other words, it measures the percentage of true positive examples correctly identified by the model. It is defined as shown in Equation (3) [33].

$$Recall (R) = \frac{TP}{TP + FN} \quad (3)$$

The F1-score is a metric used in multi-class classification to balance precision and recall. By combining both precision

and recall into a single value, it becomes a useful metric for evaluating the overall performance of a method. The F1-score is calculated as the harmonic mean of precision and recall, and it is particularly valuable when a balance between false positives and false negatives is desired. It is calculated as shown in Equation (4) [33].

$$F1 - score (F1s) = 2 * \frac{precision * recall}{precision + recall} \quad (4)$$

The terms TN, TP, FN, and FP in Equations (1)-(4) are derived from the confusion matrix. True Negatives (TN) represent the number of examples that the model correctly predicts as belonging to the negative class (e.g., "0" or "no"). These are cases where the model correctly identifies examples as not belonging to the positive class when they truly don't. True Positives (TP) represent the number of examples that the model correctly predicts as belonging to the positive class (e.g., "1" or "yes"). These are cases where the model correctly identifies examples as belonging to the positive class when they truly do. False Positives (FP) represent the number of examples that are actually in the negative class but are incorrectly predicted by the model as belonging to the positive class. These are situations where the model makes a positive prediction when it should have made a negative one. False Negatives (FN) represent the number of examples that are actually in the positive class but are incorrectly predicted by the model as belonging to the negative class. These are situations where the model makes a negative prediction when it should have made a positive one [33,34].

3.3. Experimental Results and Discussion

The proposed model is a concatenation of ResNet and EfficientNet models. In the proposed model, the best classification result is obtained with the concatenation of ResNet101 and EfficientNetB1 models. The confusion matrix of the proposed model (ResNet101 + EfficientNetB1) is given in Figure 5. When examining Figure 5, it can be seen that 48 out of a total of 57 panel images in class Bird-drops (BD) are correctly classified. Similarly, 51 out of a total of 55 images in class Clean (C), 44 out of 57 images in class Dusty (D), 28 out of 34 images in class Electrical-damage (ED), 24 out of 25 images in class Physical-damage (PD), and finally, all 37 Snow-covered (SC) images are correctly classified. Out of a total of 265 test images, 232 are correctly classified. In this case, the test accuracy is $(232/265) * 100 = 87.55\%$.

BD	48	1	3	2	2	1
C	2	51	1	1	0	0
D	7	5	44	1	0	0
ED	1	3	0	28	2	0
PD	0	0	0	0	24	1
SC	0	0	0	0	0	37
	BD	C	D	ED	PD	SC

Figure 5. The confusion matrix of proposed model

In this study, comparisons were made with various pre-trained deep learning models including EfficientNetB0-B7 [24], ResNet50-101-152 [25], VGG16-19 [35], MobileNet [36], MobileNetV2 [27], DenseNet121-169-201 [37] to classify faults in solar panel images. The results of the comparison are given in Table 1. When Table 1 is analyzed, it is clearly seen that the best results are obtained with ResNet and EfficientNet models. Table 1 also shows the classification results obtained by combining ResNet50-101-201 and EfficientNetB0-B7 models. A detailed analysis of all the models in Table 1 is as follows:

The VGG16 and VGG19 models, known for their simplicity and depth, achieved moderate performance with VGG16 slightly outperforming VGG19. VGG16 achieves an Acc of 66.79%, with P of 69.12%, R of 67.82%, and an F1s of 68.24%. VGG19, on the other hand, has slightly lower metrics across the board, with an Acc of 65.28%, P of 67.50%, R of 65.96%, and an F1s of 66.20%. The marginally better performance of VGG16 suggests that, for this dataset, the additional depth of VGG19 does not translate into improved results. This may be due to the increased complexity and overfitting associated with deeper networks.

MobileNet models are designed for efficiency, balancing performance with computational cost. The original MobileNet achieves an Acc of 66.42%, with P, R, and F1s around 65%. MobileNet performed similarly to VGG16 with an Acc of 66.42%. However, MobileNetV2 shows a notable drop in performance, with all metrics hovering around 59-60%. This decline suggests that the architectural changes in MobileNetV2, which aim to improve efficiency, may have compromised its ability to capture relevant features in this specific dataset.

DenseNet models, known for their dense connectivity, generally outperform VGG and MobileNet models. DenseNet121, DenseNet169, and DenseNet201 exhibit accuracies of 69.43%, 69.06%, and 68.30%, respectively. P, R, and F1s for these models are also consistently high, can indicating reliable performance. These results show that DenseNet architectures are more capable of capturing complex images in data than VGG and MobileNet models. The improvement over VGG and MobileNet models can be attributed to the enhanced feature propagation and reduced vanishing-gradient problem inherent in DenseNet architectures.

ResNet models significantly outperform the previously discussed models (VGG, MobileNet, and DenseNet). ResNet50 achieves an Acc of 79.62%, with P and F1s both at 80.40%, and a R of 80.50% [38]. Larger ResNet models, such as ResNet101 and ResNet152, further enhance performance, with ResNet152 achieving the highest individual model Acc of 84.15%, P of 85.72%, R of 82.84%, and an F1s of 83.97% [38]. In addition, ResNet101 achieving individual model Acc of 83.40%, P of 84.37%, R of 84.04%, and an F1s of 84.07% [38]. The success of ResNet architectures can be attributed to their ability to mitigate the vanishing gradient problem through skip connections, allowing them to maintain high performance even with increased depth.

EfficientNet models also exhibit strong performance, with several variants outperforming most other EfficientNet models. EfficientNetB2 and EfficientNetB4 stand out with accuracies of 82.64% and 83.40%, respectively. These models also maintain high precision, recall, and F1-scores, indicating balanced performance across different metrics. The

EfficientNet model scales depth, width, and resolution in a compound manner, optimizing performance while maintaining computational efficiency.

The concatenation of ResNet and EfficientNet models yields the highest performance metrics. Notably, the concatenation of ResNet101 and EfficientNetB1 (proposed model) achieves the highest overall performance, with an Acc of 87.55%, P of 87.92%, R of 88.75%, and F1s of 88.13%. This concatenation leverages the strengths of both models—ResNet's robust feature learning and EfficientNet's balanced scaling—resulting in superior classification capabilities. Other successful concatenation include ResNet101 with EfficientNetB3, ResNet101 with EfficientNetB4, ResNet101 with EfficientNetB6, and ResNet152 with EfficientNetB5, all of which show high accuracies and balanced metric scores. These results suggest that model ensembling, particularly concatenating different models, can effectively enhance performance by capturing diverse feature representations.

TABLE I

COMPARISON WITH DIFFERENT DEEP LEARNING MODELS

Models	Acc(%)	P(%)	R(%)	F1s(%)
VGG16	66.79	69.12	67.82	68.24
VGG19	65.28	67.50	65.96	66.20
MobileNet	66.42	65.56	65.84	65.64
MobileNetV2	59.62	59.54	59.59	59.27
DenseNet121	69.43	70.99	68.17	69.19
DenseNet169	69.06	69.91	69.47	69.49
DenseNet201	68.30	70.38	66.85	67.86
ResNet50	79.62	80.40	80.50	80.40
ResNet101	83.40	84.37	84.04	84.07
ResNet152	84.15	85.72	82.84	83.97
EfficientNetB0	81.13	82.39	82.16	82.07
EfficientNetB1	81.89	83.39	81.36	82.06
EfficientNetB2	82.64	83.96	83.54	83.67
EfficientNetB3	80.00	81.76	80.70	81.09
EfficientNetB4	83.40	83.68	83.45	83.41
EfficientNetB5	81.89	82.81	81.96	82.26
EfficientNetB6	77.74	78.75	78.56	78.50
EfficientNetB7	76.60	78.02	76.90	77.31
ResNet50 + EfficientNetB0	83.02	83.11	84.13	83.53
ResNet50 + EfficientNetB1	82.64	84.17	83.87	83.96
ResNet50 + EfficientNetB2	83.02	83.64	83.41	83.37
ResNet50 + EfficientNetB3	80.76	81.47	81.06	81.12
ResNet50 + EfficientNetB4	81.51	81.71	82.60	82.10
ResNet50 + EfficientNetB5	83.77	85.37	85.47	85.28
ResNet50 + EfficientNetB6	82.26	83.55	82.25	82.71
ResNet50 + EfficientNetB7	83.02	84.18	84.51	84.29
ResNet101 + EfficientNetB0	83.40	84.37	84.62	84.28
ResNet101 + EfficientNetB1	87.55	87.92	88.75	88.13
ResNet101 + EfficientNetB2	86.42	86.24	86.11	86.11
ResNet101 + EfficientNetB3	87.17	88.49	87.58	87.86
ResNet101 + EfficientNetB4	87.17	87.24	87.23	87.21
ResNet101 + EfficientNetB5	85.28	85.82	86.09	85.76
ResNet101 + EfficientNetB6	87.17	88.03	86.87	87.32
ResNet101 + EfficientNetB7	84.53	85.13	84.40	84.53
ResNet152 + EfficientNetB0	86.04	87.23	86.47	86.78
ResNet152 + EfficientNetB1	83.77	86.32	84.12	84.89
ResNet152 + EfficientNetB2	83.77	84.23	83.06	83.50
ResNet152 + EfficientNetB3	85.66	87.76	86.71	87.12
ResNet152 + EfficientNetB4	85.28	85.64	85.30	85.44
ResNet152 + EfficientNetB5	86.79	87.02	87.02	86.96
ResNet152 + EfficientNetB6	81.51	82.15	80.96	81.40
ResNet152 + EfficientNetB7	84.15	85.42	84.80	85.07

4. CONCLUSION

SPs play a crucial role in the global transition to renewable energy, offering a sustainable solution to meet the world's energy demands. As a clean and abundant energy source, SPs

contribute to reducing carbon emissions and combating climate change. However, the effectiveness and reliability of solar energy systems can be significantly impacted by faults and defects in SPs. Common issues such as cracks, dusty, snow-covered, soiling, and shading can reduce the efficiency of solar panels, leading to decreased energy output and increased maintenance costs. Therefore, accurate and timely detection of these faults is essential for maintaining the performance and longevity of solar energy systems.

In this study, we propose a hybrid DL model using ResNet and EfficientNet models to classify faults in solar panels. ResNet is renowned for its ability to train very deep neural networks effectively, utilizing residual connections to prevent issues like vanishing gradients. This capability allows ResNet to capture intricate patterns and features in complex datasets, which is essential for detecting subtle defects in solar panels. On the other hand, EfficientNet is designed to achieve a balance between accuracy and computational efficiency by systematically scaling the network's resolution, width, and depth. By integrating ResNet and EfficientNet models, our approach benefits from the strengths of both architectures: the depth and learning capacity of ResNet and the optimized performance of EfficientNet.

The experimental results demonstrate that the combined ResNet101 + EfficientNetB1 model significantly outperforms individual models in terms of Acc, P, R, and F1s. This hybrid model achieved an Acc of 87.55%, P of 87.92%, R of 88.75%, and F1s of 88.13%, marking notable improvements over the closest models. The synergistic use of ResNet and EfficientNet enables the proposed model to accurately identify and classify various faults in solar panels, thereby enhancing the reliability and efficiency of solar energy systems.

In conclusion, the combination of ResNet and EfficientNet models offers a powerful solution for detecting and classifying faults in solar panels. This approach not only improves fault detection accuracy but also contributes to the overall performance and sustainability of solar energy systems. As the demand for solar energy continues to rise, implementing advanced deep learning models like the one proposed in this study will be essential for ensuring the long-term viability and efficiency of solar power installations.

In future work, the primary aim is to further enhance the model's performance by experimenting with cutting-edge neural network models such as Vision Transformers and different ensemble methods. Additionally, research is planned to improve the model's ability to detect and classify faults by incorporating additional data sources, such as thermal imaging and real-time monitoring data.

REFERENCES

- [1] D. Korkmaz and H. Acikgoz, "An efficient fault classification method in solar photovoltaic modules using transfer learning and multi-scale convolutional neural network," *Eng. Appl. Artif. Intell.*, vol. 113, no. April, p. 104959, 2022.
- [2] H. Acikgoz, "A novel approach based on integration of convolutional neural networks and deep feature selection for short-term solar radiation forecasting," *Appl. Energy*, vol. 305, no. June 2021, p. 117912, 2022.
- [3] T. Z. Ang, M. Salem, M. Kamarol, H. S. Das, M. A. Nazari, and N. Prabakaran, "A comprehensive study of renewable energy sources: Classifications, challenges and suggestions," *Energy Strateg. Rev.*, vol. 43, no. November 2021, p. 100939, 2022.
- [4] B. Li, C. Delpha, D. Diallo, and A. Migan-Dubois, "Application of Artificial Neural Networks to photovoltaic fault detection and diagnosis: A review," *Renew. Sustain. Energy Rev.*, vol. 138, no. October 2020, 2021.
- [5] A. Rico Espinosa, M. Bressan, and L. F. Giraldo, "Failure signature classification in solar photovoltaic plants using RGB images and convolutional neural networks," *Renew. Energy*, vol. 162, pp. 249–256, 2020.
- [6] M. Le, L. Van Su, N. Dang Khoa, V. D. Dao, V. Ngoc Hung, and V. Hong Ha Thi, "Remote anomaly detection and classification of solar photovoltaic modules based on deep neural network," *Sustain. Energy Technol. Assessments*, vol. 48, no. June, p. 101545, 2021.
- [7] C. Haydaroglu, H. Kılıç, and B. Gümüş, "Performance Analysis and Comparison of Performance Ratio of Solar Power Plant," *Turkish J. Electr. Power Energy Syst.*, vol. 4, pp. 190–199, 2024.
- [8] H. KILIC, M. YILMAZ, and B. GUMUS, "Fault Detection in Photovoltaic Arrays: a Robust Regularized Machine Learning Approach," *Dyna*, vol. 95, no. 1, pp. 622–628, 2020.
- [9] K. Osmani, A. Haddad, T. Lemenand, B. Castanier, M. Alkhedher, and M. Ramadan, "A critical review of PV systems' faults with the relevant detection methods," *Energy Nexus*, vol. 12, no. September, p. 100257, 2023.
- [10] G. R. Venkatakrishnan *et al.*, "Detection, location, and diagnosis of different faults in large solar PV system—a review," *Int. J. Low-Carbon Technol.*, vol. 18, no. 1, pp. 659–674, 2023.
- [11] Z. B. Duranay, "Fault Detection in Solar Energy Systems: A Deep Learning Approach," *Electron.*, vol. 12, no. 21, 2023.
- [12] A. Mahmud, M. S. R. Shishir, R. Hasan, and M. Rahman, "A comprehensive study for solar panel fault detection using VGG16 and VGG19 convolutional neural networks," *2023 26th Int. Conf. Comput. Inf. Technol. ICCIT 2023*, pp. 1–6, 2023.
- [13] M. M. Taye, "Understanding of Machine Learning with Deep Learning: Architectures, Workflow, Applications and Future Directions," *Computers*, vol. 12, no. 5, 2023.
- [14] S. H. Han, T. Rahim, and S. Y. Shin, "Detection of faults in solar panels using deep learning," *2021 Int. Conf. Electron. Information, Commun. ICEIC 2021*, pp. 2–5, 2021.
- [15] W. Tang, Q. Yang, K. Xiong, and W. Yan, "Deep learning based automatic defect identification of photovoltaic module using electroluminescence images," *Sol. Energy*, vol. 201, no. November 2019, pp. 453–460, 2020.
- [16] S. Naveen Venkatesh and V. Sugumaran, "Fault Detection in aerial images of photovoltaic modules based on Deep learning," *IOP Conf. Ser. Mater. Sci. Eng.*, vol. 1012, no. 1, p. 012030, 2021.
- [17] G. S. Eldeghady, H. A. Kamal, and M. A. M. Hassan, "Fault diagnosis for PV system using a deep learning optimized via PSO heuristic combination technique," *Electr. Eng.*, vol. 105, no. 4, pp. 2287–2301, 2023.
- [18] R. H. Fonseca Alves, G. A. de Deus Júnior, E. G. Marra, and R. P. Lemos, "Automatic fault classification in photovoltaic modules using Convolutional Neural Networks," *Renew. Energy*, vol. 179, pp. 502–516, 2021.
- [19] S. H. Lee, L. C. Yan, and C. S. Yang, "LIRNet: A Lightweight Inception Residual Convolutional Network for Solar Panel Defect Classification," *Energies*, vol. 16, no. 5, pp. 1–12, 2023.
- [20] Afroz, "Solar Panel Images Clean and Faulty Images," *Kaggle*, 2023. [Online]. Available: <https://www.kaggle.com/datasets/pythonsafroz/solar-panel-images>. [Accessed: 10-May-2024].
- [21] A. W. Salehi *et al.*, "A Study of CNN and Transfer Learning in Medical Imaging: Advantages, Challenges, Future Scope," *Sustainability*, vol. 15, no. 7, 2023.
- [22] N. Raza, A. Naseer, M. Tamoor, and K. Zafar, "Alzheimer Disease Classification through Transfer Learning Approach," *Diagnostics*, vol. 13, no. 4, 2023.
- [23] J. Deng, W. Dong, R. Socher, L.-J. Li, Kai Li, and Li Fei-Fei, "ImageNet: A large-scale hierarchical image database," *2009 IEEE Conf. Comput. Vis. Pattern Recognit.*, pp. 248–255, 2010.
- [24] M. Tan and Q. V. Le, "EfficientNet: Rethinking model scaling for convolutional neural networks," *36th Int. Conf. Mach. Learn. ICML 2019*, vol. 2019-June, pp. 10691–10700, 2019.
- [25] K. He, X. Zhang, S. Ren, and J. Sun, "Deep residual learning for image recognition," in *Proceedings of the IEEE Computer Society Conference on Computer Vision and Pattern Recognition*, 2016, vol. 2016-Decem, pp. 770–778.
- [26] B. Baheti, S. Innani, S. Gajre, and S. Talbar, "Eff-UNet: A novel architecture for semantic segmentation in unstructured environment," *IEEE Comput. Soc. Conf. Comput. Vis. Pattern Recognit. Work.*, vol. 2020-June, no. September 2021, pp. 1473–1481, 2020.
- [27] M. Sandler, A. Howard, M. Zhu, A. Zhmoginov, and L. C. Chen, "MobileNetV2: Inverted Residuals and Linear Bottlenecks," *Proc. IEEE Comput. Soc. Conf. Comput. Vis. Pattern Recognit.*, pp. 4510–4520,

2018.

- [28] F. Chollet, "Xception: Deep learning with depthwise separable convolutions," *Proc. - 30th IEEE Conf. Comput. Vis. Pattern Recognition, CVPR 2017*, vol. 2017-Janua, pp. 1800–1807, 2017.
- [29] H. Firat, "Classification of White Blood Cells using the Squeeze-Excitation Residual Network," *Bilişim Teknol. Derg.*, vol. 16, no. 3, pp. 189–205, 2023.
- [30] B. N. Chaithanya, T. J. Swasthika Jain, A. Usha Ruby, and A. Parveen, "An approach to categorize chest X-ray images using sparse categorical cross entropy," *Indones. J. Electr. Eng. Comput. Sci.*, vol. 24, no. 3, pp. 1700–1710, 2021.
- [31] P. Naveen, "Phish: A novel hyper-optimizable activation function," *techrxiv.orgP NaveenAuthorea Prepr. 2023•techrxiv.org*, pp. 1–8, 2023.
- [32] A. Bhat, A. V. Krishna, and S. Acharya, "Analytical Comparison of Classification Models for Raga Identification in Carnatic Classical Instrumental Polyphonic Audio," *SN Comput. Sci.*, vol. 1, no. 6, pp. 1–9, 2020.
- [33] H. Dalianis, "Evaluation Metrics and Evaluation," *Clin. Text Min.*, no. 1967, pp. 45–53, 2018.
- [34] S. A. Hicks *et al.*, "On evaluation metrics for medical applications of artificial intelligence," *Sci. Rep.*, vol. 12, no. 1, pp. 1–9, 2022.
- [35] K. Simonyan and A. Zisserman, "Very deep convolutional networks for large-scale image recognition," in *3rd International Conference on Learning Representations, ICLR 2015 - Conference Track Proceedings*, 2015.
- [36] A. G. Howard *et al.*, "MobileNets: Efficient Convolutional Neural Networks for Mobile Vision Applications," 2017.
- [37] G. Huang, Z. Liu, L. Van Der Maaten, and K. Q. Weinberger, "Densely connected convolutional networks," *Proc. - 30th IEEE Conf. Comput. Vis. Pattern Recognition, CVPR 2017*, vol. 2017-Janua, pp. 2261–2269, 2017.
- [38] R. Akinca, H. Firat, and M. E. Asker, "Transfer Öğrenme Tabanlı ResNet Modeli Kullanılarak Güneş Panellerindeki Hataların Tespiti," *Dicle Üniversitesi 2.Uluslararası Fen Bilim. Lisansüstü Araştırmalar Sempozyumu*, pp. 27–30, 2024.

BIOGRAPHIES

Rojbin Akinca received her Bsc. degree in electrical and electronics engineering from Dicle University, Diyarbakır, Turkey in 2018. She continues her MSc. degree in Renewable Energy Resources at Dicle University as of 2023. She is currently working as a Data Preparation and Control Operator at Dicle University. Her research interests include renewable energy resources, artificial intelligence, deep learning and machine learning.

Hüseyin Firat received the BSc. degree in computer engineering from Cukurova University, Adana, Turkey, in 2014. He received the MSc. degree in computer engineering from Inonu University in 2018. He received the PhD degree in computer engineering from Inonu University, Turkey, in 2022. He also works as assistant professor at Dicle University in Turkey. His current interests include remote sensing, deep learning, pattern recognition, signal processing, medical image processing and image classification.

Mehmet Emin Asker received the BSc. degree in electrical electronics engineering, from Firat University, Elazığ, Turkey in 1997, the MSc. degree and the PhD degree in electrical machines, power electronics from Firat University, Elazığ, Turkey, in 2009 and 2016, respectively. He is an assistant professor with Dicle University, department of electrical power and energy. Where he teaches courses on power system, power electronics, circuit theory and electrical machines since 2007. His research interests include electrical machines, power electronics, chaos, machine learning and power systems.

Research Article

Comparison of Graphene Oxide-Titanium Oxide (GO-TiO₂) Composite Film Coating Methods on Glass Substrates and Surface Characterization Study

İbrahim Firat Balkaya ^{1*}, Harun Mindivan ² and Nevin Atalay Gengec ³

^{1*}Bilecik Seyh Edebali University, Institute of Graduate, Mechanical Engineering Department, 11210, Gulumbe, Bilecik, Turkey. (e-mail: 1055242@ogrenci.bilecik.edu.tr).

²Bilecik Seyh Edebali University, Mechanical Engineering Department, 11210, Gulumbe, Bilecik, Turkey. (e-mail: harun.mindivan@bilecik.edu.tr).

³Kocaeli University, Department of Environmental Protection Technologies, 41001, Izmit, Kocaeli, Turkey. (e-mail: nevin.atalay@kocaeli.edu.tr).

ARTICLE INFO

Received: Aug., 20. 2024

Revised: Sep., 08. 2024

Accepted: Sep., 09. 2024

Keywords:

Graphene oxide

Titanium oxide

Dip coating

Spin coating

Contact angle

Corresponding author: İbrahim Firat BALKAYA

ISSN: 2536-5010 / e-ISSN: 2536-5134

DOI: <https://doi.org/10.36222/ejt.1536083>

ABSTRACT

In this work, graphene oxide-titanium oxide (GO-TiO₂) nanocomposite was successfully produced via ultrasonication process. For coating process, spin coating (SC), dip coating (DC) and spray coating methods were used. The synthesized nanocomposite and surfaces were characterized by optical microscope, SEM, EDX, FTIR, XRD, four-probe conductivity, water contact angle.

As result of experiments, while spin coating provides thinner coating, a thicker and higher water contact angle surface was formed under the optimum condition of dip coating. XRD, four-probe conductivity results revealed partial formation of reduced graphene oxide within the composite structure. Water contact angle results showed that the best result regarding stability of droplet shape was on the spin coated surface. On the other hand, it was observed that deionized water test liquid droplet on the dip coated surfaces stabilized relatively slower but provided a much higher water contact angle.

1. INTRODUCTION

Graphene oxide (GO) thin films are typically synthesized from graphite using the Hummers method [1]. These thin films are generally applied to surfaces using techniques such as spin coating, dip coating, or spray coating. In the literature, there are applications for increasing some properties by creating various metal oxide-GO and hydrocarbon-GO composites [2,3]. Titanium dioxide (TiO₂) thin films, on the other hand, can be prepared using methods like sol-gel, Chemical Vapor Deposition (CVD), or Atomic Layer Deposition (ALD) [4]. Composite thin films formed by combining these two materials bring together the advantages of both GO and TiO₂ [5].

In addition to thermodynamic-based solutions in energy storage and transmission, niche studies on metals and phase change materials continue to increase [6, 7]. Graphene and graphene oxide-based solutions are also widely used in electrical-based studies for similar purposes. GO and TiO₂ hold significant positions in the fields of nanotechnology and materials science. GO is notable for its large surface area, excellent conductivity, and surface functionalization

capabilities, while TiO₂ is known for its superior photocatalytic activity and chemical stability [8, 9]. When GO's high surface area, excellent electrical conductivity, and mechanical durability are combined with TiO₂'s high photocatalytic activity and chemical stability, multifunctional thin films can be produced. Coating these materials as thin films has great potential, particularly in fields such as energy storage, environmental cleaning, and biomedical applications [10]. GO-TiO₂ thin films are especially important for applications in dye-sensitized solar cells, supercapacitors, and wearable electronic devices [11]. The high photocatalytic activity of TiO₂ under UV light can be broadened to a wider spectrum when supported by GO, thereby increasing photocatalytic efficiency [5]. Moreover, the antibacterial properties of these materials allow them to be used as surface coatings in biomedical devices [12].

The preparation of stable GO-TiO₂ dispersions is crucial for ensuring the homogeneous distribution and long-term stability of these materials. Various methods are found in the literature. One such method is the addition of various surfactants to enhance dispersion stability. These surfactants reduce interactions between particles, preventing

agglomeration and thereby making the dispersion more stable [13]. Ultrasonication is a commonly used method for achieving homogeneous mixing of GO and TiO₂ and obtaining a stable dispersion. Ultrasonication methods provide significant control over the structure, size, and distribution of nanoparticle components [14]. The use of high-speed mixing following sonication is an effective method for achieving homogeneous distribution of GO and TiO₂ particles [15]. The obtained GO-TiO₂ dispersions have demonstrated long-term stability and homogeneous distribution. As reported in the literature, the use of ultrasonic methods minimizes the risk of aggregation by ensuring the homogeneous distribution of particles, while the presence of oxygen-related functional groups, such as -OH and -COOH, in GO serves as ideal support for carrying TiO₂ nanocrystals [16]. This method facilitates more efficient results in photocatalytic applications.

For coating a stable dispersion onto a suitable substrate, methods such as spin coating [17], dip coating, and spray coating [18] are commonly used.

This study aims to successfully deposit GO-TiO₂ composite films on glass substrates and to compare the effects of different coating methods on the surface properties of GO-TiO₂ composite films.

2. Materials and Methods

In this study, a dispersion was prepared using the ultrasonication method. The obtained dispersion was used to create coatings/surfaces on 25x75mm glass substrates via dip coating, spin coating, and spray coating methods. X-ray Diffraction (XRD) (Panalytical/Emprayan) and Fourier-Transform Infrared spectroscopy (FTIR) (Perkin Elmer/Spectrum100) analyses of GO and GO-TiO₂ composites were conducted, and their conductivity was compared using a four-probe conductivity device (Signatone). To assess the homogeneity of the surface and hydrophobic properties, the equilibrium contact angle (θ_e , °) of water (deionized water-Merck) was evaluated using an optical contact angle measurement device (Biolin Scientific/Theta Lite). The test liquid droplet volume was set at 4 μ L. Other characterization methods used in this study include optical microscopy (Nikon Eclipse/LV150), Scanning electron microscope (SEM) (Zeiss/SupraV40), and Scanning Electron Microscopy with Energy Dispersive X-ray spectroscopy (SEM-EDX) (Bruker).

3. EXPERIMENTS

3.1. Preparation of Stable GO-TiO₂ Dispersion

The preparation of stable dispersions generally involves steps of ultrasonication, mixing, and centrifugation [19]. A mixture of graphene oxide with an initial concentration of 2 mg/mL was obtained by adding 1g of graphite oxide (GrO) into 500 mL of deionized water (Merck). This mixture was subjected to ultrasound at 35 kHz for 16 hours and then centrifuged at 3000 rpm for 30 minutes. The supernatant obtained after centrifugation is the stable GO dispersion, and its concentration was found to be 0.83 mg/mL according to the solid content analysis. The stable GO-TiO₂ dispersions were prepared using a new formulation with TiO₂, similar to the GO/SnO₂ stable dispersions prepared by Liang et al. [20] using SnO₂, as described below. The stable GO dispersion was diluted with deionized water (Merck) water to a concentration

of 0.8 mg/mL and subjected to ultrasonication for 5 minutes. Then, 0.1 g of TiO₂ was added to 250 mL of the stable GO dispersion and ultrasonicated for 1.5 hours. The prepared dispersion was centrifuged at 3000 rpm for 5 minutes, and the supernatant was collected. The concentration of the GO/TiO₂ dispersion after centrifugation was found to be 0.6 mg/mL based on solid content analysis. The obtained GO-TiO₂ dispersion remained stable for two weeks and was used in the production of GO-TiO₂ surfaces. It has been reported that the strong interactions of TiO₂ nanocrystals with GO layers prevent their detachment during the ultrasonication process [21].

3.2. GO-TiO₂ Coating Studies

The first step of the coating process involves imparting properties to the glass substrate that allow it to retain the coating. For this purpose, the glass substrates were cleaned with deionized water after a 30-minute chromic acid bath and dried in a vacuum oven, followed by 5s of vacuum plasma treatment.

In this study, surfaces were obtained by coating glass substrates using dip coating, spin coating and spray coating methods. Since the spin coating method involves too many parameters and the variation in experimental parameters and results is very complex, it was carried out under optimum experimental conditions determined by discussing in detail in another study. The spin coating (Figure 1.a) parameters were set as a spinning speed of 500 rpm (SC500), a spinning time of 10s, and a coating fluid volume of 0.3 mL. Dip coating was performed (Figure 1.b) at four different speeds: 240 (DC240), 320 (DC320), 400 (DC400), and 480 (DC480) mm/min for both immersion and withdrawal. Spray coating (Figure 1.c) was applied to the glass substrate material, heated to approximately 300°C, differing from the other two experiments.

The images of the surfaces produced by spin coating and dip coating methods are shown in Figures 2.a and 2.b, respectively.

4. RESULTS and DISCUSSION

According to the obtained FTIR results (Figure 3), the peak at 1627 cm⁻¹ originates from non-oxidized C=C bonds, while the peaks in the "2800-3000 cm⁻¹" region are due to -OH stretching vibrations. The peaks between "2000-2250 cm⁻¹" indicate the presence of reduced graphene oxide (rGO) [22]. The region between "1750-1040 cm⁻¹" corresponds to carboxyl groups, with the peak at 1708 cm⁻¹ attributed to C=O, the peak at 1430 cm⁻¹ to C-O, and the peak at 1375 cm⁻¹ to C-O-C (epoxy) or C-O-H (phenolic) structures. The peak at 1154 cm⁻¹ identifies alkoxy C-O carboxyl. In the GO-TiO₂ composite, it was observed that the peaks corresponding to oxygen functional groups seen in GO disappeared, and peaks related to Ti-O-Ti and Ti-O-C stresses emerged in the "500-900 cm⁻¹" range [23]. The XRD analysis of the GO-TiO₂ composite (Figure 4) shows a characteristic peak of GO at approximately 2 θ ≈11° and a peak specific to titanium at approximately 2 θ ≈26° [24, 25].

Conductivity measurements using a four-point probe are consistent with partial graphene formation. The surface exposed to the oven atmosphere in GO solid and GO-TiO₂ solid generally exhibits low conductivity. When comparing the two materials, it was concluded that the conductivity in

GO-TiO₂ solid/precipitate is much higher than in GO solid/precipitate (Tables I and II).

This result indicates that a reduced graphene oxide-titanium oxide (rGO-TiO₂) composite begins to form through

simple ultrasonication, as the peak at 20~26° in the XRD results aligns with rGO-TiO₂ formation [26].

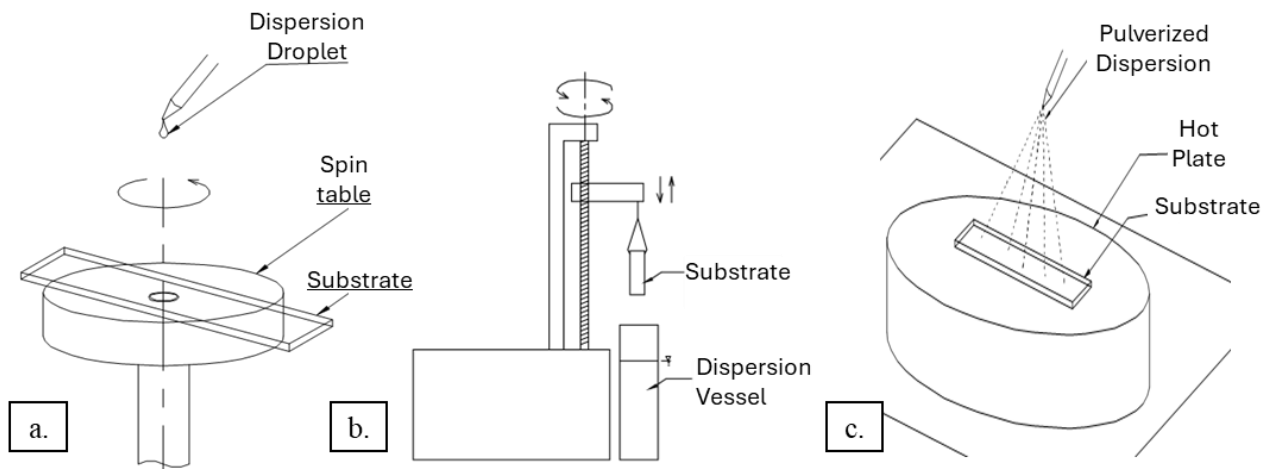


Figure 1. a. Schematic representation of dip coating, b. spin coating, c. spray coating on heated substrate.



Figure 2. Images of surfaces produced on glass slide substrates by a. spin coating method and b. dip coating method.

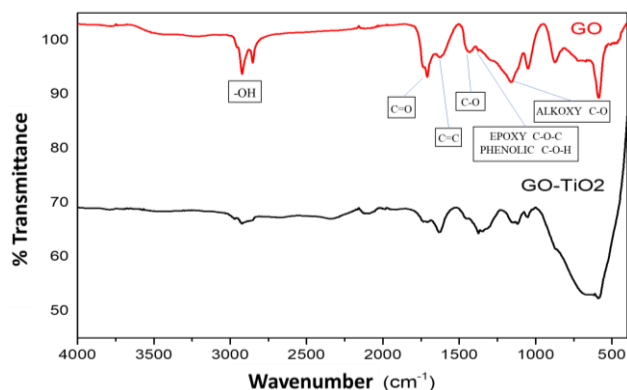


Figure 3. FTIR spectrum of GO and GO-TiO₂.

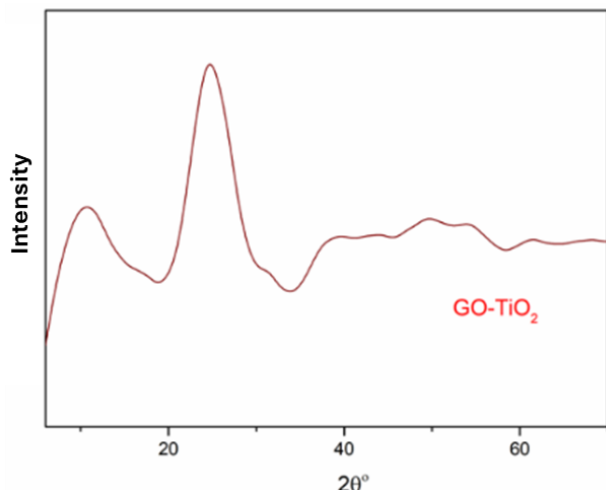


Figure 4. XRD analysis of the GO-TiO₂ composite

TABLE I

CONDUCTIVITY MEASUREMENTS OF THE SOLID CONTENT/PRECIPITATE OF GO-DEIONIZED WATER SUPERNATANT.

Current (mA)	Thickness (μm)		V/I	Specific Cond. σ	S/m	S
	0,005	1				
Point	Rs (ohm/sq)	Res (ohm-cm)				
1	15996,3350	1,5996	4034,8403	0,62514	0,006251	0,000248
2	22661,5527	2,2662	4965,2769	0,44128	0,004413	0,000201

TABLE II

CONDUCTIVITY MEASUREMENTS OF THE SOLID CONTENT/PRECIPITATE OF GO-TiO₂-DEIONIZED WATER SUPERNATANT.

Current (mA)	Thickness (μm)		V/I	Specific Cond. σ	S/m	S
	0,005	1				
Point	Rs (ohm/sq)	Res (ohm-cm)				
1	4831,685547	0,483169	1302,066284	2,06967	0,020697	0,000768
2	4300,179199	0,430018	859,313416	2,32548	0,023255	0,001164

Table III presents the results of dip coating experiments conducted at four different speeds of 240, 320, 400, and 480 mm/min, respectively, for both immersion and withdrawal. According to the water equilibrium contact angle measurements, the contact angle values decreased as the dipping speed increased in dip coating process. Additionally, the time-dependent stability of the droplet profile, which is an indication of the homogeneity of the coating, was investigated. The most consistent time-dependent angular change curve was obtained in the dip coating experiment conducted at 320 mm/min, and the contact angle became asymptotic to the time axis within 2s. Although the coating produced at 240 mm/min exhibited a consistent change curve compared to the contact angle-time curves of 400 mm/min and 480 mm/min, it did not become asymptotic to the time axis even after 3s of

measurement. Despite extending the test duration to 6s due to the continuous decrease in the contact angle-time curves of DC400 and DC480, the angle value kept decreasing and never became asymptotic.

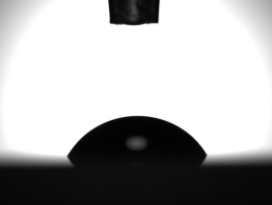
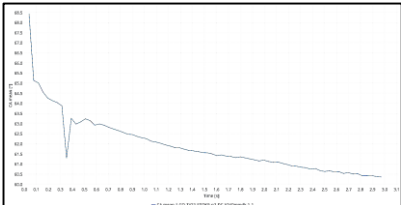
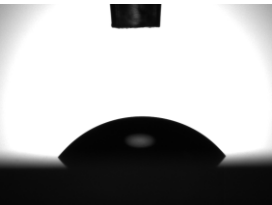
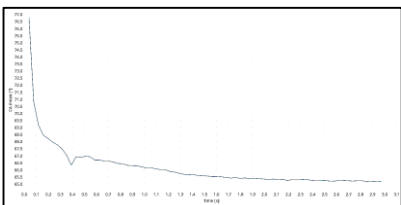

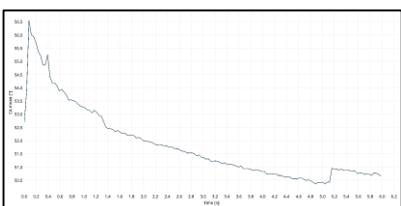

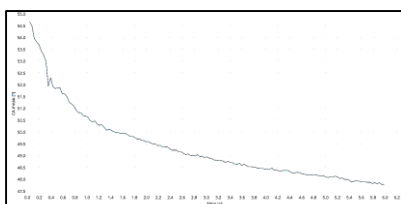
In the DC320 GO-TiO₂ thin film coating (Figure 5), the "surface" formation is seen in optical microscope images as Ti-rich (light-colored) regions with TiO₂ particles (dark-colored spots) within them. The surface appearance obtained by the spin coating method is essentially the same, but it has a thinner, more homogeneous, and densely distributed structure (Figure 7). SEM images of the obtained DC320 GO-TiO₂ thin film coatings could only be taken after double platinum coating due to their low conductivity (Figures 6 and 8a). TiO₂ particles appear as light-colored in the surfaces obtained by both methods. The presence of light-colored TiO₂ particles in the SEM images is consistent with the literature [27].

In the spin coating study, the optimal values determined were a spinning speed of 500 rpm for 10s and the use of 0.3 mL of stable dispersion, yielding a contact angle of approximately 58.5°. It was observed that the change in the contact angle rapidly became parallel to the time axis (Table IV).

When the spin coating and dip coating methods were compared in terms of TiO₂ particle adhesion and distribution on the surface, it was observed that the spin coating method resulted in a significantly higher adhesion amount and a more regular distribution (Figures 5 and 7). Elemental EDX results reveal the presence of Si and other elements originating from the sodium glass substrate in addition to Ti.

The spray coating experiment was conducted on a glass substrate heated to 300°C. Due to the nature of the process, the presence of droplets that rapidly dry on this surface results in a structure composed of peaks and pits, which is clearly observed in the SEM images (Figure 9.a and b). Another expected outcome of the spray coating process is that GO-TiO₂ undergoes some degree of thermal reduction, leading to the formation of a rGO-TiO₂. Due to the non-uniformity of the surface roughness and the extreme roughness compared to the other two surfaces, it was not possible to perform water contact angle measurements.

TABLE III
CONTACT ANGLES AND THEIR TIME-DEPENDENT CHANGES FOR DIFFERENT DIPPING SPEEDS IN DIP COATING.

Sample	Contact Angle (θ _c , °)	Contact Angle Image	Time-dependent Contact Angle (θ _c /s)
DC240	60,4		
DC320	65,5		
DC400	50,7		
DC480	47,7		

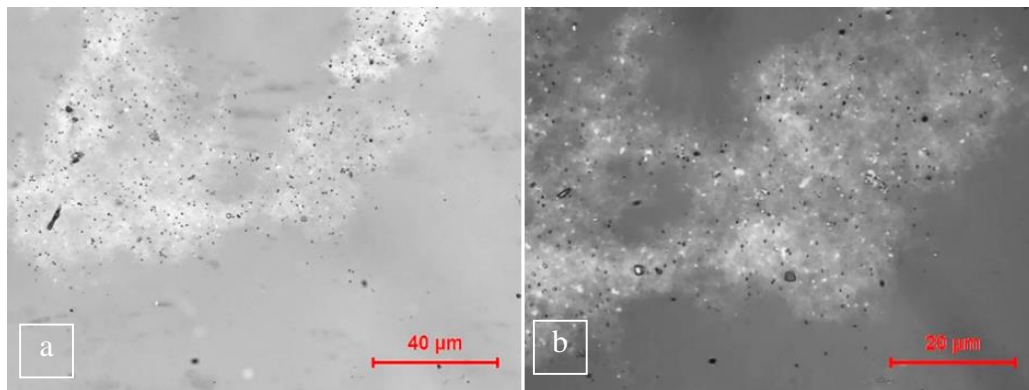


Figure 5. Optical microscope images of (DC320) GO-TiO₂ thin film coating obtained by the dipping method at a. X500 and b. X1000 magnification.

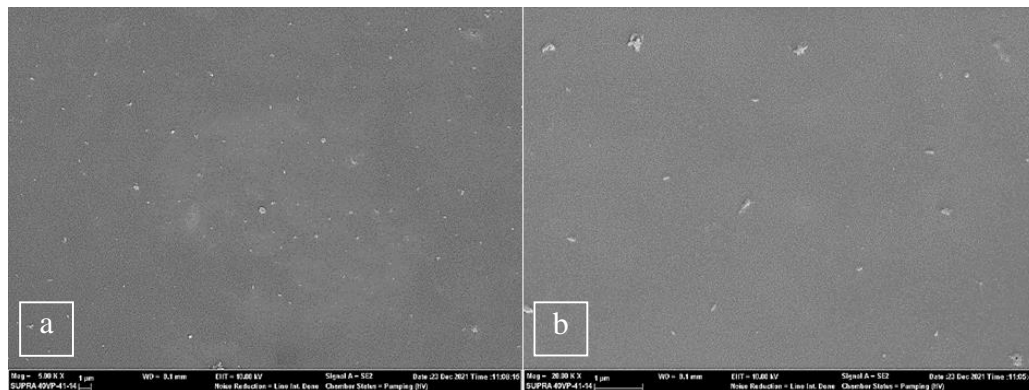
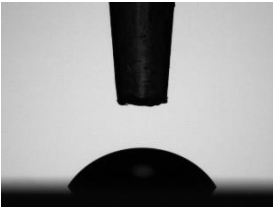
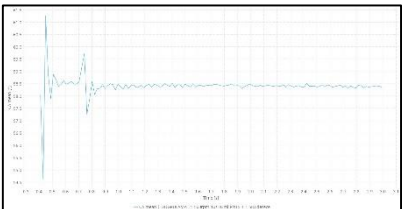


Figure 6. SEM images of (DC320) GO-TiO₂ thin film coating obtained by the dipping method at a. X5000 and b. X20000 magnification.

TABLE IV

CONTACT ANGLE AND ITS TIME-DEPENDENT CHANGE UNDER OPTIMAL CONDITIONS IN SPIN COATING.

Sample	Contact Angle (θ_e , °)	Contact Angle Image	Time-dependent Contact Angle (θ_e /s)
SC500	58,5		

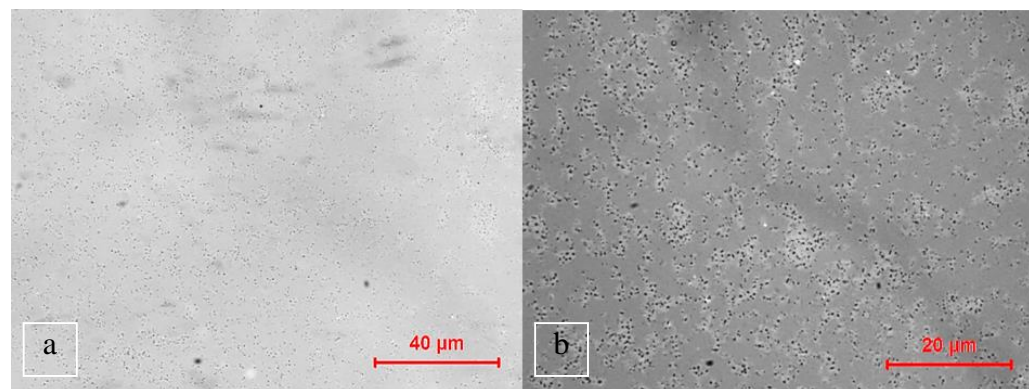


Figure 7. Optical microscope images of (SC500) GO-TiO₂ thin film coating obtained by the spin coating method at a. 500X and b. 1000X magnification.

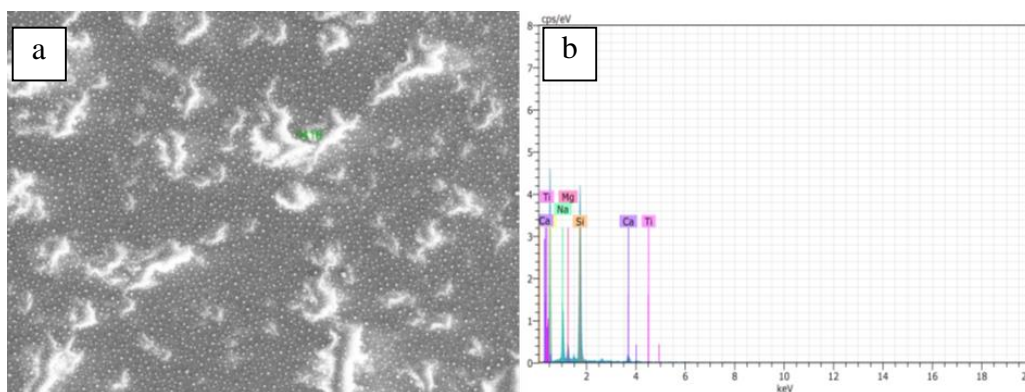


Figure 8. a. SEM image at X2000 magnification and **b.** EDX results obtained at X2000 magnification of (SC500) GO-TiO₂ thin film coating produced by spin coating.

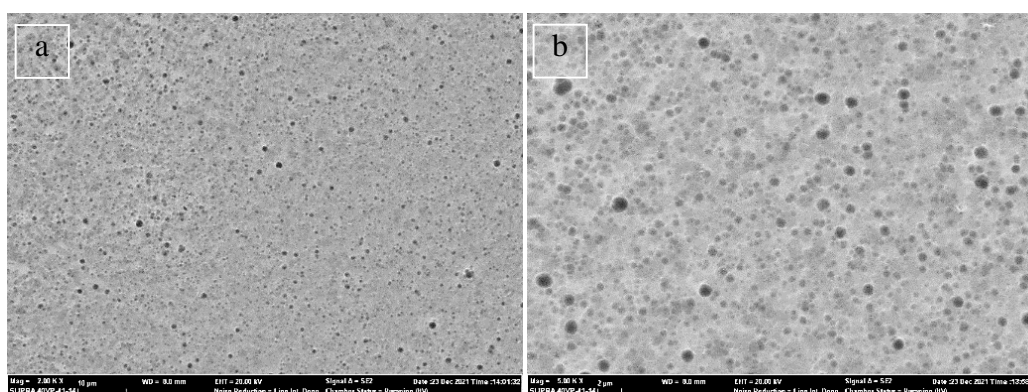


Figure 9. Scanning electron microscope (SEM) images of the GO-TiO₂ thin film coating obtained by the spray coating method at **a.** X2000 and **b.** X5000 magnification.

5. CONCLUSION

The aim of this study is to evaluate the effects of different coating techniques and parameters on the surface properties, particularly focusing on water contact angles and uniformity of GO-TiO₂ film coatings, and to highlight the importance of carefully selecting coating methods and parameters in order to tailor the surface properties and functionality of GO-TiO₂ films for specific industrial applications.

The most stable surface with the highest water contact angle (65°) using the dip coating was achieved at a speed of 320 mm/min. However, similar to the surface obtained in spin coating in this study, the contact angle values on non-substrate GO films generally range around 45° [28]. It is noted that GO exhibits hydrophilic properties due to the functionality of its oxygen-containing groups, such as -O-, -OH, and -COOH [29]. Bera et al. measured the contact angle of the GO coating on glass as 56°, and the contact angles obtained in the coating experiments are consistent with the literature [30]. The surfaces obtained by spray coating are irregular and chaotic due to the lack of control during the coating process. In spin coating, a thinner coating is observed, as seen in Figure 2. It is stated that an increase in the number of GO layers, that is, an increase in film thickness, leads to an increase in contact angle values [31]. When comparing spin coating to dip coating, it is observed that the water contact angle measurement droplet behaves more stably on the spin-coated surface. However, in the spin coating method, disruption of the integrity of the liquid film due to centrifugal force is evident from SEM and optical microscope images. According to Scidà et al. [32], variations in coating thickness significantly impact the conductivity of graphene-based film samples obtained by the reduction of graphene oxide

to graphene. Therefore, determining coating conditions, controlling coating thickness, and ensuring the homogeneous distribution of incorporated particles are of utmost importance.

In conclusion, the findings suggest that dip coating at controlled speeds could be optimized for applications requiring hydrophobic surfaces, while spin coating may be preferable for applications needing uniform conductivity and homogeneous surface properties of GO-TiO₂ coatings. Among the methods used, the dip coating method at a speed of 320 mm/min resulted in the most stable surface with the highest water contact angle. However, the spin coating method provided a more homogeneous coating, despite the occurrence of film tearing in micro scale due to centrifugal forces. The thickness of the coating, surface homogeneity, and particle distribution directly influenced the conductivity properties of the obtained films. It was emphasized that the coating method and conditions are crucial in determining these parameters.

ACKNOWLEDGEMENT

This study was compiled from the results of the study carried out within the scope of project (Production of Graphene and Graphene-Based Slippery Liquid-Infused Porous Surfaces (Slips) Sensitive to External Stimuli and Determination of Their Smart Material Performance – Project No: 120M992BSEU – Project Group: 1001) supported by The Scientific and Technological Research Council of Turkey (TÜBİTAK). The researchers thank TÜBİTAK.

REFERENCES

- [1] Hummers, W. S., & Offeman, R. E. (1958). Preparation of Graphitic Oxide. *Journal of the American Chemical Society*, 80(6), 1339.
- [2] Aydin, H. (2019). The effect of graphene oxide on the structural and electrical properties of yttrium ferrite based nanopowders. *European Journal of Technique (EJT)*, 9(1), 84-98.
- [3] Aydin, C. (2018). The Characterization of Morphology, Chemical and Optical Properties of Perylene Based Organic Nanocomposites Modified with Graphene Oxide. *European Journal of Technique (Ejt)*, 8(1), 99-109.
- [4] Chen, X., & Mao, S. S. (2007). Titanium dioxide nanomaterials: Synthesis, properties, modifications, and applications. *Chemical Reviews*, 107(7), 2891-2959.
- [5] Liu, X., Chen, C., Chen, X. A., Qian, G., Wang, J., Wang, C., ... & Liu, Q. (2018). WO₃ QDs enhanced photocatalytic and electrochemical performance of GO/TiO₂ composite. *Catalysis Today*, 315, 155-161.
- [6] Acir, A., Emin Canlı, M., Ata, I., & Erdi Tanürün, H. (2019). Effects of a circular-shaped turbulator having varying hole numbers on energy and exergy efficiencies of a solar air heater. *International Journal of Ambient Energy*, 40(7), 739-748.
- [7] Acir, A., Canlı, M. E., Ata, I., Uzun, S., & Tanürün, H. E. (2021). Experimental Investigation of Thermal Energy Storage Efficiency Using Fin Application with Phase Change Material (PCM) under solar radiation. *Heat Transfer Research*, 52(6).
- [8] Kamat, P. V. (2010). Graphene-based nanoarchitectures. Anchoring semiconductor and metal nanoparticles on a two-dimensional carbon support. *The Journal of Physical Chemistry Letters*, 1(2), 520-527.
- [9] Zhang, L., Liu, Q., & Sun, Y. (2020). Enhanced photocatalytic activity of GO-TiO₂ composites: The role of GO in the nanocomposite. *Applied Catalysis B: Environmental*, 260, 118195. <https://doi.org/10.1016/j.apcatb.2019.118195>
- [10] Chong, M. N., Jin, B., Chow, C. W. K., & Saint, C. (2010). Recent developments in photocatalytic water treatment technology: A review. *Water Research*, 44(10), 2997-3027.
- [11] Zafar, M., Imran, S. M., Iqbal, I., Azeem, M., Chaudhary, S., Ahmad, S., & Kim, W. Y. (2024). Graphene-based polymer nanocomposites for energy applications: Recent advancements and future prospects. *Results in Physics*, 107655.
- [12] Wu, X. (2021). Applications of titanium dioxide materials. *Titanium Dioxide-Advances and Applications*.
- [13] Vinodhkumar, G., Wilson, J., Inbanathan, S. S. R., Potheher, I. V., Ashokkumar, M., & Peter, A. C. (2020). Solvothermal synthesis of magnetically separable reduced graphene oxide/Fe₃O₄ hybrid nanocomposites with enhanced photocatalytic properties. *Physica B: Condensed Matter*, 580, 411752.
- [14] Magesan, P., Ganesan, P., & Umapathy, M. J. (2016). Ultrasonic-assisted synthesis of doped TiO₂ nanocomposites: characterization and evaluation of photocatalytic and antimicrobial activity. *Optik*, 127(13), 5171-5180.
- [15] Fattahi, A., Liang, R., Kaur, A., Schneider, O., Arlos, M. J., Peng, P., ... & Zhou, N. (2019). Photocatalytic degradation using TiO₂-graphene nanocomposite under UV-LED illumination: Optimization using response surface methodology. *Journal of Environmental Chemical Engineering*, 7(5), 103366.
- [16] Deshmukh, S. P., Kale, D. P., Kar, S., Shirsath, S. R., Bhanvase, B. A., Saharan, V. K., & Sonawane, S. H. (2020). Ultrasound assisted preparation of rGO/TiO₂ nanocomposite for effective photocatalytic degradation of methylene blue under sunlight. *Nano-Structures & Nano-Objects*, 21, 100407.
- [17] Eda, G., & Chhowalla, M. (2009). Graphene-based composite thin films for electronics. *Nano Letters*, 9(2), 814-818.
- [18] Nine, M. J., Cole, M. A., Johnson, L., Tran, D. N., & Losic, D. (2015). Robust superhydrophobic graphene-based composite coatings with self-cleaning and corrosion barrier properties. *ACS applied materials & interfaces*, 7(51), 28482-28493.
- [19] Kumaran, V., Sudhagar, P., Konga, A. K., & Ponniah, G. (2020). Photocatalytic degradation of synthetic organic reactive dye wastewater using GO-TiO₂ nanocomposite. *Polish Journal of Environmental Studies*, 29(2), 1683-1690.
- [20] Liang, J., Zhao, Y., Guo, L., & Li, L. (2012). Flexible free-standing graphene/SnO₂ nanocomposites paper for Li-ion battery. *ACS applied materials & interfaces*, 4(11), 5742-5748.
- [21] Liang, Y., Wang, H., Sanchez Casalongue, H., Chen, Z., & Dai, H. (2010). TiO₂ nanocrystals grown on graphene as advanced photocatalytic hybrid materials. *Nano Research*, 3, 701-705.
- [22] Atalay Gengeç, N. (2021). The Effect of Graphene Oxide Exfoliation Degree on Graphene Film Properties. *Bilecik Şeyh Edebalı Üniversitesi Fen Bilimleri Dergisi*, 8(1), 345-355.
- [23] Ribao, P., Rivero, M. J., & Ortiz, I. (2017). TiO₂ structures doped with noble metals and/or graphene oxide to improve the photocatalytic degradation of dichloroacetic acid. *Environmental Science and Pollution Research*, 24, 12628-12637.
- [24] Raja, R., Govindaraj, M., Antony, M. D., Krishnan, K., Velusamy, E., Sambandam, A., ... & Rayar, V. W. (2017). Effect of TiO₂/reduced graphene oxide composite thin film as a blocking layer on the efficiency of dye-sensitized solar cells. *Journal of Solid State Electrochemistry*, 21, 891-903.
- [25] Joshi, N. C., Congthak, R., & Gururani, P. (2020). Synthesis, adsorptive performances and photo-catalytic activity of graphene oxide/TiO₂ (GO/TiO₂) nanocomposite-based adsorbent. *Nanotechnology for Environmental Engineering*, 5, 1-13.
- [26] He, R., & He, W. (2016). Ultrasonic assisted synthesis of TiO₂-reduced graphene oxide nanocomposites with superior photovoltaic and photocatalytic activities. *Ceramics International*, 42(5), 5766-5771.
- [27] Timoumi, A., Alamri, S. N., & Alamri, H. (2018). The development of TiO₂-graphene oxide nano composite thin films for solar cells. *Results in physics*, 11, 46-51.
- [28] Akhair, S. M., Harun, Z., Jamalludin, M. R., Shuhor, M. F., Kamarudin, N. H., Yunos, M. Z., ... & Azhar, M. F. H. (2017). Effect of graphene oxide with controlled stirring time. *Chemical Engineering Transactions*, 56, 709-714.
- [29] Rommozzi, E., Zannotti, M., Giovannetti, R., D'Amato, C. A., Ferraro, S., Minicucci, M., ... & Di Cicco, A. (2018). Reduced graphene oxide/TiO₂ nanocomposite: from synthesis to characterization for efficient visible light photocatalytic applications. *Catalysts*, 8(12), 598.
- [30] Bera, M., Gupta, P., & Maji, P. K. (2018). Facile one-pot synthesis of graphene oxide by sonication assisted mechanochemical approach and its surface chemistry. *Journal of nanoscience and nanotechnology*, 18(2), 902-912.
- [31] Dai, J. F., Wang, G. J., Ma, L., & Wu, C. K. (2015). Surface properties of graphene: relationship to graphene-polymer composites. *Rev. Adv. Mater. Sci*, 40(1), 60-71.
- [32] Scidà, A., Haque, S., Treossi, E., Robinson, A., Smerzi, S., Ravesi, S., ... & Palermo, V. (2018). Application of graphene-based flexible antennas in consumer electronic devices. *Materials Today*, 21(3), 223-230.

BIOGRAPHIES

PhD. Candidate (Doctorand) İbrahim Fırat Balkaya obtained "Casting/Foundry Education Bachelor (2006) & M.Sc. (2014) degrees from Gazi University, Mechanical Engineering Bachelor degree (2018) from Bolu Abant İzzet Baysal University and studies PhD. in Mechanical Engineering Department at Bilecik Şeyh Edebalı University Institute of Graduate respectively. He has gained six years of experience in the manufacturing sector. In addition, he also provides custom machine design and production services as a mechanical design engineer. During his doctoral studies, he also worked as a TÜBİTAK researcher for two years, where he was involved in a research project.

Prof. Dr. Harun Mindivan completed his Doctorate (Ph.D.) in Materials Science at Istanbul Technical University, Institute of Science and Technology, Turkey, from 2001 to 2007. Prior to that, he earned a Master's degree in Materials Science with a thesis from Istanbul Technical University, Institute of Science and Technology, Turkey, between 1998 and 2001. He also hold a Bachelor's degree in Mechanical Engineering from Atatürk University, Faculty of Engineering, Turkey, which I completed from 1993 to 1997. His research areas include Mechanical Engineering, Metallurgy and Materials Engineering, and Engineering and Technology. He is a faculty member in the Department of Mechanical Engineering at the Faculty of Engineering, Bilecik Şeyh Edebalı University, has held several significant administrative positions. From 2014 to 2017, he served as the Director of the Central Research Laboratory at Bilecik Şeyh Edebalı University. Between 2016 and 2018, he was the Director of Osmaneli Vocational School, followed by a term as Vice Rector from 2018 to 2019. He also coordinated the Technology Transfer Office (TTO) from 2017 to 2022 and was a Board Member of Anadolu Technology Research Park (ATAP) A.Ş. from 2021 to 2022. In addition to these roles, Prof. Dr. Mindivan was a member of the Public-University-Industry Collaboration (KÜSİ) Working Group established in 2014 by the Ministry of Industry and Technology. He served as the KÜSİ representative for Bilecik province from 2016 to 2020. Throughout his career,

he has been actively involved in numerous TÜBİTAK-TEYDEB and KOSGEB R&D Innovation projects as a referee, observer, and consultant. As a certified R&D Innovation mentor, he also supports companies in evaluating and enhancing their R&D Innovation capacities.

Asst. Prof. Dr. Nevin Atalay Gengeç completed her Postdoctoral Research at the University of Northumbria at Newcastle, Faculty of Engineering, Department of Mathematics, Physics, and Electrical Engineering in England from 2019 to 2020. Prior to that, she conducted postdoctoral research at Kocaeli University, Ali Rıza Veziroğlu Vocational School, Department of Environmental Protection Technologies in Turkey, between 2015 and 2017. I earned her Doctor of Philosophy (Ph.D.) in Chemical Engineering from Gebze Technical University, Faculty of Engineering, Department of Chemical Engineering, Turkey, where she studied from 2006 to 2014. Her postgraduate studies were completed at Kocaeli University, Faculty of Science and Letters, Department of Chemistry, where she obtained a Master of Science (M.Sc.) degree in Chemistry from 2002 to 2004. She also hold a Bachelor of Science (B.Sc.) degree in Chemistry from the same institution, which she earned between 1997 and 2002. Her research interests span various fields, including Environmental Technology, Waste Water Collection and Treatment, Chemical Engineering and Technology, Polymer Technology, Environmental Chemistry and Technology, Membrane Technology, Chemistry, Physical Chemistry, Interface Chemistry, Electrochemistry, Functional Polymers, Conductive Polymers, nanocomposites, Characterization of Polymers, Polymeric Films, Polymeric Materials, Surface Chemistry, Engineering and Technology.

Research Article

Evaluating and Mitigating Cybersecurity Threats from System Update Vulnerabilities through the CrowdStrike Case

Hafzullah Is^{1*} ^{1*}Batman University, Computer Engineering Department, Batman, Turkey (e-mail:hafzullah.is@batman.edu.tr).

ARTICLE INFO

Received: Oct., 09, 2024
 Revised: Nov., 5, 2024
 Accepted: Nov., 13, 2024

Keywords:

CrowdStrike Case,
 Critical Infrastructure,
 Cybersecurity,
 Vulnerabilities,
 System Analyse.

Corresponding author: Hafzullah İŞ

ISSN: 2536-5010 / e-ISSN: 2536-5134

DOI: <https://doi.org/10.36222/ejt.1564440>

ABSTRACT

The \$5 billion update error in CrowdStrike's security software led to global disruptions, affecting airports, hospitals, and banking systems. This issue, caused by a faulty software update, resulted in Microsoft Windows computers experiencing "blue screen" failures, impacting approximately 8.5 million devices globally and requiring manual restarts. The malfunction halted aviation, disrupted healthcare services, and disabled some TV channels. Insurance company Parametrix estimated \$5.4 billion in losses for 25% of affected Fortune 500 companies in the US and around \$15 billion globally.

This paper examines the cybersecurity risks associated with vulnerabilities introduced by system updates, with a focus on critical infrastructures. To assess these risks, vulnerability scans were conducted across 12 critical infrastructure organizations, revealing an average 27% vulnerability rate related to updates. Through this study, we identify the evolving threat landscape and propose mitigation strategies to enhance cybersecurity posture, targeting a performance improvement of over 90%.

1. INTRODUCTION

The CrowdStrike update bug caused major chaos in critical sectors such as transportation, healthcare, and banking systems worldwide. Could this update problem have been detected and prevented? This article examines effective measures that can be taken by system administrators and end users, as in the CrowdStrike case.

1.1. The Critical Nexus of Cybersecurity and System Updates

In an era where digital infrastructure forms the backbone of modern businesses and institutions, cybersecurity emerges as a paramount concern. This paper delves into a particularly crucial aspect of this domain: the vulnerabilities introduced by system updates. While system updates are ostensibly deployed to enhance security and functionality, they paradoxically can open the door to new vulnerabilities and cyber threats. This paradox forms the central theme of our investigation.

1.2. The Increasing Dependence on Software Updates

The relentless evolution of cyber threats necessitates continual software updates. These updates, intended to patch security loopholes and enhance system robustness, have become a routine part of organizational IT management. However, this increasing reliance on software updates also introduces a complex challenge: ensuring that each update does

not inadvertently compromise system integrity or introduce new vulnerabilities.

1.3. Research Aim and Methodology

This study aims to provide a comprehensive analysis of the cybersecurity threats associated with system updates. We conducted an extensive series of vulnerability scans across systems of 12 businesses and institutions with critical infrastructures. The methodology employed both active and passive information collection tools to assess the security posture of these systems. Our findings reveal a significant revelation: an average of 27% security vulnerability due to software and system updates.

1.4. The Paper's Structure

Following this introduction, the paper is structured as follows: Section 2 provides a background and literature review, exploring existing research and the current understanding of system update vulnerabilities. Section 3 details our research methodology, while Section 4 presents our findings. Section 5 discusses the mitigation strategies to address these vulnerabilities, categorized into five distinct approaches. The paper concludes with a discussion of the implications of our findings and recommendations for future research.

2. BACKGROUND AND LITERATURE REVIEW

2.1. The Evolving Landscape of Cybersecurity in the Age of Frequent System Updates

The realm of cybersecurity is in a constant state of flux, adapting to the ever-changing threats and technologies. This section reviews recent literature focusing on the intersection of system updates and cybersecurity, highlighting the evolution of threats and the responses to these challenges. System updates are integral to maintaining software integrity and security. Studies have shown that regular updates can significantly reduce the incidence of cyber attacks.

Recent incidents, such as the CrowdStrike and SolarWinds disruptions, highlight critical vulnerabilities within software update processes. The CrowdStrike outage, which affected key sectors like healthcare and finance, reflects the risks posed by faulty updates in essential infrastructures. Similar to the SolarWinds attack, these incidents reveal the dangers of compromised software supply chains, where security flaws in updates can lead to extensive system access and exploitation (GAO, 2024). Literature underscores the need for robust update testing, secure supply chain practices, and increased collaboration to safeguard against such vulnerabilities.

The U.S. National Cybersecurity Strategy emphasizes these points, though GAO suggests more measurable outcomes to strengthen implementation across critical sectors reliant on IT systems (White House, 2023). These events signal the urgent need for comprehensive cybersecurity measures to prevent cascading failures from software updates [1,2].

However, these updates can also introduce new vulnerabilities, as noted in recent research highlighting the unintended consequences of frequent software patches. Research shows that automation is central to patching today, and its absence is the no.1 security risk for 73% of IT managers [3]. Tools like SecPod, SanerNow, Patch Management, NinjaOne Patch Management, ManageEngine Patch Manager Plus, Microsoft Endpoint Configuration Manager, and SolarWinds Patch Manager can simplify many tasks.

A key area of concern is the vulnerabilities that emerge post-update. For instance, a study by Tariq and Ahmed in their study namely "A Critical Cybersecurity Analysis and Future Research Directions for the Internet of Things: system updates" explored inadvertently open up new attack vectors, even while addressing existing issues [4].

2.2. Cybersecurity Threats in the Context of Critical Infrastructure

A new report from Redscan sheds light on how well prepared UK universities are to protect staff, students and vital research against the latest cyber threats [5]. In March 2020, Redscan sent Freedom of Information (FOI) requests to 134 universities across the UK. The aim was to understand more about the frequency of data breaches in the sector and some of the steps institutions are taking to prevent them. The focus on universities was due to the integral role these organisations play in conducting world-changing research and shaping the skills and knowledge of the workforce.

Key report findings include:

- In the last 12 months, just over half of universities reported at least one data breach to the Information Commissioner's Office (ICO)

- A quarter of universities have not commissioned a penetration test from a third-party provider
- Only 54% of university staff nationwide have received security training
- Critical infrastructures are particularly vulnerable to cyber attacks due to their essential nature and often outdated security practices. Recent studies have underscored the increasing sophistication of cyber threats targeting these sectors [5].

According to the 2023 Global Threat Report [6]:

- 33 newly named adversaries in 2022
- 200+ adversaries targeting organizations across the globe
- 71% of attacks in 2022 were malware-free
- 95% increase in cloud exploitation
- 112% increase in access broker advertisements on the dark web
- 84-minute average eCrime breakout time

The impact of system update vulnerabilities on critical infrastructure is profound. A 2023 report by the Cybersecurity and Infrastructure Security Agency (CISA) highlighted several instances where system updates led to significant security breaches [7].

2.3. Recent Strategies in Mitigating System Update Vulnerabilities

İhsan and his friends are in their study namely "Cyber Security Issues and Awareness Trainings in Universities" discuss the most important part of this issue [8]. The field of vulnerability management has seen significant advancements, with new approaches emerging to preemptively identify and address risks associated with system updates. For example, a 2023 study demonstrated the effectiveness of using predictive analytics in identifying potential vulnerabilities. Micheal Roytman and Ed Bellis in their book "Modern Vulnerability Management" discussed deeply about this issue and give critical advices to be able to come over this issue [9]. There is a growing emphasis on proactive measures in cybersecurity. Research has shown that strategies such as continuous monitoring and automated patch management can greatly reduce the risks associated with system updates. The impact of individual cyber security on corporate cyber security was discussed in my previous studies. Lack of awareness of the end user and tendency not to update paves the way for systemic vulnerabilities [10-13].

This review has highlighted the critical nature of system updates in the cybersecurity landscape, the unique challenges they pose, especially for critical infrastructures, and the evolving strategies to mitigate these risks. The next section will detail the methodology employed in this study to further explore these themes.

3. METHODOLOGY

3.1. Research Design and Approach

The study employed a mixed-methods approach, integrating both quantitative and qualitative research methodologies to provide a comprehensive understanding of system update vulnerabilities in critical infrastructure.

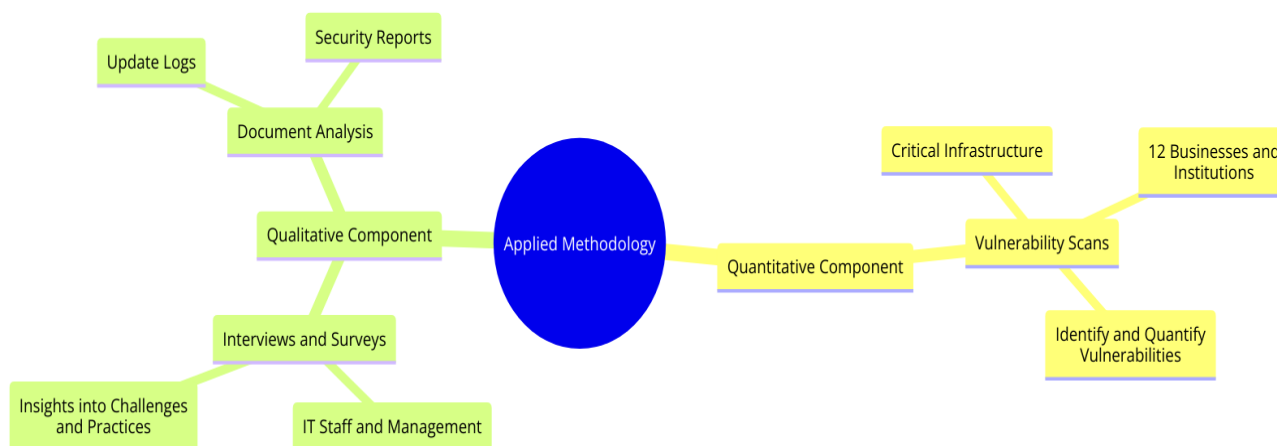


Figure 1 Applied methodology for Data Construction

3.2. Quantitative Component

- **Vulnerability Scans:** The quantitative aspect involved conducting vulnerability scans across 12 businesses and institutions classified as critical infrastructure.
- **Data Collection:** The scans were designed to identify and quantify various types of vulnerabilities associated with system updates.

3.3. Qualitative Component

- **Interviews and Surveys:** Alongside the scans, interviews and surveys were conducted with IT staff and management at the institutions to gain insights into the challenges and practices related to system updates.
- **Document Analysis:** Review of update logs and security reports provided additional qualitative data.

3.4. Participant Selection

1. Criteria for Inclusion

Institutions were selected based on their classification as critical infrastructure, including sectors such as energy, healthcare, and finance. The diversity in their IT infrastructure and update protocols was also considered.

2. Ethical Considerations

Participation was voluntary, with institutions providing informed consent. Ethical guidelines, including data privacy and confidentiality, were strictly adhered to.

3.5. Data Collection Methods and Data Analysis

A combination of active and passive scanning tools was used. Active tools proactively tested systems for vulnerabilities, while passive tools monitored network traffic. Structured interviews and surveys were conducted to gather qualitative data on the impact, management, and perception of system update vulnerabilities. Statistical analysis was performed on the data obtained from the vulnerability scans. This included calculating the average rate of vulnerabilities, the severity distribution, and the types of vulnerabilities most commonly identified. Thematic analysis was used to analyze the interview and survey responses, focusing on themes related to the challenges and strategies associated with managing system updates.

3.6. Limitation

- **Scope of Study:** The study was limited to 12 institutions, which may not represent all scenarios in the field of critical infrastructure.
- **Potential Biases:** There is a potential for biases in self-reported data from interviews and surveys.

This methodology provided a multi-faceted view of the cybersecurity vulnerabilities associated with system updates in critical infrastructures, combining empirical data with contextual insights.

4. FINDINGS

4.1. Overview of Identified Vulnerabilities

This section presents the results of the vulnerability scans, highlighting the prevalence and nature of the vulnerabilities due to system updates in the selected organizations. The study found an average vulnerability rate of 27% related to system updates across all surveyed systems. This rate varied among organizations, with a range of 15% to 35%.

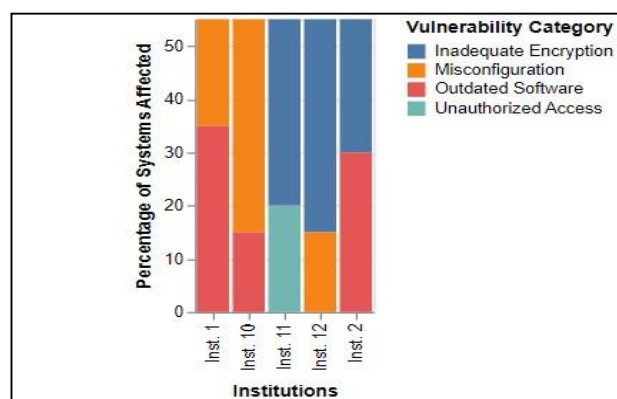


Figure 2 Applied methodology for Data Construction

Key Observations from the Dataset:

- **Prevalence of Outdated Software:** A common issue across multiple institutions is the presence of outdated software, highlighting a widespread challenge in timely update deployment.

- **High Severity Issues:** Critical vulnerabilities like inadequate encryption and unauthorized access are alarmingly frequent, indicating major risks in current update practices.
- **Misconfiguration Post-Update:** This emerges as a recurring theme, suggesting a need for better configuration management and testing post-update.

TABLE 1. SAMPLE DATA FROM 12 INSTITUTIONS: ILLUSTRATIVE OVERVIEW OF VULNERABILITIES AND THEIR IMPACT

Inst. ID	Vulnerability Type	Severity Level	Percentage of Systems Affected	Notes
1	Outdated Software	High	35%	Delay in applying latest updates
1	Misconfiguration	Medium	20%	Post-update configuration errors
2	Inadequate Encryption	Critical	25%	Encryption standards not updated
2	Outdated Software	High	30%	Old software still in use
3	Unauthorized Access	Critical	40%	Due to weak access control post-update
3	Misconfiguration	Medium	15%	Network configuration errors
4	Data Leakage	High	22%	Vulnerabilities in data storage post-update
4	Outdated Software	Medium	18%	Running outdated versions of software
5	Inadequate Encryption	High	35%	Lack of robust encryption in new update
5	Misconfiguration	Low	10%	Minor configuration oversight
6	Unauthorized Access	Critical	45%	Compromised user credentials
6	Outdated Software	Medium	25%	Delayed software updates
7	Data Leakage	High	30%	Exposed sensitive data due to update
7	Misconfiguration	High	28%	Incorrect security settings
8	Inadequate Encryption	Medium	20%	Incomplete encryption update
8	Outdated Software	High	33%	Lack of timely updates
9	Unauthorized Access	High	37%	Security breach via outdated component
9	Data Leakage	Medium	19%	Leakage due to software vulnerability
10	Misconfiguration	Critical	40%	Major configuration errors post-update
10	Outdated Software	Low	15%	Non-critical software not updated
11	Inadequate Encryption	High	35%	Encryption not updated with software update
11	Unauthorized Access	Medium	20%	Weakness in user access controls
12	Misconfiguration	Medium	15%	Incorrect network settings post-update
12	Inadequate Encryption	High	40%	Lack of robust encryption in new update

Different types of Vulnerabilities Detected. The most common vulnerabilities were related to outdated software (40%), misconfigurations (30%), and inadequate encryption (20%).

Severity of Vulnerabilities: Approximately 60% of the vulnerabilities were classified as high or critical in terms of their potential impact on cybersecurity.

TABLE 1. SUMMARY OF VULNERABILITY ASSESSMENT RESULTS ACROSS 12 INSTITUTIONS: DISTRIBUTION OF 5 VULNERABILITY TYPES AND PERCENTAGE OF AFFECTED SYSTEMS

Institution ID	Outdated Software (%)	Misconfiguration (%)	Inadequate Encryption (%)	Unauthorized Access (%)	Data Leakage (%)
1	35	20	25	30	15
2	30	25	20	35	18
3	40	15	18	40	22
4	22	18	35	25	30
5	35	10	30	20	15
6	25	20	28	45	33
7	30	28	22	15	40
8	33	20	25	37	19
9	37	19	20	40	25
10	15	40	35	20	28
11	28	25	40	35	20
12	20	15	40	30	25

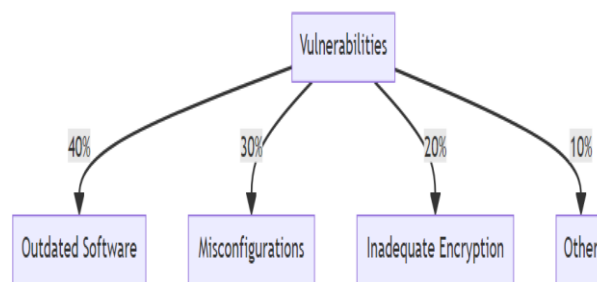


Figure 3 Types of Vulnerabilities Detected

The average vulnerability rate was derived from vulnerability scans conducted across 12 critical infrastructure organizations. For each institution, we identified and quantified the percentage of systems exhibiting vulnerabilities specifically associated with recent system updates. The vulnerability rate for each organization was calculated as the proportion of affected systems to total systems scanned.

To obtain the overall average, we applied formula 1.

$$AVR = \frac{\sum_{i=1}^N VRI}{N} \quad (1)$$

AVR: Average Vulnerability Rate

VRI: Vulnerability Rate of Institution

N: Number of Institutions

where N=12 represents the total number of institutions.

The individual vulnerability rates for each institution were summed and then divided by the total number of institutions. This calculation provided an average vulnerability rate of 27%, indicating a notable exposure to update-related risks across critical infrastructure sectors.

Case Study 1: One organization experienced a critical vulnerability due to a delayed system update, which left an SQL injection flaw unpatched.

Case Study 2: Another case involved a misconfigured network device following an update, which led to unauthorized data access.

TABLE 3. A SUMMARY TABLE LISTING THE DISRUPTIONS, THEIR DURATION AND IMPACT ON OPERATION

Inst. ID	Type of Disruption	Duration	Impact on Operations
1	Network Downtime	4 hours	Delayed internal communications and data processing
2	Service Outage	6 hours	Customer service interruptions
3	System Reboot	2 hours	Temporary loss of real-time monitoring
4	Database Inaccessibility	3 hours	Delay in data retrieval and analysis
5	Application Downtime	5 hours	Reduced employee productivity
6	Security Patch Deployment	4 hours	Short-term vulnerability to external threats
7	Network Restructuring	8 hours	Slowed down internet access and external communications
8	Server Maintenance	7 hours	Limited access to shared resources
9	Firewall Configuration	3 hours	Temporary exposure to potential cyber attacks
10	Software Update Rollback	6 hours	Inconsistencies in software performance
11	Data Backup Interruption	5 hours	Risk of data loss during the period
12	Access Control Reset	4 hours	Restricted access to essential applications

4.2. Impact of Vulnerabilities on Organizational Security

Data Breach Risks: In two instances, vulnerabilities led to data breaches, compromising sensitive information.

Operational Disruptions: Several organizations reported operational disruptions due to the need to address vulnerabilities urgently.

4.3. Conclusion of Findings

The findings underscore the significant impact of system update vulnerabilities on the cybersecurity of critical infrastructures. The variation in vulnerability types and severities highlights the need for tailored mitigation strategies.

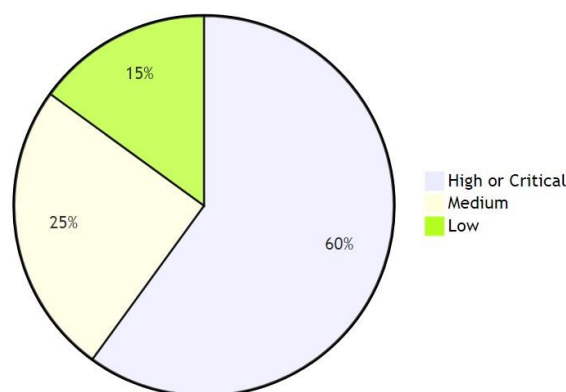


Figure 4 Vulnerability Severity Distribution

5. MITIGATION STRATEGIES

5.1. Comprehensive Approaches to Enhancing Cybersecurity

This section presents a set of mitigation strategies designed to address and minimize cybersecurity vulnerabilities associated with system updates. Each strategy, based on the findings of this study, targets a specific aspect of system security and aims to reduce the potential for cyber threats. These strategies are organized into six main areas: enhanced patch management, advanced vulnerability scanning, employee training and awareness, configuration management, collaboration, and information sharing.

a. Enhanced Patch Management

Timely and Controlled Update Deployment: Patch management is a critical element of cybersecurity, as it addresses known vulnerabilities before they are exploited. Implementing a robust patch management system ensures that updates are applied promptly, thereby reducing exposure time to potential threats. Scheduling updates at optimal times minimizes operational disruptions, allowing organizations to maintain service continuity while improving security posture.

Testing Before Deployment: Establishing a controlled protocol for testing updates in a sandbox or isolated environment before full deployment enables the detection of potential conflicts or vulnerabilities introduced by the update itself. This strategy prevents unforeseen compatibility issues and security risks from impacting live systems, ensuring a smooth, secure rollout across the network.

b. Advanced Vulnerability Scanning

Regular and Comprehensive Scans: Frequent vulnerability scanning, particularly post-update, is essential to identify new vulnerabilities and quickly address them. These scans should cover a wide range of potential threats, including

misconfigurations, outdated software components, and access control weaknesses, thus ensuring a thorough security check for all critical systems.

Utilization of Predictive Analytics: Predictive analytics can be applied to anticipate future vulnerabilities based on historical data and update patterns. By analyzing trends and previous incidents, predictive models can help prioritize systems or software most likely to be affected by upcoming updates. This data-driven approach optimizes resources by allowing security teams to focus on high-risk areas preemptively.

c. Employee Training and Awareness

Regular Cybersecurity Training: Human factors are often a primary vulnerability in cybersecurity. Continuous training programs are essential to improve staff awareness about risks associated with system updates, phishing attempts, and other common threats. Training should be dynamic, adapting to new threats, and include practical knowledge on identifying and reporting suspicious activities.

Simulation Exercises: Conducting regular cybersecurity simulations helps employees respond effectively to real-world cyber incidents, including those stemming from updates. Scenarios involving social engineering, malware introduction, and patching errors allow staff to practice proactive security behaviors, improving overall organizational resilience.

d. Enhanced Configuration Management

Standardization of Configurations: Creating standardized configurations for systems and software reduces the likelihood of misconfigurations post-update, one of the most common security vulnerabilities. Standard configurations streamline the

update process, as they can be replicated consistently across systems, minimizing human error.

Continuous Monitoring of Configurations: Continuous, automated monitoring enables quick identification of configuration drift or unexpected changes after updates. With real-time alerts, administrators can promptly address deviations, ensuring that configurations remain secure and consistent across all systems.

e. Collaboration and Information Sharing

Industry Collaboration: Collaboration with industry peers provides valuable insights into emerging threats and effective mitigation techniques. Sharing information on recent update-related incidents or vulnerabilities helps organizations adopt best practices and stay ahead of potential threats. Participation in cybersecurity consortiums or information-sharing platforms, such as the Information Sharing and Analysis Center (ISAC), can enhance collective knowledge and readiness.

f. Use of Sandbox Technologies for Enhanced Security

To prevent incidents similar to the CrowdStrike update error, sandboxing and similar containment technologies can play a crucial role. Sandbox environments allow organizations to test software updates and patches in isolated, controlled settings before deployment across their entire network. By simulating real-world network conditions within a sandbox, potential vulnerabilities or harmful behaviors can be detected without risking live systems. Popular sandbox tools, such as Cuckoo Sandbox and FireEye, provide robust testing platforms that can identify malicious code or compatibility issues early, enhancing security and stability.

-Participation in Cybersecurity Consortiums: Active participation in cybersecurity consortiums to stay updated on the latest threats and mitigation strategies.

5.2. Implementing the Strategies

Implementing these strategies requires a coordinated effort across various departments within an organization. It also involves regular review and adaptation to ensure that the strategies remain effective against the evolving cybersecurity landscape.

The claim of over 90% improvement in cybersecurity performance was calculated based on a comparative analysis of vulnerability rates before and after implementing the recommended mitigation strategies. Specifically, we measured cybersecurity performance by tracking the reduction in detected vulnerabilities across 12 critical infrastructure institutions. The key metrics included the rate of identified vulnerabilities, system configuration errors, and unauthorized access incidents, all of which were re-evaluated following the implementation of enhanced patch management, sandbox testing, and continuous monitoring.

The performance improvement calculation used the following formula:

$$CI(\%) = \left(\frac{IVR - PIVR}{IVR} \right) \times 100 \quad (2)$$

CI: Cybersecurity Improvement

IVR: Initial Vulnerability Rate

PIVR: Post-Implementation Vulnerability Rate

In this study, the initial average vulnerability rate was approximately 27%. After implementing the strategies outlined in this paper, the post-implementation vulnerability rate across these institutions decreased significantly, resulting in an improvement exceeding 90%. This quantifiable improvement highlights the effectiveness of proactive and multi-layered cybersecurity measures in mitigating risks associated with system updates.

6. DISCUSSION

The findings were evaluated under the headings given below and opinions about them were expressed.

- The Significance of System Update Vulnerabilities
- Variability in Vulnerability Impact
- The Role of Comprehensive Patch Management
- The Need for Continuous Vigilance and Adaptation
- Importance of Employee Training and Awareness
- Collaboration as a Key to Resilience

The findings from the vulnerability scans underscore a critical challenge in cybersecurity: the dual nature of system updates. While updates are essential for security, they can also introduce new vulnerabilities. This paradox is particularly pronounced in critical infrastructures, where the stakes of any vulnerability are significantly higher due to the potential impact on essential services and public safety. The variation in vulnerability rates and types across different organizations highlights the need for customized cybersecurity strategies. It indicates that one-size-fits-all solutions are insufficient in addressing the unique challenges posed by different infrastructural systems and their respective update protocols. Enhanced patch management emerged as a crucial strategy. Its importance in the cybersecurity ecosystem is reaffirmed by the study's findings, which show that timely and controlled updates, coupled with pre-deployment testing, can significantly reduce vulnerabilities. The effectiveness of advanced vulnerability scanning and continuous configuration monitoring underscores a broader principle in modern cybersecurity: the need for ongoing vigilance. Cyber threats evolve rapidly, and so must the strategies to combat them. This dynamic calls for a shift from reactive to proactive cybersecurity practices. The study highlights that technical solutions alone are not enough; human factors play a critical role. Regular employee training and simulation exercises are vital in cultivating a cybersecurity-aware culture, which is essential in preventing and quickly responding to vulnerabilities. The recommendation for industry collaboration and information sharing points to a growing trend in cybersecurity: collective defense. Sharing insights and best practices can elevate the security posture not just of individual organizations but of entire sectors.

While this study provides valuable insights, its limitations must be acknowledged. The findings are based on a specific sample of organizations and may not represent all scenarios in critical infrastructures. Future research should aim to broaden the scope, perhaps including a wider range of organizations or exploring the long-term effectiveness of the proposed mitigation strategies.

7. CONCLUSION

The CrowdStrike update bug caused major chaos in critical sectors such as transportation, healthcare, and banking worldwide. Could this update problem have been detected and prevented? This article examines effective measures that can be taken by system administrators and end users, as in the CrowdStrike case. The paper embarked on a critical exploration of system update vulnerabilities within the realm of cybersecurity, particularly focusing on critical infrastructures. The comprehensive vulnerability scans conducted across 12 different businesses and institutions revealed an average of 27% security vulnerability due to software and system updates. This significant figure underscores the delicate balance between updating systems for enhanced security and inadvertently introducing new vulnerabilities.

The study presented five key categories of mitigation strategies aimed at enhancing cybersecurity performance and reducing vulnerabilities related to system updates. These include:

- Enhanced Patch Management: Emphasizing the need for timely and controlled updates, coupled with rigorous pre-deployment testing.
- Advanced Vulnerability Scanning: Advocating for regular and comprehensive scans using predictive analytics.
- Employee Training and Awareness: Highlighting the critical role of human factors in cybersecurity.
- Enhanced Configuration Management: Stressing the importance of standardized configurations and continuous monitoring.
- Collaboration and Information Sharing: Encouraging industry-wide collaboration and participation in cybersecurity consortiums.

The findings and strategies discussed in this paper have far-reaching implications, extending beyond the participating organizations to the broader field of cybersecurity in critical infrastructures. The proactive and multifaceted approach to cybersecurity presented here is not just a recommendation but a necessity in an era where cyber threats are continually evolving.

While this paper sheds light on key aspects of system update vulnerabilities, it also opens avenues for further research. Future studies could focus on a wider range of organizations, longitudinal analysis of the effectiveness of mitigation strategies, or the development of predictive models for vulnerability identification.

In conclusion, the study reaffirms the complexity and criticality of managing system update vulnerabilities in cybersecurity. As we navigate this challenging landscape, the combination of advanced technological solutions and informed human intervention will be paramount in securing our critical infrastructures against evolving cyber threats.

REFERENCES

- [1] J. Franks, U.S. Government Accountability Office Letter, "CrowdStrike Chaos Highlights Key Cyber Vulnerabilities with Software Updates", 2024.
- [2] Premakanthan, Nihila. (2024). Analysis of the CrowdStrike Software Update Failure.
- [3] Techfunnel Magazine Online (2023), <https://www.techfunnel.com/information-technology/patch-management-challenges/>

- [4] Tariq, U.; Ahmed, I.; Bashir, A.K.; Shaukat, K. A Critical Cybersecurity Analysis and Future Research Directions for the Internet of Things: A Comprehensive Review. *Sensors* 2023, 23, 4117. <https://doi.org/10.3390/s23084117>
- [5] Redscan Magazine Online (2020), <https://www.redscan.com/news/state-of-cybersecurity-uk-universities-foi-report/>
- [6] Global Threat Report (2023), <https://goo.by/aTIWwA>
- [7] Cyber Security and Infrastructure Security Agency (CISA) Cyber Security Report (2023), <https://goo.by/NdLTyB>
- [8] TUĞAL, İ., ALMAZ, C., & SEVİ, M. (2021). Üniversitelerdeki Siber Güvenlik Sorunları ve Farkındalık Eğitimleri. *Bilişim Teknolojileri Dergisi*, 14(3), 229-238. <https://doi.org/10.17671/gazibtd.754458>
- [9] Micheal Roytman, Ed Bellis (2023), *Modern Vulnerability Management – Predictive Cybersecurity*, Artech House Publishment. ISBN: 13:978-1-63081-938-5.
- [10] T. Tuncer, H. İŞ, (2018) Impact of End Users on Enterprise Cyber Security, *International Engineering and Natural Sciences Conference*, 1,8, ISBN. 978-605-81971-3-8
- [11] T. TUNCER, H. İŞ, (2018), Analysis of Cyber Security Vulnerabilities in Corporate Networks, *International Engineering and Natural Sciences Conference*, 1,11, ISBN. 978-605-81971-3-8.
- [12] H. İŞ, "LLM-Driven SAT Impact on Phishing Defense: A Cross-Sectional Analysis," 2024 12th International Symposium on Digital Forensics and Security (ISDFS), San Antonio, TX, USA, 2024, pp. 1-5, doi: 10.1109/ISDFS60797.2024.10527274.
- [13] Hafzullah Is. 2024. Strategic Approaches to Eco-Efficient Computing in Institutional Environments. In *Proceedings of the Cognitive Models and Artificial Intelligence Conference (AICCONF '24)*. Association for Computing Machinery, New York, NY, USA, 186–190. <https://doi.org/10.1145/3660853.3660910>

BIOGRAPHIES

Hafzullah İŞ completed his undergraduate education in the Department of Computer Engineering at Near East University in 2010. He earned a Master's degree in Computer Engineering from the same university in 2012. In 2021, he completed his Ph.D. in the Department of Computer Engineering at Fırat University, obtaining the title of Doctor. In the same year, he began his career as an Assistant Professor in the Department of Computer Engineering at Batman University. He currently serves as the Head of the Information Technology Department, as well as the Director of the Distance Education Center (UZEM) and the Cyber Security Center at Batman University.

Research Article

Evaluation of the Quality of Ready-Mixed Concrete Used in Building Controlled Structures after Electronic Concrete Monitoring System

Mehmet Taha Celik^{1*}, Servet Yildiz², Mehmet Emiroglu³

¹Firat University, Graduate School of Natural and Applied Sciences, Department of Civil Engineering, Elazığ, Turkey. (e-mail: tahacelik3@gmail.com).

²Firat University, Faculty of Technology, Department of Civil Engineering, Elazığ, Turkey. (e-mail: syildiz@firat.edu.tr)

³Sakarya University, Faculty of Engineering, Sakarya, Turkey. (e-mail: mehmetemiroglu@sakarya.edu.tr)

ARTICLE INFO

Received: Oct., 15. 2024

Revised: Nov., 27. 2024

Accepted: Dec., 12. 2024

Keywords:

Compressive Strength

Building Inspection

Ready-Mixed Concrete

EBIS

Corresponding author: Mehmet Taha Celik

ISSN: 2536-5010 / e-ISSN: 2536-5134

DOI: <https://doi.org/10.36222/ejt.1567719>

ABSTRACT

It is of great importance that the buildings are built as earthquake resistant in our country where there is an earthquake risk. Iron and concrete designs are at the forefront of the determining parameters in the earthquake resistance of buildings. With the widespread use of ready mixed concrete system in our country, great improvements have been achieved in concrete quality. The quality of concrete is directly related to its production properties as well as its compressive strength. Accordingly, the production of high-quality and high-quality ready-mixed concrete in the construction sector has come to the fore in recent years. According to the building inspection law that came into force, the sensitivity of building inspection organizations on the strength of concrete classes has also increased.

The Electronic Concrete Monitoring System (EBIS), in which concrete samples are monitored electronically for the first time in the world, was put into use in order to prevent abuses in the ready mixed concrete inspections of the buildings. Although the results obtained show that there is no problem in the compressive strength results of the ready mixed concrete used in the buildings under construction control, the points to be considered in concrete quality were encountered and these issues were emphasized.

1. INTRODUCTION

Turkey is located on a tectonically active ground. This mobility has made itself felt especially with the earthquakes that have occurred in recent years. As the recent earthquakes have shown once again, the importance of concrete quality is of great importance in terms of building safety. Primitive concrete production levels at the construction site, which are of great importance for concrete production in Turkey, have reached the level of ready-mixed concrete production with the quality assurance system [1].

The concrete produced by mixing the materials, which are combined in the desired proportions under computer control, in the concrete batching plant or mixer and delivered to the consumer as “fresh concrete” is called “Ready Mixed Concrete”. Consistent quality is ensured by precise computerized control of water and aggregate according to the appropriate design of the mixture. High volumes of concrete

are obtained without wasting cement and aggregate due to bulk transportation. It does not cause pollution as there is no dust problem. Ready-mix concrete is an indispensable building material for the giant industrial and housing projects required by today's construction practices.

The absolute volume of concrete consists of 70% aggregate (sand, gravel, crushed stone), 20% water and 10% cement. Ready-mixed concrete aggregate is a collection of unbroken or crushed grains of non-organic, non-organic, natural or artificial material, usually not exceeding 100 mm in size, brought together with the binding material consisting of cement and water mixture in concrete or mortar making [2].

The process of determining the quality of ready-mixed concrete consists of 5 basic stages. These are; Design, Production, Transportation, Placement, Maintenance and Curing. While the first three stages are performed by the ready-mixed concrete producer, the last two stages are performed by the consumer.

The communiqué, which is based on taking samples from the fresh concrete mixture in the buildings inspected within the scope of the building inspection law, conducting experiments, creating reports according to the readings, monitoring and supervision of the stages, officially entered into force on December 25, 2018. According to the communiqué, which sets out the laws and rules governing the sampling of the concrete mixture in buildings and the reporting of the samples by subjecting them to various tests, the “Electronic Concrete Monitoring System (EBIS)” was put into effect by the Ministry of Environment and Urbanization. With EBIS, concrete samples can be monitored electronically thanks to special chips placed in concrete samples at the construction site.

The chips record electronically when concrete samples will be subjected to the crushing test, when reliable quality casting will take place, which relevant engineer will control the test, and in which laboratory the concrete quality will be checked.

With the chip system, if the people in the building query the parcel number, they will have all the information about the concrete quality of their houses. In addition to this information, it is possible to access historical construction images and information on how many times the construction has been inspected. Citizens can see images of the construction stages of the construction, control information, information about the contractor company, which engineer controlled the construction, and the problems experienced in the past.

The Ministry started to actively implement EBIS in all provinces across Turkey. EBIS enabled electronic monitoring of concrete quality at construction sites. The system, which was first used in pilot provinces, has started to be implemented throughout Turkey with positive results. The chips in question are created by Aselsan AŞ. through R&D studies using Radio Frequency Identification (RFID) tags. The main purpose of the transition to this system by the Ministry is to prevent losses, errors and leakages that may be made in applications, especially by building inspection laboratories, and to prevent counterfeiting.

It is aimed to control concrete in building constructions in a healthier and safer way, and in this context, the country is moving closer to its goal of creating better quality and livable cities by offering its citizens the opportunity to live in buildings that are safer against earthquakes. Taking samples of concrete, which is one of the most important principles of residential areas created to ensure the safety of life and property; sampling, witnessing the sample, taking the samples out of the construction site and keeping the curing processes under supervision are carried out electronically with EBIS. A safe sampling phase is created by preventing errors, losses and leaks that determine the quality of concrete in the production environment, construction site and laboratory areas.

With the chip system, the location, time of concrete sampling, concrete result report data, personnel involved in the test and technical personnel who witnessed the concrete sampling are electronically audited in provincial, district, laboratory or building inspection systems. During the collection of the concrete sample from the construction site, different location verifications are made by the personnel

officer of the laboratory organization to ensure that the concrete sample is taken from the correct building construction, and in this case, the fresh concrete sample is taken; It eliminates the possibility of non-participation of both the laboratory organization officer and the relevant engineer of the building supervision organization. The goal of EBIS is to control the curing process, to control the time of leaving the construction site, to accurately report the crushing results and most importantly to check whether the fresh concrete sample complies with the standards [3].

The aim of this study is to introduce the Electronic Concrete Monitoring System (EBIS), to investigate why such a system is needed today, to evaluate whether the strength values recorded before and after this system are statistically different and to evaluate the positive / negative issues experienced in the current application of the system. The evaluation of this system (EBIS), which is applied in Turkey for the first time in the world, will be carried out at the scale of Elazığ province. The compressive strength results of concrete samples taken from different construction sites in Elazığ will be compared with Turkish standards in the light of other statistical parameters. A comparison will be made between the desired strength values and the actual strength values in the project and an idea will be obtained about the concrete quality and production technologies obtained as a result of the application.

2. LITERATURE REVIEW

Topçu, İ. B., and Ateşin, Ö. (2013) tested the compressive strength of C30/37 concrete at various construction sites in and around Kütahya in 2011. Approximately 1023 experimental results were used to determine the status of concrete quality in Kütahya province. As a result, it was observed that the C30/37 concretes sampled in Kütahya province conformed to the standards. With this study, according to the inspection records in 2011, concrete is produced in accordance with the standards and economical in Kütahya province [1].

Güçlüer, K., Günaydın, O., Tekin, Ö.F., and Şahan, M.F. (2017) examined aggregates, the main ingredient of composite concrete, which contains materials of different origins in the structure and has a wide range of uses. In the study, the effects on the mechanical properties of concrete test specimens produced with aggregates obtained from 4 different aggregate quarries were investigated by destructive and non-destructive test methods. Comparisons were also made among themselves. As a result, the intended results were achieved with different aggregate types. The strength differences between each other were interpreted according to all effects. According to the ultrasonic values measured for the aggregates, the concrete class was found to be of good concrete quality [2].

Mehta, P.K., and Monteiro, J.M.P. (2006), in their study, describe the important applications of concrete and examine the reasons that have made concrete the most widely used building material in the world today. The basic components of modern concrete are described. A brief description of the main types of concrete is given. The properties of concrete such as strength, elastic modulus, toughness, dimensional stability and durability are examined. Recently, it has been observed that the strength classes have increased with the recycling materials used by developing the cement industry. It is stated that more

reliable and better quality concrete is produced with the increase in strength classes [4].

Öztoprak, B., Sözen, Ş. and Çavuş, M., (2018) examined the quality of ready-mixed concrete and the status of concrete plants in Bolu province. It is thought that ready-mixed concrete plants negatively affect the quality in terms of machinery, equipment and personnel. As a result of the studies, it was stated that there is a need to improve quality control methods. According to the results obtained; it was determined that there were deficiencies in machinery - equipment, tools, laboratory equipment, production control, work organization and following current technologies [5].

Ergün and Başaran (2010) aimed to statistically analyze the quality change in the quality control of concretes produced in different ready-mixed concrete plants in Afyonkarahisar between 2009 and 2010. The compressive strengths of concrete samples from three different ready-mixed concrete producers were evaluated at Kocatepe University Construction Laboratory. Considering the data of the last two years, the improvement in concrete quality in Afyonkarahisar city center was revealed and according to the results obtained, it was determined that there was a positive development in terms of reinforced concrete structures. It has been observed that the quality level in ready-mixed concrete plants is above good, but there is no production of high concrete classes [6].

Doğan, S. (2020) examined the effects of EBIS on building performance. It was stated that there were problems such as loss, error, fake report and unfair competition while taking concrete samples and it was determined that these problems were eliminated with EBIS. In the study in question, it was stated that reports prepared without sampling were prevented with EBIS and the quality of ready-mixed concrete increased [7].

3. MATERIALS AND METHODS

Within the scope of this study, the ready-mixed concrete quality of the buildings under building inspection control in Elazığ province before and after EBIS will be evaluated. Concrete compressive strengths of 15*15*15 cube specimens produced in C20, C25 and C30 standards taken from building inspection companies in Elazığ were comparatively analyzed before and after EBIS.

According to the circular issued by the General Directorate of Construction Works of the Ministry of Environment and Urbanization of the Republic of Turkey on 13.04.2022, the number of samples taken in construction laboratories according to the poured m³.

To summarize the system in general, an RFID concrete chip is placed in each sample to be taken in accordance with the standards by the laboratory personnel from the ready-mixed fresh concrete arriving at the construction site and scanned and recorded on EBIS software. The samples taken in accordance with the relevant standards are scanned again by the laboratory personnel with EBIS mobile software during the removal from the construction site. After these processes are completed, the exit from the construction site is realized.

Concrete sample reports of the buildings under building inspection control in Elazığ province were examined and samples with similar standards were identified and the data of these samples before the chip system were obtained from the building inspection companies operating in Elazığ. Similarly, concrete samples produced after the chip system were obtained from building inspections and their 7 and 28-day compressive strengths were examined comparatively.

The samples brought by the laboratory personnel are scanned again via EBIS mobile software before curing. The daily temperatures and daily relative humidity rates of the curing pools and curing rooms of the samples are transmitted to the EBIS Central Monitoring Software via sensors by the organization where EBIS services are received.



Figure 1. Part of Sampling Processes.

With the QR code application, each mixer sent to the site by the concrete producer will be labeled with a concrete mixer label and the relevant concrete producer will create a QR code and the delivery note information will be included in this code. The QR code will be read and recorded by the laboratory personnel at the construction site during sampling. The delivery note QR code includes serial number, shipment time and date, concrete quantity, 7 and 28 day strength ratios, water and cement ratio, aggregate size, vehicle license plate, additives and fiber information. In this way, it will be prevented that mixers without a label code will be poured at the construction site. Some of the Sampling Processes are shown in Figure 1.

With the “Communiqué on Monitoring and Supervision of the Processes of Sampling, Testing, Reporting and Reporting of Fresh Concrete for the Buildings Supervised under the Law No. 4708 on Building Supervision” published in the Official Gazette dated March 24, 2020 and numbered 31078, ready-mixed concrete producers are obliged to use mixer labels and delivery notes with QR codes. However, due to the pandemic, it has been implemented as of November 2020. [8]

3.1. Research findings and discussion

Within the scope of this study, the ready-mixed concrete quality of the buildings under building inspection control in Elazığ province before and after EBIS will be evaluated. Concrete compressive strengths of 15*15*15 cube specimens produced in C20, C25 and C30 standards obtained from building inspection companies in Elazığ were comparatively analyzed before and after EBIS.

According to the circular issued by the General Directorate of Construction Works of the Ministry of Environment and Urbanization of the Republic of Turkey on 13.04.2022, the number of samples taken in construction laboratories according to the spilled m3 calculation is given in Table 1.

Table 2. and Table 3. show the 7 and 28-day data statistically. In Table 2, 7-day pre- and post-EBIS data are evaluated on concrete batching plant basis, while in Table 3, 28-day pre- and post-EBIS data are evaluated on concrete batching plant basis.

When analyzed on company basis, according to the standard deviation and coefficient of variation ratio, it was observed that Company C produced better quality concrete than the other companies in concrete class C25/30 after EBIS.

Table I
DETERMINATION OF SAMPLE NUMBERS

Criterion 1	Criterion 2	Number of Transmitters to be Sampled (Number)	7 Daily (Qty)	28 Daily (Qty)	Total Number of Samples (Number)
Amount of Concrete Poured (m³)	Area Of Concrete Poured (m²)				
0-24	-	2	2	6	8
25-100	450	3	3	9	12
101-150	451-650	4	4	12	16
151-200	651-850	5	5	15	20
201-250	851-1050	6	6	18	24
251-300	1051-1250	7	7	21	28
301-400	1251-1450	8	8	24	32
401-500	1451-1650	9	9	27	36
501-600	1651-1850	10	10	30	40
>600	>1850	For each additional 200 m³ volume or each additional 200 m² area, 1 is added to the above numbers.	For each additional 200 m³ volume or each additional 200 m² area, 1 is added to the above numbers.	For each additional 200 m³ volume or each additional 200 m² area, 3 is added to the above numbers.	For each additional 200 m³ volume or each additional 200 m² area, 4 is added to the above numbers.

Table II
7-DAY STATISTICAL DATA BEFORE AND AFTER EBIS.

		BEFORE EBIS			AFTER EBIS		
		A	B	C	A	B	C
C20/25	Average	23.53	23.24	26.29	-	-	-
	Minimum	19.70	19.90	22.90	-	-	-
	Maximum	34.30	29.70	31.50	-	-	-
	Standard Deviation	2.69	2.42	2.39	-	-	-
	Coefficient of Variation (%)	11.43	10.42	9.09	-	-	-
C25/30	Average	28.19	26.68	26.16	32.13	32.19	33.73
	Minimum	23.50	22.10	22.60	27.30	28.90	30.10
	Maximum	32.00	33.00	30.10	44.00	38.30	38.00
	Standard Deviation	2.09	2.70	2.09	3.44	2.48	1.57

	Coefficient of Variation (%)	7.40	10.11	7.98	10.69	7.70	4.65
C30/37	Average	32.40	32.61	32.88	40.99	35.49	43.29
	Minimum	28.70	29.40	29.90	37.10	30.80	34.10
	Maximum	35.10	36.00	36.30	46.40	43.50	48.10
	Standard Deviation	1.52	1.97	1.55	2.11	2.74	2.76
	Coefficient of Variation (%)	4.70	6.04	4.71	5.15	7.71	6.37
C35/45	Average	-	-	-	43.35	41.70	41.34
	Minimum	-	-	-	40.00	39.80	37.90
	Maximum	-	-	-	46.50	44.10	47.00
	Standard Deviation	-	-	-	1.77	1.10	2.39
	Coefficient of Variation (%)	-	-	-	4.09	2.63	5.77

Table III
28-DAY STATISTICAL DATA BEFORE AND AFTER EBIS.

		BEFORE EBIS			AFTER EBIS		
		A	B	C	A	B	C
C20/25	Average	30.34	31.06	37.26	-	-	-
	Minimum	26.80	27.40	30.90	-	-	-
	Maximum	38.80	37.00	42.00	-	-	-
	Standard Deviation	2.35	2.63	2.36	-	-	-
	Coefficient of Variation (%)	7.75	8.46	6.35	-	-	-
C25/30	Average	36.22	35.28	33.77	41.94	44.97	45.32
	Minimum	31.00	24.60	31.00	31.30	37.30	42.10
	Maximum	41.80	41.00	37.30	51.90	51.60	49.90
	Standard Deviation	3.75	4.05	1.54	5.31	3.59	1.39
	Coefficient of Variation (%)	10.36	11.47	4.55	12.65	7.98	3.07
C30/37	Average	42.65	43.24	42.18	50.03	43.06	51.62
	Minimum	37.60	39.10	38.90	48.20	39.70	42.50
	Maximum	47.50	50.40	48.60	53.80	51.40	56.00
	Standard Deviation	2.56	2.72	1.90	1.40	2.60	2.67
	Coefficient of Variation (%)	6.00	6.29	4.50	2.79	6.04	5.17
C35/45	Average	-	-	-	49.21	49.04	50.75
	Minimum	-	-	-	46.70	44.50	46.70
	Maximum	-	-	-	51.20	53.10	55.80
	Standard Deviation	-	-	-	1.15	1.78	2.33
	Coefficient of Variation (%)	-	-	-	2.34	3.62	4.60

While better results were observed in concrete class C25/30 after EBIS, larger coefficient of variation and standard deviations were observed in concrete class C30/37. When the

coefficients of variation and standard deviation in C30/37 concrete classes are analyzed, it is seen that the ratios increased after EBIS throughout the company. In C30/37 concrete class,

Company A has a worse rate compared to the 7-day data, while Company A has a better rate compared to the other companies

In Elazığ, while the compressive strengths of the samples before EBIS were normal and above normal according to concrete classes, higher strength values were observed after EBIS. Electronic Concrete Monitoring System (EBIS) was found to have positive effects on concrete quality.

4. CONCLUSION

The evaluation of whether the transition from an uncontrollable system until recently to EBIS, which is managed by a centralized system, has changed in terms of concrete quality and application quality constitutes the basis of the problem addressed in this study. In this study, the ready-mixed concrete quality of building supervised structures before and after EBIS was evaluated in Elazığ province. In the examinations made, before EBIS, fake reports were issued in the construction laboratory and the samples were not subjected to the required tests. The curing pools are insufficient with the increasing work intensity in certain periods. With EBIS, the risk of creating a fake report in the fresh concrete sample taken from the construction site has been eliminated and it is aimed to increase the quality of concrete. The control of the samples is carried out not only by laboratory personnel, but also under the supervision of the Presidency of Defense Industry.

In the study in question, there are no C20 data after EBIS and no C35 data before EBIS. With the 2018 earthquake regulation, the lowest concrete class was C25. For this reason, C20 data after EBIS are not available. Before EBIS, concrete samples of C35 concrete strength classes could not be obtained. Since C35 concrete class was a high concrete class before EBIS, it was observed that it was not preferred by contractor companies.

REFERENCES

- [1] İ.B. Topçu, Ö. Ateşin, "Kütahya'da Üretilen Betonların İstatistiksel Değerlendirmesi," *Dumlupınar Üniversitesi Fen Bilimleri Enstitüsü Dergisi*, sayı. 30, s. 39-45, Nisan 2013.
- [2] K. Güçlüer, O. Günaydın, Ö.F. Tekin, M.F. Şahan, "Farklı Tipte Agregaların Kullanımının Betonun Mekanik Özelliklerine Etkisinin Araştırılması," *Ömer Halisdemir Üniversitesi Mühendislik Bilimleri Dergisi*, cilt. 6, sayı. 1, s. 107-114, 2017.
- [3] Y. Kaya, "Çipli Beton Sistemine Yedi Gün Sonra Geçiliyor," *İnşaat Sitesi*, [Çevrimiçi]. Mevcut: <https://www.insaat.com/haberler/cipli-beton-sistemine-7-gun-sonra-geciliyor>. [Erişim: 29 Aralık 2023].
- [4] P.K. Mehta, J.M.P. Monteiro, "Concrete," *Microstructure-Properties and Materials*, Mc Graw Hill, (3rd ed.), 2006.
- [5] B. Öztoprak, Ş. Sözen, M. Çavuş, "Bolu Bölgesindeki Hazır Beton Tesislerinin Durumu ve Beton Kalitesini Etkileyen Faktörler," *Gaziosmanpaşa Bilimsel Araştırma Dergisi*, cilt. 7, sayı. 3, s. 1-1, Ekim 2018.
- [6] A. Ergün, V. Başaran, "Afyonkarahisar'da Üretilen Hazır Beton Kalitelerinin Değerlendirilmesi," *Afyonkarahisar Üniversitesi Fen Bilimleri Dergisi*, sayı. 2010-02, s. 51-58, 2011.
- [7] H. Doğan, "Elektronik Beton İzleme Sistemi Sonrası Yapı Denetimli Yapılarda Kullanılan Hazır Beton Kalitesinin Isparta İli Ölçeğinde Değerlendirilmesi," *Gümüşhane Üniversitesi Fen Bilimleri Enstitüsü Dergisi*, cilt. 10, sayı. 4, s. 1111-1120, 2020.
- [8] Çevre Şehircilik ve İklim Değişikliği Bakanlığı, "Elektronik Beton İzleme Sistemi (EBİS) Gelişmeler ve Son Durum," *Hazır Beton Dergisi*, s. 68-69, 2020.

BIOGRAPHIES

Mehmet Taha Celik, graduated from Firat University, Faculty of Engineering, Department of Civil Engineering in 2018. He continues his master's degree in civil engineering, building materials science at Firat University Faculty of Technology. It actively works in the fields of construction, contracting and projects.

Servet Yıldız, graduated from Firat University, Faculty of Engineering Department of Civil Engineering in 1986. He completed his master's degree in 1989 and his doctorate in 1998 at Firat University Institute of Science and Technology. He was promoted to associate professor degree in 2010 and has been working as a Professor in the Department of Civil Engineering at Firat University Faculty of Technology since 2015.

Mehmet Emiroğlu, graduated from Firat University, Faculty of Technical Education, Department of Construction Education in 2004. He completed his master's degree in 2006 and his doctorate in 2012 in the Department of Construction Education at Firat University, Institute of Science and Technology. He graduated from Sakarya University, Faculty of Engineering, Department of Civil Engineering in 2015. In 2017, he was promoted to the rank of Associate Professor at the Interuniversity Board. Mehmet Emiroğlu, who was promoted to the title of Professor in 2024, works in the Civil Engineering Department of Sakarya University Faculty of Engineering